BIOCERAMIC COATING ON Ti ALLOY USING MAGNETRON SPUTTERING FOR ORTHOPEDIC APPLICATIONS

A thesis submitted in
partial fulfilment of the requirements
for the degree of

DOCTOR OF PHILOSOPHY

By

Rasmi Ranjan Behera

(126103003)

Department of Mechanical Engineering

Indian Institute of Technology Guwahati

June – 2019

DEPARTMENT OF MECHANICAL ENGINEERING

INDIAN INSTITUTE OF TECHNOLOGY GUWAHATI

GUWAHATI-781039, ASSAM

INDIA

CERTIFICATE

It is certified that the work contained in the thesis entitled **"Bio-ceramic Coating on Ti alloy using Magnetron Sputtering for Orthopedic Applications"** submitted by **Mr. Rasmi Ranjan Behera** to the Indian Institute of Technology Guwahati for the award of the degree of Doctor of Philosophy has been carried out under my supervision in the Department of Mechanical Engineering, Indian Institute of Technology Guwahati. This work has not been submitted elsewhere for the award of any other degree or diploma.

(Dr. Mamilla Ravi Sankar)

Assistant Professor

Department of Mechanical Engineering,

Indian Institute of Technology Guwahati,

Guwahati-781039, India

June, 2019

DEPARTMENT OF MECHANICAL ENGINEERING

INDIAN INSTITUTE OF TECHNOLOGY GUWAHATI

GUWAHATI-781039, ASSAM

INDIA

DECLARATION

I declare that,

a. The work contained in this thesis is original and has been done by me under the guidance of my supervisor.
b. The work has not been submitted to any other institute for any degree or diploma.
c. I have followed the guidelines provided by the institute in preparing this thesis.
d. I have confirmed to the norms and guidelines given in the ethical code of conduct of the institute.
e. Whenever I used materials (data, theoretical analysis, figures and text) from other sources, I have given their detail in references.

Rasmi Ranjan Behera

DEDICATED

TO

MY PARENTS AND FAMILY

ACKNOWLEDGEMENT

"Starting something can be easy; it's finishing is the highest hurdle". The journey of doctoral study is always a difficult and challenging task. Throughout this long journey, I have gained a lot by learning to persevere despite hardship. I would never have successfully completed this thesis without the assistance of numerous people who I am indebted to. Their direction, advice, support and contributions have proved invariable along the way.

First and foremost, I would like to express my special appreciation and respect to my supervisor, Dr. M. Ravi Sankar, who has been a tremendous mentor for me. I appreciate all his contributions of time, ideas and funding to make my PhD experience productive and stimulating. The joy and enthusiasm he has for his research were contagious and motivational for me, even during the tough times in my PhD pursuit. Thank you very much sir for your advice on my research, as well as my career, has always been priceless.

I offer my sincere thanks to my doctoral committee members, Prof. S. Kanagaraj, Prof. Pankaj Biswas and Prof. Praveen Tripathy for their insightful comments and encouragement, and also for the hard questions which incented me to widen my research from various perspectives.

I am also fortunate and grateful to receive the experimental lab facilities as well as guidance from Prof. Lalit M. Pandey (Department Bioscience and Bioengineering) and Prof. D. Pamu (Department of Physics). It was fantastic to have the opportunity to work with them through various collaborations and their valuable suggestions and concise comments have always been a source of inspiration to me.

My sincere gratefulness to past and present departmental heads Prof Pinakeswar Mahanta, Prof. Anoop K. Dass and Prof. Santosh K. Dwivedy for their kind permission for enrollment, registration and several important supports at IIT Guwahati.

I would thankful to various publishers for using some of the figures in the introduction and literature survey of this thesis.

Next, I would like to express my special sense of gratitude to Mr. Nandan Kanan Das, assistant workshop superintendent and all the staffs of the workshop specially Mr. Mrinal Sarma and Mr. Dilip Chetri for extending their help in various works related to my experiment. I sincerely acknowledge the assistance received from Mr. Saiffuddin Ahmed,

and Mr. Jiten Basumatary in various experimental proceedings. I also wise to express my gratitude to the Central Instruments Facility, IIT Guwahati for providing technical support especially to Dr. Kulakamal Senapati. Furthermore, I would like to thank Dr. Sidananda Sarma for providing XRD and FTIR facilities required for my work.

"A good friend is like a four leaf clover hard to find and lucky to have", I have been fortunate to be surrounded myself by some amazing friends for their helping hands, beautiful hearts and miscellaneous talents: Abshar, Apurba, Kishor, Sachin, Abhishek, Ambesh, Purnendu, Bhaskor, Sashank, Guru, Subhra, Jitendra, Rajendra, Harvendra, Piyush, Ramesh, Tarun, Anisha, Subash, Prathamesh, Mayuri, Deepak, Vignesh, Avnish, Devarshee, Suvayan, Varun, Swati, Aquib, Aman, Sunayan, Palomi, Rahul, Prahlad, Ishita, Indrajeet, Venky, Asha, Manavendra, Chandrabhanu, Smarti, Sumit, Shivesh, Shyam, Johnney, Muthuraja, Bibhas, Arbind and others. I am thankful to for you all for your kind support, help, motivation and presence in my PhD career and life.

It is my pleasure to acknowledge the help provided by my Utkalika family members: Sai, Himadri, Soumya, Saibal, Anand, Siba, Pratap, Bibhuti, Himanshu, Sandeep, Subhasish, Priyanka, Anil, Jayashree, Chitta, Ankan, Uttam, Santosh, Sritam, Bikash, Sanjeev, Sanjukta, Tapaswini, Sikha, Pyari, Manoj, Prakash, Dilip, Biswajeet, Niranjan, Ranjan, Manas, Bighna, Abhishek and all other group members. Thank you all for your support and presence for which I felt staying in home.

"The love of a family is life's greatest blessings". In this precious moment of my life, I would like to express my deep sense of gratitude to my parents, Mr. Bijay Kumar Behera and Mrs. Bidyut Lata Behera for their love, blessings and constant encouragement throughout my life. I would like to thanks my brother Mr. Chitta Ranjan Behera, sister in law Mrs. Tanushree Das, my sister Mrs. Priya Darsani Behera, brother in law Mr. Debabrata Behera for their love, support and best wishes. I would like to express my love to my beloved wife Mrs. Sanjana Palei for her patience, support and gratitude towards me and my family at the toughest time of PhD life. I want to offer my sincere gratitude to all extended members and relatives of my family. You have always been inspiring, supporting and teaching me to understand the true value of human life.

Rasmi Ranjan Behera

ABSTRACT

The demand for artificial implants has been increasing day by day due to their requirement for bone repairs and replacements in dental and orthopedic applications. Titanium alloy (Ti-6Al-4V) is widely used for load-bearing applications due to its superior mechanical properties. However, due to its bio-inertness, poor bonding occurs between implants and surrounding tissues resulting in poor osteointegration. On the other hand, calcium phosphate (CaP) is broadly used as the bio-material, as it has superior biological properties such as bioactivity, osteoconductivity and osteointegration. However, implants composed solely of CaP, cannot be used for load-bearing applications due to different defects arising from its poor mechanical properties. This problem can be sorted out by coating a thin layer of CaP bio-ceramic on the surface of Ti-6Al-4V substrate.

Several coating techniques are used for coating of CaP bio-ceramic on Ti-6Al-4V implant. However, these processes have at least one of following shortcomings: cracks on the surface or in the intersection of coating and substrate, poor long-term bonding of coating on the substrate, non-uniformity of coatings, and thermal decomposition of coating material. Among the different methods, the attention has been focused on the radio frequency (RF) magnetron sputtering process. RF magnetron sputtering has the ability to produce a uniform coating with strong bonding between coating and substrate. Different compositions are added to CaP bio-ceramic with different percentages to improve the structural, mechanical as well as biological properties. Furthermore, the surface texturing is also taken into consideration with the bio-ceramic coating to improve the biological properties of the implant. Therefore, in the present study, the attention is focused on to develop and improve the quality of bio-ceramic coated implant in order to enhance the functionality, durability and biological response of the implant.

In this study, the surfaces of Ti-6Al-4V substrates were modified by bio-ceramic coating using RF magnetron sputtering. In order to achieve a bio-ceramic coating without cracks and thermal decomposition, RF magnetron sputtering was used to coat biphasic calcium phosphate (BCP) on Ti-6Al-4V. BCP consists of HA and beta-tricalcium phosphate (β-TCP). BCP is mainly used in artificial tooth and bone implants due to higher protein

adsorption and osteoinductivity compared to HA alone. Hence, BCP films were deposited on Ti-6Al-4V at a particular set of sputtering parameters with varying the sputtering time. BCP film thickness of 400 nm, 700 nm and 1000 nm were obtained when sputtered for 4h, 6h and 8h, respectively. The effect of film thickness on surface roughness, wettability, mechanical properties and *in vitro* bioactivity was investigated. Uniform films with no crack and thermal decomposition were found. The hydrophilicity enhanced (contact angle decreased from 89.6±2° to 61.2±2°) with the increase in film thickness as the surface roughness increased from 112 nm to 153 nm. Excellent adhesion strength of all the BCP films to Ti-6Al-4V substrate was found, as no cracking of film up to the scratch load of 2.3 N and no significant delamination up to 7.8 N was observed. Among all the films, 1000 nm sputtered film resulted the highest increase in apatite layer (weight percentage from 44.87% to 86.7%) when dipped into simulated body fluid (SBF) for 14 days. Thus, sputtering of BCP films improves wettability, adhesion properties as well as bioactivity of Ti-6Al-4V, which can be applied for orthopedic implants. From all these findings, it can be concluded that RF sputtering is advantageous compared to laser cladding regarding CaP bio-ceramic coating on Ti-6Al-4V.

To further improve the biological performance as well as adhesion between coating and substrate, TiO_2 was added to the BCP and deposited on Ti-6Al-4V by RF magnetron sputtering. Two different compositions such as 25% TiO_2-75% BCP and 50% TiO_2-50% BCP films were deposited and compared with 100% BCP film. Post deposition, some films were annealed at 700 ^oC for 2 h to investigate the effect of heat treatment on different properties. The wettability significantly enhances with an increase of TiO_2 weight percent in the BCP films due to the increase in surface roughness. The value of critical load (L_{c2}) for 100% BCP film improved from 8.7 N to 14.8 N (25% TiO_2-75% BCP film) and more than 19 N (50% TiO_2-50% BCP film), indicating improvement in bonding strength with TiO_2 addition. The fetal bovine serum (FBS) adsorption decreased from 7.23 to 4.42 $\mu g/cm^2$ with TiO_2 weight percentage varied from 0 to 50%. Cell adhesion and proliferation were maximum for 50% TiO_2-50% BCP followed by 25% TiO_2-75% BCP, 100% BCP film and significantly higher compared to uncoated Ti-6Al-4V, however after annealing all the films exhibited less cyto-compatibility. Globular apatite structure was observed on all modified surfaces after 7 days immersion in simulated body fluid SBF; however, the growth rate was higher for 50 TiO_2-BCP films. All these results revealed that the addition of TiO_2 in BCP

film (without annealing) is advantageous for improving the bonding strength as well as the cyto-compatibility of implants, which can be used for long-term dental and orthopedic applications. Furthermore, annealing improves the adhesion strength; however, it significantly degrades the biological performances.

Not only the surface chemistry but also surface roughness plays an essential role on the biological behavior of the metallic implant. Hence, in order to achieve a better biological performance, the effect of both the surface roughness and surface chemistry is taken into consideration simultaneously, in the present study. Therefore, laser surface texturing (LST) was carried out on Ti-6Al-4V surface using Nd-YAG laser with a particular set of parameters and three different overlapping factors: 0%, 25% and 50%. Later, BCP film was coated on bare as well as textured Ti-6Al-4V specimens using RF magnetron sputtering for 7 h. In addition, annealing was performed at 700 ºC for 2 h with some sputtered specimens for comparative study. It was found that the nano-rough ($R_a \approx 94$ nm) surface of bare Ti-6Al-4V became micro-rough ($R_a \approx$ 1-2 µm) surface having micro-grooves, after LST. The wettability of textured Ti-6Al-4V significantly enhanced after BCP sputtering resulting in super-hydrophilic (17-21º) surface; however, the wettability deteriorated to 68-81º after annealing. The amount of protein adsorption increased from 5.3 to 8.1 µg/cm^2 with enhancement of hydrophobicity of the Ti-6Al-4V surface. The BCP deposited textured substrates exhibited higher bioactivity, cell adhesion, as well as cyto-compatibility compared to BCP deposited bare Ti-6Al-4V despite lesser protein adsorption. Among these, BCP deposited on 50% overlapping factor Ti-6Al-4V (BCP-50% Ti-6Al-4V) had maximum cell adhesion and proliferation. However, annealing deteriorated the cell spreading and adhesion. Hence, these findings revealed that the BCP film deposited on a micro-roughness textured surface enhances the wettability, cell adhesion and proliferation as well as bioactivity of the implant, which can be beneficial for orthopedic implants.

Finally, it can be summarized that RF magnetron sputtering is a better technique for deposition of CaP bio-ceramic on Ti-6Al-4V implant. TiO_2 addition in BCP film enhances the biological performance as well as adhesion behavior of implant compared to BCP film; hence, it can be a good choice for the long-term application of orthopedic and dental implants. In addition, surface texturing on Ti-6Al-4V with 1-2 µm roughness followed by BCP film deposition is a better option for the orthopedic as well as dental applications.

TABLE OF CONTENTS

LIST OF FIGURES

LIST OF TABLES

ABBREVIATIONS

CaP	Calcium phosphate
LC	Laser cladding
RF	Radio frequency
LED	Laser energy density
HA	Hydroxyapatite
TiO_2	Titania
FGM	Functionally graded material
BCP	Biphasic calcium phosphate
β-TCP	beta-tricalcium phosphate
CA	Contact angle
SBF	Simulated body fluid
FBS	Fetal bovine serum
LST	Laser surface texturing
Nd:YAG	Neodymium-doped yttrium aluminum garnet
100 BCP	100 wt.% BCP
25TiO_2-BCP	25 wt.% TiO_2-75 wt.% BCP
50TiO_2-BCP	50 wt.% TiO_2-50 wt.% BCP
OF	Overlapping factor
BCP-(0% OF)Ti-6Al-4V	BCP deposited on 0% OF textured Ti-6Al-4V
BCP-(25% OF)Ti-6Al-4V	BCP deposited on 25% OF textured Ti-6Al-4V
BCP-(50% OF)Ti-6Al-4V	BCP deposited on 50% OF textured Ti-6Al-4V
BCP-bare Ti-6Al-4V	BCP deposited on bare Ti-6Al-4V
SS	Stainless steel
Ti	Titanium
Al	Aluminium
V	Vanadium
ISO	International Organization for Standardization
FDA	Food and Drug Administration

PS	Plasma spraying
IBAD	Ion-beam-assisted deposition
MAPLE	Matrix-assisted-pulsed laser evaporation
PLD	Pulsed laser deposition
MAO	Micro-arc oxidation
EPD	Electrophoretic deposition
DMD	Direct metal deposition
LSA	Laser surface alloying
DLM	Direct laser melting
LENS	Laser engineered net shaping
LACS	Laser-assisted cold spraying
CL	Coating layer
TL	Transition layer
HAZ	Heat affected zone
CW	Continuous wave
WG	Water glass
PVA	Polyvinyl alcohol
α-$Ca_2P_2O_7$	Alfa-dicalcium pyrophosphate
$Ca_3(PO_4)_2$	Tricalcium phosphate
CaO	Calcium oxide
$CaTiO_3$	Calcium titanate
$CaCO_3$	Calcium carbonate
OPC1	Osteoprecursor cells
Y_2O_3	Yttria
Si-HA	Silicate-containing HA
EDS	Energy dispersive spectroscopy
$(CH_2OH)_3CNH_2$	Tri-hydroxymethyl aminomethane
$NaHCO_3$	Sodium bicarbonate
$K_2HPO_4 \cdot 3H_2O$	Dipotassium hydrogen phosphate trihydrate
$MgCl_2 \cdot 6H_2O$	Magnesium chloride hexahydrate
$CaCl_2$	Calcium chloride

Na_2SO_4	Disodium sulphate
DMSO	Dimethyl sulphoxide
WEDM	Wire-electro discharge machining
FESEM	Field emission scanning electron microscopy
FETEM	Field emission transmission electron microscope
PSA	Particle size analyzer
XRD	X-ray diffractometry
BCA	Bicinchoninic acid
PBS	Phosphate buffered saline
SDS	Sodium dodecyl sulphate
DMEM	Dulbecco modified essential medium
PI	Propidium iodide
PP	Polypropylene
MTT	3-(4,5-Dimethylthiazol-2-Yl)-2,5-Diphenyltetrazolium Bromide
SAED	Selected area electron diffraction
IFFT	Inverse fast Fourier transform
CTE	Coefficient of thermal expansion
at%	Atomic percentage
wt%	Weight percentage
ECM	Extracellular matrix
FN	Fibronectin
DI	Deionized
CCD	Charged coupled device
COF	Coefficient of friction
AFM	Atomic force microscopy
100 BCP-ann	100% BCP after annealing
25 TiO_2-BCP-ann	25 TiO_2-BCP after annealing
50 TiO_2-BCP-ann	50 TiO_2-BCP after annealing
FTIR	Fourier-transform infrared spectroscopy

NOTATIONS

R_a	Centre line average height
P_{avg}	Average power
SS	Scanning speed
D	Laser beam size
P_{peak}	Peak power
PD	Laser pulse duration
f	Laser pulse repetition rate
I	Input current
V	Applied voltage
η	Efficiency of the laser
F	Laser fluence
G	Temperature gradient
R	Solidification rate
θ	Young contact angle for ideal surface
r	Surface roughness factor
θ^*	Apparent contact angle
L_c	Critical load
L_{c1}	Lower critical load corresponding to cracking of coating
L_{c2}	Critical load corresponding to delamination of coating
R_q	Root mean square roughness
S_{kew}	Skewness

Chapter-1

Introduction

1.1 Background and motivation

Over the past few decades, different cases of musculoskeletal related diseases such as osteoarthritis, rheumatoid arthritis, and osteonecrosis are increasing each year. These diseases occur due to injuries, tumors, infections and osteoporosis in human hard tissue. Effective medical treatment is needed to address musculoskeletal-related disease. Joint replacement is a medical surgery procedure to alleviate pain and disability in those suffering from musculoskeletal disease. The number of cases of joint replacement surgery undertaken each year continues to increase. In America in the year 2010, the total number of hip and knee replacements was estimated at 2.5 million and 4.7 million, respectively (Kremers et al., 2015).

Biomaterials are artificial or natural materials, used for fabricating structures or implants, to replace the lost or diseased biological structures, that would help to regain form and function. There are three major classes of metals used for developing orthopedic implants today: stainless steel (316L SS), cobalt chromium (Co-Cr) alloys and titanium (as alloys and commercially pure). The low modulus of Ti and its alloys (110 GPa) compared to 316L SS (210 GPa) and Co-Cr alloys (240 GPa), endows Ti with mechanical properties that make it useful for implant applications (Ratner and Hoffman, 2013; Ratner et al., 2004). Although the strength of titanium alloys is similar to that of 316L SS, its density is ~55% lower than steel, yielding a very high specific strength (strength per density) in the range of 20-25 $kgf/mm^2/g/cm^3$ making titanium and its alloys an important implant material for orthopedic applications (Ratner and Hoffman, 2013; Ratner et al., 2004). Due to the excellent corrosion resistance, relatively low modulus, good fatigue strength, formability and machinability, Ti and its alloys can be widely used for load-bearing implants. In addition, due to their bioinert nature resulting from a stable oxide layer that forms on the surface, Ti and its alloys have been extensively investigated as implant materials. The stability and corrosion resistance of Ti is provided by the naturally occurring titanium dioxide layer present on the surface of the metal protects the metal from further oxidation (Schutz, 1987).

There is not only high demand of orthopedic surgeries for new patients every year, but also higher demand for patients who must receive revision surgeries. The failure of implants after surgery occurs due to various factors such as are instability, aseptic loosening, infection, wear/corrosion, fibrous encapsulation, osteolysis, ingrowth failure, and periprosthetic fracture (Dobzyniak et al., 2006; Losina et al., 2004). Since these operations are painful to endure, expensive and occasionally more complex than the primary joint replacement surgery, it would be ideal if the life of the implant exceeded the lifetime of the patient. Unfortunately, these implants often work loose over time and require revision surgeries to re-secure or insert new hardware. The expected in-service life of total knee replacements is between 10 to 15 years before this revision is required (Fehring et al., 2001). The successes of these procedures are highly dependent on a number of factors including competency of the surgeon, post operation infections, and the interaction between the implant and the surrounding tissue. From an implant design perspective, little can be done to improve the skill of the surgeon so it is necessary to focus primarily on materials optimization to promote natural tissue integration. In addition, implant loosening accounts for 70% of the cases for revision surgery. Therefore, great effort has been made to develop suitable implant materials with zero-rate revision surgery (Choong, 2009).

Despite of having a number of suitable properties, the main problem associated with the use of Ti and its alloy is not to support new bone tissue in-growth and vascularization. In addition, Ti and its alloy have a much higher elastic modulus than natural bone, i.e., 5 GPa and 110 GPa for bone and Ti, respectively (Legeros and Craig, 1993). This biomechanical mismatch causes an insufficient stress transfer to bone, leading to bone resorption (stress shielding) and may lead to aseptic loosening of implants after a few years of implantation, which results in revision surgery (Oshida, 2010). The implant material needs to bear load which has an effect of shielding the surrounding skeleton from its usual stress level (Maya et al., 2012). The biocompatibility of commonly used Ti alloys, such as Ti6Al4V, is also an important concern in these applications due to the potential adverse reactions of metal ions with the surrounding tissues once these ions are released from the implant surfaces (Okazaki et al., 1998). Aluminum and vanadium ions can cause neurological disorder and toxic reactions, respectively. This medical situation can be prevailed over only with a rapid bone formation that can help to fill deficient bone and fix the implant firmly to the adjacent bone.

To achieve this, the implant material surface must be capable of recruiting bone forming cells (osteoblast) to colonize, thereby initiating bone formation. Due to these ever-increasing human needs, active research on long lasting biomaterial implants is booming.

The long term inertness of Ti and Ti6Al4V towards human tissues after implantation is a major drawback due to a lack of direct chemical bonding between the implant and host tissues. To address the existing problems of high elastic modulus of pure Ti and the potential toxicity of Ti6Al4V implants, certain surface treatments are necessary to enhance the performance of the implants. An appropriate surface modification technique not only would retain the bulk attributes of Ti6Al4V, but also improve its specific surface properties. The modifications of the surface can be achieved either by changing the surface chemistry through coating the bioactive material on the Ti6Al4V or by varying the surface roughness through surface texturing process. Bioactive materials are commonly applied onto metallic biomaterials to provide an attachment mechanism for the implant materials onto the living bone. One way to improve the healing process is the application of a calcium phosphate (CaP) based bioceramic coating, i.e., a synthetic ceramic resembling bone mineral composition onto the surface of orthopedic implants. The CaP layer is able to promote the bio-integration process due to its ability to adsorb molecules of water and proteins, thus stimulating new bone tissue growth around the implant (Surmenev et al., 2014).

Currently plasma spray is the most commonly used technique for depositing a CaP layer. However, a plasma sprayed coating often exhibits poor adhesion between the substrate and coating, resulting in delamination, which leads to fibroblast formation and subsequently prevents the production of bone tissue. Radio frequency (RF) magnetron sputtering is a versatile method for depositing CaP onto metals because it offers excellent adhesion and a uniform and homogenous coating. Different CaP bioceramics such as β-tricalcium phosphate (β-TCP), hydroxyapatite (HA) and biphasic calcium phosphate (BCP) are used for different biomedical applications. HA has higher stability with lower absorption rate, whereas, β-TCP has higher bioactivity due to its bio-integration and rapid dissolution among different CaP ceramics (Heimann, 2013; Ogose et al., 2005). BCP is a mixture of β-TCP and HA; hence, the combined properties allow one to tailor the rate of dissolution to some extent. A general pattern of bio-resorption of different CaP ceramics is as follows: HA < BCP < β-TCP (Ebrahimi et al., 2017). Furthermore, BCP exhibits higher hydrophobicity than HA, but

lower than β-TCP (Wang et al., 2012). Thus protein adsorption is more by BCP due to hydrophobic interactions, resulting in better osteoinductivity than HA (Wang et al., 2012). Because of excellent biocompatibility, BCP is used extensively in delivery of hormones, repair of nasal spectrum, bone and tooth implants as well as synthetic bone graft materials. Although HA coatings have been applied widely for bone implants, there is limited research on the BCP coating on Ti6Al4V alloy. Considering the hydrophobicity and protein adsorption of BCP; it was selected as the coating material deposited on the surface of Ti6Al4V using RF magnetron sputtering. This study evaluated the physical, structural, mechanical properties and in vitro bioactivity of the BCP sputtered Ti6Al4V with different thicknesses.

Higher functionality and longevity of the orthopedic implants have motivated the development of new materials that have improved biological properties as well as stronger bonding between coating and substrate. It has been reported that TiO_2 coatings secreted higher bone markers than silica and calcium phosphate; thereby indicating that TiO_2 supports osteoblast growth and bone remodeling (Verket et al., 2012). However, to date, the use of composite coating of TiO_2 and BCP is still limited. It was anticipated that the TiO_2 addition would enhance the biological performance as well as the mechanical stability of BCP coating with the substrate. In regard to enhance the biocompatibility as well the bonding strength of coating with the Ti6Al4V implant, BCP-TiO_2 composite was deposited onto Ti6Al4V. The effect of TiO_2 content in the BCP coating on physical, structural, mechanical as well as biological properties was investigated. The bonding strength of the coating with Ti6Al4V substrate was evaluated to determine the effect of TiO_2 addition in the improvement of bonding strength of BCP coating. Cell adhesion and proliferation tests were conducted to determine the effectiveness of TiO_2 in the biological performance of the coatings.

In addition, surface texturing has also been gaining interest as a surface modification method on Ti6Al4V due to its ability to improve biocompatibility and its flexibility in controlling the surface area and topography as well as wettability of the implant. Although surface texturing has been widely used to enhance osteointegration of the implant, to date there is no study reported yet on BCP deposition laser textured Ti6Al4V as a potential material for bone implants. It was expected that the simultaneous effect of surface texturing and BCP coating would improve the wettability as well as the biocompatibility of the

implant. In this study, Ti6Al4V surface was modified by laser texturing followed by BCP deposition using RF magnetron sputtering. This study evaluated the physical, structural and biological properties of the newly developed Ti6Al4V having various surface topography with BCP coating.

This study investigates the effects of both coating and texturing used to modify Ti6Al4V in terms of their structural properties, mechanical properties, and *in vitro* biological performances. The coating, texturing and post-deposition processes affect different properties of a biomaterial, such as surface roughness, surface topography, chemical composition, crystallinity, surface chemistry and wettability (Bächle and Kohal, 2004; Hoppe et al., 2011). All these properties affect the essential initial interaction and growth of protein adsorption as well as bone cells on an implant (Bächle and Kohal, 2004; Okauchi-Yabuuchi et al., 2008; Schmidt et al., 2002). Having further understanding of the process-structure-property relationship would provide guidelines for implant design and control (Surmenev et al., 2014), such as controlling its biocompatibility or bioactivity depending on the intended application. Overall, the development of modified Ti6Al4V will contribute to long-term bone implant performance, which will improve life quality and reduce the economical burden on society.

1.2 Aim and objective of the thesis

The limited lifespan of orthopaedic implants coupled with increasing global demand have caused the occurrence of implant failure to rise. Modification of current existing implant coatings such as HA may prolong the service life of Ti-based orthopaedic implants. However, BCP can be used as coating material for fast bone remodeling due to the combined properties of HA and β-TCP which regulate the rate of dissolution with the stability, resulting in better osteoinductivity than HA. The detachment of CaP coating is affected by many factors such as coating method, processing parameters, coating thickness and coating structure. RF magnetron sputtering has the ability to produce thin and well-adhered coatings which may alleviate the problem of CaP delamination and particle release. However, CaP particles might be liberated from the coating due to the movement at the implant–bone interface, which can ultimately lead to failure of the artificial implant. Therefore, the adhesion strength of CaP coating should be taken into account for prolong service life of the artificial implant. TiO_2 can be incorporated with the CaP in order to enhance the adhesion

strength of the coating, as TiO_2 possess higher chemical stability. The fabrication (coating) and post deposition processes, such as annealing, affect properties such as chemical composition, structure, topography, and dissolution. As-deposited CaP coating is amorphous which releases Ca^{2+} and $(PO_4)^{3-}$ components that are essential for bone proliferation and mineralization. The amorphous structure however, is less stable in human body. This problem is solved after annealing of CaP coating, which converts the amorphous structure to crystalline. However, with the crystalline structure of CaP coating the dissolution is less, that reduces cell proliferation and mineralization. Hence, the annealing of these CaP surfaces is carefully controlled so that the coating's integrity and subsequent biofunctionality can be maintained. Furthermore, the surface texturing of the implant affects the surface area, surface roughness and topography as well as wettability of the implant, which controls protein adsorption and cell adhesion. Hence, the simultaneous effect of BCP coating with surface texturing may enhance the osteointegration of orthopedic implant.

With the aim to bridge the gaps in the literature as reviewed in Chapter 2, the present study is driven by the need to produce biomaterials that mimic bone structural, mechanical and biological properties to enhance implant longevity and functionality. The objectives of this study are as follows:

1. Fabrication and characterization of BCP coating deposited on Ti-6Al-4V using RF magnetron sputtering with different film thickness.
2. To prepare BCP, 25%TiO_2-BCP and 50%TiO_2-BCP films on Ti-6Al-4V using RF magnetron sputtering with and without annealing.
3. Deposition of BCP film on the textured Ti-6Al-4V (having three different overlapping factors) fabricated by laser surface texturing.
4. To investigate the morphology, structure, surface roughness, wettability and adhesion strength of the as-deposited coatings and the effects of post-deposition heat treatments.
5. Study of *in vitro* bioactivity, protein adsorption, cell adhesion and proliferation on the above modified substrates.

1.3 Organization of thesis

Current thesis is organized into 6 chapters based on the above five objectives with references and appendices at the end.

Chapter 2 discusses the literature review of biomaterials, historical as well current biomaterials used in implants, need for surface modification and coating of metallic implant for biomedical applications. Different coating processes with their advantages and shortcomings are described briefly. A short discussion about the most commonly used biomaterial such as CaP-based hydroxyapatite and TiO_2 is elaborated. A brief literature review on CaP coating on Ti and its alloy by RF magnetron sputtering are discussed. Relevant literatures in the area of CaP sputtering and its effect on structural properties, mechanical performance and biological behaviors are presented. Finally, the summary and gaps in the literature, different challenging issues, plan of the present thesis are described.

Chapter 3 deals with the deposition of biphasic calcium phosphate (BCP) films on Ti-6Al-4V by RF magnetron sputtering process. The effect of film thickness on surface morphology, roughness and wettability are investigated. A comparative study of the scratch test as well as *in vitro* bioactivity with various film thickness is carried out.

Chapter 4 investigates different BCP-TiO_2 films are fabricated on Ti-6Al-4V by RF magnetron sputtering and compared with BCP film. The modified surfaces are also annealed to study the effect of heat treatment on mechanical and biological performances. The modified surfaces are physically and chemically characterized in terms of surface morphology, phase composition, surface roughness, wettability. The adhesion behavior is investigated by conducting the scratch test on the modified surfaces. In addition, the different biological properties such as protein adsorption, *in vitro* bioactivity, cell adhesion and proliferation are determined and compared.

In Chapter 5, surface texturing with different overlapping percentage is carried out on Ti-6Al-4V using Nd:YAG laser. Afterwards, BCP film is deposited by RF magnetron sputtering. Surface morphology, phase composition, surface roughness, wettability of different modified surfaces are performed. Fetal bovine Serum (FBS), simulated body fluid (SBF) and MG63 osteoblast like cells are used to study protein adsorption, *in vitro*

bioactivity, cell adhesion and proliferation, respectively. The effect of texturing with the different overlapping factors on biological properties are investigated and compared with BCP coated non-textured Ti-6Al-4V.

Chapter 6 summarizes the main findings of the present work and also gives directions for future research in the field of bioceramic coating. The outcome of the present work in the form of various journal papers and conferences is reported.

Chapter 2

Literature Review

This chapter reviews the existing literature on various methods of surface coating of CaP bio-ceramic material and their implications on adhesion strength and biological performance (Protein adsorption and cellular behavior). Different factors governing the adhesion strength and cellular behavior of the coating are reviewed in depth. At the end, the effect of surface texturing on the protein adsorption and cell adhesion is discussed.

2.1 Biomaterials overview

Biomaterial is defined as the foreign material, either naturally derived or artificially synthesized, which interacts with the biological systems for the replacement and repair of damaged tissues and organs, leads to improvement in the quality of life (Hench and Polak, 2002). The advantages of using biomaterials include (i) a lower risk for transmission of diseases, (ii) a reduced risk of infection, and (iii) the availability of many materials for a variety of specialized applications (Ratner et al., 2004, 2006). These biomaterials are used as implant in human body for various applications such as hip replacement, knee implant, dental implant, cardio-vascular devices, maxillofacial reconstruction, needles, catheters, tooth fillings, and bone plates etc. (Geetha et al., 2009; Ratner et al., 2006). Studies on biomaterials commenced around five decades ago. The implants have been developed up to certain extent; however, the research is still in the process of improvement on many aspects. Recent developments include bioactive biomaterials with improved capability to facilitate new bony tissue in-growth after implantation (Hench and Polak, 2002). Moreover, depending on the functions and biological environment, hemo-compatibility and osseo-compatibility are crucial *in vivo*. Hence, biomaterials design requires understanding of diverse disciplines that include clinical medical sciences, materials science and engineering. The specific nature of biomaterials includes polymers, metals, ceramics and composites of these materials; which are all designed with specific functionality in mind. That means they are designed separately based on the particular application. In order to obtain a good quality implant, the biomaterial should require certain essential properties to perform, which is described in the following section.

2.1.1 Criteria of ideal bone implant

An ideal bone implant material should have osteoconductive, osteoinductive and osteointegration ability (Bauer and Muschler, 2000). Furthermore, other key criteria for implant performance include biocompatibility and mechanical compatibility. In addition, the implant waste after degradation should not cause harmful effects to the body. Osteoconduction is a process by which bone is directed to conform to a material's surface, while osteoinduction is the ability of an implant to induce osteogenesis. An inductive agent will stimulate undifferentiated cells to form preosteoblasts. According to Branemark et al., osteointegration could be defined as the attachment and growth of bone cells and surrounding tissues into the implant providing lasting, specific clinical functions without initiating rejection mechanisms (Branemark et al., 2001). Biocompatibility is a property of the implant does not cause any toxic, allergic or inflammatory reactions within the body (Geetha et al., 2009; Ratner et al., 2004). If the implant material is toxic, the periprosthetic tissue dies (Geetha et al., 2009; Nuss and von Rechenberg, 2008). If the material is inert or biotolerant, i.e. biologically inactive and non-toxic, a fibrous tissue can form. Without true integration into the implant, the ultimate result is rejection. However, if the material is biologically active and non-toxic (bioactive), interfacial bone formation occurs, leading to osteointegration and implantation.

The elements responsible for the building of bone are osteoblasts (bone-forming cells), osteoclasts (cells which break down or resorb bone) and osteocytes (mature bone cells). They regulate the process of homeostasis, i.e. the growth, development, repair and remodelling of bone (Rho et al., 1998). The process of bone formation is alternatively termed osteogenesis or ossification. Osteoblasts synthesize the organic components of bone, i.e. collagen, glycoproteins and proteoglycan (Nuss and von Rechenberg, 2008). Also, osteoblasts migrate from connective tissue to the membranes and deposit bony matrices around themselves to form mature osteocytes (Hoppe et al., 2011). Early growth and maturation of immature cells on an implant determine the long term service life of the implant (Okauchi-Yabuuchi et al., 2008). The post-implantation bone healing process, at the cellular level, involves various cells, a signal transduction pathway, hormones and growth factors; all of which have been described in detail in literature (Anil et al., 2011; Bächle and Kohal, 2004; Nag and Banerjee, 2012; Nuss and von Rechenberg, 2008; Okauchi-Yabuuchi

et al., 2008; Vandrovcova et al., 2012). The attachment, proliferation, differentiation and ultimately the long-term viability of these cells is mediated by extra cellular matrix (ECM) molecules such as fibronectin and associated integrins. The ECM molecules are available from the cell or from the cell culture media.

In addition to high mechanical strength, the Young's modulus is a critical mechanical property in an artificial device when designing materials for bone implant applications. Other fundamental requirements for an ideal orthopaedic biomedical implant include high wear resistance, good fatigue properties if used under cyclic loading, no adverse tissue reactions, and high corrosion resistance. Figure 2.1 illustrates the desirable criteria of an ideal bone implant.

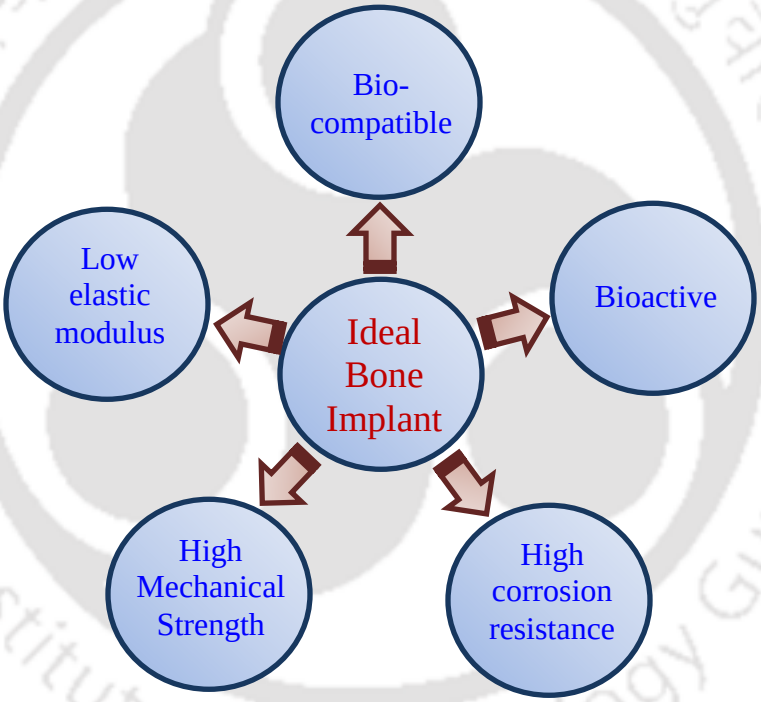

Figure 2. 1: *Criteria of an ideal bone implant*

2.2 Historical development of biomaterials

Before the 20th century, naturally derived materials were used to help repair and augment the body. For example, shaped wood was used as structural replacements for tissues lost during trauma or disease, whilst in ancient Egypt, seashells were used as teeth replacements (Sahoo et al., 2013). In the early 20th century, synthetic polymers, metallic alloys and ceramics started to be used. Rapid advancements in technology and increased efficacy led to a range of

applications such as dental restoratives, artificial hip joints and contact lenses. Advancements in molecular biology in the 1970s, genomics in the 1990s and proteomics in the 2000s contributed significantly to the design and development of the current range of biomaterials. Biomolecular enhancement of biomaterials refers to their bioactive components which utilize well established molecular pathways to elicit a biological response.

The historical development of bone-related biomaterials, with focus on load-bearing, total joint replacement (TJR) implants, is now briefly described. Arthroplasty, the surgical replacement of joints (Mantripragada et al., 2013), initially made use of stainless steel for load-bearing, total joint replacement implants. 316L stainless steel was used primarily for temporary devices such as hip nails, fracture screws and plates. However, with the rise in total TJR surgery, it became evident that the very high modulus of stainless steel was unsuitable due to problems with stress-shielding and corrosion. Cobalt-chromium-molybdenum (Co-Cr-Mo) alloys were then developed, but high modulus and biocompatibility issues rendered this material unsuitable for load-bearing applications. Bone cements were used to fix the implant into bone. In order to resolve issues regarding the adverse effects of bone cement wear particles that may ultimately require revision surgery (Wang et al., 2004), the concept of uncemented implants was birthed in the 1960s (Mohseni et al., 2014; Yang et al., 2005). Uncemented implants rely on biological fixation using the natural bone cells of the body. Backtrack to the mid-1970s, Ti-alloys started to gain popularity due to their lower modulus, being closer to that of bone, combined with good levels of specific strength, biocompatibility, superior osseointegrative ability and higher corrosion resistance. Commercially pure titanium (CpTi;) was the first Ti product to be used due to its naturally-occurring surface passivating oxide film which provides corrosion resistance and reduces the risk of metal ion release (Geetha et al., 2009; Ratner et al., 2004; Schmidt et al., 2002). CpTi, however, exhibits limited specific strength and hence limited its use to e.g. dental implants, pacemaker cases and hip cup shells. The need to improve on strength for load-bearing applications for TJR led to the development of an alloy originally developed for aerospace applications, i.e. Ti-6Al-4V extra-low interstitial alloy made from Ti with 6 wt% Al and 4 wt% V. It exhibits an elastic modulus of ~ 110 GPa which is half that of 316L stainless steel. Whilst it has been used successfully for TJR, it was found that V is cytotoxic and causes adverse tissue reaction. However, further studies found that both V and

Al ions released from the alloys into the body could cause long-term health problems, such as osteomalacia (softening of the bones), Alzheimer's disease (a type of dementia) and peripheral neuropathy (peripheral nerve damage) (Lee, 2014). These circumstances led to developments of new and improved orthopaedic implant materials (Nag and Banerjee, 2012).

2.3 Current materials used in implants

Four major classes of materials, i.e. polymeric, metallic, ceramic and composite, have been used as biomaterials (Brown et al., 2010; Ratner et al., 2006). Even though each of the materials has certain advantages for the particular application; however, they exhibit particular drawback which is not suitable for that application. Table 2.1 shows the current biomaterials used in the bioimplant; whereas, advantages and disadvantages of the most commonly used biomaterials are given in Table 2.2. Ceramics such as calcium phosphate and bioactive glass have been studied as bone graft scaffolds and showed excellent bioactivity, osteoconductive and biocompatible features. However, low strength, brittleness, inelasticity, low impact resistance and low toughness of these ceramics are a hindrance for use as bone implants (Chen et al., 2011).

Table 2. 1: Overview of biomaterials used for biomedical implants (Nuss and von Rechenberg, 2008; Ratner et al., 2006)

Implant	Material
Skeletal system	
Joint replacements e.g. hip, knee	Polyethylene, 316LV (stainless steel; SS), Titanium (Ti), Ti-6%Al-4%V (Ti64 or Ti6Al4V) alloy
Bone cement	Poly(methyl) methacrylate (PMMA)
Bony defect repair	Hydroxyapatite (HA)
Bone plate for fracture fixation	Cobalt-chromium (Co-Cr) alloy, 316LV (stainless steel; SS)
Dental implant	Calcium phosphate, polyethylene, Ti, Ti-Al-V alloy, SS
Cardiovascular system	
Catheter	Silicone rubber, Teflon, polyurethane
Blood vessel prosthesis	Polyurethane, Dacron, Teflon
Heart valve	Carbon, reprocessed tissue, SS
Organs	
Heart-Lung machine	Silicone rubber
Artificial kidney (hemodialyser)	Hydrogel e.g. Cellulose, polyacrylonitrile

Artificial Heart Skin repair template	Polyurethane Silicone-collagen composite
Senses Corneal bandage Cochlear replacement Contact lens	 Hydrogel, Collagen Platinum electrodes Hydrogel, Silicone-acrylate

Table 2. 2: Advantages and disadvantages of materials used in biomedical applications (Chen et al., 2011)

Material	Advantage	Disadvantage
Metals Titanium and alloys Tantalum Magnesium Stainless steel Cobalt chromium	• Biocompatible • Light weight • Cytocompatibility • High corrosion resistance (Ti and Ta) • Biodegradable (Mg) • Excellent mechanical strength suitable for load bearing • Ductile	• No direct bonding to tissue • High elastic modulus • Low corrosion resistance (Mg)
Ceramics Bioglass Hydroxyapatite Aluminium Oxide	• Biocompatible • Bioactive • Strong in compression	• Brittle • Weak in tension • Low impact resistance
Polymers Polyester PUL PMMA PLLA PEG	• Biodegradable • Ductile • Easy to fabricate • Light weight	• Low mechanical strength • Bioinert

Porous polymers such as polyurethane (PUR), poly (lactic co-glycolic acid) (PLGA), polylactide (PLLA), and poly-DL-lactide (PDLLA) are also attractive candidates for applications as implants because they provide a conducive environment for cell adhesion, proliferation and differentiation. Studies of polyesters as biomaterials for bone regeneration applications have increased due to their history of clinical success (Pantojas et al., 2009). Biodegradable polymers are also favorable for scaffolds due to their flexibility to control the degradation rate through copolymerization. However, their bioactivity and mechanical strength are drawbacks for load bearing applications.

As already discussed that metals and their alloys, such as titanium, stainless steel, and chromium cobalt generally have high mechanical strength, which is suitable for load bearing bone substitutes. Table 2.3 is a summary of the mechanical properties of bone and bone implant materials. Moreover, metallic based biomaterials exhibit high tensile strength that is not a feature of polymers or ceramics, thus favorable for load bearing applications. However, the inertness of metal alloys towards human tissues after implantation is a major drawback, as they lack direct chemical bonding between the material and host tissue. In the case of titanium, the implant may loosen due to the significant difference between the elastic modulus of titanium and natural bone that causes stress shielding (Kujala et al., 2003). The elastic modulus of Ti alloy (Ti-6Al-4V) is in the range of 55-110 GPa which is significantly higher than natural bone (Legeros and Craig, 1993). Another drawback of Ti-6Al-4V is the release of Al and V ions from the alloys into the body, which could cause long-term health problems. The inability of the metals to biodegrade leads to additional surgery. Hence, all these circumstances led to developments of new Ti alloy or surface modification of Ti-6Al-4V to achieve improved orthopaedic implant materials. In this study, the main focus is given to surface modification of Ti-6Al-4V with bioactive coating.

Table 2. 3: Mechanical properties of bone and bone implants materials (Legeros and Craig, 1993).

Material	**Elastic modulus GPa**	**Tensile strength (10^{-3}) GPa**
Cortical bone	20	150
Cancellous bone	3	5
Stainless steel	200	700
Co-Cr-Mo alloys	230	500
Titanium	110	500
Ti-6Al-4V	110	950
Hydroxyapatite ceramics	20	100[a]
Glass ceramics	30	200[a]
PMMA	3	80

[a] Bend strength values

2.4 Need for surface modification

Over the last few decades consistent improvements and innovations have been carried out to obtain huge and sustainable progress in the biomaterials development, which results in advanced medical devices and implants (Bhatia et al., 2013; Holzapfel et al., 2013). The expectation on future implants is long-term clinical performance with zero revision surgery. Revision surgery is undesirable due to health, social and economical implications, and is sometimes more complex than the primary surgery. The main reasons behind revision surgery are poor osteointegration at the implant-bone interface, aseptic loosening and infections. Aseptic loosening that may occur after long term implantation is mainly due to (i) the biomechanical mismatch of the implant and surrounding tissues, and (ii) fibrous tissue formation that leads to implant mobility. One way to overcome the biomechanical mismatch is to lower the elastic modulus by designing novel materials or modifying the surface of the biomaterials.

In recent years, considerable attention has been given to the surface modification of biomaterials, because the surface of material plays a crucial role when an implant or any other biomaterial comes in contact with biological environment. At these surfaces of material not the bulk material, a cascade of processes/reactions occurs such as protein adsorption, cell adhesion, proliferation and differentiation. The modified surface allows bone to grow and locks the artificial implant for enhanced fixation because of various binding interactions occurs due to surface chemistry and surface topography. The surface modification has been achieved either changing the surface chemistry or by varying the surface topography using texturing and coating process, respectively. Surface texturing of material enhance the surface roughness which favors the cell attachment and proliferation because of higher surface area. Surface coating of the biomaterial known as bioactive coating resolves the problem of poor osteointegration from the coating material and achieves the superior mechanical properties from the metal base.

2.5 Bioactive coating

Bioactive coating is a surface modification process that changes the composition, structure and morphology of a surface with maintaining the mechanical properties and improving the bioactivity of the biomaterials so that they could exhibit a higher apatite-inducing

ability that leads to rapid osteointegration. Surface modification of an implant could produce an active apatite layer, which can be used as a bonding interface that stimulates bone apatite and collagen production (Chen et al., 2008). According to Kokubo, bone apatite and collagen production took place on the apatite layer (Kokubo, 1991). It has been suggested that altering the nanostructured surface morphology will influence the apatite-inducing ability and improve osteoblast adhesion and differentiation (Li et al., 2007). Different types of bioactive materials such as calcium phosphate, bioglass, TiO_2, ZrO_2, Al_2O_3 etc. are used as coating material for orthopedic application. Among them calcium phosphate (CaP) is widely used as the bioactive material on metallic base material.

2.5.1 Calcium phosphate

Calcium phosphate (CaP) also known as apatite refers to a group of calcium phosphate minerals has been widely used to accelerate healing processes and widely used in conjunction with metals as a bioactive coating material. CaP is able to promote the bio-integration process due to its ability to adsorb water and proteins; thereby stimulating new bone tissue growth around the implant. CaP ceramics for bone tissue applications include tricalcium phosphate (TCP), octocalcium phosphate (OCP), hydroxyapatite ($Ca_{10}(PO_4)_6(OH)_2$, HA), and biphasic calcium phosphate (BCP) (Suzuki et al., 2007). With variable amounts of Ca and P, CaP has varied structural and physical characteristics, as well as biocompatibility (Evis and Webster, 2011; Nuss and von Rechenberg, 2008; Tampieri et al., 2000). Deviations in the Ca/P ratio are extensively studied to understand the different biological properties (Bailey et al., 2009). Ca/P deviations can arise with subtle modifications to the method of preparation from their preparation chemistry (Nuss and von Rechenberg, 2008; Tampieri et al., 2000), to coating parameter (Xu and Khor, 2007), with annealing procedures acting to modify its crystallinity (Nuss and von Rechenberg, 2008; Yonggang et al., 2007). Calcium phosphates can exist in either an amorphous or crystalline state (Combes and Rey, 2010).

Uncoated Ti alloy is usually insufficient for adequate bone cell attachment. Hence, implant surfaces are normally surface modified with synthetic HA (Geetha et al., 2009; Ratner et al., 2006). In order to influence healthy bone cell growth on the implant, a synthetic HA coating should resemble the properties of biological HA and not that of diseased e.g. osteoporotic bone (Kourkoumelis et al., 2012). Experiments involving HA require an

appraisal of the Ca/P ratio because Ca and P atoms are the most stable atoms present in calcium apatite and, most importantly, Ca/P ratio of a calcium phosphate compound is linked to its properties (Bailey et al., 2009; Ciobanu et al., 2009; Ergun et al., 2007). Different Ca/P ratios effectively determine the phase which affects the biomedical performance. In order to illustrate the importance of Ca/P ratio, below is a table of the ratios of different calcium phosphate compounds and their biocompatibility (Table 2.4) (Bohner, 2000). CaP has the natural facility to bond directly to bone. Degradation rate is usually regarded as a critical factor since it determines successful tissue integration. Studies have shown that HA exhibited a relatively a lower degradation rate, while TCP showed a much faster rate.

Table 2. 4: The biological importance of main calcium phosphate (CaP) compounds (Bohner, 2000; Koch et al., 2007)

Name	Formula	Ca/P	Biological relevance
Monocalcium phosphate monohydrate (MCPM)	$Ca(H_2PO_4)_2.H_2O$	0.50	It is very soluble and acidic. Therefore, it is not biocompatible on its own. Used in combination with other CaP in commercial products.
Dicalcium phosphate anhydrate (DCPA) or Monetite	$CaHPO_4$	1.00	Biodegradable, osteoconductive, and biocompatible. May play a role in bone fracture healing.
Dicalcium phosphate dihydrate (DCPD) or Brushite	$CaHPO_4.2H_2O$	1.00	Osteoconductive, biocompatible and biodegradable. May be precursor of HA in bone. Large amounts cause inflammation.
Octacalcium phosphate (OCP)	$Ca_8H_2(PO_4)_6.5H_20$	1.33	Precursor of calcium phosphates in bones and teeth. Attempts to obtain OCP have been unsuccessful, slow crystallization.
Calcium-deficient hydroxyapatite (CHDA)	$Ca_{10-x}(HPO_4)_x(PO_4)_{6-x}(OH)_{2-x}$ $(0<x<2)$	1.33-1.67	Complex chemistry. Poorly crystalline, of submicron dimensions. Unlike natural HA, impurities are absent. Used in bone cements
Biological apatite (BA)	$Ca_{8.3}(PO_4)_{4.3}(CO_3\text{-}HPO_4)_{1.7}$ $(OH)_{0.3}$BA=carbonated CDHA (x=1.7)	1.38–1.93	Hydroxyapatite of natural bone. Complex chemistry. Poorly crystalline with submicron dimensions, difficult to reproduce
Tricalcium	$Ca_3(PO4)_2$	1.5	Obtained synthetically. Degradable in

phosphate (phase β, whitlockite) (β-TCP)	(rhombohedral)		the body. Used as bone substitute/ coating.
Tricalcium phosphate (phase α) (α-TCP)	$Ca_3(PO4)_2$ (monoclinic)	1.5	Obtained by heating β-TCP above 1125^{o}C. It is different to β-TCP in terms of crystallography, and more soluble. Used in bone cements.
Hydroxyapatite (HA)	$Ca_{10}(PO_4)_6(OH)_2$	1.67	Formed using high temperature. Highly crystalline, most stable in aqueous solution, most biocompatible CaP compound. Most popularly used CaP for commercial products such as Endobon (Merck, Germany).
Amorphous calcium phosphate (ACP)	$Ca_x(PO_4)_y.nH_2O$	1.2–2.2	Very soluble in liquid. May be used as main component in bone cements.

Synthetic stoichiometric HA has a Ca/P ratio of 1.67 is biocompatible, osteoconductive, thermodynamically stable at physiological pH (7.4) and promotes healthy bone healing; (Geetha et al., 2009; Hoppe et al., 2011), even in diseased bone (Nuss and von Rechenberg, 2008). As can be seen (Table 2.4), naturally-occurring HA is poorly crystalline with an absence or near-absence of the hydroxyl group with various substitutions and vacancies (Combes and Rey, 2010; Rho et al., 1998). Mimicking the exact structure and chemistry of biological HA would be ideal, but technology has yet to advance enough for researchers to be able to do so, but work is being done to move towards that goal and the work is based on the calcium phosphate compound, stoichiometric HA, that yields the significant and consistent biological results. Post-deposition treatment (annealing) of a calcium phosphate coating may cause deviations in the Ca/P ratio which may lead to the formation of tricalcium phosphate (TCP) or other compounds (Koch et al., 2007). On the other hand, annealing of HA produces crystalline form of HA which exhibits bio-integration with no adverse fibrous tissue formation. Crystalline HA is a more desirable coating than amorphous HA due to its ability to provide a better substrate for a different cell (Hu et al., 2007). Amorphous HA tends to dissolve in human fluid more easily and leads to loosening. In addition, nanocrystalline HA is more pertinent than microcrystalline HA because of its structural similarity with apatite (Dumbleton and Manley, 2004).

Furthermore, different CaP bioceramics are found to possess different osteoconductivity, depending upon their rate of bio-resorption (Prosolov et al., 2017; Ratner and Hoffman, 2013). HA has higher stability with lower absorption rate, whereas, β-TCP has higher bioactivity due to its bio-integration and rapid dissolution among different CaP ceramics (Heimann, 2013; Ogose et al., 2005). Biphasic calcium phosphate (BCP) is a mixture of β-TCP and HA; hence, the combined properties allow one to tailor the rate of dissolution to some extent. A general pattern of bio-resorption of different CaP ceramics is as follows: HA < BCP < β-TCP (Ebrahimi et al., 2017). Hence, TCP and BCP can be successfully applied when fast bone remodeling is desired (Jin et al., 2010; Lukić et al., 2011). Furthermore, BCP exhibits higher hydrophobicity than HA, but lower than β-TCP (Wang et al., 2012). Thus protein adsorption is more by BCP due to hydrophobic interactions, resulting in better osteoinductivity than HA (Wang et al., 2012). Because of excellent biocompatibility, BCP is used extensively in delivery of hormones, repair of nasal spectrum, bone and tooth implants as well as synthetic bone graft materials (Zhang et al., 2011b; Zhu et al., 2008). Therefore, physical, structural and biocompatibility characteristics of BCP coating in its amorphous and crystalline forms need to be researched.

2.5.2 Titanium dioxide (TiO_2)

Titanium dioxide (TiO_2) is another bioactive compound that has been applied as a coating material and scaffold material for biomedical applications. For scaffold applications, TiO_2 showed sufficient compressive strength suitable for load bearing applications. Studies have found that TiO_2 coating enhances the wettability of Ti alloy as well as cell adhesion and spreading, indicating biocompatibility in nature (Advincula et al., 2006; Balla et al., 2009; Majeed et al., 2015). The presence of TiO_2 on the surface of metal implant was observed to improve the formation of apatite layer after immersion in simulated body fluid (SBF) (Balla et al., 2009; Zhao et al., 2006a). Further the deposition of TiO_2 thin film increased wear and corrosion resistance in terms of decreasing the coefficient of friction and increasing the hardness of surface (Balla et al., 2009; Khalili et al., 2013; Krishna et al., 2011). Several deposition methods have been used to apply TiO_2 coatings, including anodization, sol gel electrophoretic coating, magnetron sputtering, laser assisted deposition and slurry coating. In a study conducted by Verket et al., they compared the protein release from normal human osteoblast on three different materials for coating (i.e., TiO_2, silicon dioxide, and calcium

phosphate). They reported that TiO_2 coatings secreted higher bone markers than silica and calcium phosphate; thereby indicating that TiO_2 supports osteoblast growth and bone remodelling (Verket et al., 2012). Due to high hardness and wear resistance, TiO_2 has been used as coating layer on hip and knee implants. TiO_2 is either used as interlayers or composite layers with the CaP and coated using different coating processes such as electrophoretic deposition (Albayrak and Altintas, 2010; Araghi and Hadianfard, 2015b), micro-arc oxidation (Hao et al., 2017; Liu et al., 2016), thermal spraying (Rocha et al., 2018), sputtering (Boyd et al., 2008) etc. However, questions can be raised about the true efficacy of TiO_2-CaP composite coating on mechanical as well as biological performances.

2.6 Surface modification techniques

This section provides an overview on various surface modifications related to biomedical implant materials. Since the early 1980s, research has been focused on CaP coating for the modification of bone implant (Surmenev et al., 2014). Several techniques have been used to modify the surface of the metal alloy by coating it with a thin layer of CaP. All these methods are broadly divided into two categories: (1) physical deposition techniques and (2) wet chemical techniques. Different physical deposition methods used for CaP coating are plasma spraying (PS) (Dong et al., 2017; McPherson et al., 1995), ion-beam-assisted deposition (IBAD) (Rabiei et al., 2006; Yoon et al., 2009), matrix-assisted-pulsed laser evaporation (MAPLE) (Bigi et al., 2009), RF magnetron sputtering (dos Santos et al., 2012; Surmeneva and Surmenev, 2015a), and pulsed laser deposition (PLD) (Duta et al., 2017; Fernández-Pradas et al., 2002). Another method laser cladding (LC) is also used to modify the metallic surface with CaP coating in an effective way (Wang et al., 2008; Zheng et al., 2008). On the other hand, different wet chemical techniques include micro-arc oxidation (MAO) (Legostaeva et al., 2013; Terleeva et al., 2010), sol-gel (Nguyen et al., 2004; Zhang et al., 2011a), electrospray deposition (Bosco et al., 2012), electrochemical deposition (Ge et al., 2011; Qiu et al., 2011), electrophoretic deposition (EPD) (Boccaccini et al., 2010; Farnoush et al., 2015) and dip coating (Choi et al., 2003; Li et al., 1996).

All these methods of CaP coating have some advantages and limitations. Each method has at least one of following shortcomings: (1) poor long-term bonding of coating on substrate, (2) non-uniformity of coatings and (3) thermal decomposition of coating material.

Dip coating/sintering, for example, can degrade the mechanical properties of metal implants and lead to low bond strength and impurity of HA (Li et al., 1996). Electrophoretic deposition has the same problems as dip coating/sintering, also leads to non-uniform thickness of HA, shrinkage and cracking due to the densification during sintering (Wang et al., 2002). TiO_2 has been deposited using techniques such as plasma spraying (Zhao et al., 2006a), electrophoretic deposition (Khalili et al., 2013), sol-gel coating (Advincula et al., 2006), magnetron sputtering (Krishna et al., 2011). Among all these techniques, plasma spraying is most commonly used for coating implant devices with HA due to its reproducibility and economic efficiency (Boyd et al., 2006; Roşu et al., 2012). However, the coating produced by this method presents poor coating/substrate adherence and is lack of uniformity in terms of both morphology and crystallinity. Due to rapid cooling cracks are generated in plasma spray coating (Lin et al., 1994). The high temperature attained during the plasma deposition can result in thermal decomposition of HA, which can produce calcium oxide that is extremely toxic for cells. In addition, other problems have been revealed after long term implantation using plasma spray coatings, such as delamination, resorption, biodegradation of the thick coating and mechanical instability (Kweh et al., 2002).

Moreover, the differences in thermal expansion between the metallic substrate and the ceramic coating can lead to coating detachment after the application of a mechanical load during or after implantation. The coating fragments detached from the implant are one of the main causes of inflammation identified after performing the surgical procedures. Consequently, osteolysis and aseptic loosening of implants due to coating delamination/detachment and the presence of toxic compounds are reported as the major causes of implant failure (Liang et al., 2004). The bond strength of HA coating was found to be 64. 8 MPa by Han et al. (2007), which was significantly higher than plasma sprayed bond strength for HA coating of 5.3 MPa. Thus, improving the adhesion strength of thermal spray coatings is a major concern for bone or dental applications. Magnetron sputtering has been regarded as an efficient method to produce coatings that are amorphous, with controlled crystallography and other properties (Mayrhofer et al., 2002; Yang et al., 2005). For example, an *in vivo* study on dogs demonstrated that magnetron sputtering calcium phosphate on metal implants achieved equivalent or higher bond strengths, and percentage bone contact, at the bone–implant interface, as compared with plasma-sprayed HA (Thian et al., 2007).

A summary of the characteristics of the various coating techniques for calcium phosphate is presented in Table 2.5. Each technique has its own benefits and drawbacks. However, sputtering is the most promising method due to its ability to produce dense and thin coatings, as well as provide good bond strength (Surmenev, 2012). In regard to coating deposition, sputtering is known as a flexible process due to its ability in coating complex 3D geometries and have concluded that it brings several advantages, such as relative low cost, bio-adhesion and thin film coatings (0.5-3 μm) (Brohede et al., 2009). Hence, magnetron sputtering of bio-ceramic coating like CaP and TiO_2 coating is reviewed in this study.

Table 2. 5: Advantages and limitations of different coating techniques for CaP coating (Surmenev, 2012; Yang et al., 2005)

Method	**Thick-ness**	**Advantages**	**Limitations**
Plasma spraying	30-200 μm	Low cost; high deposition rate; porous surface; micro rough surface	Decomposition due to high temperature; amorphous coating and cracks due to rapid cooling; non-uniform thickness
Ion beam assisted deposition	0.03-4.0 μm	Uniform coating thickness; high reproducibility; dense pore-free coating; high bonding strength	Expensive; amorphous coating; high dissolution rate in body fluid
Pulsed laser deposition	0.05-5.0 μm	Crystalline and amorphous coating; dense and porous coating	Expensive; high substrate temp. (350-750 ºC) required for crystalline coating
Dip coating	0.05-0.5 mm	Inexpensive; fast coating process; able to coat complex specimen	Requires high sintering temperature; thermal expansion mismatch
Sol-gel	< 1 μm	Low processing temp.; can coat complex surface; relatively cheap	Required controlled atmosphere for processing; expensive raw materials
Electro phoretic deposition	0.1-2.0 mm	Rapid deposition rate; complex surface can be coated; uniform coating	Cracks produced in the coating; high sintering temperature required

Biomimetic coating	< 30 µm	Low processing temp.; can coat complex surface; can form bonelike apatite	Time consuming; requires replenishment and a constant pH of simulated body fluid
Sputtering	0.04-3.5 µm	Dense and uniform coating; high bonding strength	Time consuming; expensive; amorphous coating

2.7 Radio frequency (RF) magnetron sputtering

Sputtering is a physical vapor deposition process which involves ejection of neutral atoms from a target surface using energetic particle bombardment. The energetic particles used in the sputtering process are argon ions, which can be easily accelerated towards the cathode by means of an applied electric potential, hence bombarding the target and ejecting neutral atoms from the target. These ejected atoms are then transferred and condensed onto the substrate to form a coating. Plasma energy is usually used to generate the high-energy particles. (Mattox, 2010; Surmenev, 2012; Yang et al., 2005). Sputtering has been used in many applications such as the semiconductor, photovoltaic and automotive sectors. There are several sputtering methods, such as magnetron sputtering, ion beam sputtering (IBS), and reactive sputtering (Liu et al., 2004).

Magnetron sputtering is one option to overcome the problems such as delamination and low bond strength that may arise with plasma spray methods. The deposition process can be performed at low temperatures, thus reducing the inconvenience related to the thermal decomposition or phase transformation. Magnetron sputtering enables lower pressures to be used, because a magnetic field allows trapping of the secondary electrons near the target. This induces more collisions with neutral gases and increases plasma ionization. Direct current (DC) magnetron sputtering may be ineffective for insulating materials as resistance may cause the build-up of charged particles on the materials surface. Pulse DC can sometimes be an effective means to prevent this. The comparably low frequency of the pulse can provide limitation to highly insulating materials such as glasses (Aufderheide, 2006). In contrast, radio frequency (RF) magnetron sputtering is an improved ion-sputtering method which can deposit low conductivity materials (Harsha, 2005) by preventing the build-up of positive particles on non-conducting target surfaces by alternating between positive and

negative electron flow. It enables the ionic momentum at negative current to outweigh the electron flow at positive current, hence the greater mass of approaching ions in comparison to electron build up results (Aufderheide, 2006). The schematic diagram of RF magnetron sputtering is given in Figure 2.2 consisting of RF generator, magnetron, cooling system, vacuum chamber, matching network. The factors influencing the different properties such as structural, mechanical and biological behavior are described in the following section.

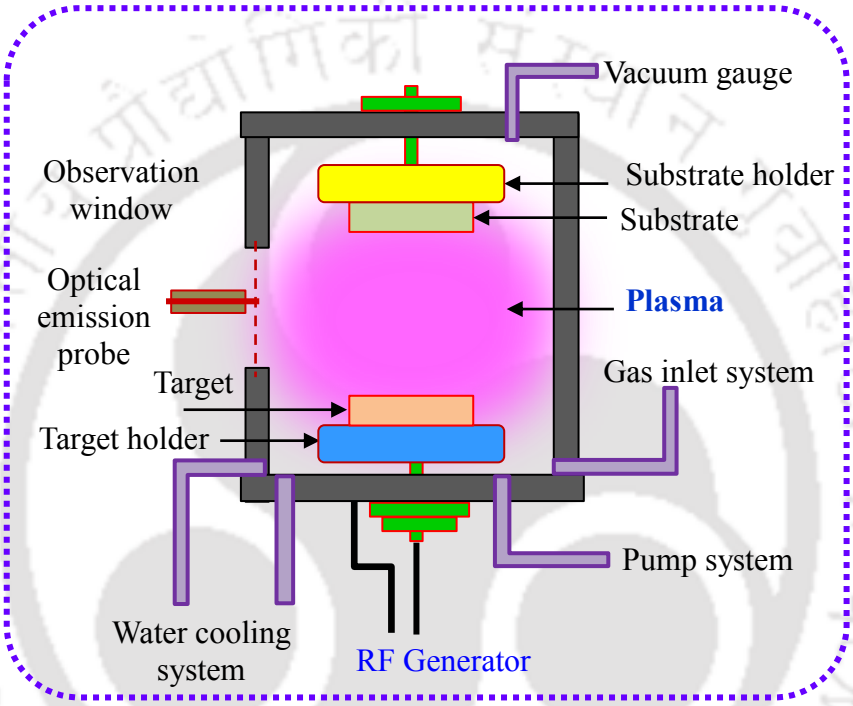

Figure 2. 2: *Schematic diagram of radio frequency magnetron sputtering experimental set up.*

2.8 Structural properties of CaP coating

Investigations using sputtering for different calcium phosphates have been done by many researchers. Among the CaP deposited materials, HA (Boyd et al., 2015; Mukhametkaliyev et al., 2017; Surmenev, 2012) and TCP (Boyd et al., 2011; Wolke et al., 2003) depositions are most widely studied for biomedical applications. For the first time HA coating by RF sputtering was carried out in early 1990s by Jansen et al. (1993), Wolke et al. (1994) and Yamashita et al. (1994). HA coating using RF sputtering were explored by a number of groups and has been found to be an appropriate coating method, producing uniform, continuous thin coatings without any micro cracks, surface and bulk porosity (Badea et al.,

2016; Pichugin et al., 2008; Surmeneva and Surmenev, 2015b). In addition, the initial substrate surface roughness has not influenced by RF sputtering, which makes the coatings beneficial in clinical trials (Hong et al., 2010; Pichugin et al., 2008; Surmenev et al., 2011). The main CaP coating characteristics include the surface morphology, chemical composition with Ca/P ratio, phase composition and structure. The quality and integrity of CaP coating are directly influenced by deposition control parameters that include discharge power, working pressure, gas flow rate, gas composition, target composition, sputtering time, substrate temperature, target-substrate distance, substrate form, post-heat treatment or negative substrate bias (Boyd et al., 2003; Jansen and Leon, 2009; Mattox, 2010; Surmenev et al., 2011). Careful control of these variables can produce either HA coatings with high crystallinity or reactive coatings containing other calcium phosphate phases. The surface morphology plays a crucial role in the overall success of an implant. Either rough or flat surface morphology is needed in any clinical case (Variola et al., 2011).

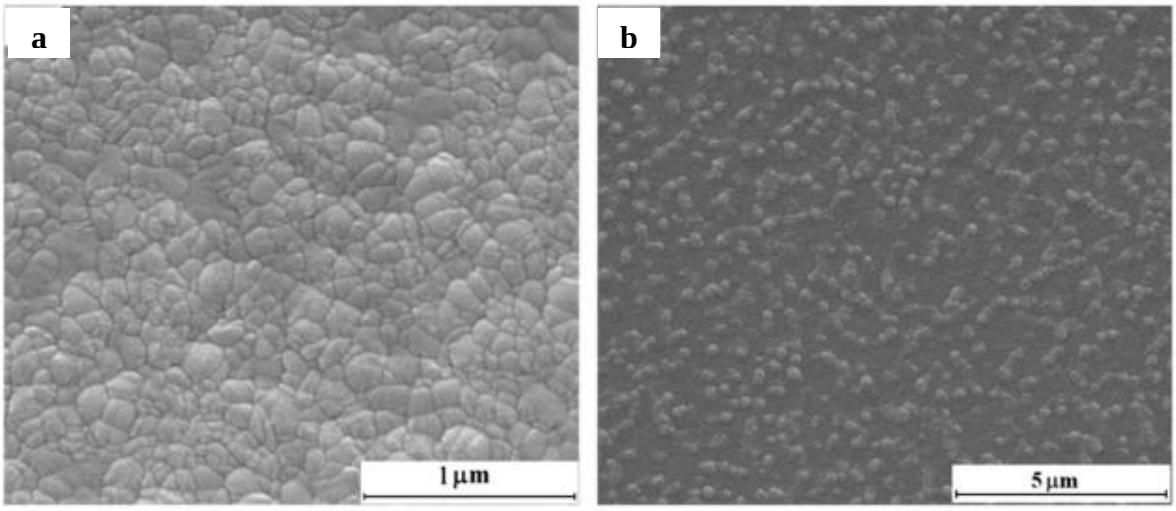

Figure 2. 3: *The typical patterns of the surface morphology of RF magnetron sputter deposited coatings: (a, b) RF power—290 W, deposition time 180 min, working atmosphere—argon. The substrate holder was grounded (a), and DC-bias of−100 V was applied (b) (Surmenev, 2012).*

Figure 2.3 shows the surface morphology of CaP coating deposited by RF sputtering at RF power of 290 W, deposition time 180 min, argon atmosphere. The typical pattern of the

RF sputtering film shows uniform, continuous grains without any cracks, however, the size of grains are different due to use of different bias voltage (Surmenev, 2012). Wan et al. (2007) identified that discharge power directly influenced the coating thickness by increasing this with the discharge power. A similar trend was shown for sputtering time. In regards of substrate form, deposition rate was higher on a solid plate target than on a powder lump. The thickness of deposited film onto a powder target was thinner. It has also been noted that sputtered films possess higher adhesion to the substrate compared to the evaporation method (Wan et al., 2007).

The chemical composition of the outermost coating surface is important because it will be in direct contact with bone tissue and dissolves first at the initial stage of implantation. The homogeneous distribution of Ca and P on the film surface is also crucial because the segregation phenomena are usually responsible for the formation of the undesired second phases (Socol et al., 2010). The Ca/P ratio is one of the main characteristics of a biocompatible film and it can be seen that the CaP films with different Ca/P ratios, including that close to Ca/P = 1.67, which is typical for stoichiometric HA are obtained using RF magnetron sputtering (Berezhnaya et al., 2010; Socol et al., 2010; Surmenev et al., 2011). This ratio also depends on the applied sputtering control parameters. An overview of the Ca/P ratio of CaP coatings is presented in Table 2.6, which shows a variation in stoichiometry in the CaP coatings found by different authors. Surmenev et al. (2011) investigated the composition and properties of the calcium phosphate coating deposited by RF sputtering under variable negative bias, deposition time and position of the substrate relative to the target erosion zone. The Ca/P ratio was found in between 1.53 and 3.88 with variation of negative substrate bias, deposition time and RF power. With increase in negative substrate bias, the Ca/P ratio increases, whereas the Ca/P decreases with the increase in sputtering time. Van Dijk et al. (1996) deposited CaP film and studied the effect of annealing from 400-1200 ºC temperature. Cracks were found in the film beyond the temperature of 400 ºC and the Ca/P ratio decreased from 2.05 to 1.80 when annealing temperature increased from 400-1200 ºC. After annealing at a temperature of 600 °C or more the XRD showed crystalline hydroxyapatite (HA) coatings. However, the second phase, present in the coatings, changed from tetra-calcium phosphate to calcium oxide to β-tricalcium phosphate with increasing annealing temperature. Boyd et al. (2011) also observed that for films

annealed at 600 °C and 700 °C, the Ca:P ratio decreased, whilst at 500 °C, Ca:P ratio were reported to increase, explained by volatile phosphorous evaporating from the surface at lower annealing temperatures. This phenomenon was also observed for *in situ* annealing at 700 °C. Results showed that complete diffusion of a rutile Ti layer to the surface of the coating occurred at temperatures of 700 °C. The difference in behavior between *in situ* and post annealing has been attributed to the oxygen content in the annealing environment facilitating the formation of TiO_2 and its subsequent diffusion through the coating layers, to prevent phosphorous evaporation and yield a higher phosphorous content at higher temperatures in air. Oxidation of the TiO_2 layer may occur at a lower rate in argon. Berezhnaya et al. (2010) obtained lower Ca/P ratio of 1.1-1.2 and 1.2-2.3 after annealing of CaP sputtering film at 900-1000 ºC.

Table 2. 6: The Ca/P ratio of the coatings prepared at different conditions of RF magnetron sputtering

Deposition conditions	Type of coating	Ca/P ratio	Reference
As-deposited	HA	1.93	(Jansen et al., 1993)
As-deposited	HA	1.50-2.0	(Wolke et al., 1994)
As-deposited and annealed at 1200 °C	Amorphous CaP Crystalized HA, TCP	2.05 1.80	(Van Dijk et al., 1996)
As-deposited	CaP	2.09-2.29	(Boyd et al., 2003)
As-deposited, post annealed at 500, 600 and 700 °C	Amorphous CaP	1.42 2.47-1.82	(Boyd et al., 2008)
As-deposited in an inert atmosphere	HA	1.4	(Socol et al., 2010)
As-deposited	HA	1.73 ±0.08	(Hong et al., 2010)
As-deposited	HA	1.6–2.6	(Jansen and Leon, 2009)
As-deposited and annealed at 900–1000 °C	HA	1.1–1.2 and ~1.2–2.3	(Berezhnaya et al., 2010)

As-deposited in Ar atmosphere	CaP	~1.15	(Toque et al., 2009)
In situ annealed at 500, 600, 700 °C, respectively	CaP	1.43, 1.53, 2.01	(Boyd et al., 2011)
As-deposited before and after 0.9% NaCl exposure	HA	1.67–1.75 and 1.56–1.65	(Surmenev et al., 2010)
As-deposited in Ar atmosphere	B-type carbonated HA	1.8	(Sima et al., 2010)
As-deposited	CaP, HA	1.53–3.88	(Surmenev et al., 2011)

Like Ca/P ratio, the phase composition and structure influence the coating behavior *in vitro* and *in vivo* (Klein et al., 1994; Sun et al., 2001). These phase compositions and the structures of the coating also depend on the sputtering control parameters. Despite the utilization of a partially crystalline target RF magnetron sputtering usually produce amorphous coatings or CaP compounds (Jansen and Leon, 2009; Sima et al., 2010; Surmenev et al., 2010; Zhao et al., 2006b). It is well known fact that the amorphous phase in CaP coatings easily dissolves and hence loses long-term stability in clinical use (Surmenev, 2012). Though it is critical to maintain the integrity of HA coatings, controlling the heat-treatment temperatures and heating environment (air, water vapor) results in conversion of amorphous coatings to HA ones of different degrees of crystallinity (Jansen and Leon, 2009; Johnson et al., 2006; Yonggang et al., 2007). Annealing *in situ* at 297–527 °C (Pichugin et al., 2008; Surmenev et al., 2010; Surmenev et al., 2011) or after deposition usually at the temperature of 320–700 °C in an inert gas, water vapor, air or vacuum enhances the films crystallinity (Nelea et al., 2007; Porter et al., 2004; Thian et al., 2006b; Toque et al., 2009; UEDA et al., 2009; Van Dijk et al., 1996).

Yoshinari et al. (1997) heat treated deposited coatings with infrared radiation at 300, 400, 500, 600 and 700 °C. Degradation was observed in SBF such that amorphous coatings heat treated at 300 °C degraded within 1 day whilst 600 °C were deemed optimal as steady degradation was observed. At 700 °C coatings did not degrade. Observation of the diffraction data showed absence of any amorphous phase from 500 °C suggesting that complete crystallization by 700 °C stabilized the coating layer. Prosolov et al. (2017) found crystalline state after annealing the different as deposited quasi-amorphous BCP films at 700

°C. On the other hand, Boyd et al. (2011) observed hybrid HA-TiO_2 crystalline state after annealing of HA film deposited on Ti alloy. One of the main factors that influence the nature of a growing coating is the substrate temperature during deposition. Nelea et al. (2004) found that a substrate temperature of 550 °C gave a crystalline calcium phosphate. Similarly, Pichugin et al. (2008) observed high intensity crystalline HA film at a substrate temperature of 500 °C. The as-deposited HA coatings of a sufficient crystallinity were also prepared by increasing the RF power (Pichugin et al., 2008; Surmenev et al., 2010; Surmenev et al., 2011) without *in situ* and post annealing. Narushima et al. (2005) deposited CaP films as amorphous at 75 W deposition power; however, formed crystallographic orientation of HA thin films at higher RF power of 100 and 150 W. This was attributed to an increase in thermal energy upon condensing at the substrate causing crystallization of the coating.

2.9 Mechanical performance

The adhesion strength of the CaP-based coatings determines the overall success of an implant which mainly depend on different parameters such as phase and chemical composition, and crystallinity of the coating (Pichugin et al., 2008; Snyders et al., 2008). The investigation of the coating bond strength or adhesion strength is typically performed according to pull-off test (Gadow et al., 2010), tensile adhesion test (Singh et al., 2011; Yang et al., 2009) or shear strength (Gomes et al., 2010). The ISO 13779-2:2008 standard requirement for tensile adhesion strength of HA coatings in the surgical implant application is 15 MPa (Huang et al., 2010; ISO, 2008; Xue et al., 2007). Vilotijević et al. (2011) found 33.0 MPa adhesion strength during plasma spraying of HA coating which thickness varied between 250-300 μm. According to Lopez-Heredia et al. (2008), the loading stress on the hip joint during the gait is around 35 MPa. Hence, it should be more than 35 MPa. Another technique to study thin films adhesion strength is the scratch test (Johnson et al., 2006; Mohseni et al., 2014; Rabiei et al., 2006; Surmeneva et al., 2015; Toque et al., 2010). The CaP coatings produced by sputtering have been reported to possess significantly higher coating-metal interfacial bonding strength compared to plasma spraying coatings (Jansen and Leon, 2009; Pichugin et al., 2008). A comprehensive review by Mohseni et al. (2014) of HA on Ti-6Al-4V concluded that magnetron sputtering produced the greatest interfacial adhesion from nine deposition methods of plasma spraying, hot isostatic pressing, thermal spray coating, dip

coating, pulsed laser deposition, electrophoretic deposition, sol gel, ion beam assisted deposition and sputtering.

Pichugin et al. (2008) using the scratch-test observed that the as-sputtered coatings of the thickness less than 1.6 μm on Ti did not delaminate until the indenter reached the substrate-coating interface. The typical failure mechanisms of RF magnetron sputter deposited coatings of different thicknesses are presented in Figure 2.4. The mode of damaging the CaP coating with the thickness greater than 1.6 μm differed from that of the thinner CaP coatings. The destruction of the coatings with the thickness less than 1.6 μm occurred only after its perforation (Figure 2.4 (a)), whereas thicker coatings collapsed by exfoliation, splits and chips along the scratching direction (Figure 2.4 (b)). According to the results of acoustic emission and friction coefficient tests all coatings with a thickness up to 2.7 μm had high adhesion strength to Ti and NiTi. The reason for high adhesion strength is a thin oxide layer of TiO_2 that promotes a formation of a strong covalent bond between the substrate and CaP coating with the energy above 0.5 eV (Pichugin et al., 2008).

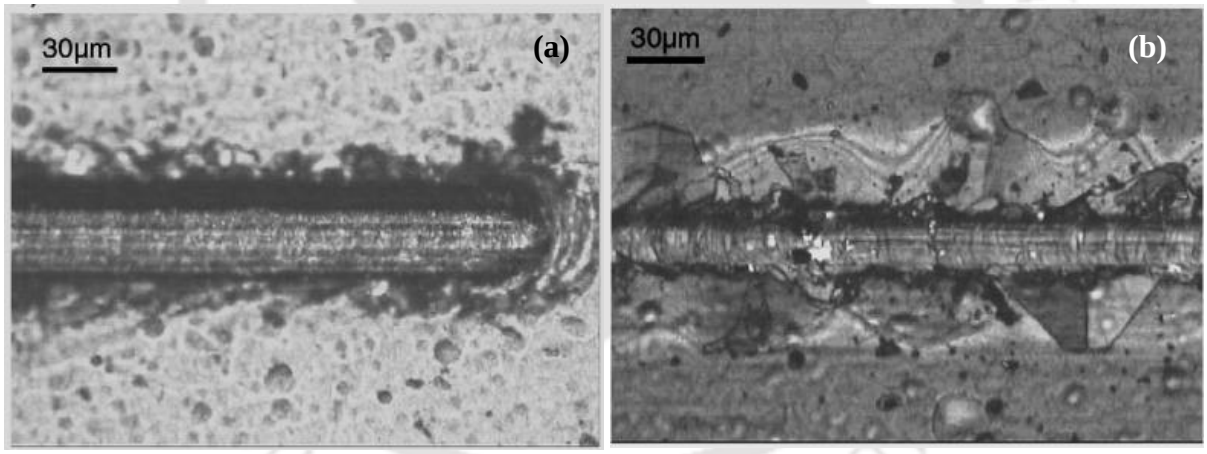

Figure 2. 4: *Scratch tests on a CaP coating (thickness (a) 1.6 μm and (b) 2.7 μm) on Ti. Scratch were made at (a) 2 N and (b) 0.66 N, respectively (Pichugin et al., 2008).*

The adhesion behavior is highly dependent upon deposition parameters, coating thickness and adhesion test parameters. Toque et al. (2010) conducted scratch test from 0.4 N to 1 N at progressively increasing load on HA coatings applied to 316L stainless steel using RF sputtering. The failure modes were recorded to indicate cohesive and adhesive failures with increasing load. As deposited coatings initially failed by trackside cracking, then trackside delamination as the tensile stresses built up behind the indenter with eventual

steady delamination as the crack width was constant. The annealed coating failed by progressive delamination whilst the signs of fracture associated with brittle failure diminished. Annealing plays an important role on adhesion strength of HA coating on Ti alloy. Rabiei et al. (2006) observed enhancement in adhesive and cohesive strength during ion beam assisted deposition of functionally graded crystalline HA coating with *in situ* heat treatment. The continuous atomic bombardment during deposition has the effect of improving the atomic mobility, increasing film density, and improving film homogeneity, which lead to increased adhesive and cohesive strength. This strength was found to be higher than the HA films prepared by sputtering and post-deposition annealing. A comparison of ion beam sputtered Ca:P coatings was conducted by Ong et al. (1992) via pull off strength for amorphous, and heat treated coatings. As deposited amorphous, quenched and furnace cooled coatings had pull of strengths of 38.0 ± 8.2 MPa, 17.0 ± 6.5 MPa and 9.0 ± 9.0 MPa respectively, with failure either occurring at the coating interface or cohesively. The sputter coated HA films on metals were found to be of low crystallinity. The low crystallinity increases the rate of dissolution of the coating in the living body. Post-treatment thermal process can be used to crystallize the film, hence reducing the possibility of dissolution. However, conventional thermal treatment in the electric furnace increases the likely formation of cracks and may degrade the HA films (Mohseni et al., 2014; Ozeki et al., 2001). With conducting the scratch test on HA and HA-1.2% Si coating, Surmeneva et al. (2015) found different deformation behaviors of the films. In case of pure HA coatings, failure occurred due to a low cohesion of the coating, whereas the crystalline Si-HA coating containing 1.2 at.% Si deformed plastically without detaching from the titanium substrate.

Many authors reported that adhesion strength could still be enhanced during various coating techniques using different interlayers such as HA/Ti bond coat (Rakngarm and Mutoh, 2009; Roy et al., 2011a), TiO_2/Ti/TiN (Berezhnaya et al., 2010; Boyd et al., 2011; Mohseni et al., 2015; Quirama et al., 2017), ZrO_2 (Nelea et al., 2000), HA/SiO_2 (Morks, 2008), Al_2O_3 (Nelea et al., 2000), as well as Al_2O_3/TiO_2 (Singh et al., 2011). These interlayers can reduce the mismatch of thermal expansion coefficients between HA and substrates or increase the surface area of the material, wettability and heat conductivity, thus increasing the coatings bonding strength without affecting biocompatibility. Sima et al. (2010) reported that bond strength of the carbonated HA structures successfully increased by

~24% when an intermediate CHA_xTi_{1-x} (x=0–1) composite buffer layer was introduced. In the case of annealed (550 °C/1 h) graded RF magnetron sputter deposited coatings, the failure occurred within the glue layer at 84.80±0.78 MPa without damaging the film integrity. Since this value represents the bonding limit of the epoxy adhesive as confirmed by the manufacturer, the true coating-substrate adhesion strength could be even higher. A study by Ding et al. (1999) investigated on a series of thin (< 10 μm), single layered HA/Ti coatings deposited on Ti–6Al–4V substrate using an RF magnetron-assisted sputtering system. For the experiments, six HA/Ti targets with different compositions (95HA/5Ti, 90HA/10Ti, 85HA/15Ti, 75HA/25Ti, 50HA/50Ti, and 25HA/75Ti) were prepared. Generally, it was found that the coating with higher Ti contents resulted higher adhesion strengths. The highest adhesion strength (of the 25HA/75Ti coating), evaluated was even higher than 80 MPa, which exceeded the maximum value achievable using the bonding resin in the pull-out test. Mohseni et al. (2015) found 44.57% improvement in adhesion strength between HA coating and Ti-6Al-4V substrate during sputtering by applying a Ti/TiN thin film as an interfacial layer. The adhesion strength of calcium phosphate ($CaPO_4$) was enhanced by 62% due to inclusion of TiN/TiO_2 intermediate layers, as reported by (Quirama et al. (2017)). This was attributed to improvement in chemical and physical bonding between the Ti-6Al-4V substrate and HA.

It was discussed that different oxide phases can be formed on Ti or Ti-6Al-4V prior to the CaP film growth by pulse laser deposition in water vapor atmosphere (Dinda et al., 2009; Saju et al., 2009), which can degrade the coating adhesion strength. Berezhnaya et al. (2010) also reported that 0.2 μm thick TiO_2 interlayer in the HA/Ti system inhibited Ti oxidation, and the reaction intermediates formed during high temperature heat treatment (900–1000 °C) enhance the adhesion between the Ti and HA. However, reported about enhancement of adhesion between HA and Ti-6Al-4V after sputtering and subsequent annealing at 700 °C and 800 °C by forming HA/TiO_2 hybrid coatings. This HA/TiO_2 hybrid coating was formed due to the thermal diffusion occurs between HA and oxide of substrate formed during annealing in air (Boyd et al., 2011; Boyd et al., 2008). Since, the presence of TiO_2 and annealing of CaP sputtering gives disparity in the adhesion behavior; therefore, further investigations on the improvement in bond strength between implant surface and coatings are needed.

2.10 Biological performance

Along with mechanical properties, the biological behavior of new porous biomaterials is another fundamental criterion to be considered for a material to become successful candidate for implants. The commonly used biocompatibility test on biomaterials is the *in-vitro* cell culture experiment using osteoblasts. *In vitro* investigations play a crucial role in the biological assessment of new biomaterials and allow the estimation of several aspects of both cell interactions with artificial materials and the behavior of implants in a biological environment. Consequently, *in vitro* studies partly mimic some aspects of the cell function and signaling activated after the implantation of a foreign material *in vivo.* After implantation into the human body, the implant surface will immediately contact the physiological fluid, which contains numerous ions and proteins that guide the adhesion of particular cell types to the surface. Figure 2.5 shows the schematic diagram of different processes occurs at the interface of biomaterials after implantation into a living system.

A number of biological assessments have been carried out by the researchers to test the CaP-coated metallic material. Every dedicated biomaterial should be biocompatible and show good bioactivity in order to achieve a long lasting performance as an implant. Hence, in this study, the focus is given consideration to different aspects of *in vitro* bioactivity, cellular behavior and protein adsorption of the CaP based metallic material.

2.10.1 Bioactivity of CaP coatings in biological fluids

In vitro bioactivity properties of any material or modified surface can be achieved by evaluating the growth of apatite in simulated body fluid (SBF), which has ion concentrations similar to human blood plasma for certain days (Arce et al., 2016). Bioactivity regulates the formation of calcium phosphate apatite layer on a bio-implant surface, which indicates the interaction between implant with surrounding bone and soft tissues (Surmenev et al., 2014). Immersion into SBF or any other type of body fluid is widely considered as the first indication of the bioactivity of a biomaterial in contact with bone (Surmenev, 2012; Surmeneva et al., 2013). A significant number of bioactivity studies of CaP-based coatings have been performed *in vitro* in SBF (Mello et al., 2007; Surmeneva et al., 2013; van der Wal et al., 2006), Hanks' solution (Tlotleng et al., 2014), and phosphate-buffered saline (UEDA et al., 2009). Mello et al. (2007) carried out the SBF test by immersing the calcium phosphate

film in the fluid for 10 days. A well-crystallized mineral phase composed of plate-like crystal was formed. Similarly, Surmeneva et al. (2013) also observed plate-like structure of apatite layer after immersing the Si-HA sputtered specimen in SBF for 14 days and the increase in apatite layer was found after 28 days immersion in SBF. When the modified surface is exposed to SBF, first the calcium ion deposits followed by formation of a phosphate layer on the surface; like this the growth of bone-like apatite is initiated (Yang et al., 2009).

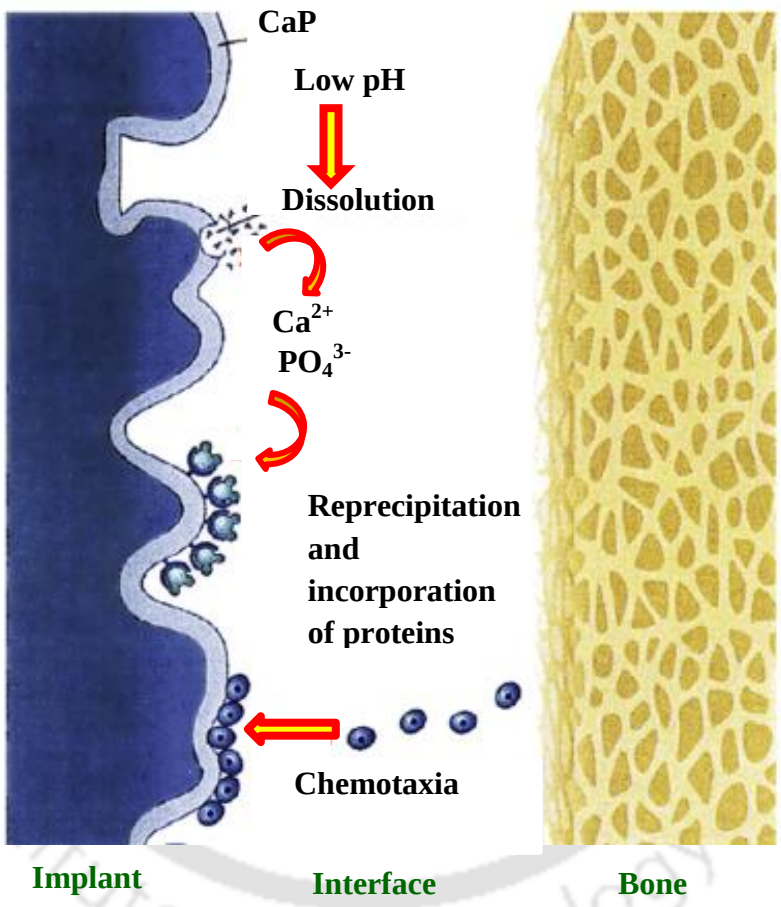

Figure 2. 5: *Schematic representation of osteoconduction induced by CaP coating. A decrease in the local pH leads to the partial dissolution of the coating and subsequent release of calcium and phosphate ions. The ions reprecipitate and incorporate into apatite crystals with the collagen matrix. The increased concentrations of calcium and phosphate ions stimulate chemotaxis (Cunningham et al., 2009).*

Bioactivity also named as bio-mineralization is initiated by the electrostatic interaction of the surface functional groups with the calcium and phosphate ions in the body fluids, and is strongly controlled by the properties of the CaP coatings themselves (Lee et al.,

2006a; Surmeneva et al., 2011). The dissolution of CaPs upon soaking in SBF is a process that depends mainly on the following properties of the fluid: the phase content, crystallinity, and the morphology (d'Haese et al., 2010; Surmenev et al., 2014). The CaP coatings are degradable with the following order of relative solubility: CaO >> α-tricalcium phosphate (TCP) > β-TCP > amorphous calcium phosphate (ACP) > tetracalcium phosphate (TTCP) > oxyhydroxyapatite/oxyapatite (OHAp/OAp) > HA (Surmenev et al., 2014; Wang and Zreiqat, 2010). Thian et al. (2006a) found the enhancement of the kinetics of apatite nucleation on the coated surface in SBF after annealing of magnetron sputtered silicon doped HA film. It was suggested that a nanocrystalline structure can offer a higher number of nucleation sites for the formation of apatite crystals because of the high surface energy of the grain boundary, leading to a more rapid precipitation of apatite crystals. Hahn et al. (2011) also obtained same result when studied the bioactivity of the as-deposited hydrothermally treated HA coatings in SBF. The enhanced bioactivity of hydrothermally treated samples compared with those of furnace-heated samples was explained by their smaller crystallite size. The surface morphology of apatite layer on Ti and HA coated Ti after immersion in SBF for 7 and 14 days are shown in Figure 2.6, where globular structure of apatite can be seen.

Surface composition mainly affects the bioactivity when exposed to SBF. Composition like HA, TCP, TiO_2 when immersed in SBF generates OH bond (Balla et al., 2009; Paital and Dahotre, 2009). With presence of these negatively charged OH^- ions on the surface, Ca^{2+} ions from the SBF are moved towards the sputtered surface and subsequently the negatively charged PO_4^{3-} ions which lead to form apatite nuclei on the surface. Surface roughness also plays an important role in apatite formation. Arce et al. (2016) observed higher apatite formation on calcium titanate and HA film deposited by RF sputtering due to higher surface roughness. It was explained that because a higher roughness surface implies a greater amount of cavities where Ca^{2+} and PO_4^{3-} ions penetrates and hence, more nucleation of precipitation occurs. The effect of different factors on the bioactivity has been studied; however, simultaneous acting of more than one factor makes complexity and hence leaves the scope to explore the understanding of process-structure-property relationship.

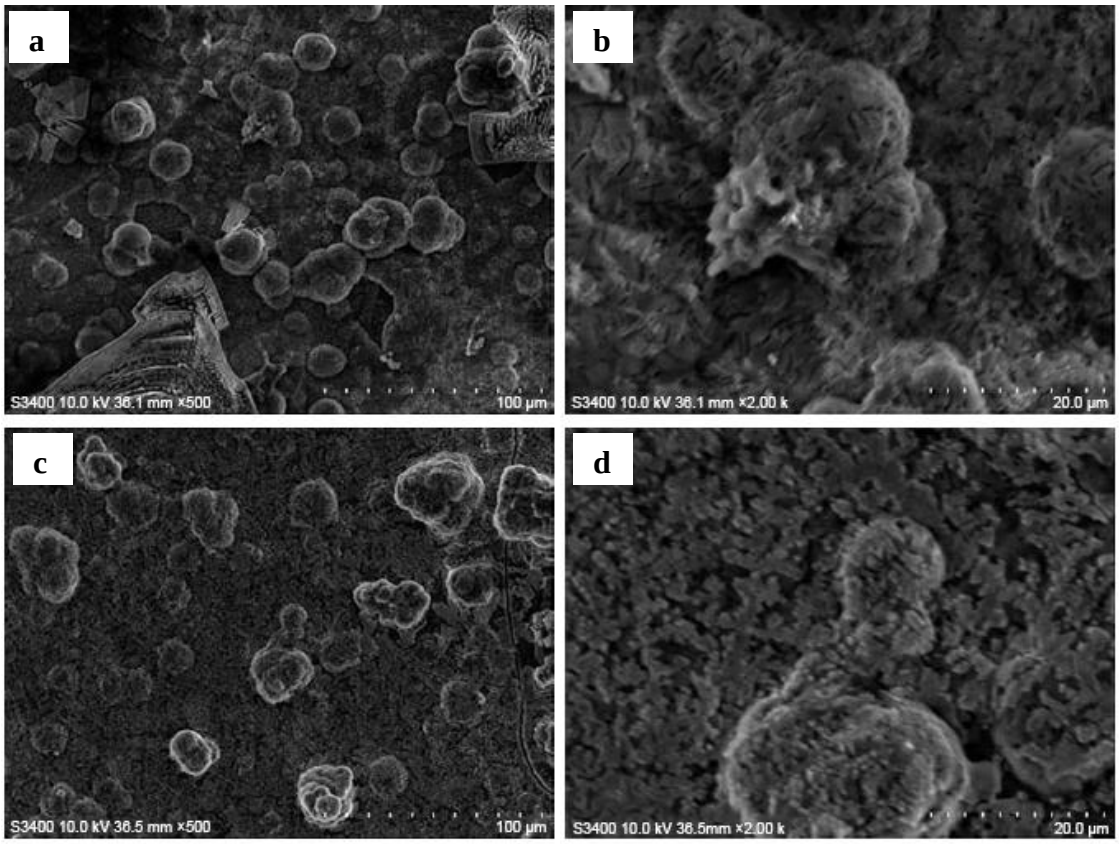

Figure 2. 6: *Surface morphology of apatite layer formed on (a, c) Ti and (b, d)HA coating after immersion in SBF for 7 and 14 days (Huang et al., 2018).*

2.10.2 Cell-CaP surface interactions

The cellular behavior on the surface of biomaterial shows the biocompatibility of that material, which can be performed by *in vitro* cell culture experiment using osteoblasts (Hasan et al., 2018b; Surmenev et al., 2014). The behavior of osteoblast cells was determined by investigating the number of adhering and proliferating cells. It has been revealed from the *in vitro* cell culture of different cell lines that the CaP coating enhanced the cellular adhesion, proliferation and differentiation, in order to promote bone regeneration when compared to uncoated substrates (dos Santos et al., 2012; Mello et al., 2007; Socol et al., 2010; Surmenev, 2012). The cells like MC3T3-E1, MG63 and human bone-derived seeded on the surface of a CaP coated material synthesize a number of osteoblastic phenotypic proteins and promote the secretion of extracellular matrix (ECM) (Bächle and Kohal, 2004; Richard et al., 2006). Every dedicated biomaterial should be biocompatible and show good bioactivity in order to achieve a long lasting performance as an implant.

The cellular response (attachment, spreading and differentiation) of various materials such as Ti, magnesium alloys, stainless steel 316L, ceramics and polymers are significantly improved with CaP coating, describing the cytocompatibility of those materials (Hong et al., 2010; Ueda et al., 2007; Xue et al., 2007). Mello et al. (2007) investigated *in vitro* experiments using murine osteoblasts on HA coated pure Ti and oriented silicon prepared by RF magnetron sputtering. They showed that cells rapidly adhere, spread and proliferate and the highest proliferation of human osteoblasts was achieved on HA coated Ti substrates. It has been seen that the morphology of cells changed with the proliferated time and specific morphological patterns obtained in the different surfaces and interfaces. Roy et al. (2011b) fabricated HA coating on Ti using plasma spraying technique and studied the cytotoxicity by culturing human fetal osteoblast cells (hFOB) on coated surfaces. *In vitro* studies indicated that the HA coatings promoted hFOB cell attachment and proliferation. Socol et al. (2010) synthesized HA thin films on PMMA substrates using pulsed laser deposition and magnetron sputtering. Cell viability, proliferation and adhesion tests in osteosarcoma SaOs2 cell cultures were performed to validate the bioactive behavior of the structures. Cells grown on these coatings exhibit behavior similar to those grown on the standard borosilicate glass control: increased viability, good proliferation, and optimal cell adhesion. Sima et al. (2010) used RF sputtering to prepare highly adherent carbonated hydroxyapatite (CHA) thin films and investigated cell adhesion and differentiation using human mesenchymal stem cells (hMSCs). The results showed that bone cells were grown over the surface of CHA coatings for periods between a few hours and 21 days. The results demonstrated the capacity of CHA coating to support hMSCs adhesion and osteogenic differentiation ability.

2.10.2.1 Effect of surface topography

It has been reported that the different surface factors, such as chemistry, roughness energy, and crystallinity influence the cellular response to a biomaterial (Berube et al., 2005; Cairns et al., 2010; Surmenev et al., 2014; UEDA et al., 2009). Among these the surface roughness and topography play a major role in the osteointegration of implants. Cairns et al. (2010) deposited CaP thin films onto Ti substrates with varying topography in nanometer range such that this is reflected in the CaP surface features. A fibronectin (FN) ad-layer was then deposited from solution onto each surface and the response of MG63 osteoblast-like cells

investigated. The results revealed that in all cases, the presence of the adsorbed FN layer on the CaP thin films improved MG63 cell adhesion, proliferation and promoted early onset differentiation. Moreover, the nature and scale of the response were shown to be influenced by the underlying CaP surface topography. Specifically, MG63 cell on FN-coated CaP thin films with regular topographical features in the nanometer range showed statistically significant differences in focal adhesion assembly, osteocalcin expression and alkaline phosphase activity compared to CaP thin films that lacked these topographical features. Moura et al. (2010) evaluated the effect of a bioactive ceramic coating, in the nano thickness range, onto a moderately rough surface on the osteogenic behavior of human bone cells. The cells were cultured over Ti-6Al-4V disks of different surfaces: as-machined (M), alumina-blasted/acid etched (AB/AE), and alumina-blasted/acid-etched 300–500 nm thickness amorphous Ca- and P-based coating obtained by ion beam-assisted deposition (Nano). The results revealed that at 1 day, AB/AE and Nano showed higher adhesion than the M surface ($p < 0.001$). Higher adhesion was observed for the M than the Nano surface at 7 days ($p < 0.005$). The percentage of cells at day 1 was significantly higher for the Nano compared to M surface ($p < 0.03$).

Like nano-surface topography, the microtopography also affects the cellular behavior. Matsuzaka et al. (2003) investigated the attachment and growth of osteoblast-like cells on Smooth and microgrooved (groove depth 0.5–1.5 μm, groove- and ridge width 1–10 μm) polystyrene substrates. It was shown that on the smooth and wider grooved substrates, focal adhesions were spread throughout the surface. However, on narrow grooves focal adhesions were always positioned on the edges of surface ridges only. Apparently, most extracellular matrix (ECM) was produced by the cells that directly adhered to the substrate. The microtopography creates an environment, i.e. the so-called niches that are favorable for cells and cell–ECM interactions and increases the production of growth factors (Lu and Leng, 2009; Matsuzaka et al., 2003). In addition, the microtopography provides increased differentiation of osteogenic cells, which results in a high activity of alkaline phosphate (ALP) and osteocalcin synthesis (Novaes Jr et al., 2010). Gittens et al. (2011) reported that the osteoblast proliferation was regulated by nano-structure; however, the presence of microstructure was mainly responsible for osteoblast differentiation. On the other hand, Schwartz et al. (2009) reported that cell differentiation was promoted by micro-structure,

whereas cell proliferation was reduced. Thereby, micro-/nano-hierarchical structure was developed in order to accelerate both cell proliferation and differentiation (Zhao et al., 2010).

The surface roughness has not always been shown to be beneficial for the proliferation of osteoblastic cells; in fact, there are reports that have described a negative cellular response. It was shown that the proliferation of MG63 cells cultured on Ti, blasted Ti and Ti plasma-coated with Ti hydride powder decreased with increasing surface roughness, whereas differentiation increased (Schwartz et al., 2001). García-Gareta et al. (2013) compared mesenchymal stem cells (MSCs) proliferation and osteogenic differentiation between calcium-phosphate (CaP) coatings on polished and sand blasted Ti-6Al-4V discs prepared by biomimetic and electrochemical deposition. The results showed that MSCs proliferated more when cultured on the nano-sized BioM coatings compared to uncoated and electrochemically coated discs. Further, MSCs proliferated more on polished surfaces than on sandblasted coatings. Both the coatings induced osteogenic differentiation, which was greater on electrochemical coatings and SB discs. Influences of surface roughness in the nanoscale range and chemical composition on osteoblast-like cell behavior was studied by Lee et al. (2009). It was revealed that cell adhesion, spreading, proliferation and differentiation appear to be partly dependent on surface roughness. These cellular responses were more active on a smoother surface than on a rough surface, but were more pronounced on a moderate surface. These contradictory results suggest that the cell responses may be mediated not only by the surface roughness but also by other surface properties, i.e. chemical composition.

2.10.2.2 Effect of surface chemistry

Chemical composition also plays a vital role on cellular behavior. Different compositions have been added with the CaP coating either as dopant or composite coating. Many researchers incorporated ions like strontium, silicon, fluoride, zinc, cobalt or silver into CaP lattice and studied the different cellular behaviors (Surmenev et al., 2014; Surmeneva et al., 2015; Surmeneva et al., 2017; Türk et al., 2019). On the other hand, many researchers used $CaTiO_3$, ZrO_2, Ti, graphene oxide, Al, Ta_2O_5, TiO_2 etc. with the HA as the composite coating using different processes to study different behaviors (Arce et al., 2016; Boyd et al., 2008; Karimi et al., 2016; Kumari and Majumdar, 2017; Sun and Huang, 2018; Surmeneva et al.,

2016; Yılmaz et al., 2019). However, in this study the focus is given to TiO_2-CaP composite coating as TIO_2 provides the chemical as well as mechanical stability with corrosion resistance to CaP coating as already described in the above section. In addition, TiO_2 can be the potential material for bone implant, as it exhibits the biocompatibility properties, as reported by Majeed et al. (2015). MC3T3-E1 osteoblast cells were used to investigate the cell density and cell spreading on TiO_2 film fabricated by RF sputtering. It was found that, the surface having higher roughness and higher wettability exhibited maximum cell density and spreading. Since TiO_2 exhibits better mechanical as well as biocompatibility behavior, some researchers used it with CaP as composite coating. Dimitrievska et al. (2011) investigated the *in vitro* osteoinductive potential of plasma-sprayed 10% HA-TiO_2 coating using mesenchymal stem cells (MSCs) culture. The TiO_2–HA nanocomposite coatings demonstrated three times higher hydrophilicity than HA coatings. It demonstrated increased proliferation and osteoblastic differentiation on the nanostructured TiO_2–HA coatings than the current golden standard HA coating.

Kuwabara et al. (2012) studied the surface roughness and surface electric charge of a HA-TiO_2 hybrid coating fabricated by dual sputtering deposition technique using radiofrequency sputtering. Rat bone marrow-derived osteoblast-like cells were cultured on HA/TiO_2 hybrid surfaces with different electric charges. The attachment and spreading behavior of these cells were significantly increased on the hybrid surface and it was revealed that the surface electric charge on a titanium surface is an important factor for enhancing biological responses. Amaravathy et al. (2014) developed HA and HA/TiO_2 coatings on magnesium alloys to increase the biocompatibility and reduce the corrosion rate. It was observed that HA/TiO_2 coating exhibit higher hydrophilicity compared to HA coating. *In vitro* studies showed that HA–TiO_2 coated alloy exhibited higher osteoinduction compared to HA coated alloy. Cell culture studies proved higher cell attachment and proliferation on composite coated alloy by controlling the release of magnesium ions into the surrounding body tissue.

2.10.2.3 Effect of crystallinity

Besides the surface topography and surface chemistry, crystallinity of the CaP film also affects the biological performance of the implant. Amorphous or less crystalline HA phases

have been found to be more soluble in body fluids, and a high dissolution rate may have an adverse effect on the long-term reliability of an implant (Roy et al., 2011b). In addition, according to Hu et al. (2007), more cells are adsorbed and proliferate on a well crystallized HA coating than on an amorphous HA coating with comparable particle size. Roy et al. (2011b) reported the bioactivity of a highly crystalline (HA grains in the size range of 15–20 nm) nano-HA coating deposited on commercially pure Ti using an inductively coupled RF plasma spray. This study revealed an improvement in cell attachment and spreading on HA-coated Ti compared with uncoated Ti. Putkonen et al. (2009) found low adhesion strength of MC3T3-E1 cells on as deposited HA coating compared with the cells on the annealed film at 500°C. The cytoskeleton structures of cells were assayed, and it was suggested that the surface crystallinity may induce the appearance of focal adhesion points inside the filopodia structures and influence cell migration and spreading (Figure 2.6). Round cells with no clear organization of cytoskeleton can be seen on the as-deposited film; whereas, clear lamellipodia and filopodia structures on the annealed, crystallized film. On contrary, dos Santos et al. (2012) found that amorphous HA coatings (50 °C substrate temperature) prepared by RF magnetron sputtering with a higher dissolution rate induced greater cell spreading and less proliferation compared with carbonate-containing crystalline HA (500 °C post annealing temperature) and a pure Ti surface. The cellular adhesion was studied through the observation of the density of the actin fibre network, which is considered to be the result of cell flattening and spreading. The well-developed actin fibres in SaOS-2 osteoblast cells on the surface of both samples were examined. However, the cell spreading on the HA50°C surface was higher than that obtained on HA500°C.

Some studies have shown that ionic products from the dissolution of the coating stimulate osteoblast responses (Dos Santos et al., 2009; dos Santos et al., 2012; Gao et al., 2014). A β-TCP coating exerts a positive effect on osteoblastic proliferation compared with a Ti substrate. The Ca and P ions dissolved from the β-TCP ceramic might contribute to the enhanced proliferation rate of osteoblasts cultured on this material (dos Santos et al., 2012). Other studies have also reported that CaPs with poor crystallinity and high solubility can induce very high osteoconduction i.e. more favorable for initial cell attachment and proliferation (Gaasbeek et al., 2005; Wang et al., 2010). However, there are reports that low-

crystallinity CaP coatings exhibit a negative cellular response i.e. reduced cell proliferation and attachment (Hong et al., 2003; Lee et al., 2006b; Roguska et al., 2011).

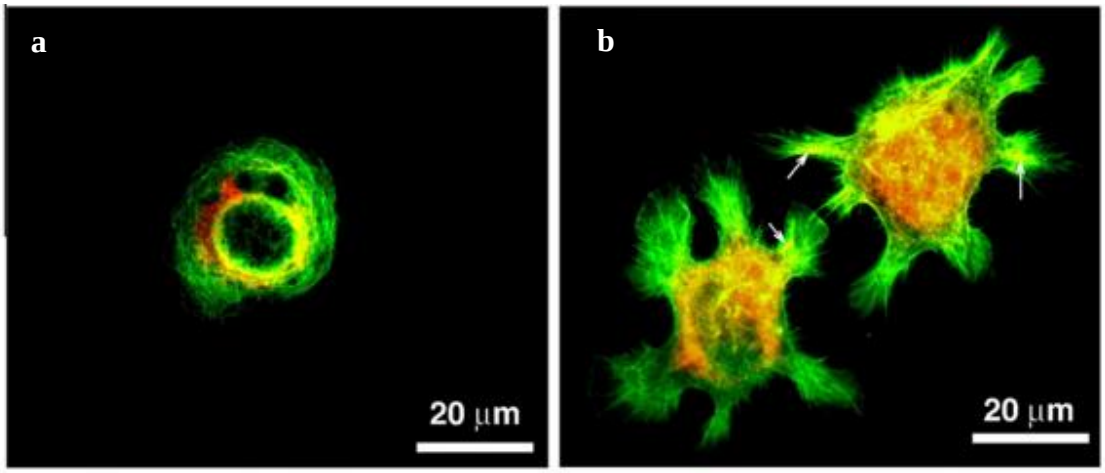

Figure 2. 7: *Cytoskeletal actin of MC 3T3 E1 cells grown on (a) as-PLD-deposited and (b) annealed HA films on silicon wafer. Cytoskeletal actin was stained by Alexa 488-labelled phalloidin (green) with a monoclonal antibody followed by Alexa 546-labelled anti-mouse antibody (red) (Putkonen et al., 2009).*

From the above survey, it can be observed that the cellular behavior of CaP coating is a complicated chemical and biological process. Besides the surface topography and chemistry, crystallinity, surface charge, wettability and protein adsorption affect the interaction between cells and interface. In addition, there is some disparity on the effect of different factors on the cell adhesion and proliferation behavior which need to be find out with the surface-property relationship.

2.11 Summary and Gaps in the Literature

Bone implant longevity with zero rate revision surgery is the ultimate goal for researchers to continue pursuing efforts to improve biomaterials performances. This literature review highlighted the various factors that contribute on the successful bone implant performances.

Studies on the development of Ti-6Al-4V as bone implant materials gained a substantial portion of research work amongst various types of metals due to their good corrosion resistance and excellent strength. However, problems, such as adverse reactions after implantations due to the release of toxic metal ions, implant-associated infections, and biomechanical mismatch still persist. Development of CaP coated Ti-6Al-4V as bone implant

materials have been growing since the last three decades due to their properties that enables cell adhesion and spreading and also overcoming the aseptic loosening problem. Based on the literature review, it is well understood that RF magnetron sputtering has been used as preferable coating method for bioactive material due to formation of uniform, continuous, well adhered thin film suitable for orthopedic applications.

Among the different CaP bioceramics, β-TCP has higher bioactivity due to its bio-integration and rapid dissolution rate in the body fluid; whereas, it's lower stability restricts its use in orthopedic application. Hence, HA has been widely used as coating material for orthopedic implant due to its higher stability with lower absorption rate, when contacted with the body fluid. However, when fast bone remodeling is desired, BCP can be used as the coating material for orthopedic implant due to the combined properties of HA and β-TCP which regulate the rate of dissolution with the stability. Furthermore, BCP exhibits higher hydrophobicity than HA. Thus, protein adsorption is more by BCP due to hydrophobic interactions, resulting in better osteoinductivity than HA. Therefore, physical, mechanical and biological characteristics of BCP coating on Ti-6Al-4V need to be researched.

The detachment of CaP coating is affected by many factors such as coating method, processing parameters, coating thickness and coating structure. CaP particles might be liberated from the coating due to the movement at the implant–bone interface, which can ultimately lead to failure of the artificial implant. Therefore, adhesion strength of CaP coating should be taken into account for prolong service life of the artificial implant. In order to overcome these problems, biocompatible TiO_2 can be incorporated with the CaP as the composite coating by various surface modification techniques as the composite possess higher chemical stability compared to apatite. However, higher percentage of TiO_2 may reduce the overall biological performance of implant. Hence, the different combination of CaP-TiO_2 composite coating should be studied. In addition, RF magnetron sputtering has been shown to produce thin and well adhered CaP films with the appropriate characteristics for the cell surface interactions. However, the stability of as-deposited CaP coatings can limit their application, *in vivo,* due to amorphous structure. Previous studies have shown that highly crystalline CaP coatings are less likely to dissolve than amorphous layers. Annealing has been used to convert the amorphous phase to crystalline structure. However, the increasing time or temperature of annealing led to produce crack or decomposition of CaP

layer into TCP and CaO. It is desirable that the annealing of these CaP surfaces is carefully controlled so that the coating's integrity and subsequent biofunctionality can be maintained.

The biological performances (protein adsorption and cell behavior) of CaP coated metallic material are influenced by surface chemistry as well as surface topography. The effect of surface topography on the biological performances are well studied but their effects have still created disparity among the researchers, and hence leave scope to explore the deepen understanding of the process-structure-property relationship. In addition, the biological performances of the developed materials have been well investigated either varying the surface chemistry or surface topography. The simultaneous effect of surface chemistry as well as surface topography may obtain excellent biological performance of bone implant materials, hence need to researched.

The objectives of the present study are already described in chapter 1. The plan of the work carried out in this thesis is represented in Figure 2.8.

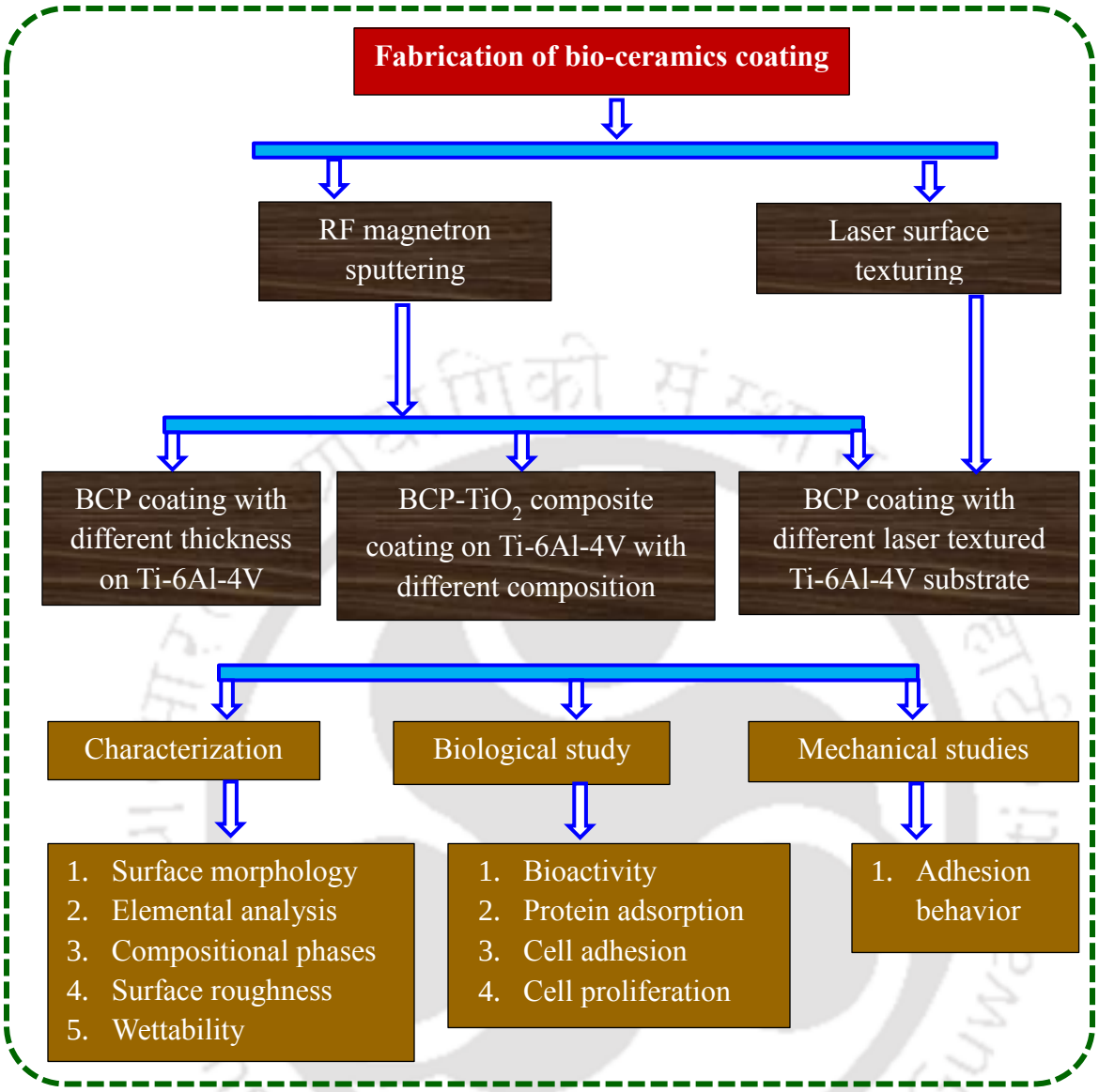

Figure 2.8: *Plan of work carried out in this thesis.*

Chapter 3

Mechano-Tribological Properties and *In Vitro* Bioactivity of Biphasic Calcium Phosphate Deposition on Ti-6Al-4V

3.1 Theme of work

From the literature review it was found that many studies have been investigated on magnetron sputtering of HA on Ti and its alloy; however, limited studies are available on BCP coating on Ti-6Al-4V using sputtering. Since, BCP has the combined properties of HA and β-TCP which regulate the rate of dissolution with the stability, it can be used as the coating material for orthopedic implant when fast bone remodeling is desired. Furthermore, BCP exhibits higher hydrophobicity than HA. Thus, protein adsorption is more by BCP due to hydrophobic interactions, resulting in better osteoinductivity than HA. Hence, it is essential to deposit the BCP films by magnetron sputtering and investigate the different physical, mechanical and biological characteristics of BCP coating for better understanding the process-structure-property inter-relationship that would provide guidelines for better implant design.

This chapter describes the fabrication and characterization of BCP films on Ti-6Al-4V along with the analysis of adhesion behavior and *in vitro* bioactivity of the films. Initially, the HA powder was synthesized from the raw fish scale with the cutting and polishing of Ti-6Al-4V substrate. BCP target was fabricated from the HA powder and used to coat the Ti-6Al-4V. RF magnetron sputtering was used to deposit BCP films on the Ti-6Al-4V surface for 4 h, 6 h and 8 h deposition time in order to obtain three different film thicknesses. Subsequently, physicochemical, mechanical and biological properties of these films were investigated using various characterization techniques. Structural and chemical analysis was performed using field emission scanning electron microscopy (FESEM), energy dispersive X-ray spectroscopy (EDS), x-ray diffraction (XRD) and RAMAN spectroscopy. The thickness of the BCP films was measured using a stylus profilometer. The surface roughness was evaluated using non-contact type profilometer. The surface wettability was examined using a contact angle test through goniometer. The adhesion behavior of the coatings was evaluated using a scratch test. To assess the *in-vitro* behavior of the films, an *in vitro*

bioactivity analysis was conducted using the simulated body fluid (SBF) immersion test. The primary objective of this chapter is to investigate the effect of film thickness on different physio-chemical properties, adhesion behavior and *in vitro* bioactivity of BCP film.

3.2 Materials and methods

3.2.1 Materials

Ti alloy (Ti-6Al-4V) was used as the substrate for the current study. Table 3.1 represents the mechanical properties of Ti-6Al-4V at room temperature whereas Table 3.2 shows the elemental composition of Ti-6Al-4V, which was confirmed by energy dispersive spectroscopy (EDS) analysis (Figure 3.1). Tri-hydroxymethyl aminomethane [$(CH_2OH)_3CNH_2$] powder was obtained from Merck, India. Hydrochloric acid (HCl), sodium chloride (NaCl), sodium bicarbonate ($NaHCO_3$), potassium chloride (KCl), dipotassium hydrogen phosphate trihydrate ($K_2HPO_4 \cdot 3H_2O$), magnesium chloride hexahydrate ($MgCl_2 \cdot 6H_2O$), calcium chloride ($CaCl_2$), disodium sulphate (Na_2SO_4), and dimethyl sulphoxide (DMSO) were procured from HiMedia, India. Double distilled water (Mili-Q, 18 mΩ, Millipore systems) was used throughout the work.

Table 3. 1: Mechanical properties of Ti-6Al-4V at room temperature

Yield strength (MPa)	Ultimate tensile strength (MPa)	Young's modulus (GPa)	% elongation	Hardness (HV)
850	957	113	11	298-302

Table 3. 2: Elemental composition of Ti-6Al-4V substrate

Element	Al	V	Ti
wt%	6.0	4.5	Balance

3.2.2 Substrate preparation

Ti-6Al-4V plates with 20×15×3 mm^3 dimension were cut by wire-electro discharge machining (WEDM, M/S Fostex FDK 7735, Japan) process and used as the substrate for RF magnetron sputtering. Ti-6Al-4V substrates were mechanically polished using SiC abrasive papers from grade 220 to 2000 grit sequentially in order to obtain fine surface. The polished

samples were further ultrasonically rinsed with acetone, deionized (DI) water and ethanol for 20 min each in order to remove oil as well as other residues from the surface of the substrate and finally stored in a desiccator before used in RF magnetron sputtering.

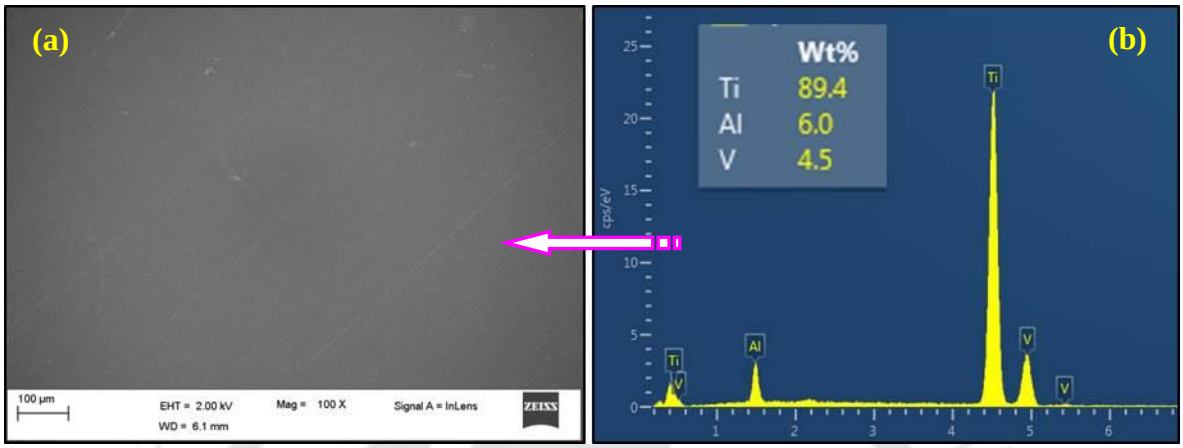

Figure 3.8: *Bare Ti-6Al-4V substrate (a) FESEM image and (b) corresponding elemental analysis.*

3.2.3 Synthesis of Hydroxyapatite (HA) powder

HA powder was used as the precursor to develop the target for sputtering process. HA powder of nanoscale dimensions was synthesized from abundantly available raw fish scales wastes using the method described previously with slight modifications (Chakraborty et al., 2011; Kongsri et al., 2013). After calcinating at 800 ºC, HA flakes were processed in high energy ball mill (M/S Fritsch, pulverisette, Germany) for 10 h to get powder in the nanometer range. The flowchart for the synthesis of HA powder from fish-scale is displayed in Figure 3.2.

The synthesized nano-HA was characterized for particle morphology, elemental composition, phase and particle size using field emission scanning electron microscopy (FESEM, M/S Zeiss-Sigma, Germany), field emission transmission electron microscope (FETEM, JEOL 2100F, Japan), energy dispersive spectroscopy (EDS) X-ray diffractometry (XRD, M/S Rigaku TTRAX 3, Japan) and particle size analyzer (PSA, M/S Beckman Coulter Delsa Nano, USA), respectively.

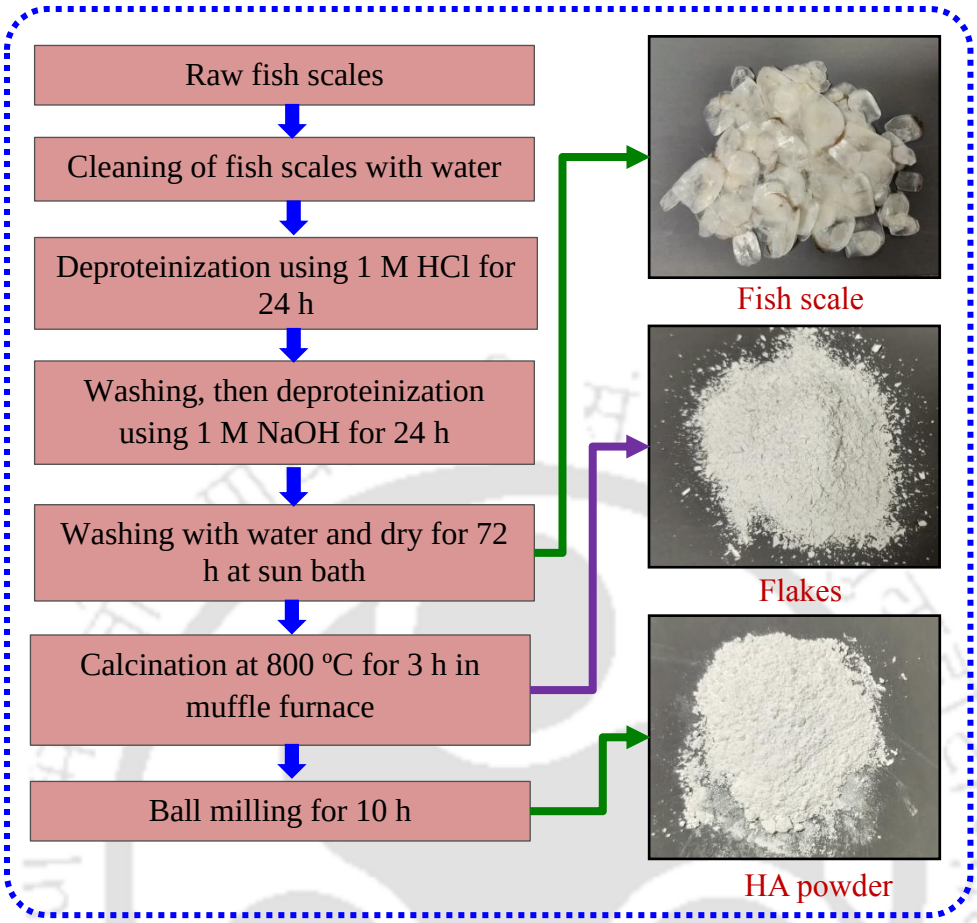

Figure 3.9: *The flowchart for the synthesis of HA powder from fish-scale and the images of step-wise products.*

3.2.4 Deposition of BCP films by RF magnetron sputtering

Coating of HA was carried out on Ti-6Al-4V substrate by RF magnetron sputtering (M/S Advanced Process Technology, India) process. The photograph of RF magnetron sputtering experimental set up is shown in Figure 3.3. A cylindrical target of 62 mm diameter and 4 mm thickness was made by sintering the compressed HA powder at 1300 °C for 5 h. The selection of sintering temperature and time was done to obtain BCP films consisting of β-TCP and HA approximately in the same proportion. The depositions were carried at room temperature. First, the coating chamber was pumped down to a base pressure of $3x10^{-6}$ mbar. Then highly pure Argon gas (99.99%) was introduced into the chamber as sputtering gas with a flow rate of 30 sccm (standard cubic centimeters per minute) during the entire sputtering process. By maintaining the pressure of sputtering chamber at $3x10^{-2}$ mbar and target to substrate distance approximately at 50 mm, the films were deposited at an RF power

of 30 W. The target was pre-sputtered in the argon ambience for 15 min in order to remove the impurities present on the target surface. Three sets of film thickness were considered in the present study by varying the deposition times (4 h, 6 h and 8 h) and keeping all other parameters constant. The sputtered substrates were taken out for further characterization.

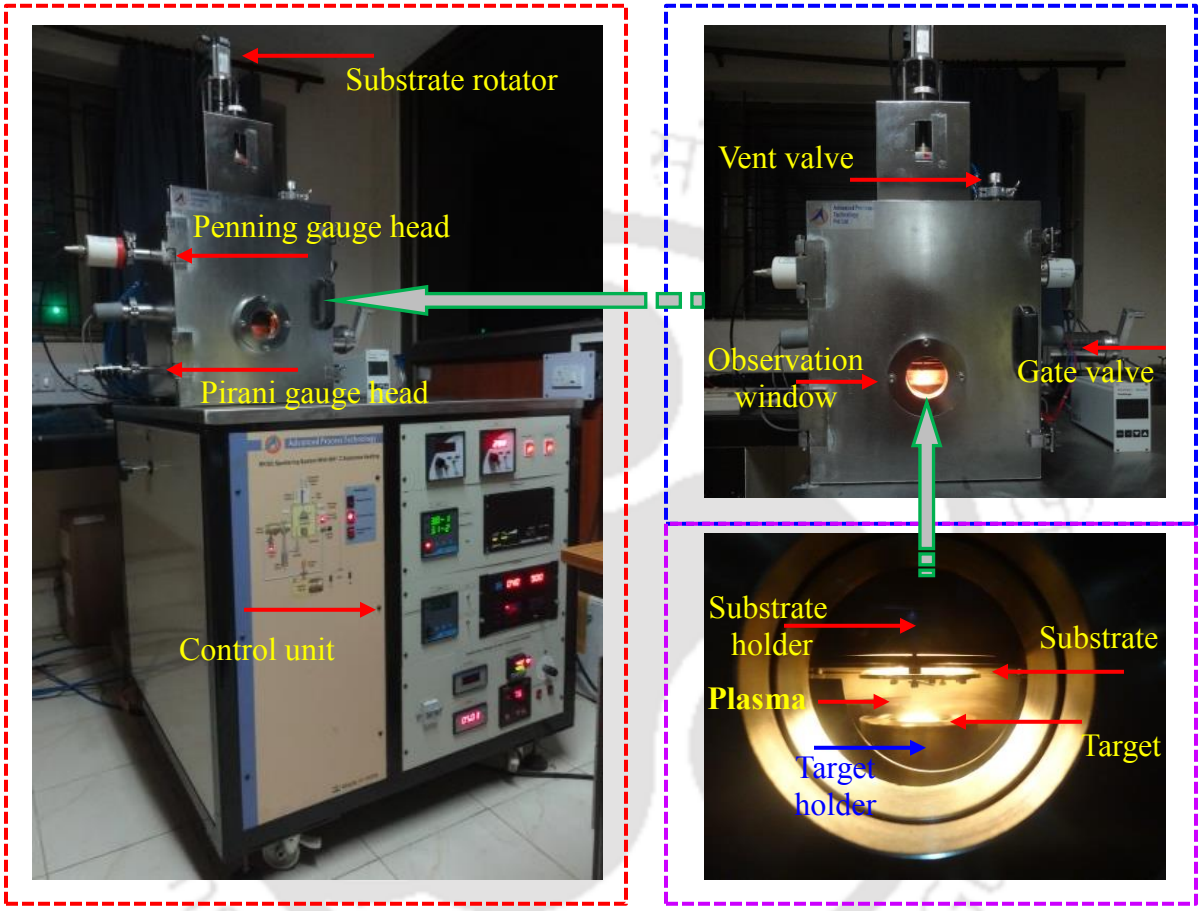

Figure 3.3: *Photograph of RF magnetron sputtering experimental set up.*

3.2.5 Characterization of films

3.2.5.1 Phase analysis

The thickness of sputtered films was evaluated by a stylus profilometer (M/S Vecco Dektak, 150). The phase composition and crystallite size of the sputtered films were analyzed by XRD with Cu-Kα radiation of wavelength 1.54059 Aº. The system was worked at 50 kV and 160 mA at room temperature. The XRD spectrums were acquired in a 2θ range of 20–70º using a scan speed of 3º/min and a step size of 0.03º. The database patterns of HA (JCPDS no. 09-0432), β-TCP (JCPDS no. 09-0169) and Ti (JCPDS no. 441294) were used to identify

the phases formed. A micro-Raman spectrometer (M/S Horiba Jobin Yvon - LabRAM, Japan) was used to acquire Raman spectra of different coatings using a helium-neon laser having a wavelength of 632.8 nm. A charged coupled device (CCD) detected the intensity of Raman scattered light and processes the data by a computer. Laser power of 13.5 mW was applied on the coated substrate. The surface morphology and elemental composition of BCP based coatings were investigated by FESEM equipped with EDS operating in a high vacuum with gold sputtered samples.

3.2.5.2 Surface roughness and wettability

The surface roughness of sputtered surfaces was evaluated using a non-contact type 3-D surface profilometer (M/S Taylor Hobson, UK). The instrument was equipped with a 20X lens having 4.7 mm focal length. 850 × 850 μm^2 area was initially scanned, and then a particular line was drawn in any direction to measure the roughness of the sputtered surface. Roughness parameter like center line average height (R_a) was recorded. A total of five random readings were taken for each sample, and the average one was considered as output response.

The wettability of surface has a significant influence on bioactivity, protein adsorption as well as cell adhesion, which generally depends upon the chemical phases and roughness of surface (Bakhsheshi-Rad et al., 2016b; Paital and Dahotre, 2009). The wettability of bare Ti-6Al-4V and BCP deposited substrates were evaluated by static sessile drop technique with simulated body fluid (SBF) droplet using contact angle goniometer (Model:HO-IAD-CAM-01B, Holmarc, India) at ambient temperature. SBF was prepared using the protocol described previously by Oyane et al. (2003). Different reagent-grade chemicals were dissolved in 700 ml distilled water in the following order: NaCl (8.026 g), $NaHCO_3$ (0.352 g), KCl (0.225 g), $K_2HPO_4.3H_2O$ (0.230 g), $MgCl_2.6H_2O$ (0.311 g), $CaCl_2$ (0.293 g) and Na_2SO_4 (0.072 g). Then the solution was buffered to pH 7.4 at 37 ºC with trihydroxymethyl aminomethane (6.063 g) and hydrochloric acid (1 M, 40 ml). SBF droplets of 2 µl volume were kept on the cleaned surface by a hypodermic syringe for a residence time of 15 s, and the advancing angle was considered as a measure of wettability. The average value of five contact angles taken at various positions was considered as the mean contact angle for each surface.

3.2.6 Mechano-tribological properties

Vickers hardness tester (M/S Buehler, USA) with a load of 100 gf (1 N) was used to determine the micro-hardness of the coating surfaces. The adhesion behavior or surface scratch resistance of sputtered substrates was investigated by using a micro scratch tester (TR-101, M/S Ducom, India). A Rockwell C diamond indenter having a tip radius of ~200 μm was equipped with this tester. In this study, a scratch test was performed in two ways by applying two types of loads. First one was with linearly increasing load from 1.0 to 9.0 N to determine the critical load (L_c) to evaluate the adhesion behavior of sputtering film with the substrate using the coefficient of friction (COF) curve and microscopic observation. Other parameters were as follows: scratch length of 8 mm, loading rate of 1 N/mm and scratch speed of 0.2 mm/s. The second one was by applying different constant loads of 1, 4 and 7 N to determine the scratch resistance of different thickness sputtered substrates by measuring scratch width and depth. The other parameters for this were as follows: 3 mm scratch length and 0.2 mm/s scratch speed. Three independent scratches were made on each different thick-sputtered substrates, and the average one was taken as the response. Optical microscopy and FESEM are used to analyze the scratches. The non-contact 3-D profilometer was utilized to measure the width and depth of the scratch tracks.

3.2.7 *In vitro* bioactivity

In vitro bioactivity tests were carried out by immersing the BCP coated substrates in SBF solution which has concentration and composition similar to human body fluid. To investigate the bioactivity, triplicate samples of each BCP film and uncoated Ti-6Al-4V were immersed in the SBF. Briefly, the samples were soaked separately in the 10 ml of SBF solution in polypropylene (PP) bottles for 14 days. The containers were tightly closed and incubated in a thermostatic chamber at 37 ± 0.5 °C. In order to maintain a pH of 7.4, a fresh solution of SBF was replaced in every 24 h. The samples following SBF immersion were rinsed gently with ethanol as well as distilled water and then kept in a hot air oven at 80ºC for 4 h to ensure complete removal of water. In order to evaluate the apatite formation on the surface of BCP films after removing from SBF solution, different characterization such as XRD, RAMAN, FESEM and EDS were carried out to evaluate the phases, surface morphology and elemental composition at the surfaces of samples, respectively.

3.3 Results and discussion

3.3.1 Characterizations of nano-HA powder

The particle morphology, elemental composition, phases and particle size of synthesized nano-HA are shown in Figure 3.4. Agglomerated HA particles with the polygonal shape having the size ranging from 100 nm to 600 nm were observed (Figure 3.4 (a)). The Ca/P ratio of synthesized HA powder was found to be 1.65 which is approximately equal to the stoichiometric Ca/P ratio of HA (Figure 3.4 (b)). The XRD pattern of synthesized HA is matched with the standard XRD pattern of HA with JCPDS no. 09-0432 (Figure 3.4 (c)). The average particle size of HA powder is found to be 357 nm (Figure 3.4 (d)). FETEM image (Figure 3.4 (e)) of HA particles show the almost spherical shape and size less than 100 nm. The typically selected area electron diffraction (SAED) pattern shows the concentric rings indicating the polycrystalline nature of HA powder (inset, Figure 3.4 (e)). Figure 3.4 (f) represents the HRTEM image of HA powder which shows easily distinguished orientation plane correspond to HA. The inset of Figure 3.4 (f) consists the inverse fast Fourier transform (IFFT) image having lattice spacing of 3.08 Å which corresponds to (211) hkl orientation plane of the respective sample.

3.3.2 Thickness of sputtered films

The thickness (T) of the sputtered film was found to be 400±20 nm, 700±40 nm and 1000±60 nm for deposition duration (t) of 4 h, 6 h and 8 h, respectively. The film thickness was increased linearly with time of deposition (T = 118.9 t). A similar type of behavior was found by Das et al. (2018) during RF magnetron sputtering of HA on Si. They found 1000 nm film thickness in 3 h with 50 W RF power; however, in this study, 1000 nm thickness film was obtained at 8 h with 30 W power, indicating less deposition rate at lower RF power.

3.3.3 Phase analysis of sputtered films

The compositional phases of the RF sputtered films are presented by XRD spectrum (Figure 3.5. Since the deposited films are grown from the vapor phase, they are amorphous in nature. So to enhance the crystallinity of the films, the sputtered substrates were subjected to annealing treatment at 700 ºC for 2 h.

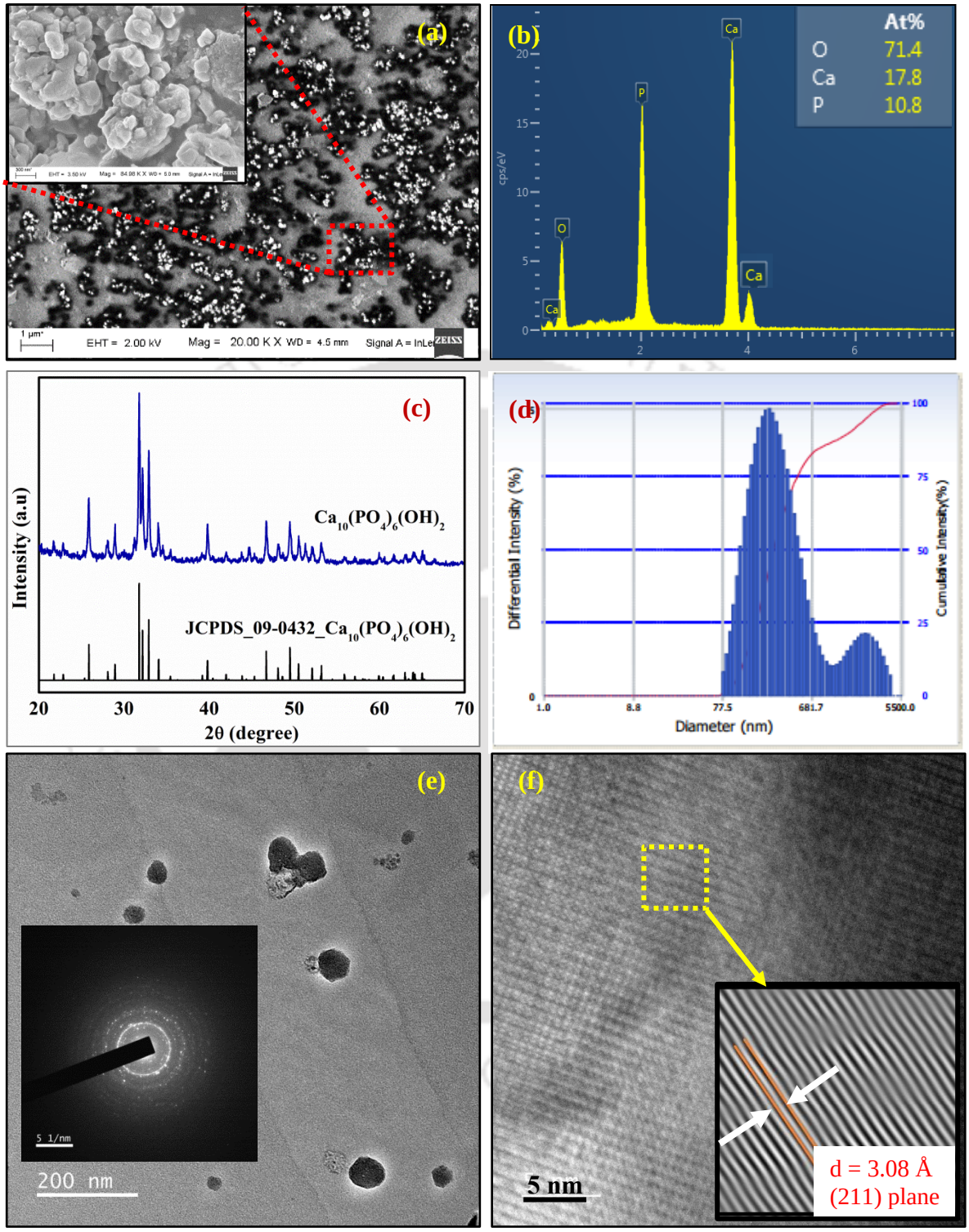

Figure 3.4: *Hydroxyapatite powder: (a) morphology, (b) elemental composition, (c) phase composition (d) average particle size (e) FETEM image (inset, SAED pattern), and (f) HRTEM image* (inset: IFFT image), *showing orientation of plane.*

The phase analysis of the sputtered films revealed the peaks of HA as well as β-TCP. Pure HA phase was found in the film without any secondary phase during RF sputtering when the target was made by sintering of HA powder at 1100 ºC for 1 h (Surmenev et al., 2011; Surmeneva et al., 2017). However, in this study, the target was sintered at 1300 ºC for 5 h. Hence, HA as well as β-TCP was obtained due to decomposition of HA at a higher temperature. The same was expected as sputtering is known to deposit films of the same stoichiometry as found in the target (Das et al., 2018).

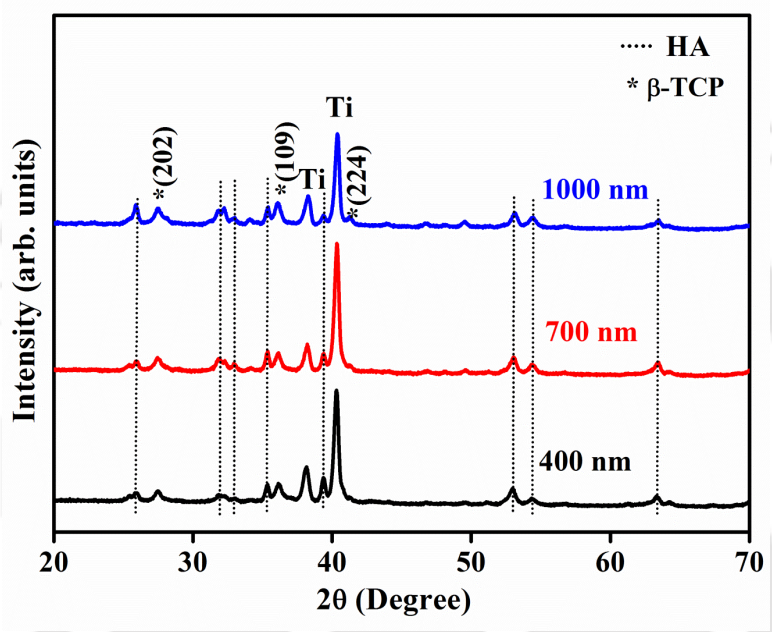

Figure 3.5: *XRD spectra of sputtered samples at various film thickness: 400 nm, 700 nm and 1000 nm.*

According to Pamu et al. (2008), the weight percentage (wt%) of individual phases present on the surface of different coating films can be calculated according to Eq. 3.1.

$$W_{HA} = \left\{ \frac{1}{\left[1 + 1.265\left(I_{\beta-TCP}/I_{HA}\right)\right]} \right\} \times 100 \qquad (3.1)$$

Where, W_{HA}, $I_{\beta\text{-}TCP}$, and I_{HA} denote the wt% of HA, the intensity of strongest reflection of β-TCP and HA, respectively. The calculated wt% of HA was found to be 43.41%, 43.53% and 44.87% for the films thickness of 400 nm, 700 nm and 1000 nm, respectively. So, the corresponding wt% of β-TCP was 56.59%, 56.47% and 55.13%. It was seen that the wt% of HA is almost similar irrespective of the increase of film thickness. This might be due to an

increase in the number of particles releasing from the target and then deposited on the substrate. However, there was no variation in the weight ratio of HA and β-TCP with respect to time. The apparent crystallite size of the films with different thickness was calculated using Scherrer's formula and was found to be 15±2 nm, 17±3 nm and 18±3 nm for films of thickness 400nm, 700nm and 1000 nm, respectively. So with increasing film thickness, there was an increase in the crystallite sizes. Probably with increasing deposition time large numbers of sputtered atoms disembarked over the well-crystallized nuclei because the already crystallized nuclei are thermodynamically most favorable sites for the incoming atoms to settle down. This reason also reflected in the increasing intensity of the peaks with increasing film thickness (Figure 3.5). The XRD results also clearly infer that with increasing thickness of the films, there is a substantial reduction in intensity of the substrate peaks which also indirectly hints at the increasing thickness of the coated layer. In such cases, the incident X-rays encounter mostly the biphasic calcium phosphate (BCP) layers and less of the substrate. The resultant reflected intensity thus produces more intense coating peaks. Das et al. (2018) and Hamrit et al. (2016) observed similar variations with film thickness during RF magnetron sputtering of HA and ZnO:Al thin film, respectively. Table 3.3 shows the wt% of HA and β-TCP, as well as the crystallite size of the different sputtering film.

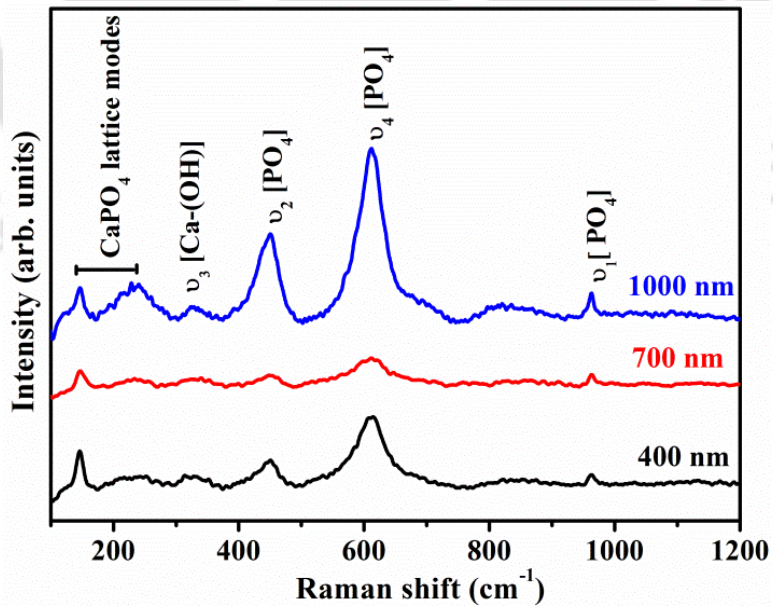

Figure 3.6: *RAMAN spectra of sputtered samples at various film thickness: 400 nm, 700 nm and 1000 nm.*

Raman spectroscopy can provide us with valuable insights into the lattice disorder and phase information due to molecular substitutions in the films. The Raman spectrum of the sputtered films is compiled in Figure 3.6. The XRD analysis revealed that the sputtered films are biphasic. Complementary results were also obtained from Raman spectra analysis of the sputtered films. The vibrational spectra of both β-TCP and HA exhibit a strong molecular character associated with the internal modes of the PO_4^{3-} tetrahedral. The vibrational normal modes of the free tetrahedron are well known and give rise to four different frequencies: ν_1, ν_2, ν_3 and ν_4. The ν_1 frequency corresponds to the symmetric stretching of the PO bonds, whereas the ν_3 frequency arises from the asymmetric P-O stretching and also P motion. The ν_2 frequency corresponds to the doubly degenerate O-P-O bending mode, and the ν_4 frequency is due to the O-P-O bending character. According to Koutsopoulos (2002), the Raman shift at 612 cm^{-1} is primarily found for β-$Ca_3(PO_4)_2$ due to O-P-O and O-P bending and stretching modes (ν_4) of the phosphate (PO_4) group. Similarly, the appearance of the band at 962 cm^{-1} bears a strong signature of HA phase formation. In pure HA this particular band appears with a very sharp intensity. However, in this case, it was found the band is of very low intensity, and this indeed justifies the claim that the films are biphasic. Prosolov et al. (2017) reported similar results from Raman spectra of biphasic calcium phosphate films where the most intense peak at 962 cm^{-1} was suppressed due to presence of secondary phases like β-TCP. The PO_4 modes were noticed to have different intensity at 450 and 610 cm^{-1} for various films giving prominence for 1000 nm thick film. A similar trend can also observe for the bands at 149 – 235 cm^{-1} that can be assigned to Ca-PO_4 lattice modes.

Table 3. 3: Wt% of HA and β-TCP, as well as crystallite size of the different sputtering film

Sputtering time (h)	Film thickness (nm)	Wt% of HA	Wt% of β-TCP	Crystallite size (nm)
4	400±20	43.41%	56.59%	15±2
6	700±40	43.53%	56.47%	17±3
8	1000±60	44.87%	55.13%	18±3

3.3.4 Surface morphology and elemental analysis

The surface morphology and corresponding EDS spectrum for different thick films are represented in Figure 3.7. All the coated samples exhibited dense, non-porous, regular grain like morphology distributed uniformly throughout the surface. This shows the features of uniform films deposited by RF magnetron sputtering. However, the average grain size, measured by Image J software was found to increase with film thickness, as shown in Table 3.4. The BCP film with 400 nm thickness possessed well-distributed small and spherical grains with an average diameter 48±9 nm (Figure 3.7 (a)). The 600 nm thick BCP film surface exhibited well-refined and distributed bigger grains with mean diameter 121±45 nm. This is in nucleation process of the crystallites with time as well as segregation of smaller crystallites into bigger grains because of the kinetic energy imparted to the film during the sputtering process (Figure 3.7 (b)). This observation is well supported by the analysis of the XRD patterns also. The 1000 nm thick BCP film was well bonded, elongated with bigger grains of 379±75 nm due to coalescence of grains. Also, some islands of grains were seen due to abrupt clustering of bigger grains (Figure 3.7 (c)). Uniformly distributed grains and increase in the grain size with the film thickness was also found during calcium phosphate sputtering on Mg alloy and Si wafer (Surmenev et al., 2011; Surmeneva and Surmenev, 2015b).

The EDS spectra characterizing the elements present in BCP films with different thickness on Ti alloy is illustrated in Figure 3.7 (a, b, c). The atomic percentage of different elements was found by scanning the full area taken at 5 KX magnifications. The presence of Ca, P and O in all three films confirmed the proposed mechanism of sputtering. In this study, the EDS spectrum was obtained by using electron beam energy of 20 keV; hence, a significant amount of substrate material (Ti, Al and V) underneath the coating was detected in the spectrum. It was observed that the percentage of Ca, P and O were increased with an increase in film thickness; however, that of Ti, Al and V were decreased, as given in Table 3.4. Due to an increase in film thickness, the penetration of the electron beam entered into the Ti-6Al-4V substrate decreased, and it detected more elements from the film. Surmenev et al. (2017) also found an increase in % of Ca with an increase in HA film thickness during RF magnetron sputtering of HA film on Ti substrate. It can be attributed to the lower binding

energy of CaO group (~91 kcal/mol) as compared to PO_4^{3-} group where the binding energy is 142 kcal/mol.

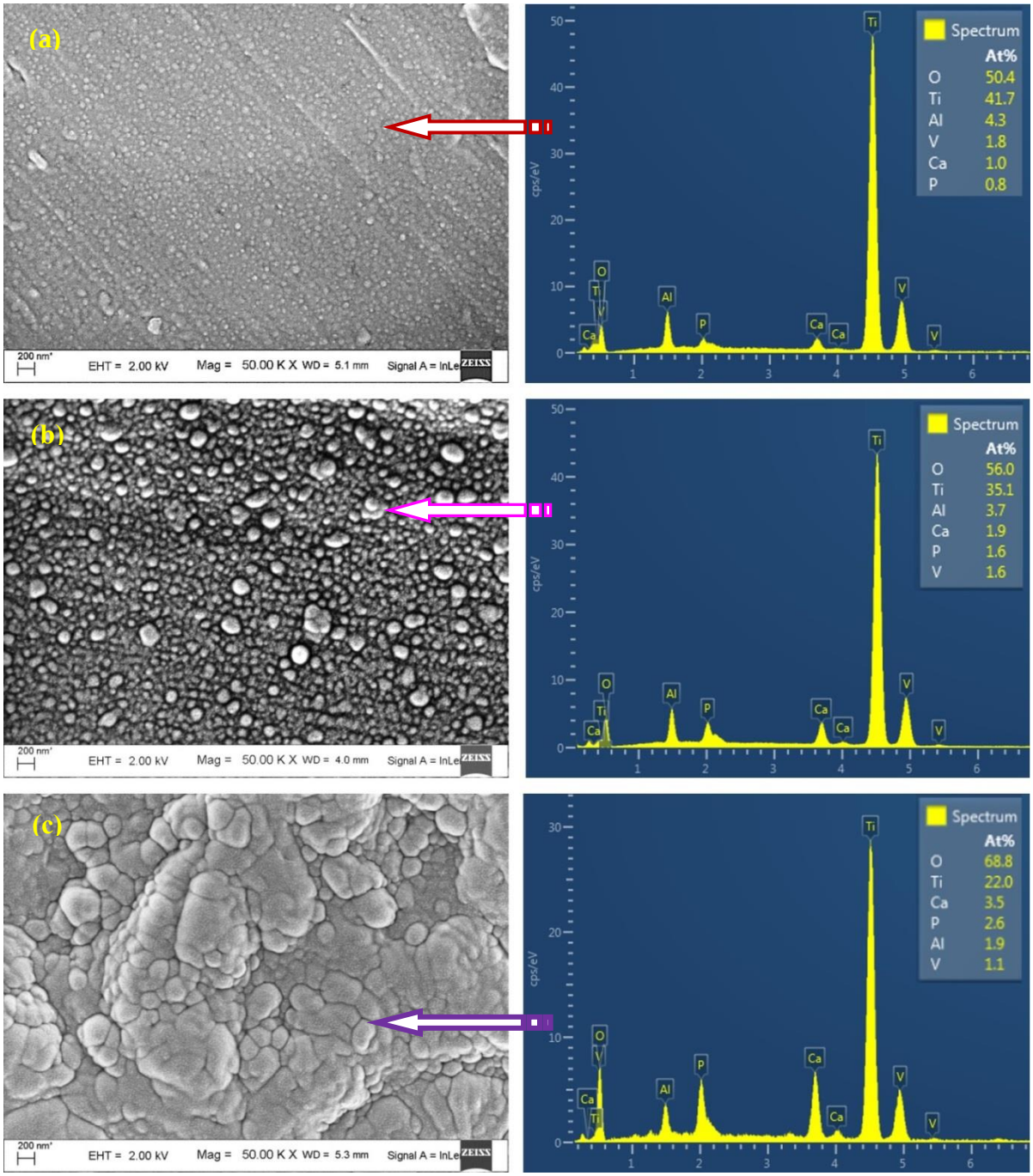

Figure 3.7: *Surface morphology and corresponding EDS analysis of different thick films: (a) 400 nm, (b) 700 nm and (c) 1000 nm.*

This makes Ca relatively easy to sputter and hence with increasing deposition times, the Ca content in the thin film increases (Prosolov et al., 2017). All these outcomes were in

good agreement with XRD and RAMAN investigations. The EDS mapping spectra confirmed the homogenous dispersion of each element on the investigated area of the sputtered surface.

Table 3. 4: Grain size and different elements (at%) present on the surface of different sputtering films

Film thickness (nm)	Grain size (nm)	Element (at%)					
		Ca	P	O	Ti	Al	V
400±20	48±9	1.0	0.8	50.4	41.7	4.3	1.8
700±40	121±45	1.9	1.6	56.0	35.1	3.7	1.6
1000±60	379±75	3.5	2.6	68.8	22.0	1.9	1.1

3.3.5 Surface roughness and wettability

The surface roughness of uncoated as well as coated films is represented in Figure 3.8. The 2-D surface profiles of uncoated Ti-6Al-4V and 1000 nm film are displayed in Figure 3.9.

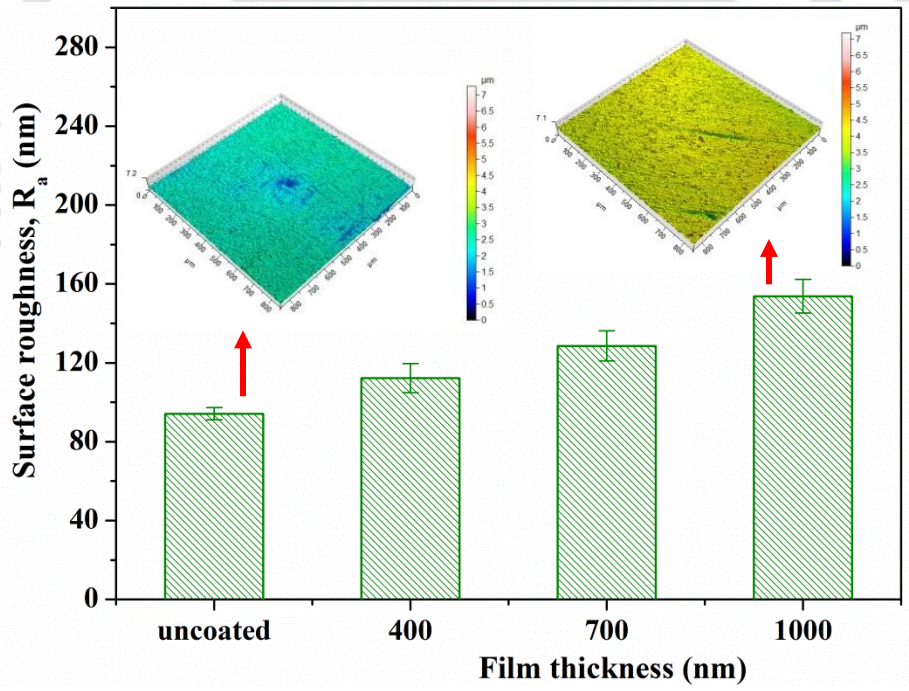

Figure 3.8: *Surface roughness (Ra) of uncoated and coated samples with different film thickness.*

Though the average surface roughness (R_a) of all the substrates was in the nanometer range, the coated substrates had higher R_a values compared to uncoated Ti-6Al-4V (Figure 3.8). However, with increasing film thickness, surface roughness gradually enhanced from 94 nm to 153 nm as the nucleation of spherical grains increased on the rougher coated surface compared to the uncoated Ti-6Al-4V substrate. Further improvement in R_a value was attributed to the presence of bigger grains and islands of grains due to coalescence as well as abrupt clustering of grains on the surface with higher film thickness, as shown in Figure 3.7. Higher surface roughness value for the thicker film was also obtained by Surmeneva and Surmenev (2015b) during HA coating on Mg alloy.

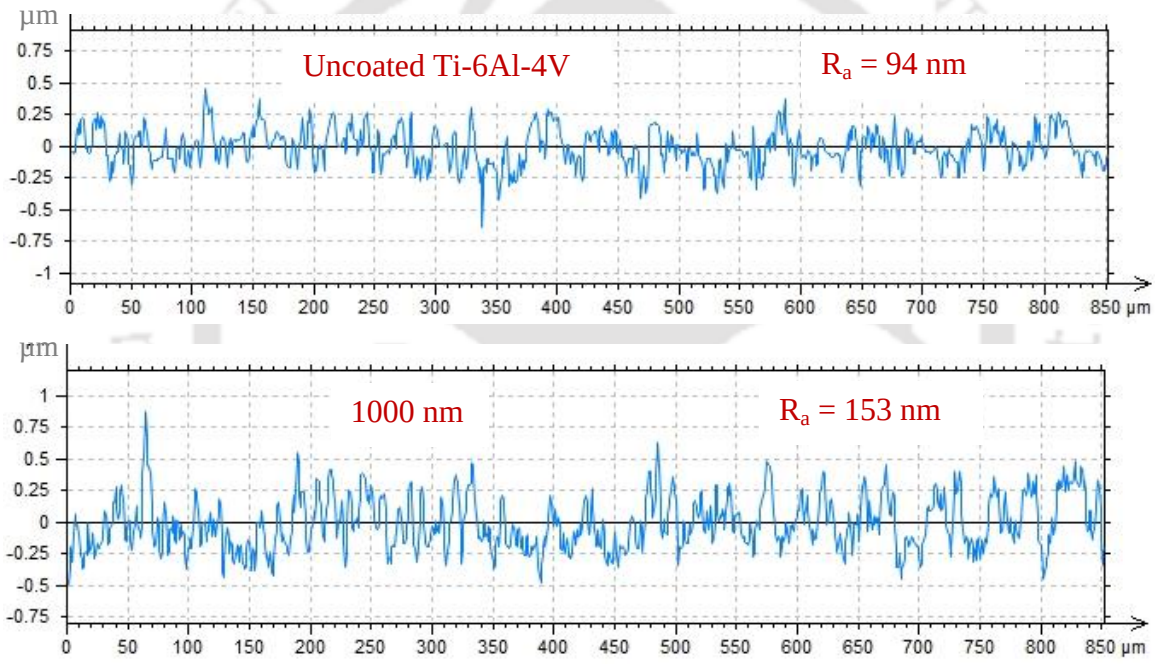

Figure 3.9: *2-D surface profiles of uncoated Ti-6Al-4V and 1000 nm film.*

Surface roughness and surface chemistry play a crucial role in the wettability of that surface (San Thian et al., 2011; Sun and Huang, 2018). Different materials deposited with various CaP thin films are hydrophilic, as reported in many pieces of literature (Dulski et al., 2018; San Thian et al., 2011; Xia et al., 2018). In this study, the SBF contact angle on the uncoated substrate was found to be 89.6º(±2º), however, it was 73.7°(±1º), 65.1°(±1º) and 61.2°(±2º) for 400 nm, 700 nm and 1000 nm thick BCP films, respectively, indicating remarkable improvement of hydrophilicity (Figure 3.10). This was attributed to the presence

of phosphate tetrahedral in HA and β-TCP lattice structure. Phosphate (PO_4^{3-}) anions are electro-negatively charged which attract the electro-positively-charged (H^+) ions strongly as well as significantly from SBF molecules. Thus, BCP coated Ti-6Al-4V showed more hydrophilicity as compared to uncoated Ti-6Al-4V.

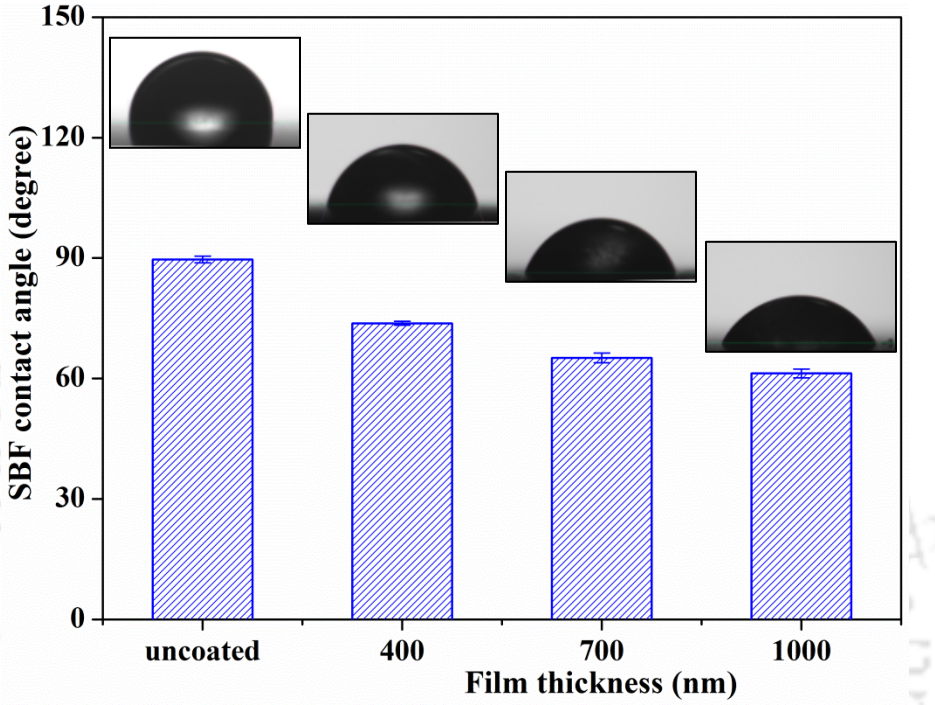

Figure 3.10: *SBF contact angle of uncoated and coated samples with different film thickness.*

On the other hand, it was revealed that the contact angle reduced with an increase in film thickness. As surface roughness increases with film thickness, there is an increase in the surface area of the films. So the SBF droplet tends to spread more that causes a decrease of the contact angle values. Surmeneva and Surmenev (2015b) also obtained a lesser contact angle with 1500 nm thick HA film on Mg alloy due to higher surface roughness compared to 700 nm thick film. The decrease in contact angle with an increase in surface roughness of sputtered film satisfies Wenzel equation (Eq. 3.2) which state that with the increase in surface roughness the wettability is enhanced when $r > 1$ and $\theta < 90°$, as also reported by Quéré (2008).

$$\mathrm{Cos}\,\theta^* = \mathrm{r}\,\mathrm{Cos}\,\theta \qquad (3.2)$$

Where, r is the surface roughness factor, θ is the Young contact angle for an ideal surface and θ^* is the apparent contact angle.

3.3.6 Micro-hardness

Micro-hardness is an important factor related to yield strength or resistance of the coated substrate, which can determine the stability, and reliability of coated film on the substrate. Figure 3.11 (a) shows the Vickers's micro-hardness of uncoated Ti-6Al-4V, as well as BCP coated substrates with different film thickness. The surface profile of a typical micro-indent is illustrated in Figure 3.11 (b). All the sputtered substrates exhibited higher micro-hardness compared to uncoated Ti-6Al-4V (324 HV). Ramesh et al. (2013) in their work revealed that HA exhibit hardness of ≈5 GPa when sintered at 1300 ºC. Similarly, Viswanath et al. (2008) found that β-TCP has an average hardness of ≈7.6 GPa; however, Ti-6Al-4V exhibit ≈3.3 GPa hardness, as reported by Samanta et al. (2018).

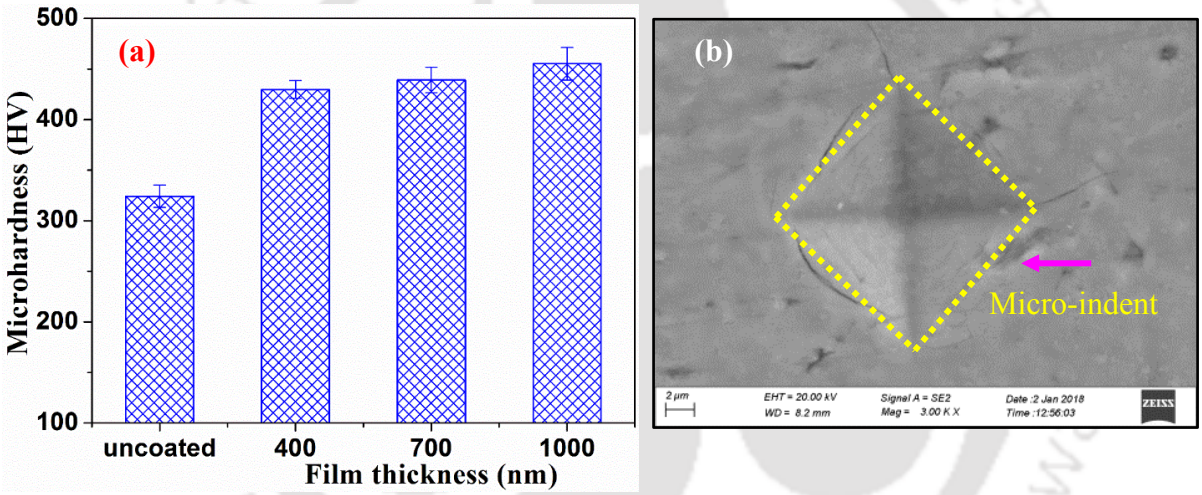

Figure 3.11: *(a) Micro-hardness of uncoated and coated samples with different film thickness and (b) surface profile of a typical micro-indent.*

Thus, due to the presence of HA as well as β-TCP bio-ceramics on the substrate surface, the depth of indentation was less as compared to uncoated Ti-6Al-4V. Hence, the sputtered substrates had a higher hardness than Ti-6Al-4V. Moreover, the micro-hardness was increased from 430±9 to 455±16 HV when BCP film thickness increased from 400 nm to 1000 nm. However, the increase in micro-hardness was not significant. This may be due to the presence of almost the same wt% of HA and β-TCP on the surface of all films irrespective of film thickness. From this, it can be concluded that the strength or resistance to indentation of BCP coated substrates is significantly higher than the uncoated Ti-6Al-4V. In

addition, the substrate with higher film thickness has slightly higher resistance to indent; hence, a little bit more stable than the substrate with lower film thickness.

3.3.7 Surface scratch resistance

The primary requisite for the long-term functioning of sputtered implants is the good adhesion or bonding between the sputtering film and the substrate surface. Micro-scratch tests are frequently performed to evaluate that adhesion of the sputtering film to the Ti-6Al-4V substrate. The COF curve and microscopic observation are used to determine the critical load (L_c) which is directly related to adhesion strength. The lower critical load, L_{c1} is the minimum load at which cracking or chipping of coating starts, while the critical load, L_{c2} corresponds to exfoliation or delamination of coating (Cui et al., 2017; Mohseni et al., 2015; Rabiei et al., 2006). Additionally, the force required to detach the coating layer from the substrate is known as the scratch force (adhesion strength). Friction can be specified to be the resistance tangential force to a relative motion between two surfaces in contact. Eq. (3.3) shows the formula for the friction force:

$$F = \mu N \qquad (3.3)$$

where N is the normal force and μ is the coefficient of friction (COF). Figure 3.12 represents COF as a function of the applied load as well as distance during the scratch test of BCP sputtered substrates with 400, 700 and 1000 nm film thickness. A similar trend of COF was obtained for all the BCP films. According to results obtained, the graph was divided into four zones: Z1 (from 1.2 to 2.3 N), Z2 (from 2.3 to 4.8 N), Z3 (from 4.8 to 7.8 N) and Z4 (from 7.8 to 9 N). Figure 3.13 shows the FESEM images of scratch tracks corresponding to different zones (as shown in Figure 3.12) on the BCP sputtered substrate with 1000 nm film thickness. After the initial run period, a small oscillation of COF (≈ 0.10 to 0.13) was seen for all the films when the applied load was varied between 1.2 to 2.3 N in Z1 zone. Because of the initial surface morphology of deposited coatings, small oscillation occurred at very low applied load. Surmeneva et al. (2015) also obtained strong oscillations of COF due to initial surface morphology of as deposited HA coating having thickness of 690 nm on Ti substrate using RF sputtering. There was no sign of disruption, chipping and cracking in the vicinity of scratch. Only impression mark was seen in the films within the applied load of 2.3 N, as shown in Figure 3.13 (a).

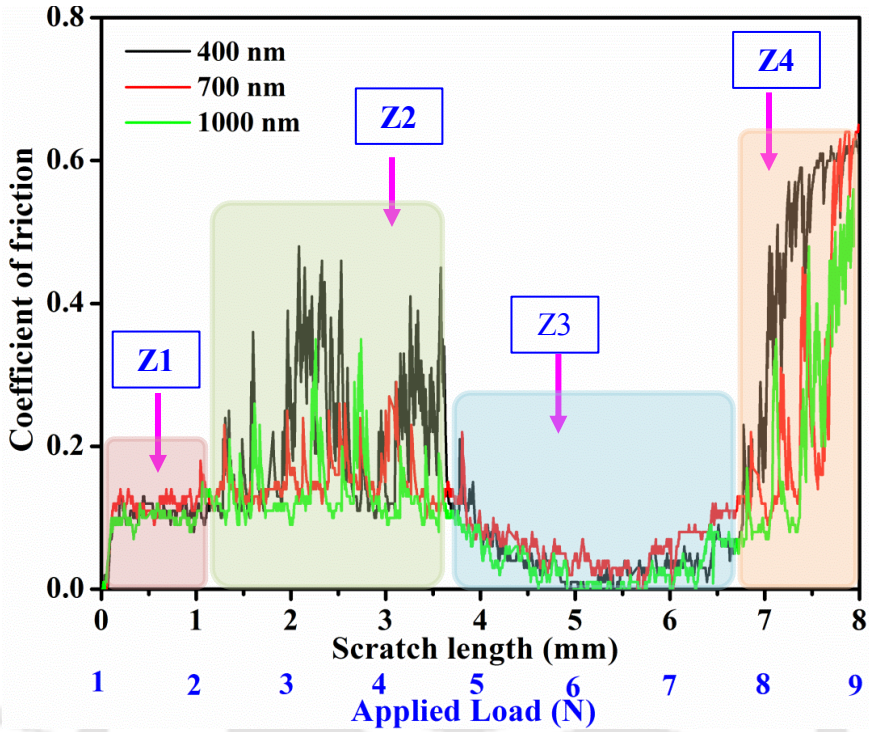

Figure 3.12: *Evolution of co-efficient of friction (COF) as a function of applied normal load using a micro-scratch test on the BCP sputtered substrates with different film thickness: 400 nm, 700 nm and 1000 nm.*

Similar types of behavior were observed for other thick films. After this zone, COF changed abruptly from 0.17 to 0.4 for all the films for load ranges 2.3-4.8 N (Z2 zone). Some localized chipping or detachment of coating was observed along the scratch path, as shown in Figure 3.13 (b). L_{c1} is the lower critical load where chipping or cracking of coating initialized. Therefore, L_{c1} was 2.3 N for all the BCP films. After this zone, COF was suddenly reduced to almost zero within the load range of 4.8-7.8 N (Z3 zone).

In this zone, regular cracks and sliding marks were observed along the scratch path (Figure 3.13 (c)). Due to high load and movement of the indenter, periodic formation, as well as removal of localized chips or particles, occurred at the contact interface. Thus sliding occurred between indenter and substrate, which caused a reduction of COF in this region. In Z4 zone, again COF was increased to 0.6 within a load range of 7.8-9.0 N. More deep cracks were seen along the scratch path and worn material was observed at the scratch edges, as shown in Figure 3.13 (d). So, exfoliation or delamination of coating occurred in this region. Hence, L_{c2} was approximately 7.8 N. Hence, the BCP-based coating failure was started from localized delamination, followed by sliding as well as cracking and finally by delamination at

the edge of the scratch path. Surmeneva et al. (2015) found similar behavior of failure during scratch test of HA-Si coating by RF sputtering.

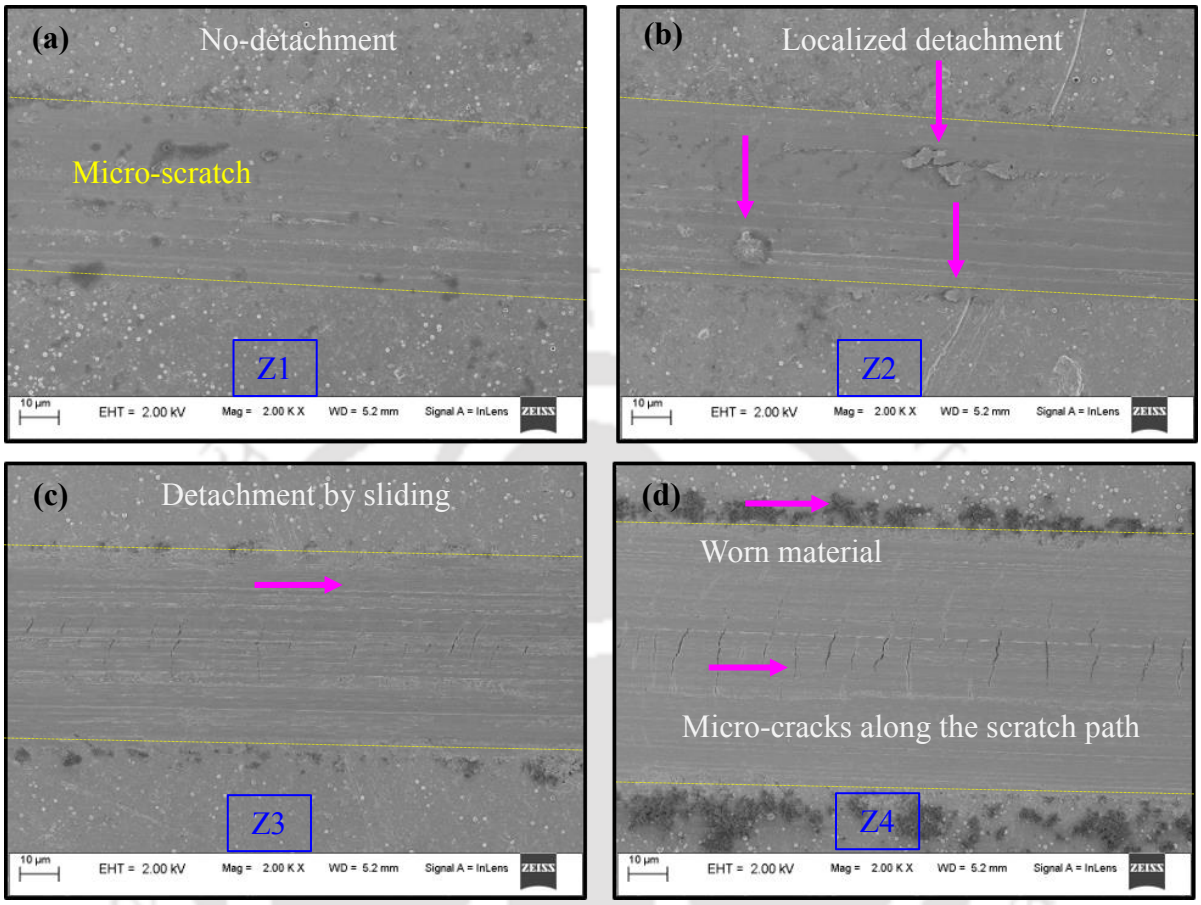

Figure 3.13: *Different failures of scratch tracks corresponding to different zones (a) Z1, (b) Z2, (c) Z3 and (d) Z4 (as shown in Figure 3.9) on the BCP sputtered substrate with 1000 nm film thickness.*

Due to the presence of same phases with the almost similar quantity of HA and β-TCP on the surface, all films exhibited a similar trend of load vs COF curve as well as critical load. During the scratch test of HA film up to 2 N loading force, Pichugin et al. (2008) found neither any detachment nor cracks in the coating. They also reported that the adhesion strength is more than 40 MPa and depends upon the sputtering film thickness and above 1.6 µm film thickness it decreases. Surmeneva et al. (2015) found delamination of 690 nm thick HA film as-deposited by RF sputtering at a scratch load of 5.85 N. The higher critical load of 7.8 N for the as-deposited BCP film in this study may be the presence of different phase β-TCP with HA. Since, the hardness of β-TCP is more than HA (Ramesh et al., 2013; Viswanath et al., 2008) and according to Amaravathy et al. (2014) harder coating

exhibits higher bonding strength. Hence, higher critical load of BCP film was obtained. Therefore, BCP film exhibits higher bonding strength than HA film. Again, with the thickness from 400 to 1000 nm, the first critical load of failure for BCP film to Ti-6Al-4V occurs at 2.3 N. Up to 7.8 N, continuous cracking and sliding is observed. No significant delamination or exfoliation of films was found, indicating good bonding or adhesion of BCP film to Ti-6Al-4V substrate (Rabiei et al., 2006).

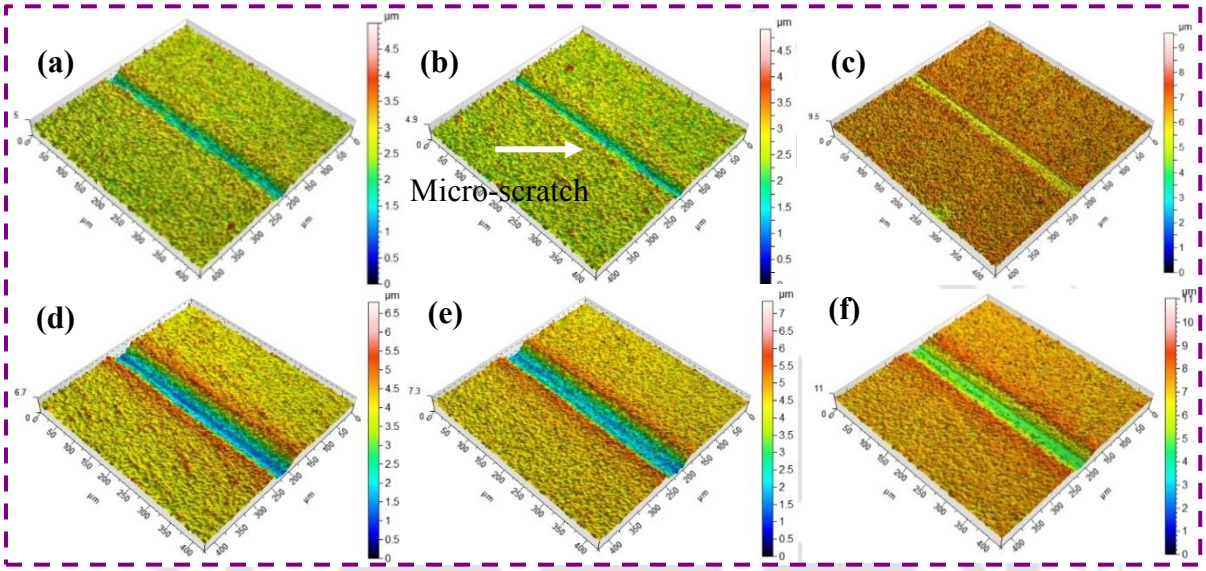

Figure 3.14: *3-D surface profiles of scratches made on sputtered samples with (a, d) 400 nm, (b, e) 700 nm and (c, f) 1000 nm film thickness at different forces 1N and 7N, respectively.*

Scratch test was also performed to determine the surface scratch resistance of the different thick sputtered substrates by measuring scratch width and depth at different constant loads (Samanta et al., 2018). Three different constant loads such as 1N, 4N and 7N were applied to each of the substrates having 400, 700 and 1000 nm film thickness. Figure 3.14 show the 3-D profilometer and optical microscopy images of scratches made on 400, 700 and 1000 nm films at 1N and 7N scratch forces, respectively. It can be clearly indicated that both the scratch width and depth were decreased with the rise in film thickness from 400 nm to 1000 nm. These indications were further verified by actual measurement of scratch width and depth with plotting the bar graph as shown in Figure 3.15.

The average scratch width decreased from 35 μm to 26 μm with increase the film thickness from 400 nm to 1000 nm when a constant normal load of 1 N was applied. Similarly, the average scratch width decreased from 50 μm to 39 μm and 61 μm to 58 μm,

with a constant load of 4 N and 7 N, respectively. A similar type of observation was also seen for the average scratch depth corresponding to film thickness and applied load. It can also be confirmed by the FESEM images demonstrated in Figure 3.16.

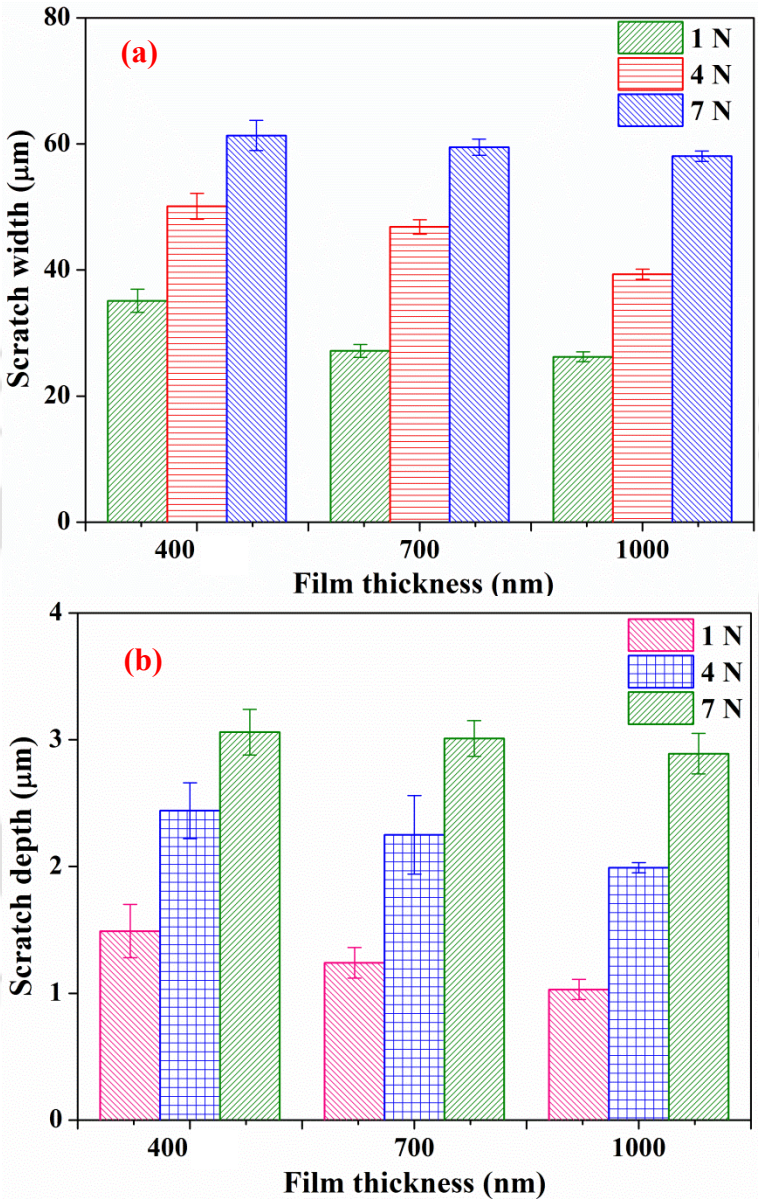

Figure 3.15: *Effect of film thickness on (a) width and (b) depth of scratches made on coated samples at different forces.*

It can be clearly observed that for all the scratch forces, the scratch widths in 1000 nm film (Figure 3.16 (a, c, e)) are slightly smaller than that made in 400 nm film (Figure 3.16 (b, d, f)). Due to the increase of BCP film thickness, the surface hardening enhanced slightly (Figure 3.11 (a)). Thus, this enhancing higher hardness provides slightly higher resistance to

scratch, so less width and depth for substrate subjected to higher film thickness. In addition, when a higher load was applied, the depth of penetration, as well as the contact area between indenter and substrate, was larger. Thus, higher scratch width and depth was resulted due to reduced surface resistance.

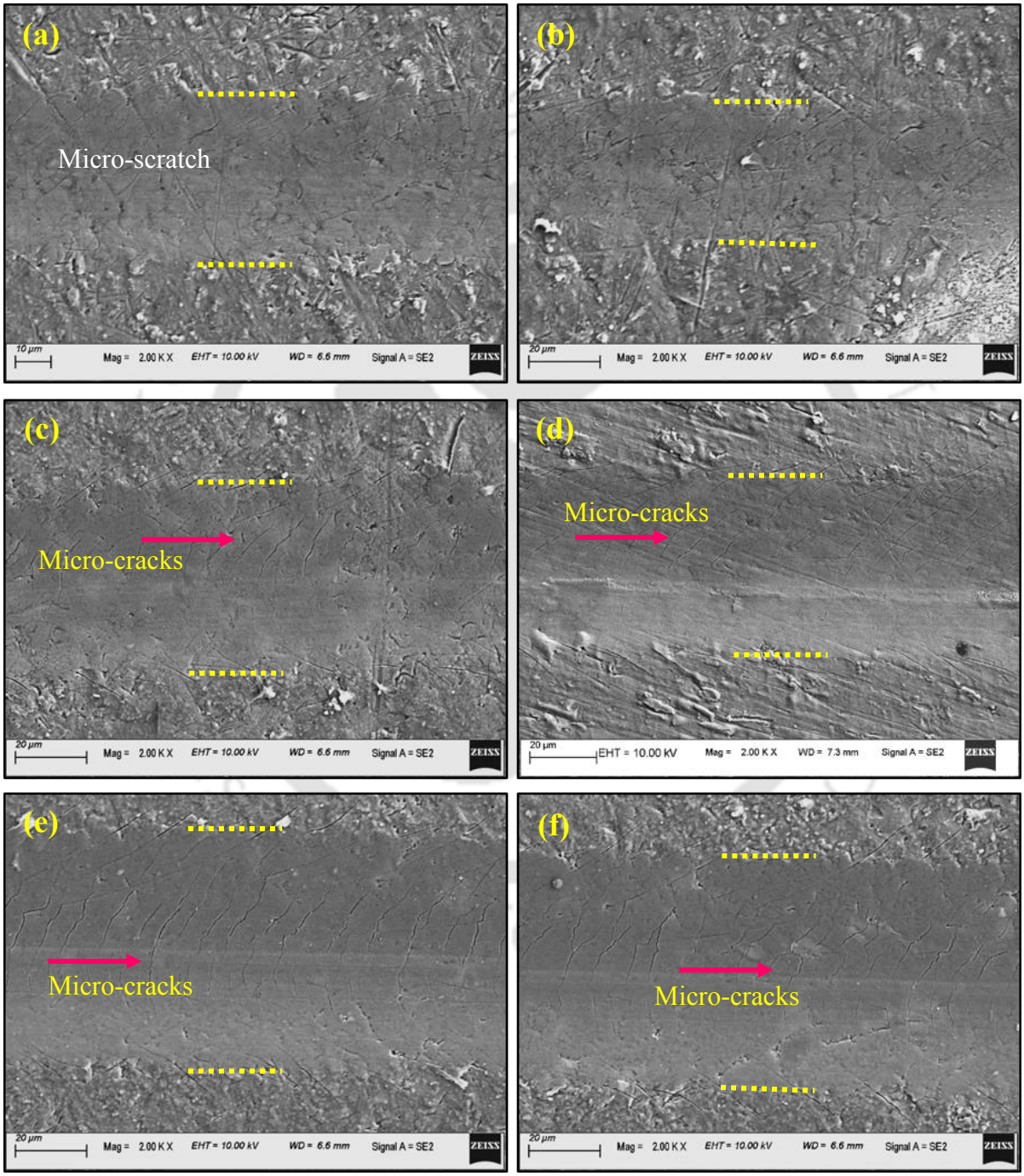

Figure 3.16: *Surface morphology of scratches made on sputtered samples with (a, c, e) 400 nm and (b, d, f) 1000 nm film thickness at different forces 1N, 4N and 7N, respectively.*

In addition, no crack was observed in the films, where 1 N scratch load was applied. As the first critical load of failure is 2.3 N for all the films, so no sign of detachment was obtained (as shown in Figure 3.16 (a and b)). However, many cracks were present in the pathway of scratches, where 4 N and 7 N loads were applied due to the reduction of scratch resistance. Also, the crack intensity increased with increase in load (Figure 3.16 (b, c, d, f)). Only continuous cracks were observed at 4 N and 7 N loads, however, no sign of spalling, chipping or delamination was found indicating good adhesion between film and substrate (Rabiei et al., 2006). Thus, it can be concluded that the surface scratch resistance improves with an increase in film thickness; however, deteriorates with increase in applied load.

3.3.8 *In vitro* bioactivity

In vitro bioactivity is the potential of an artificial implant to interact with the surrounding soft tissues and bone. This can be estimated by checking the apatite layer formation after soaking in SBF. In addition, it is regulated by properties of CaP coating (Surmenev et al., 2014). Paital et al. (2010) described that the apatite layer provides the required surface chemistry for cell adherence and its proliferation. In a previous study, Sun and Huang (2018) found apatite formation on BCP coated Ta_2O_5/Ti specimen using electrochemical deposition after two weeks of SBF immersion. In the present investigation, the apatite formation of BCP films deposited by RF sputtering was evaluated. Different thickness BCP films were immersed for 14 days in SBF followed by XRD, RAMAN, FESEM and EDS analyses. The XRD patterns after 14 days of SBF immersion were presented in Figure 3.17.

As compared to the sputtered films before SBF immersion (Figure 3.5), the films after 14 days of SBF immersion exhibited a reduction of β-TCP phase (Figure 3.18). Along with it, there was a significant improvement in the intensity of HA peaks. This clearly depicted that the films deposited by sputtering provide favorable nucleation sites for the ions of SBF to settle down and thereby assists in the growth of HA precipitation. Nimkerdphol et al. (2014) also observed apatite precipitation with the decrease in β-TCP, TTCP and CaO during immersion of HA-coated Ti (deposited by plasma spraying) in SBF solution. The wt% of β-TCP and HA of sputtered substrates before and after soaking 14 days in SBF was calculated using Eq. (3.1) moreover, the values are plotted in Figure 3.18.

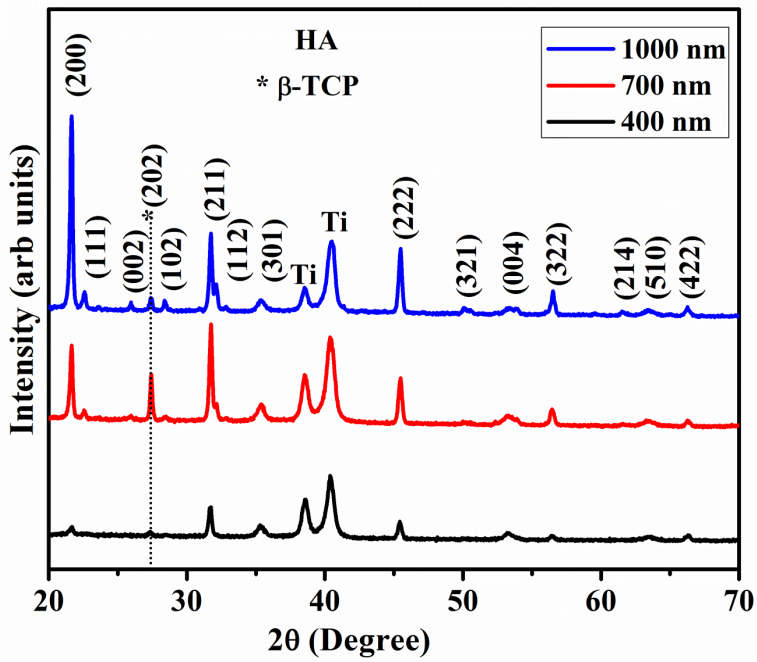

Figure 3.17: *XRD spectra of sputtered substrates with 400 nm, 700 nm and 1000 nm film thickness after soaking 14 days in SBF.*

Before SBF, all sputtered substrates had almost equal wt% HA ≈ 44%. After 14 days of SBF immersion, the wt% HA increased to 67.8 %, 69.3 % and 86.7% for 400 nm, 700 nm and 1000 nm films, respectively (Table 3.5). The highest increase in wt% of HA was observed for 1000 nm sputtered film. This was attributed to improvement in nucleation sites with film thickness so that more apatite was deposited on the film with 1000 nm thickness. As the surface roughness increased with BCP film thickness (Figure 3.8), the number of cavities increased where penetrations of Ca^{2+} and PO_4^{3-} ions from SBF increased. Hence, the nucleation sites increased where more apatite precipitation occurred (Arce et al., 2016). Moreover, the phase analysis of the film deposited over Ti-6Al-4V revealed the presence of pure HA peaks with no trace of β-TCP phases. Therefore, it can be inferred that BCP thin film deposited on Ti-6Al-4V can be very effective in the growth of HA (apatite precipitation) in SBF. Interestingly the intensity of (200) peak increases with the sputtering time showing the highest intensity for 1000 nm thick film. However, for both 700 nm and 400 nm sputtered film, the most intense peak is (211) similar to the standard JCPDS pattern (09-0432) for HA. This indicates that for the 1000 nm thick film there is a preferential growth of HA along (200) direction.

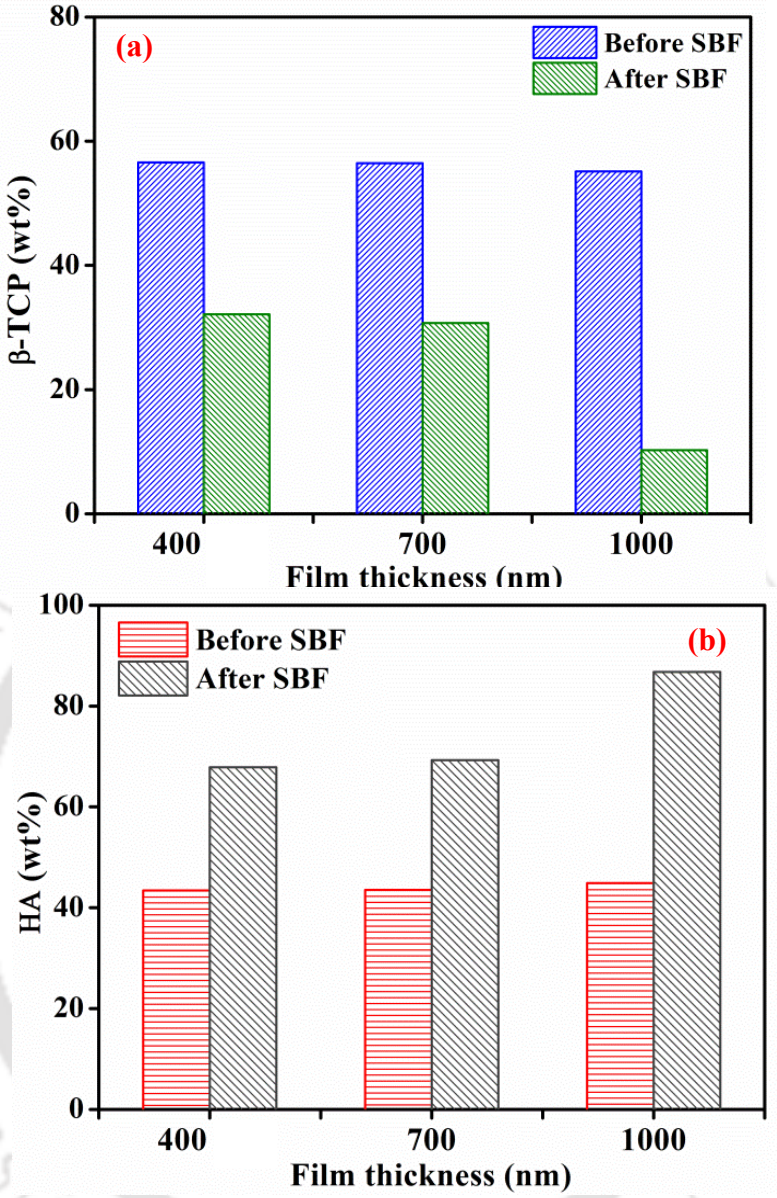

Figure 3.18: *Weight percentage of (a) β-TCP and (b) HA of sputtered film with different thickness: 400 nm, 700 nm and 1000 nm, before and after 14 days of SBF immersion.*

Therefore, it is evident that the film thickness has a remarkable influence on the growth of HA in SBF. Besides, the peaks were broad and of low intensity implying that the HA film was nano-crystalline. According to Surmenev et al. (2014), a higher number of nucleation sites were generated for a nano-crystalline structure due to high surface energy at the grain boundary. Hence, more apatite was precipitated for nano-crystalline BCP film. Sarma et al. (2016) revealed that the bone-like apatite found in living beings also bears a signature of nano-crystallinity. The apparent crystallite size of the films was calculated and

was found to be 32±2 nm, 33±2 nm and 35±3 nm for sputtered films with 400 nm, 700 nm and 1000 nm thickness, respectively, as provided in Table 3.5. The values suggest an increase in the crystallinity for higher film thickness. Surmeneva and Surmenev (2015b) found similar behavior of increase in crystallinity and crystallite size with the increase in HA film thickness during RF sputtering. In addition, as compared to pure HA film SBF immersion, BCP film is expected to provide higher apatite formation, as β-TCP in the BCP film soluble more which enrich the SBF with higher Ca^{2+} and PO_4^{3-} ions (Surmeneva 2012, 2014). Hence, higher apatite will be formed in BCP film in SBF immersion after 14 days compared to pure HA film.

The Raman spectra of the sputtered films after 14 days of SBF immersion are presented in Figure 3.19. It is interesting to see that the effect of sputtered BCP coatings on the deposition of HA by SBF. Since the sputtered films have the crystallite size in the nanometer domain, the enhanced surface area play an important role in promoting the growth of HA films from SBF.

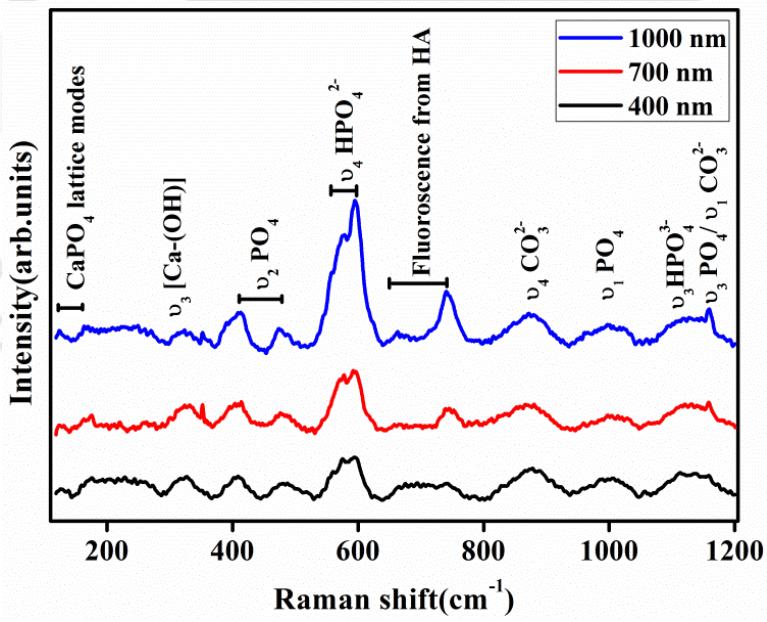

Figure 3.19: *RAMAN spectra of sputtered substrates with 400 nm, 700 nm and 1000 nm film thickness after soaking 14 days in SBF.*

In general, all the bands show an enhancement in intensity showing prominence for the sputtered film with 1000 nm thickness. The band near 600 cm^{-1} and 574 cm^{-1} are allotted to the triply degenerate bending mode ν_{4a} and ν_{4b} of O-P-O bonds of the PO_4 group,

respectively. The appearance of these bands proves that the synthesized apatite is indeed HA. Koutsopoulos (2002) reported that the band appearing at 1112 cm^{-1} is a characteristic of CO_3^{2-} ions in apatite. This band confirms that the synthesized apatite is non-stoichiometric. It is well known that the naturally occurring apatite is calcium deficient carbonated apatite, which is evidently non-stoichiometric. These results complement the findings of XRD analysis and therefore leads to the conclusion that BCP sputtered films enhance the bone-like apatite growth on their surface. In fact, with increased thickness of the sputtered films, the intensity of bone-like apatite was significantly improved which was apparent from the XRD and Raman spectra studies.

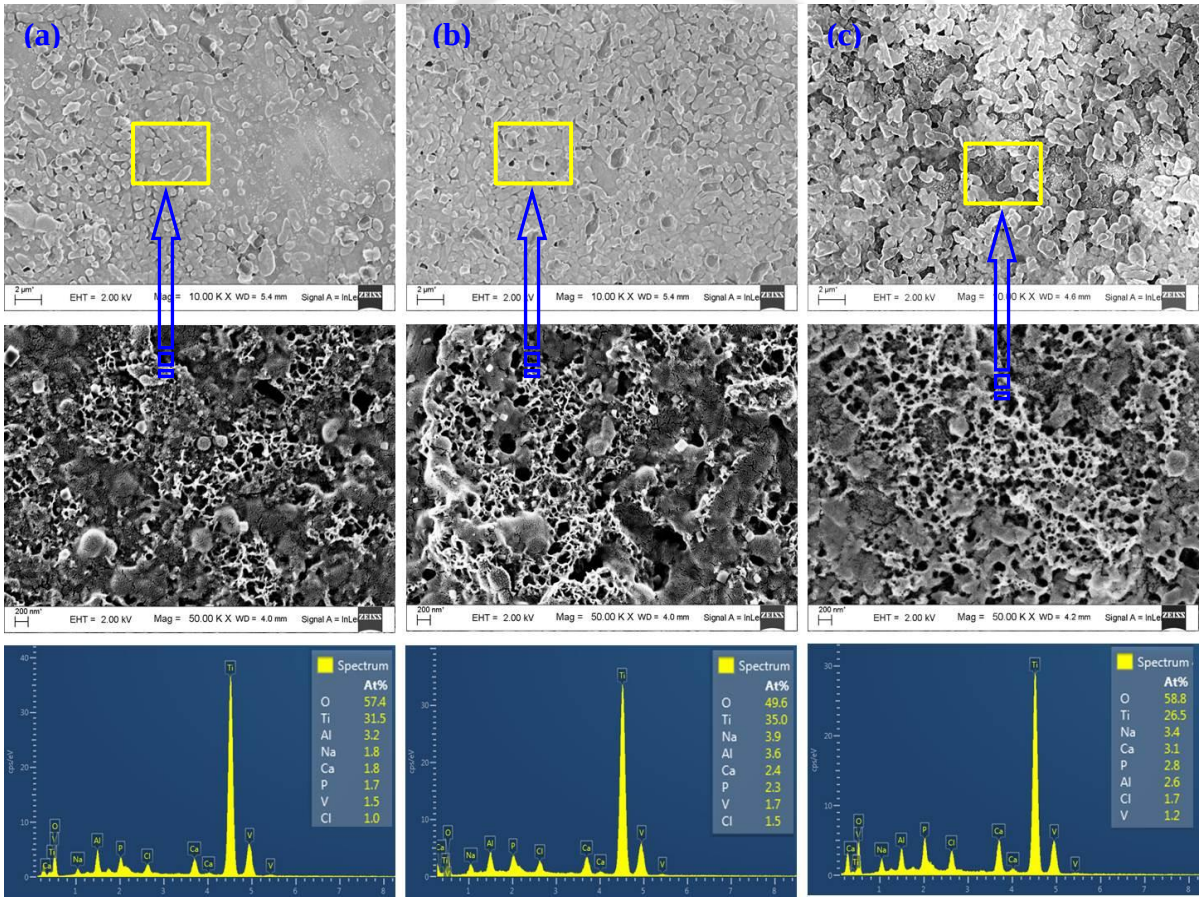

Figure 3.21: *Surface morphologies and corresponding EDS analysis of sputtered samples at film thickness: (a) 400 nm, (b) 700 nm and (c) 1000 nm after 14 days of SBF immersion.*

Figure 3.20 represents the surface morphologies as well as elemental analysis of all sputtered films after 14 days of SBF immersion. Since there was no significant amount of apatite layer on uncoated substrates even after 14 days of SBF immersion; hence, the surface

morphology and elemental analysis related to it are not provided herein. For all sputtered films, after 14 days of SBF immersion, small globular and elliptical like precipitate layer were nucleated and grew on the surface of sputtered substrates (lower magnification, Figure 3.20 (a, b, c)). In addition, the bone like structure is also seen in all the sputtered substrates after 14 days of SBF immersion (higher magnification, Figure 3.20 (a, b, c)). Li et al. (2015d) revealed that the presence of globular-like morphologies, as well as bone-like structure, is the characteristics of apatite formation, which is beneficial for osseous connection. However, the globular-elliptical as well as bone-like structure is enhanced from 400 nm to 1000 nm sputtered film. It indicates that more apatite formation occurs for the sputtered substrates with higher film thickness due to the presence of a higher number of nuclei sites.

The elements present in the deposited films at different thickness after 14 days of SBF immersion are represented in Figure 3.20 (a, b, c). It can be revealed that the individual amount of Ca and P increased for all sputtered substrates after 14 days of SBF immersion. Therefore, it can be confirmed that all the three sputtered substrates immersed in SBF had the potential to produce calcium phosphate layer more effectively as compared to uncoated substrates. In addition, the individual percentage of Ca and P is more for 1000 nm sputtered substrate as compared to other sputtered substrate, as shown in Table 3.5. This proved that more apatite formation occurs for sputtered substrates with higher film thickness. Na and Cl in the EDS spectrum reveal the presence of other compositions of SBF.

Table 3. 5: Wt% of HA and β-TCP, as well as crystallite size and elements (at%) of the different sputtering film after 14 days immersion in SBF

Film thickness (nm)	Wt% of HA	Wt% of β-TCP	Crystallite size (nm)	Element (at%)	
				Ca	P
400±20	67.86	32.14	32±2	1.8	1.7
700±40	69.28	30.72	33±2	2.4	2.3
1000±60	86.76	10.24	35±3	3.1	2.8

The calcium phosphate apatite formation on sputtered surface after SBF immersion is a process of heterogeneous nucleation and growth. Paital et al. (2010) described that HA and

β-TCP are the crucial biomaterial components, which cause bonding with the bone tissue. Due to the presence of these phases in the sputtered surface, the coating immersed in SBF solution has the potential to form apatite. Figure 3.21 shows the schematic diagram for formation of apatite layer on the sputtered surface in SBF. Paital and Dahotre (2009) reported that when sputtered substrates are immersed in SBF, O-H bonds are easily formed by β-TCP, as it resorbs with water present in SBF (Eq. 3.4).

$$3Ca_3(PO_4)_2 + H_2O \rightarrow Ca_9HPO_4(PO_4)_5OH \quad (3.4)$$

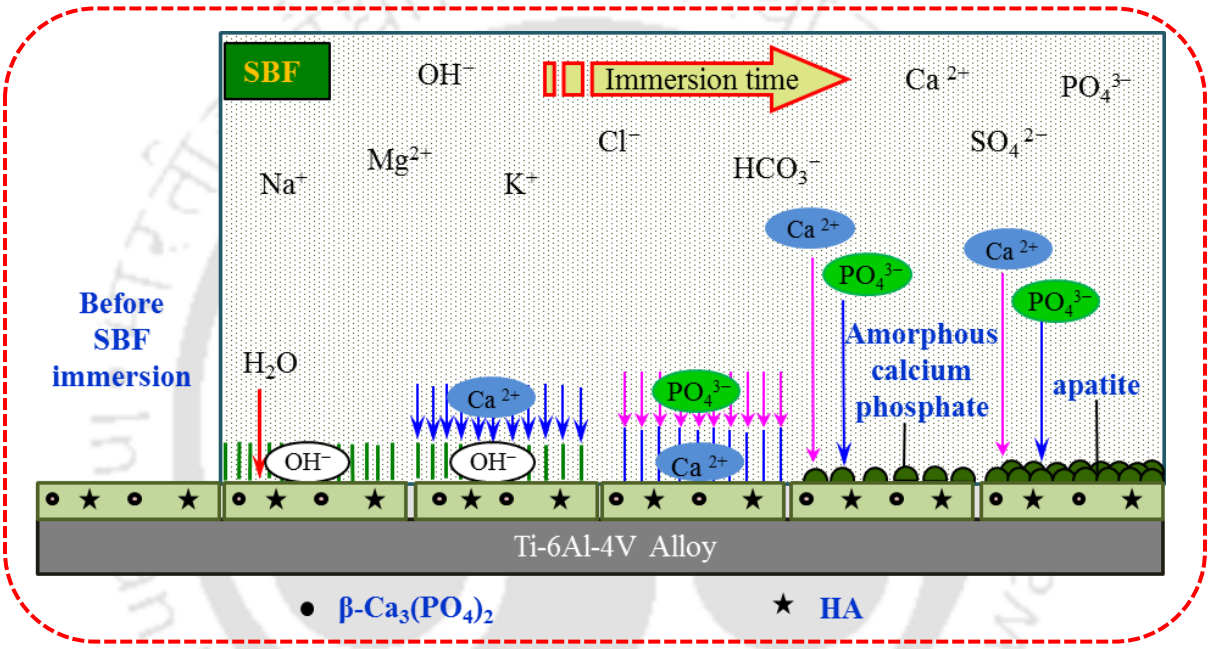

Figure 3.21: *Schematic diagram of apatite formation on sputtered substrate in SBF*

According to Kim et al. (2004), HA is extremely less soluble in SBF, however, it exposes it's hydroxyl and phosphate units in SBF, hence the surface potential becomes highly negative immediately after exposure to SBF. With presence of these negatively charged OH- ions on the surface, Ca^{2+} ions from the SBF are moved towards the sputtered surface and get accumulated there. Bakhsheshi-Rad et al. (2016b) described that the negatively charged PO_4^{3-} ions present in the SBF are attracted towards the surface and reacted, which leads to form apatite nuclei on the surface as per equation (Eq. 3.5):

$$2OH^- + 10Ca^{2+} + 6PO_4^{3-} \rightarrow Ca_{10}(PO_4)_6(OH)_2 \quad (3.5)$$

With an increase in soaking time, large amount Ca^{2+} and PO_4^{3-} ions are precipitated on the negatively charged OH^- surface and finally a thick layer of apatite is generated on the coating surface. In presence of β-TCP in the coating, BCP film can precipitate more apatite than pure HA coated substrate. This is due to solubility of β-TCP in water, the SBF solution is supersaturated with Ca^{2+} and PO_4^{3-}, which come from β-TCP. In addition, as compared to 400 nm and 700 nm sputtered film, higher apatite was precipitated on 1000 nm sputtered film. This improvement in bioactivity is attributed to the presence of more nucleation sites as well as higher wettability with SBF. This improved wettability enhances the reaction between β-TCP and water molecules present in SBF solution leads to better apatite formation for higher film thickness. This ability of BCP film to improve hydrophilicity as well as to form apatite layer can enhance the adhesion, proliferation as well as differentiation of cells which promotes osteointegration (Hasan et al., 2018b; Surmenev et al., 2014).

3.4 Findings from the research work

Biphasic calcium phosphate films were successfully deposited on Ti-6Al-4V substrate using RF magnetron sputtering process. The sputtering was carried out at room temperature and a constant RF power of 30 W, sputtering pressure of $3x10^{-2}$ mbar, and target to substrate distance of 5 cm. BCP films of 400 nm, 700 nm and 1000 nm thickness were obtained with 4 h, 6 h and 8 h sputtering time, respectively. The results showed that all the BCP films consist of a similar proportion of HA and β-TCP. In addition, all films were distributed uniformly, and the average grain size increases from 48 nm to 379 nm with the film thickness due to coalescence and clustering of particles. The wettability of Ti-6Al-4V significantly improved with the deposition of BCP film on it, due to the hydrophilic nature of BCP. Furthermore, the hydrophilicity enhanced from 73.7±1° to 61.2±1º with the film thickness as surface roughness increased from 112 nm to 153 nm, satisfying the Wenzel relation. The surface scratch resistance was also improved with the increase in film thickness as the micro-hardness of the coated substrates was enhanced from 430±9 to 455±16 HV. Excellent adhesion strength of all the BCP films to Ti-6Al-4V substrate was found, as no cracking of film up to the scratch load of 2.3 N and no significant delamination up to 7.8 N were observed. It was found that, BCP film exhibited with higher bonding strength compared to HA film. The *in vitro* bioactivity resulted in small globular and elliptical like structures on

the surface of all BCP films after 14 days of SBF immersion, which indicates the coating films possess bioactivity. Besides, there is a notable enhancement in wt% apatite on all the film surfaces compared to before immersion. The highest wt% of apatite was found to be 86.7% for 1000 nm thick BCP film after 14 days of SBF immersion. Hence, these results conclude that the sputtering of BCP films with sound adhesion strength improves the bioactivity of Ti-6Al-4V, which can be applied for artificial bone and tooth applications.

Chapter 4

Effect of TiO_2 Addition on Adhesion and Biological Behaviour of BCP-TiO_2 Composite Films Deposited by RF Sputtering

4.1 Theme of work

In chapter 3, it was revealed that BCP film with the thickness varying from 400 – 1000 nm exhibit good bioactivity compared to bare Ti-6Al-4V. Furthermore, these films have good adherence with the Ti-6Al-4V substrate. However, it is always advisable to improve the quality of the implant in terms of its functionality and durability. From the literature review, it was found that TiO_2 on the surface of the implant plays a crucial role in chemical stability as well as bio-functionality of CaP coating. To the best of our knowledge, many researchers have used TiO_2 as intermediate layer to Ti-6Al-4V and HA coating or composite coating using different surface modification techniques. However, very few studies focused on BCP-TiO_2 composite coating on Ti-6Al-4V by RF magnetron sputtering. Also, less study was addressed their adhesion as well as different biological behavior. So, it is desirable to study the effect of TiO_2 addition with BCP film on the adhesion as well as biological performance for better understanding the process-structure-property inter-relationship that would provide direction to design the orthopedic implant with better functionality and longevity.

In this chapter, the fabrication and characterization of TiO_2-BCP films on Ti-6Al-4V is described along with the analysis of adhesion behavior, protein adsorption, cell proliferation and *in vitro* bioactivity of the films. Initially, two different TiO_2-BCP targets were fabricated by mixing 25 wt% and 50 wt% TiO_2 powder individually with the HA powder followed by sintering. 25 TiO_2-BCP and 50 TiO_2-BCP films were fabricated using RF magnetron sputtering along with 100 BCP film. The deposition was carried out with the same parameters as described in chapter 3, except the substrate temperature at 400 ºC and deposition time for 7 h. Post deposition, half of these samples were annealed at 700 ºC for 2 h. Subsequently, physicochemical, mechanical and biological properties of these films were investigated using various characterization techniques. Surface morphology, elemental analysis and phase composition of different films were studied using FESEM, EDS and XRD, respectively. The surface roughness, wettability as well as adhesion behavior of

different films were investigated using atomic force microscopy (AFM), goniometer and scratch tester, respectively. In addition, different biological performancec like protein adsorption, cell adhesion and proliferation, *in vitro* bioactivity of different films were investigated and compared. Fetal brovine serum (FBS) was used as the protein to conduct protein adsorption test; whereas, MG63 cells were used for the study of cellular behavior on the different modified surfaces. The primary objective of this chapter is to investigate and compare the effect of TiO_2 addition and annealing on adhesion behavior as well as different biological properties.

4.2 Materials and methods

4.2.1 Materials

HA used in RF magnetron sputtering (chapter 3) was also employed for this study. TiO_2 powder having anatase phase was purchased from Merck (Cat. No. 1.93803.0521). Three cylindrical targets with same dimension and procedure as mentioned in section 3.2.3, chapter 3 were prepared by compressing (1) 100 wt% HA, (2) 25 wt% TiO_2 – 75 wt% HA and (3) 50 wt% TiO_2 – 50 wt% HA powders followed by sintering at 1300 °C for 5 h. The time and temperature of sintering were chosen in order to obtain BCP films containing HA and β-TCP (section 3.2.3, chapter 3). The targets were further characterized using FESEM and EDS for determination of surface morphology and elemental composition, respectively.

Ti-6Al-4V specimens with a dimension of 10 mm × 10 mm × 3 mm thickness were cut, polished and cleaned by the same procedure as described in section 3.2.2, chapter 3.

4.2.2 RF magnetron sputtering of BCP and BCP-TiO_2 films

The deposition of different films on polished Ti-6Al-4V was accomplished from different targets using RF magnetron sputtering. Same sputtering parameters and procedure (as mentioned in section 3.2.4, chapter 3) were used to deposit BCP as well as the BCP-TiO_2 film on Ti-6Al-4V in this study. However, the depositions on polished samples were carried out at a substrate temperature of 400 °C. Different conditions used for deposition are shown in Table 4.1. The films deposited from 100wt% HA, 25wt% TiO_2 – 75wt% HA and 50wt% TiO_2 – 50wt% HA targets were renamed as 100 BCP, 25 TiO_2 – BCP and 50 TiO_2 – BCP, respectively throughout the study. Further, some sputtered samples were annealed at 700 °C

for 2 h under atmospheric conditions in order to enhance the crystallinity (Prosolov et al., 2017) as well as to study the effect of annealing on different properties. The substrates were used for further characterization.

4.2.3 Characterization of modified surfaces

The thickness, phase composition, surface morphology and elemental composition of different films such as 100 BCP, 25 TiO_2–BCP and 50 TiO_2–BCP (before and after annealing) were analyzed by stylus profilometer, XRD, FESEM and EDS respectively, as described previously in section 3.2.5.1, chapter 3. The XRD results were interpreted with the database of crystallographic structures (HA - JCPDS 09-0432, β-TCP - JCPDS 09-0169), TiO_2 (rutile) - JCPDS 211276 and Ti - JCPDS 441294).

Table 4. 1: Deposition conditions used in present RF magnetron sputtering process

RF sputtering component	Present study
Target	100 BCP 25 TiO_2 – BCP 50 TiO_2 – BCP
Base pressure	$3x10^{-6}$ mbar
Working pressure	$3x10^{-2}$ mbar
Sputtering gas	Ar (30 sccm)
Target to substrate distance	50 mm
RF power	30 W
Deposition time	7 h
Substrate temperature	400 °C

4.2.4 Surface roughness and wettability

The surface roughness and topography of 100 BCP, 25 TiO_2–BCP and 50 TiO_2–BCP films on Ti-6Al-4V surfaces (before and after annealing) were determined using atomic force microscopy (AFM, Oxford-Cypher, UK) analysis. The instrument equipped with a silicon nitride tip of <10 nm radius was used to scan over a surface area of 5 × 5 μm^2 for analysis. Gwyddion software found from GNU General Public License was used for evaluating the surface roughness parameter as described previously by Hasan and Pandey (2016). Different roughness parameters such as centerline average (R_a), root mean square (R_q) and skewness (S_{kew}) were analyzed in this study.

The wettability of different films such as 100 BCP, 25 TiO_2–BCP and 50 TiO_2–BCP on polished Ti-6Al-4V (before and after annealing) was measured with goniometer using sessile drop technique reported previously in section 3.2.5.2, chapter 3. Minimum three different locations were considered to measure the contact angle on the same surface.

4.2.5 Adhesion behaviour of the films

The adhesion behavior of 100 BCP, 25 TiO_2–BCP and 50 TiO_2–BCP films (before and after annealing) was studied by using a micro scratch tester using the same procedure as illustrated section 3.2.6, chapter 3. However, the linearly increasing load range taken in this study was from 1.0 to 19.0 N, and the scratch length was 18 mm. All other parameters were the same as considered in chapter 3. Using the coefficient of friction (COF) curve and microscopic image analysis, the critical load (L_c) was evaluated which determine the adhesion strength of the films to the substrate. Minimum three scratches were done on each of the films to check the repeatability. FESEM image of the scratch was used to see the various failures at different points to analyze the adhesion behavior of different films.

4.2.6 Biological studies

4.2.6.1 Protein adsorption

Protein adsorption on surfaces is an important process which regulates cells adhesion and cyto-compatibility in tissue repair or formation (Bajpai et al., 2015). Adsorbed mass of protein on the surfaces of 100 BCP, 25 TiO_2–BCP and 50 TiO_2–BCP films (before and after annealing) was investigated using bicinchoninic acid (BCA, Sigma, India) protocol reported previously by Hasan et al. (2017) and Pandey et al. (2012). Each substrate with the known area was incubated in 10% fetal bovine serum (FBS, Gibco) prepared in phosphate buffered saline (PBS) at room temperature for 2 h. Post incubation, substrates were rinsed properly with PBS and water respectively, to remove the unbound proteins. Adsorbed proteins were desorbed using 5% sodium dodecyl sulphate (SDS, prepared in PBS, pH 7.4) for 1 h at 37 ºC and total protein estimation was carried out using BCA kit. Each experiment was carried out in triplicate (n=3) for calculating the standard deviation.

4.2.6.2 Cell morphology and adhesion

Cell culture assays were conducted using the human osteoblast-like cell line MG-63 (NCCS, Pune, India). Cells were cultured in high glucose Dulbecco modified essential medium (DMEM, Gibco) supplemented with 10% FBS and 1% antibiotic (Pen-Strep, Gibco) at 37 °C in a 5% CO_2 atmosphere. The culture medium was replaced every 2 days and cells were trypsinized (trypsin-EDTA, HiMedia, India) at 70-80% confluency and reseeded to tissue culture flasks (T25, Nunc) to maintain the cell line.

Cell morphology and adhesion study were conducted using MG63 cell line on 100 BCP, 25 TiO_2–BCP and 50 TiO_2–BCP film surfaces (before and after annealing) were investigated using FESEM after 24 h of incubation. Unattached cells were removed from samples by washing with PBS (pH 7.4), and adhered cells were fixed using 2.5% glutaraldehyde for 2 h. Post fixation, samples were washed twice with PBS followed by graded dehydration with 40%, 50%, 60%, 70%, 80%, 90% ethanol for 10 min, respectively and with 95% as well as 100% ethanol for 30 min each. Samples were then critical point dried using hexamethyl disilazane (Sigma, India) for 10 min, gold sputtered and examined using FESEM.

Cell adhesion studies on different different modified surfaces were also investigated by fluorescent imaging. For this, MG-63 cells were seeded at density $1.5x10^4$ cells/cm^2 on different samples and incubated for 12 h. Post incubation, surfaces were washed with PBS (pH 7.4) to remove non-adhered cells. Adherent cells were fixed with 4% (v/v) paraformaldehyde solution (HiMedia, India) overnight at 4ºC. Cells were later washed and treated with 2% (w/v) BSA and 0.2% (v/v) triton X100 for 6 h followed by fluorescent staining of actin filaments with FITC-Phalloidin (Sigma, India) for 12 h. Cells nuclei were stained by incubating substrates in 20 µg/ml of propidium iodide (PI, Sigma, India) for 1 h at room temperature. Post-staining, samples were washed with PBS and imaging was done using a fluorescent microscope (Nikon Eclipse Ti-S).

4.2.6.3 Cell proliferation

Cell proliferation was performed to determine the cytotoxicity of the prepared samples using the procedure described previously (Hasan et al., 2018c; Hasan et al., 2017; Jeevitha and Amarnath, 2013). Briefly, uncoated Ti alloy, 100 BCP, 25 TiO_2–BCP and 50 TiO_2–BCP film

(before and after annealing) samples were steam sterilized at 121ºC and 15 psi pressure for 20 min. Sterilized samples were transferred to 24 wells tissue culture plate (Nunc) and seeded with MG-63 cells at a concentration of 1.0×10^3 cells/cm^2 in complete DMEM media for 2, 4 and 6 days. After the specified time of incubation, the culture media was discarded, and the samples were transferred to fresh wells. Samples were later incubated in 400 µl of DMEM containing 40 µl of MTT (3-(4,5-Dimethylthiazol-2-Yl)-2,5-Diphenyltetrazolium Bromide) solution (5 mg/ml in PBS, pH 7.4). After 4 h of incubation at 37ºC and 5% CO_2, media was discarded, and 300 µl of DMSO was added to dissolve formazan crystals for 10 min. The optical density of the obtained purple color solution was measured at 570 nm using Infinite 200 Pro, Tecan instrument.

4.2.6.4 In vitro bioactivity

In vitro bioactivity test was carried out by immersing the 100 BCP, 25 TiO_2–BCP and 50 TiO_2–BCP films in SBF solution. The same protocol was considered, as described previously in section 3.2.7, chapter 3. To study this behavior, triplicate samples of each modified surfaces were soaked in SBF separately, for 7 days. In order to analyze the formation of apatite layer, these samples were investigated with XRD, FESEM and EDS for analyzing the phase, surface morphology and elemental composition of apatite, respectively.

4.3 Results and discussion

4.3.1 Characterizations of BCP and BCP-TiO_2 targets

The surface morphology and corresponding elemental analysis of 100 BCP, 25 TiO_2-BCP and 50 TiO_2-BCP targets are shown in Figure 4.1. The particles were well bonded with each other; however, the surface became rougher when more TiO_2 was added in the target due to the increase of larger TiO_2 particle size. The EDS analysis confirmed the presence of Ca, P and O which were attributed to BCP. Again, the presence of Ti in the targets confirmed the addition of TiO_2 in the BCP-TiO_2 targets, and this increased with the increase of TiO_2 wt%.

4.3.2 Characterizations of BCP and BCP-TiO_2 films

4.3.2.1 Thickness of films

The film thicknesses were found to be 540 ± 19 nm, 918 ± 33 nm and 1320 ± 56 nm for 100 BCP, 25 TiO_2-BCP and 50 TiO_2-BCP, respectively. It was found that the *f*ilm thickness

increased with increase in the amount of TiO_2 in the target. In general, bonding is improved if any constituent of the coating material matches with the substrate material (Zheng et al., 2008). In this case, although the substrates were stored in a desiccator to prevent oxidation, the exposure of the substrates to atmospheric conditions during the process of loading the substrates in the sputtering chamber, partial oxidation occurs on the surface, which leads to the development of a thin TiO_2 layer on the surface. This results a higher chemical affinity between the coating and substrate. Also, TiO_2 is a relatively easier material to sputter in comparison to BCP as have been proven in the earlier reports (Majeed et al., 2015; Pradhan et al., 2010). Therefore, the film thickness was found to be highest in case of 50 TiO_2-BCP in this study.

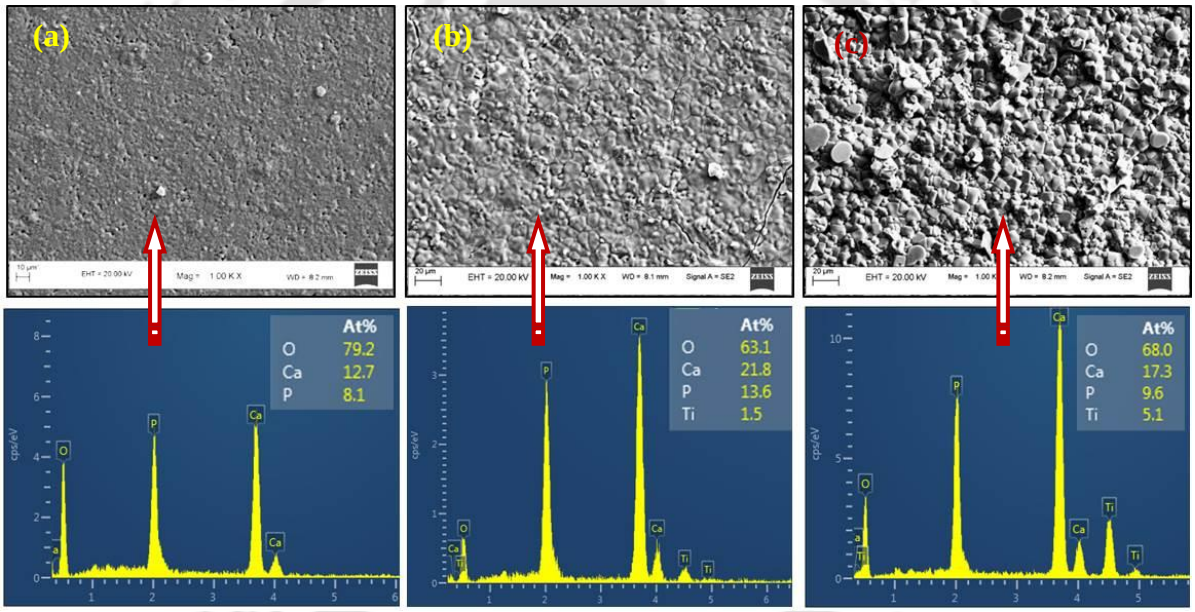

Figure 4.1: *Surface morphology and elemental analysis of (a) 100 BCP, (b) 25 TiO_2-BCP and (c) 50 TiO_2-BCP targets.*

4.3.2.2 Phase compositions and elemental analysis

The compositional phases of different films sputtered on Ti-6Al-4V are demonstrated in Figure 4.2. The deposited films before annealing were found to have less intensity peaks as compared to the films annealed at 700 ºC for 2 h (Figure 4.3). It is a well-known fact that the film deposited at room temperature are amorphous in nature, as the films were grown from the vapor phase in RF sputtering (Majeed et al., 2015). However, in this study the films were deposited at 400 ºC substrate temperature. Hence, low intensity crystalized peaks were

obtained because of the mobility of the deposited particles by the substrate heating (Bramowicz et al., 2016).

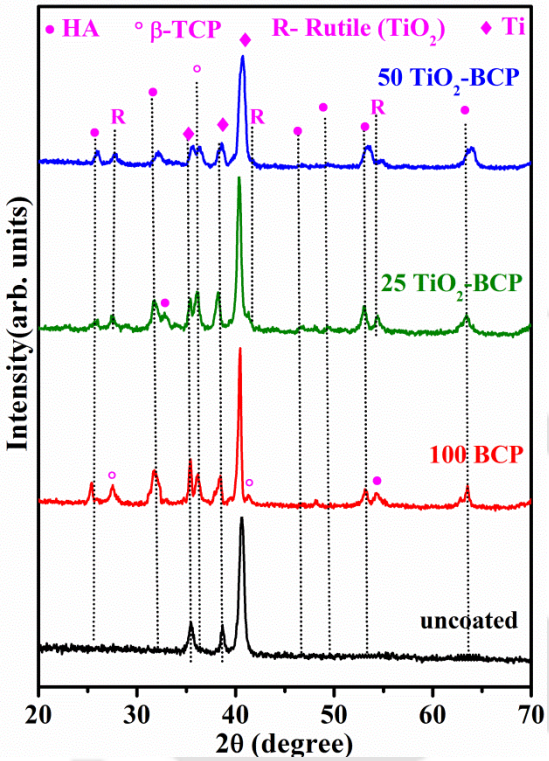

Figure 4.2: *Phases found in 100 BCP, 25 TiO_2-BCP and 50 TiO_2-BCP films after annealing.*

The crystallinity was further enhanced after thermal treatment of the films at 700 ºC for 2 h (Figure 4.3). The high-intensity peaks for all the films (after annealing) are shown in Figure 4.2. Availability of HA and β-TCP peaks in the spectra confirmed the deposition of BCP film, whereas the presence of TiO_2 (rutile) peaks in two spectra indicated the deposition of BCP-TiO_2 films. TiO_2 (anatase) phase present in the green target converted into TiO_2 (rutile) in the fabricated BCP-TiO_2 target due to a sintering temperature of 1300 ºC, which reflected in the BCP-TiO_2 films. The rutile phase of TiO_2 is the most stable high temperature polymorph of TiO_2 and is known to known to undergo a transformation from anatase to rutile at a temperature of 900 °C. The presence of Ti peaks in all spectrums is attributed to the substrate material.

The EDS analyses for all the films before and after annealing are represented in Table 4.2. The presence of Ca, P and O in all the films confirms the deposition of CaP coating on Ti-6Al-4V. Although the presence of Ti, Al and V are referred to the substrate; however, the percentage of Ti increased with the reduction of Ca and P, when wt.% of TiO_2 was increased.

This confirmed the formation of BCP-TiO_2 films on Ti-6Al-4V. Compared to the non-annealed films, annealed films consist of higher percentage of O, indicating oxide layer formation in the films after annealing. In addition, the Ca/P ratio is reduced after annealing of the films.

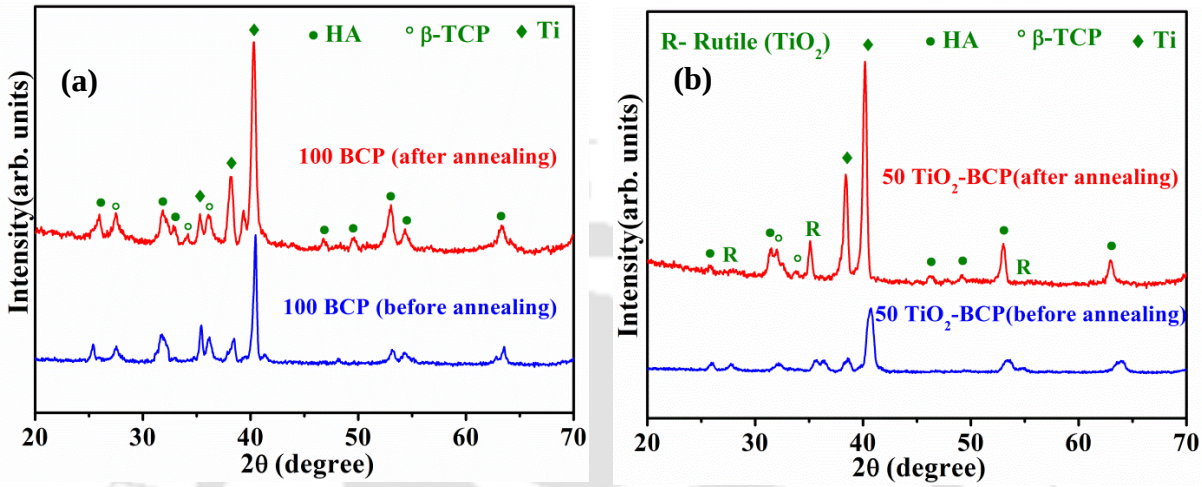

Figure 4.3: *Phases found in (a) 100 BCP and (b) 50 TiO_2-BCP film before and after annealing*

Table 4. 2: Elemental concentration (at%) of different films before and after annealing

Films on Ti-6Al-4V substrate	Elemental concentration (at%)											
	Before annealing						After annealing					
	Ca	P	O	Ti	Al	Ca/P	Ca	P	O	Ti	Al	Ca/P
100 BCP	4.3	2.9	58.8	29.6	3.1	1.48	3.8	2.7	66.7	24.5	1.3	1.41
25 TiO_2-BCP	3.3	2.4	58.5	31.0	2.9	1.37	3.4	2.6	63.3	26.5	2.9	1.31
50 TiO_2-BCP	2.2	1.7	57.3	33.8	3.6	1.29	2.8	2.4	60.4	30.1	2.8	1.17

The average crystallite size of all the films before and after annealing was determined using Scherrer equation in XRD spectrum, shown in Table 4.3. The apparent crystallite size of 100 BCP, 25 TiO_2-BCP and 50 TiO_2-BCP films before annealing were found to be 6.64±1 nm, 8.55±1 nm and 10.75±2 nm; whereas, after annealing the size was significantly increased

to 15.61±1 nm, 17.17±2 nm and 20.39±3 nm, respectively. The thermal energy provided in the post annealing treatment causes the crystallites to coalesce resulting in larger crystallites and hence improved crystallinity (Ungula et al., 2017). Ungula et al. (2017) found similar response to the improvement in crystallite size with annealing temperature. Due to the thermal energy created by annealing, the mobility of active sites enhances and with the increase in annealing temperature the process is repeated, resulting the diffraction line in a preferred orientation (Jafari et al., 2014).

Table 4. 3: Crystallite as well as particle size of the different films at different conditions

Films	Crystallite size before annealing (nm)	Crystallite size after annealing (nm)	Particle size before annealing (nm)	Particle size after annealing (nm)
100 BCP	6.6±1	15.6±1	164±55	244±51
25 TiO_2-BCP	8.5±1	17.2±2	259±49	327±43
50 TiO_2-BCP	10.7±2	20.4±3	374±69	412±87

4.3.2.3 Surface morphology

The surface morphology of 100 BCP, 25 TiO_2-BCP and 50 TiO_2-BCP films before and after annealing are shown in Figure 4.4. All the films before annealing (Figure 4.4 (a, c, e)) were non-porous, dense and homogeneous with uniformly distributed grains, which are features of films deposited by sputtering (Surmeneva et al., 2015). Furthermore, all the films comprised of regular grain like morphology. The BCP films are found to have irregular elongated grain like morphology. The addition of TiO_2 leads to the development of spherical granules which tends to increase in size with more wt.% of TiO_2. The average particle size increased from 164±55 nm to 374±69 nm with the increase in TiO_2 wt.% in the sputtering targets (Table 4.3). Hence, it can be concluded that the addition of TiO_2 significantly affects the microstructure of BCP film. The surface morphology of all the films after annealing at 700 ^oC for 2 h is shown in Figure 4.4 (b, d, f). After thermal treatment, irregular shaped nano-crystals were observed in all the specimens. Thermal treated BCP film had rectangular plate-like crystal structure (244±51 nm average particle size, (Figure 4.4 (b)) whereas, 25 TiO_2-

BCP and 50 TiO_2-BCP films exhibited polygonal crystal structure with average particle size 327±43 nm and 412±97 nm, respectively (Figure 4.4 (d, f)).

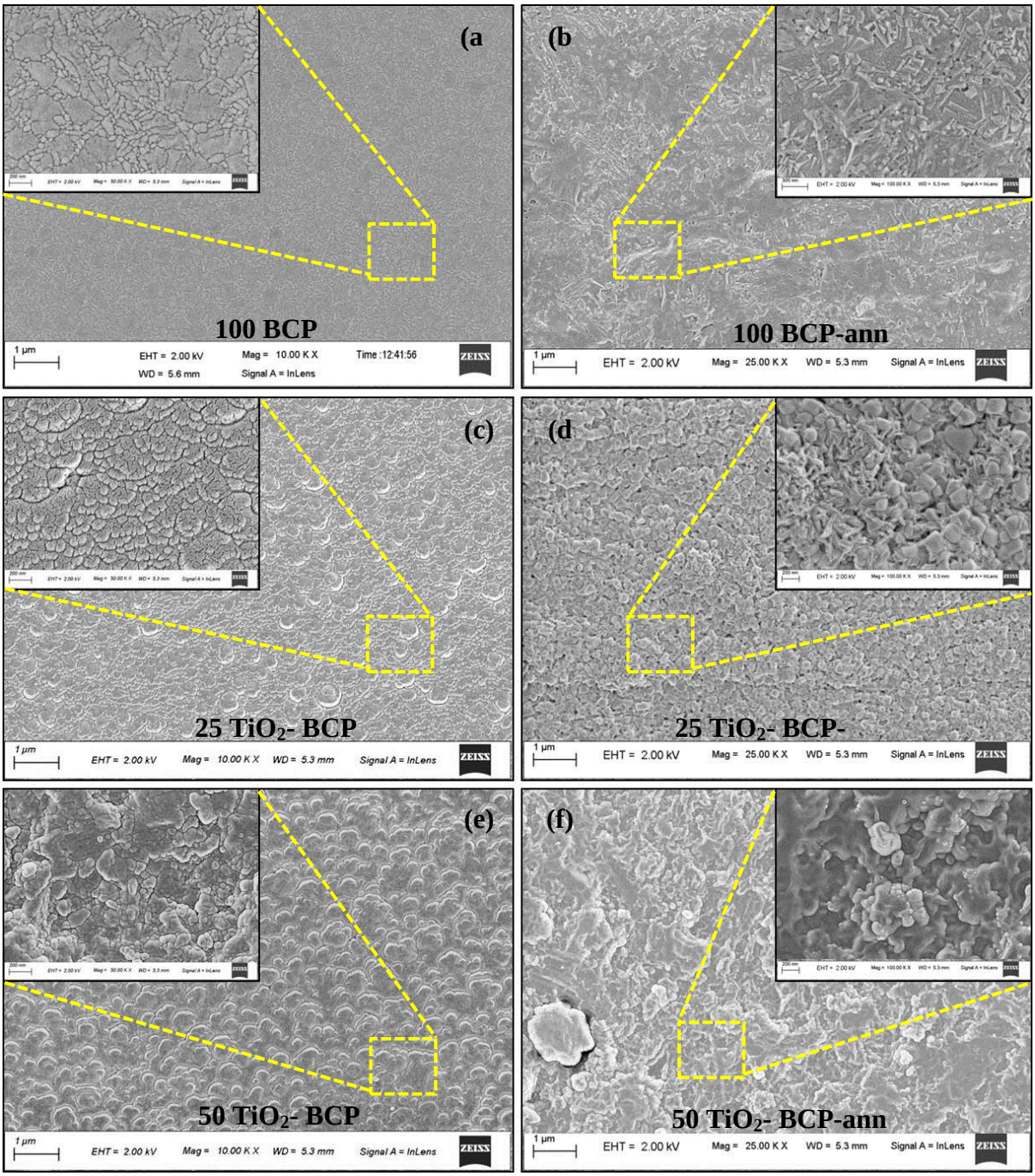

Figure 4.4: *Surface morphology 100 BCP, 25 TiO_2-BCP and 50 TiO_2-BCP films before (a, c, e) and after (b, d, f) annealing, respectively.*

It was observed that the particle size increased after annealing the films. This is attributed to thermal energy supplied by the annealing process, which resulted the

coalescence of small grains and abnormal grain growth (Du and Li, 2015; Jafari et al., 2014; Qi et al., 2017).

4.3.2.4 Surface roughness and wettability

AFM images of all films before and after annealing are demonstrated in Figure 4.5 in order to estimate the surface roughness and topography. Before annealing, AFM image of 100 BCP film exhibited grain like morphology with small spherical grains (Figure 4.5 (a)). However, both 25 TiO_2-BCP and 50 TiO_2-BCP films had spherical grains with larger grain size. Also, agglomerated grains were seen in these films (Figure 4.5 (b, c)). On the other hand, after annealing, islands like topography were observed in all the films (Figure 4.5 (d, e, f)) due to coalescence and clustering of particles. At high thermal energy, diffusion of atoms occurs at the grain boundary and results in significant grain growth and island-like morphology (Du and Li, 2015; Jafari et al., 2014; Qi et al., 2017). These results complemented with the FESEM results (Figure 4.4).

The values of different roughness parameters such as R_a, R_f and S_{kew} for each of the film before and after annealing are listed in Table 4.4. The R_a value of uncoated Ti-6Al-4V was found to be 2.2±0.4 nm. After sputtering, the roughness value increased due to the variation of topologies of the coated surfaces. Prior to annealing, 50 TiO_2-BCP film showed highest R_a value of 7.2±1.6 nm. Addition of TiO_2 increased the roughness of BCP film. After annealing, the roughness values of all the films increased, which corresponded to surface morphology (Figure 4.5). This is attributed to the formation of a number of irregular islands due to coalescence and clustering of grains, resulting in higher roughness (Surmeneva et al., 2016). R_f is the frequency of texture on the surface, which defined as the ratio of actual area to projected area of surface. The R_f value of the uncoated Ti-6Al-4V was found to be 1.00079. The R_f value of the modified surfaces are closed to 1, indicating smooth surface topographies. In similar to R_a, the R_f value increased with the addition of TiO_2 with the BCP film. The maximum value of 1.00796 is observed for 100 BCP film. Furthermore, this value increased after annealing of the films (Table 4.4). S_{kew} is another roughness parameter which is related to high peaks or deep valleys. Surfaces with high spikes have positive S_{kew}, whereas surfaces with deep valleys have negative S_{kew}. Flat polished surfaces have approximately zero S_{kew} (Surmeneva et al., 2016). 100 BCP film exhibited S_{kew} of higher positive value, indicating the presence of tall sharp spikes (Figure 4.6 (a)). Similar to that,

after annealing, the 100 BCP and 25 TiO_2-BCP films had positive S_{kew}, showing more prominent peaks with a larger area on the surface (Figure 4.6 (d, e)). On the other hand, 25 TiO_2-BCP and 50 TiO_2-BCP films before annealing had S_{kew} almost equal to zero, indicating almost flat surface (Figure 4.6 (b, c)).

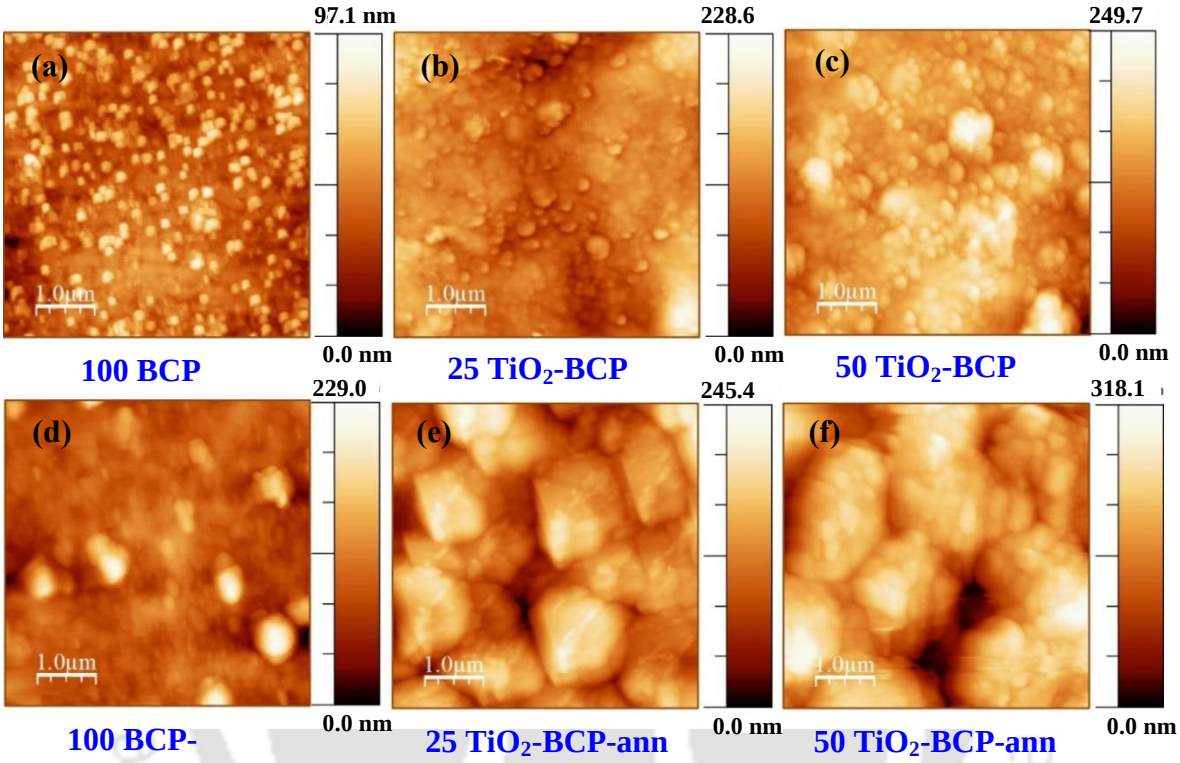

Figure 4.5: *AFM images of 100 BCP, 25 TiO_2-BCP and 50 TiO_2-BCP films before (a, b, c) and after (d, e, f) annealing (scan area 5 X 5).*

Table 4. 4: Roughness of parameters of the sputtered films before and after annealing

Films	R_a (nm)		R_f (nm)		S_{kew}	
	before annealing	after annealing	before annealing	after annealing	before annealing	after annealing
100 BCP	5.7±1.5	6.5±1.8	1.00632	1.00706	0.292	0.112
25TiO_2-BCP	6.8±1.4	8.0±1.7	1.00750	1.00852	0.068	0.168
50TiO_2-BCP	7.2±1.6	8.6±2.0	1.00796	1.01068	-0.023	-0.383

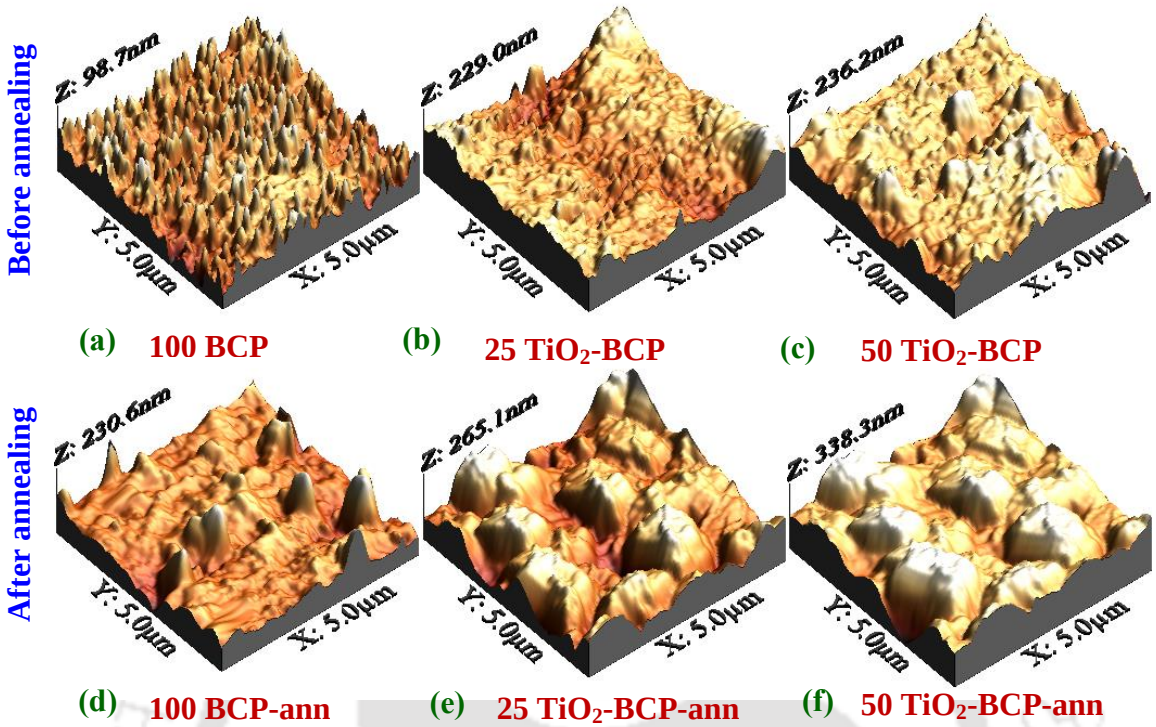

Figure 4.6: *3-D surface topography (AFM images) of 100 BCP, 25 TiO_2-BCP and 50 TiO_2-BCP films before (a, b, c) and after (d, e, f) annealing.*

Figure 4.7 shows the SBF contact angles of different sputtered surfaces before and after annealing. The contact angle on bare Ti-6Al-4V was found to be 90º(±1º) which increased to 95°(±3º) after BCP sputtering. San Thian et al. (2011) reported that the hydrophilicity of the Ti surface with HA film was due to the presence of phosphate (PO_4^{3-}) and hydroxyl (OH^-) ions, which significantly attract the electro-positively-charged (H^+) ions from SBF. However, the hydrophobicity of BCP film in the present study is attributed to nano-patterning of the surface with positive S_{kew} (Figure 4.6 (a)), which prevent the SBF droplet to spread (Surmeneva et al., 2016). With the addition of TiO_2 in the BCP film, the contact angle decreased to 73°(±2º) for 25 TiO_2-BCP film, and it further reduced to 35°(±1º) for 50 TiO_2-BCP film. As TiO_2 is hydrophilic in nature, the SBF droplets spread more on it (Balla et al., 2009; Majeed et al., 2015). Furthermore, the surface roughness enhanced with the addition of TiO_2 (Table 4.4), hence, the contacts between SBF droplet and the surface was larger due to higher surface area available, resulting in an improvement in the wettability. On the other hand, abnormal grain growth occurs by coalescence and clustering of small grains during annealing. Thus, surface void defects increase resulting in higher

surface roughness. The increase in roughness reduced the contact angle of all the films after annealing (Dinu et al., 2014; Du and Li, 2015; Qi et al., 2017). The reduction of contact angle with rise in roughness value of modified surfaces satisfies Wenzel equation (Eq. 4.1) which states that, the wettability is enhanced with the increase in surface roughness, when $R_f > 1$ and $\theta < 90°$, as also reported by Quéré (2008).

$$Cos\ \theta^* = R_f\ Cos\ \theta \qquad (4.1)$$

where θ^* is the apparent contact angle, θ is the Young contact angle for an ideal surface and R_f is the surface roughness factor.

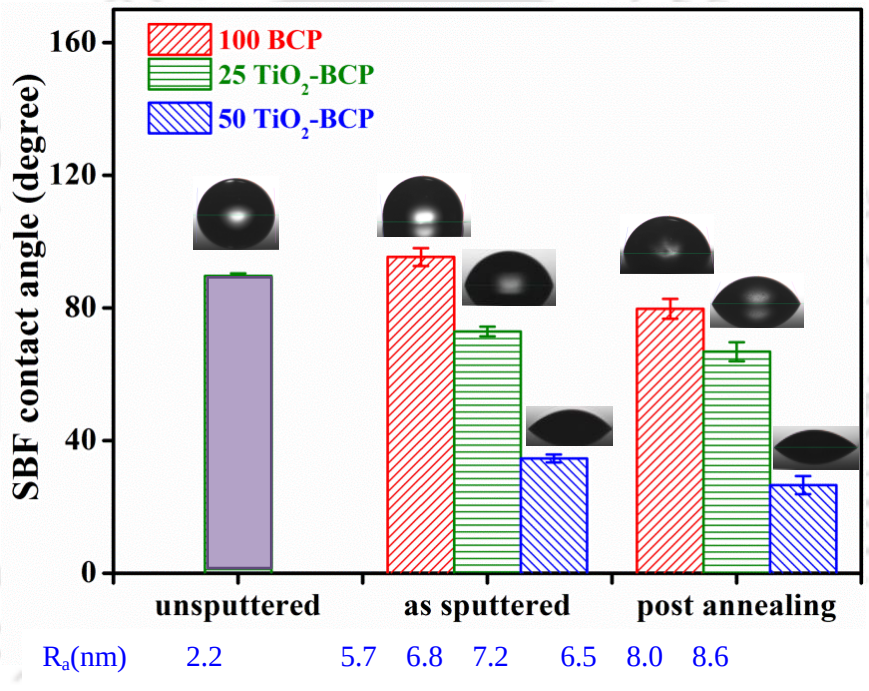

Figure 4.7: *Wettability of 100 BCP, 25 TiO_2-BCP and 50 TiO_2-BCP films before and after annealing.*

4.3.3 Adhesion behaviour

For developing implants with long-lasting, strong bonding or adhesion should develop in between the film and substrate. Scratch test provides a comprehensive measure of the bonding strength of a film to substrate. The microscopic images and coefficient of friction (COF) curve are typically used to evaluate the critical load (L_c), which is essential for determining the adhesion strength. L_{c1} is the minimum load at which the crack generation in the film starts, and L_{c2} is the minimum load at which delamination of film initiates (Cui et al.,

2017; Mohseni et al., 2015). Figure 4.8 represents the FESEM images of the scratches of 100 BCP film before and after annealing. It can be clearly observed that delamination of the films occurred at the edge of the scratch, when 4 N and 7 N loads were applied to the 100 BCP film (without annealing). On the other hand, after annealing, there was no failure at 4 N as well as 7 N. This revealed that annealing provides better bonding of the films with the substrate.

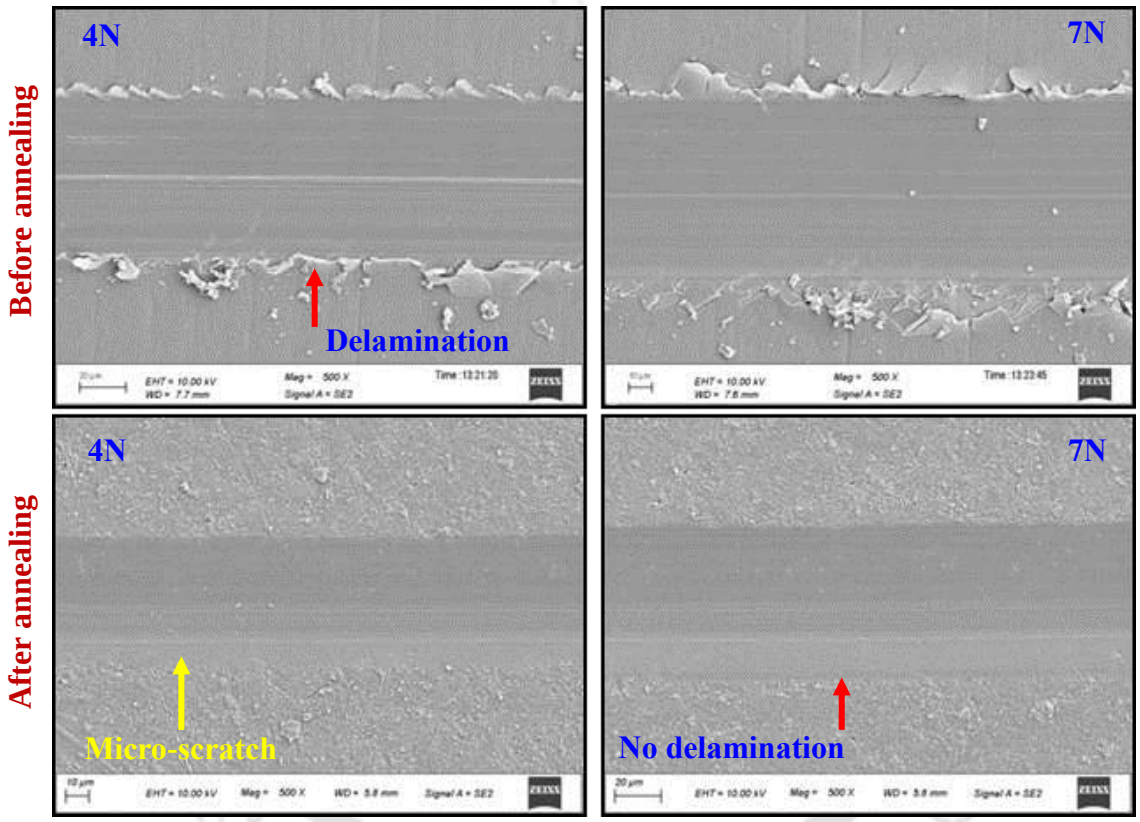

Figure 4.3: *Behavior of film after scratches made on 100 BCP film (before and after annealing) at different loads 4 N and 7 N.*

During annealing, diffusion occurs between the lower surface of the film and the upper surface of the substrate due to high thermal energy supplied. So, an interlocking between the materials of film and substrate occurs, making the bond much more strong (Mohseni et al., 2014). Hence, all other studies related to adhesion were carried out with film after annealing. Figure 4.9 illustrates the COF curves of 100 BCP, 25 TiO_2-BCP and 50 TiO_2-BCP films with respect to applied load and distance travelled by the indenter during the scratch test. In our previous study, a similar trend of COF was found for BCP films having

different thickness (Figure 3.12, chapter 3). COF with different trends were obtained for different films in the present study. For 100 BCP film, L_{c1} and L_{c2} were found at 3.4 N and 8.7 N, respectively, which is higher than previous reported data of 2.3 N and 7.8, respectively (section 3.3.7, chapter 3). However, for 25 TiO_2-BCP film, the critical load (L_{c1} and L_{c2}) was increased to 4.8 N and 14.8 N, respectively. Further L_{c1} was enhanced to 5.3 N for 50 TiO_2-BCP film, whereas, L_{c2} was beyond the maximum limit (19N). Moreover, the COF value also increased with the addition of TiO_2% with the BCP film.

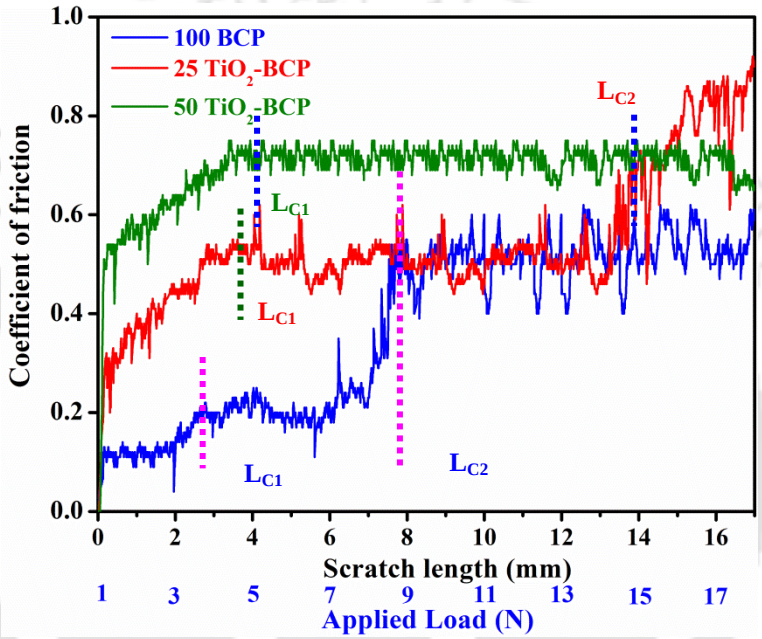

Figure 4.4: *Co-efficient of friction (COF) during dynamic micro-scratch test on different modified films after annealing.*

The FESEM images of scratch tracks at different loads for 100 BCP, 25 TiO_2-BCP and 50 TiO_2-BCP films are shown in Figure 4.10. It was observed that for 100 BCP film, no delamination was observed at 7 N load, whereas delamination was seen at the edges of the scratch track when 11 N load was applied. At 15 N load, full penetration occurred, i.e. complete delamination of the film was seen (Figure 4.10), and that has been demonstrated in the corresponding text of Figure 4.11 and 4.12. Furthermore, no delamination was observed at 11 N for 25 TiO_2-BCP film; however, exfoliation or delamination and full penetration appeared at 15 N and 19N, respectively (Figure 4.10). Again, it can be clearly seen that no delamination at the edges or at the path of the scratch, when 11 N and 15 N loads were applied to 50 TiO_2-BCP film (Figure 4.10). However, very less ejected particles were

observed on the edges of the scratches at 19 N. It indicated that, with the addition of 25%TiO_2 in the BCP film, the bonding strength of the coating enhance. The failures further reduced even at higher loads when 50%TiO_2 was added in the BCP film. Since the sputtering is an atom bombarding process, the atomic diffusion and mixing occur at the interface of the substrate and the deposited film (Mohseni et al., 2014). The chemical affinity between film and surface of Ti-6Al-4V substrate improved due to the presence of TiO_2. Hence, the mechanical interlocking effect between them enhanced, resulting in higher bonding strength (Albayrak and Altintas, 2010; Mohseni et al., 2014). Therefore, for 50 TiO_2-BCP film the bonding was much stronger as compared to other films.

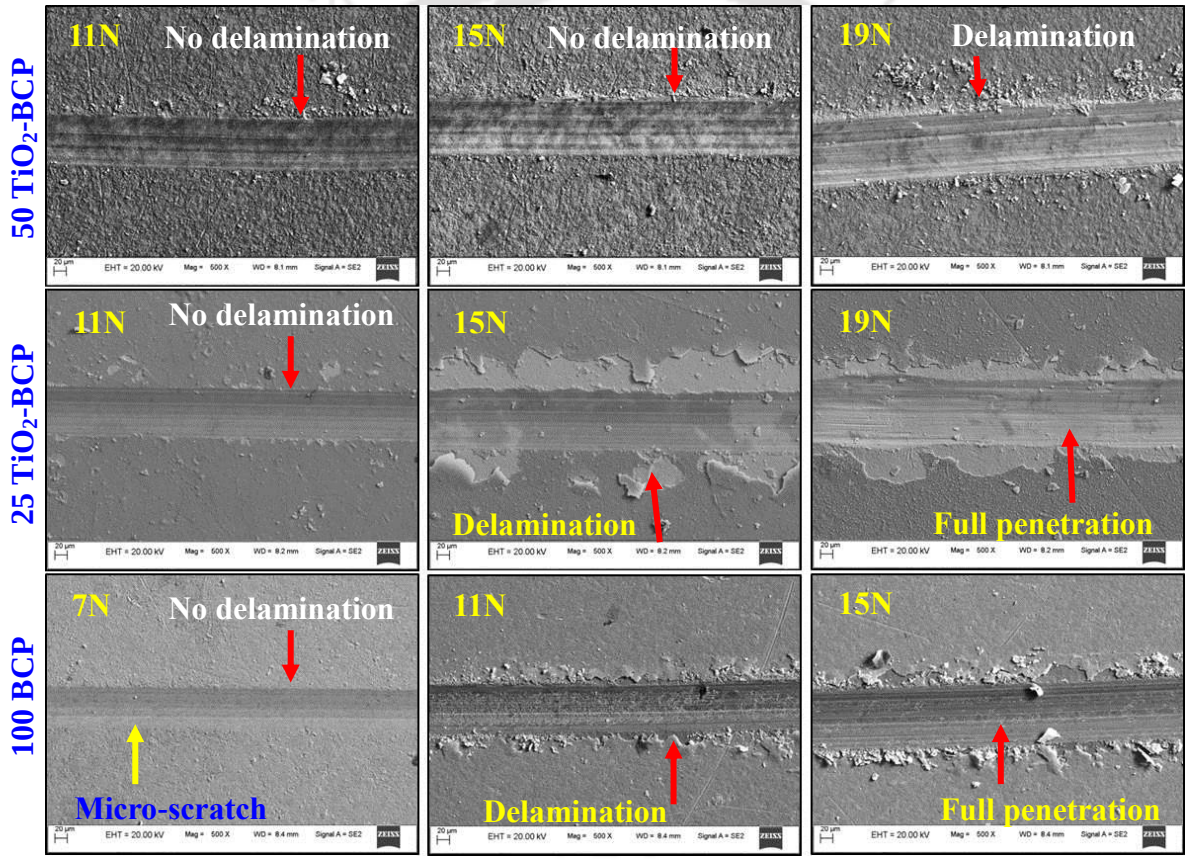

Figure 4.5: *Adhesion behavior of 100 BCP, 25 TiO_2-BCP and 50 TiO_2-BCP films (annealed) at different scratch loads.*

Pichugin et al. (2008) obtained no coating failure up to 2 N load during scratch test of HA film; whereas, Surmeneva et al. (2015) found no delamination of HA film up to 5.85 N. However, Surmeneva et al. (2017) enhanced the bonding of HA film by putting multilayer HA/Ag nanoparticle/CaP coating with Ti alloy. In the present study, up to 19 N, no

delamination of the coating was found for the 50 TiO_2-BCP films after annealing. Hence, it can be concluded that the bonding strength of the BCP film can be enhanced with an increase in TiO_2% in the film as well as annealing of the same.

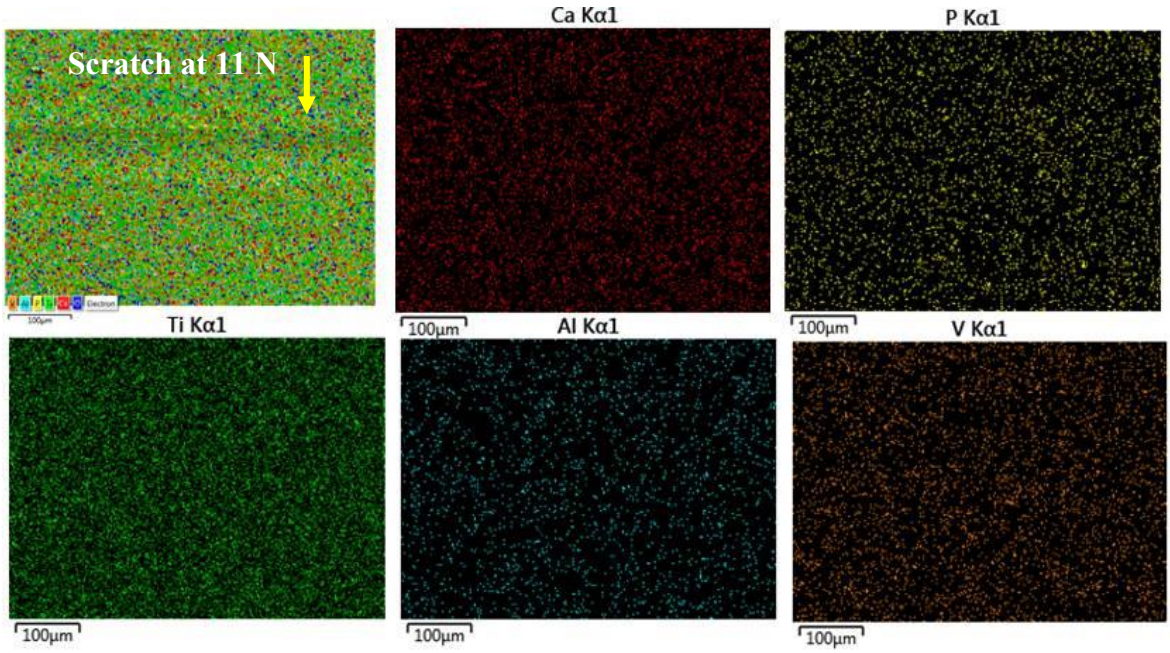

Figure 4.6: *Elemental mapping of 25 TiO_2-BCP film after scratch test at 11 N.*

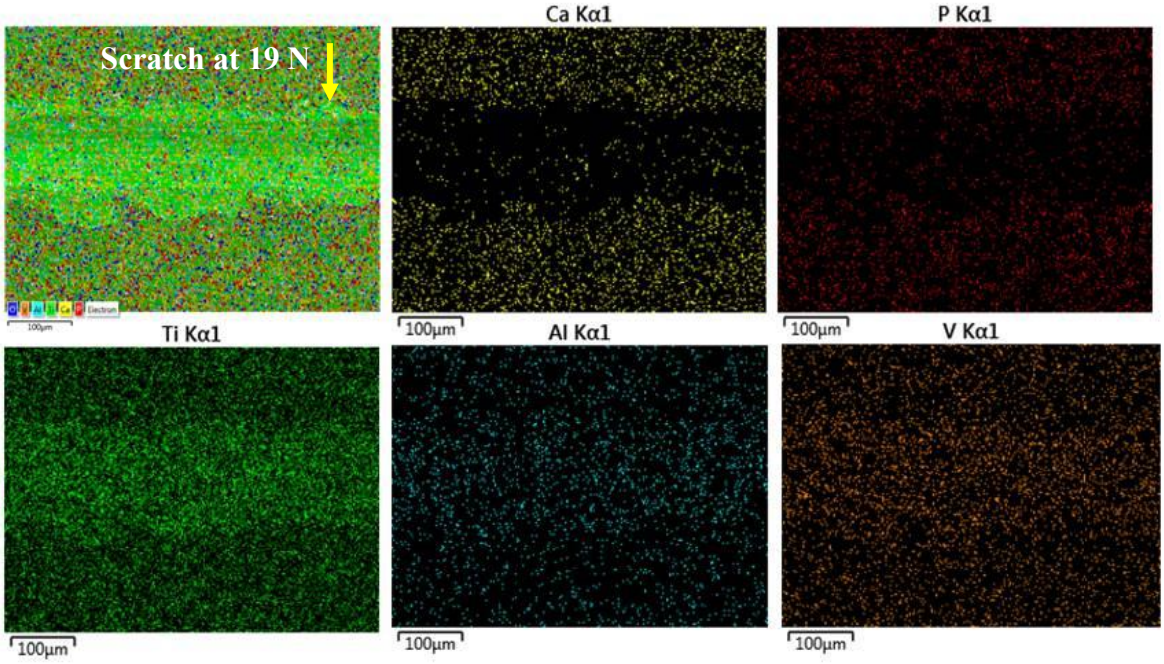

Figure 4.7: *Elemental mapping of 25 TiO_2-BCP film after scratch test at 19 N.*

Figure 4.11 and 4.12 illustrate the elemental mapping of 25 TiO_2-BCP films after the scratch test at 11 N and 19 N, respectively. It can be clearly observed that all the elements (Ca, P, O, Ti, Al, and V) were uniformly distributed even in the scratch area as well as in the vicinity of the scratch and other areas of the film (Figure 4.11). This indicated that there was no delamination of the film in the vicinity of the scratch at 11 N. On the other hand, when 19 N load was applied, only Ti, Al and V were present in the scratch area and the vicinity of scratch. Rest of the area was distributed with Ca, P and O also (Figure 4.12). This revealed that there was total delamination of the film or in other words, the load indenter had totally penetrated to the film.

4.3.4 Biological studies

4.3.4.1 Protein adsorption

During bone tissue regeneration the protein adsorption plays a crucial role, as protein from the surrounding fluids rapidly adsorb onto the surface of a bio-implant when it is implanted into a living body. Then cells get attached to the implant followed by cell proliferation and migration (Arima and Iwata, 2007; Wang et al., 2012). In the present study, 10% FBS solution was used for protein adsorption to mimic the cell culture conditions. Figure 4.13 represents the effect of contact angle as well as roughness factor on the mass of protein adsorbed on different films before and after annealing.

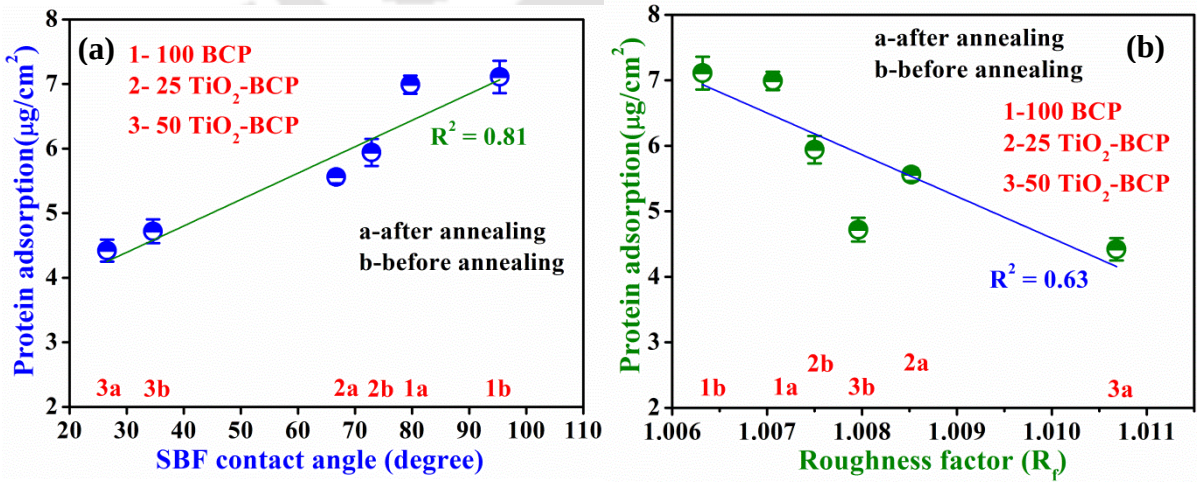

Figure 4.13: *Effect of (a) contact angle and (b) roughness factor on the mass of protein adsorbed on different films.*

The adsorbed protein mass was found to be minimum for bare Ti-6Al-4V (2.83 ± 0.15 µg/cm^2). The adsorbed protein mass was higher for other modified surfaces as compared to bare Ti-6Al-4V and increased from 4.42 ± 0.17 to 7.11 ± 0.25 µg/cm^2 with an increase in surface hydrophobicity (Figure 4.13 (a)). The protein adsorption is found to be related with contact angle (R^2 = 0.81) as shown in Figure 4.13 (a). A similar pattern of FBS adsorption with respect to contact angle was also observed by Hasan et al. (2018a) in self-assembled monolayers (SAM) functionalized silicon surfaces. Since FBS contains albumin as its major constituent, it shows albumin like adsorption behavior with respect to hydrophobicity, as previously reported by Hasan et al. (2018a), Pandey et al. (2013) and Pandey and Pattanayek (2013a). Higher adsorption of FBS on all the films compared to bare Ti-6Al-4V is due to the electrostatic hydrophobic interactions and hydrogen bonding between protein and surface. The highest protein adsorption was observed for BCP film (7.11 ± 0.25 µg/cm^2), due to the presence of protein binding sites such as Ca^{2+}, PO_4^{3-} and OH^-, which provide the major driving force for protein adsorption. Ca^{2+} binds with negative carboxylate groups and PO_4^{3-} /OH^- bind positive amino groups of protein (Wang et al., 2012). In addition, proteins generally tend to adsorb on the hydrophobic surface due to hydrophobic patches present in its structure. Due to hydrophobic interaction, protein unfolds and spreads its hydrophobic cores over the surface; hence, more protein adsorption occurred on hydrophobic BCP film (Wang et al., 2012).

Furthermore, with the addition of TiO_2, protein adsorption decreased to 5.94 ± 0.21 µg/cm^2 for 25 TiO_2-BCP and 4.72 ± 0.18 µg/cm^2 for 50 TiO_2-BCP film. TiO_2 being hydrophilic in nature induces hydrophilicity to the composite films which result in water layer formation at the interface and further prevents protein molecules to adsorb onto the surfaces (Wang et al., 2012). On the other hand, after annealing, the protein adsorption decreased corresponding to the films prior to annealing. This can also be attributed to the lesser contact angle of the film as compared to the corresponding film before annealing (Figure 4.7). dos Santos et al. (2012) found a similar quantity of proteins adsorbed on the surface of both amorphous CaP and carbonate-substituted crystalline HA coatings in culture medium containing proteins. However, in this study, the protein adsorption is somewhat less after annealing. After annealing crystallinity improves with deteriorates the solubility. Due to lower solubility, the dissolution of Ca^{2+} and PO_4^{3-} and other ions from the film reduces. This

leads to decreasing ionic strength of the solution. Lower ionic strength in the solution induces the protein to expose less polar-ionized residues to the solvent (Yongli et al., 1999). Hence, the amount protein adsorbed after annealing decreased by the lesser interaction between protein and surface binding sites of the film (Wang et al., 2012).

Figure 4.13 (b) represents the protein adsorption as function of the roughness factor of the modified films. It can be noticed that there is negative correlation between adsorbed protein mass and roughness factor (R^2 = 0.63). Although the surface roughness provides a significant spatial effect to the protein adsorption by increasing surface area (Hovgaard et al., 2008); however, may not be universally true for all the surfaces as other factors such as surface wettability also regulate the adsorption. Pisarek et al. (2011) found higher protein adsorption on smaller roughness H_3PO_4/H_2O_2-treated surface as compared to higher roughness NaOH-treated surface. Therefore, it can be concluded that FBS protein adsorption is significantly influenced by surface hydrophobicity as well as surface compositions rather than surface roughness and topography.

4.3.4.2 Cell adhesion and morphology

FESEM was used to monitor the morphology and adhesion behavior of attached MG63 cells on 100 BCP, 25 TiO_2-BCP and 50 TiO_2-BCP films (with and without annealing). The lower magnification images are intended to exhibit the cell morphology and cell density (Figure 4.14), whereas the higher magnification images represent the adhesion behavior of cells (Figure 4.15) on different modified surfaces. After 24 h of incubation, it was observed that all the modified surfaces had cells prominently adhered and distributed throughout the surfaces, as seen in Figure 4.14. However, two types of cell morphologies were noticed: (1) round shape and (2) polygonal shape. The polygonal shape represents the cells which were well spread and flattened, whereas, round shape shows the cells were less spread and pronounced. All the films (100 BCP, 25 TiO_2-BCP and 50 TiO_2-BCP) before annealing exhibited flattened polygonal shapes cells on the surfaces with higher cell spreading and cell density (Figure 4.14 (a, b, c)). On the other hand, round as well as polygonal shape cells are observed on the surface of annealed BCP and BCP-TiO_2 film (Figure 4.14 (d, e, f)). Non-spread and smaller sized cells with less density are seen on these annealed films. The polygonal shape

cells do not spread much as compared to that on the modified surfaces without annealing (Figure 4.14 (a, b, c)).

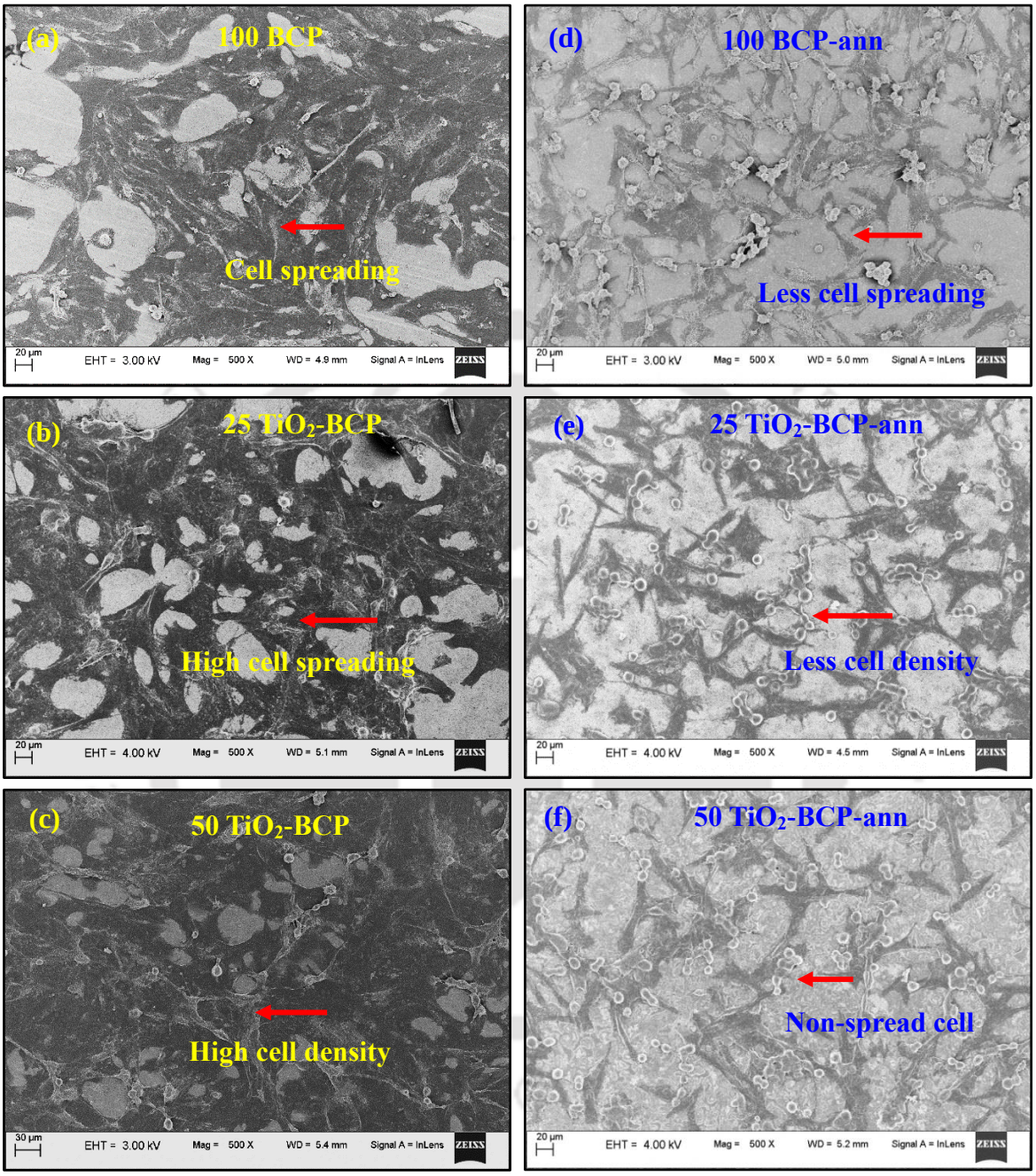

Figure 4.8: *FESEM images for MG63 cells (lower magnification) adhered after 24 h of proliferation on 100 BCP, 25 TiO_2-BCP and 50 TiO_2-BCP films (a, b, c) before annealing and (d, e, f) after annealing.*

Figure 4.15 shows the higher magnification morphology of MG63 cells on different modified surfaces in order to study to cell adhesion behavior with respect to the

corresponding surfaces. Elongated cell with longer filopodial extension (Figure 4.15 (a)), highly proliferated cell with filopodial extension (Figure 4.15 (b)) and cell-to-cell connectivity with extracellular matrix (ECM (Figure 4.15 (c)) are observed on the surface of 100 BCP, 25 TiO_2-BCP and 50 TiO_2-BCP films (without annealing), respectively.

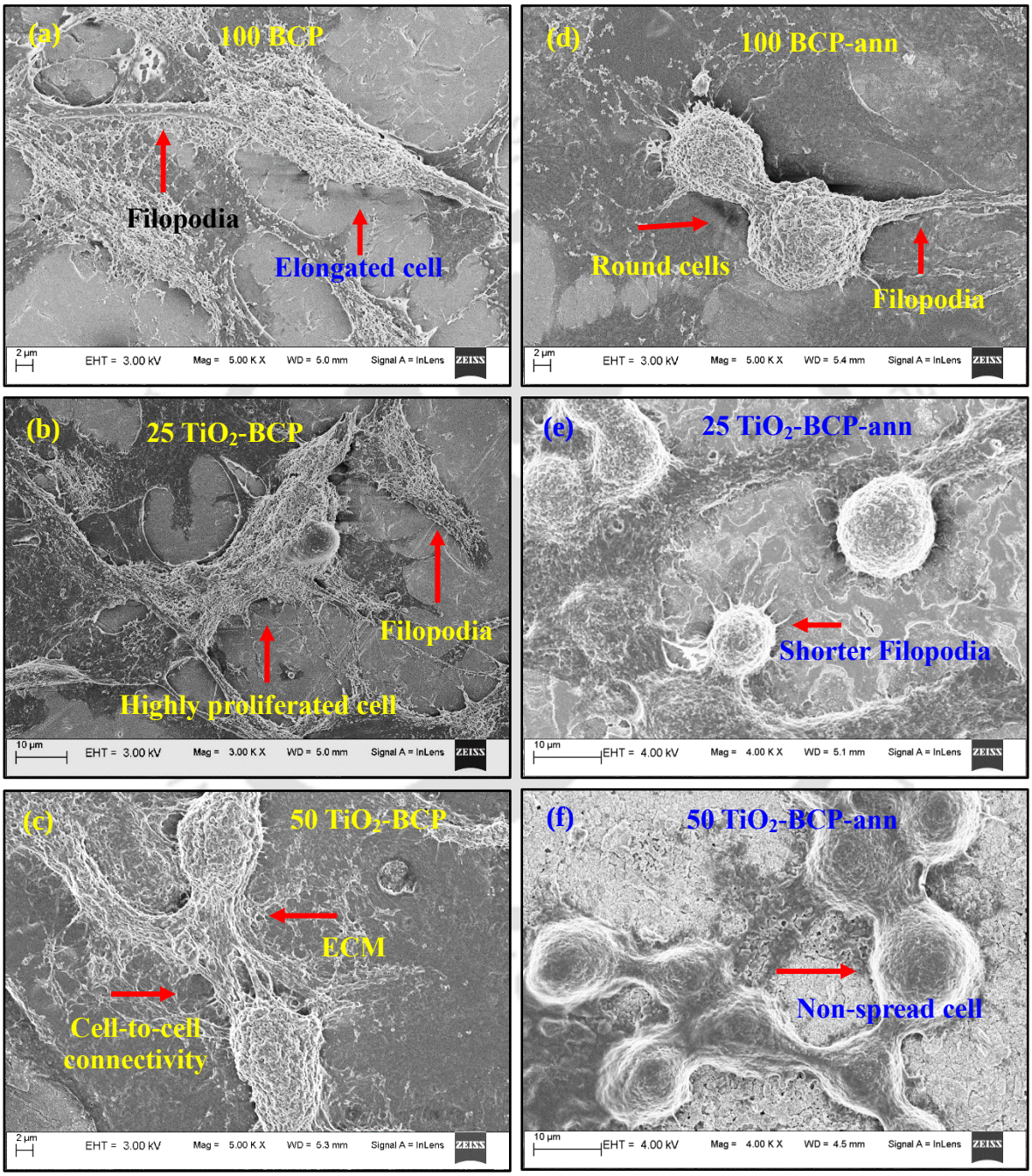

Figure 4.9: *FESEM images for MG63 cells (higher magnification) adhered after 24 h of proliferation on 100 BCP, 25 TiO_2-BCP and 50 TiO_2-BCP films (a, b, c) before annealing and (d, e, f) after annealing.*

However, round non-spread cells with very short filopodial extension are noticed on the surface of annealed 100 BCP, 25 TiO_2-BCP and 50 TiO_2-BCP films (Figure 4.15 (d, e, f)). The presence of these filopodial extensions suggests spreading and strong adherence of cells, hence, indicating a contact intimacy with the modified surface (Li et al., 2012). Cell-to-cell connectivity, the highly proliferated and elongated cells indicate synergy of reinforcements (Pandey et al., 2018).

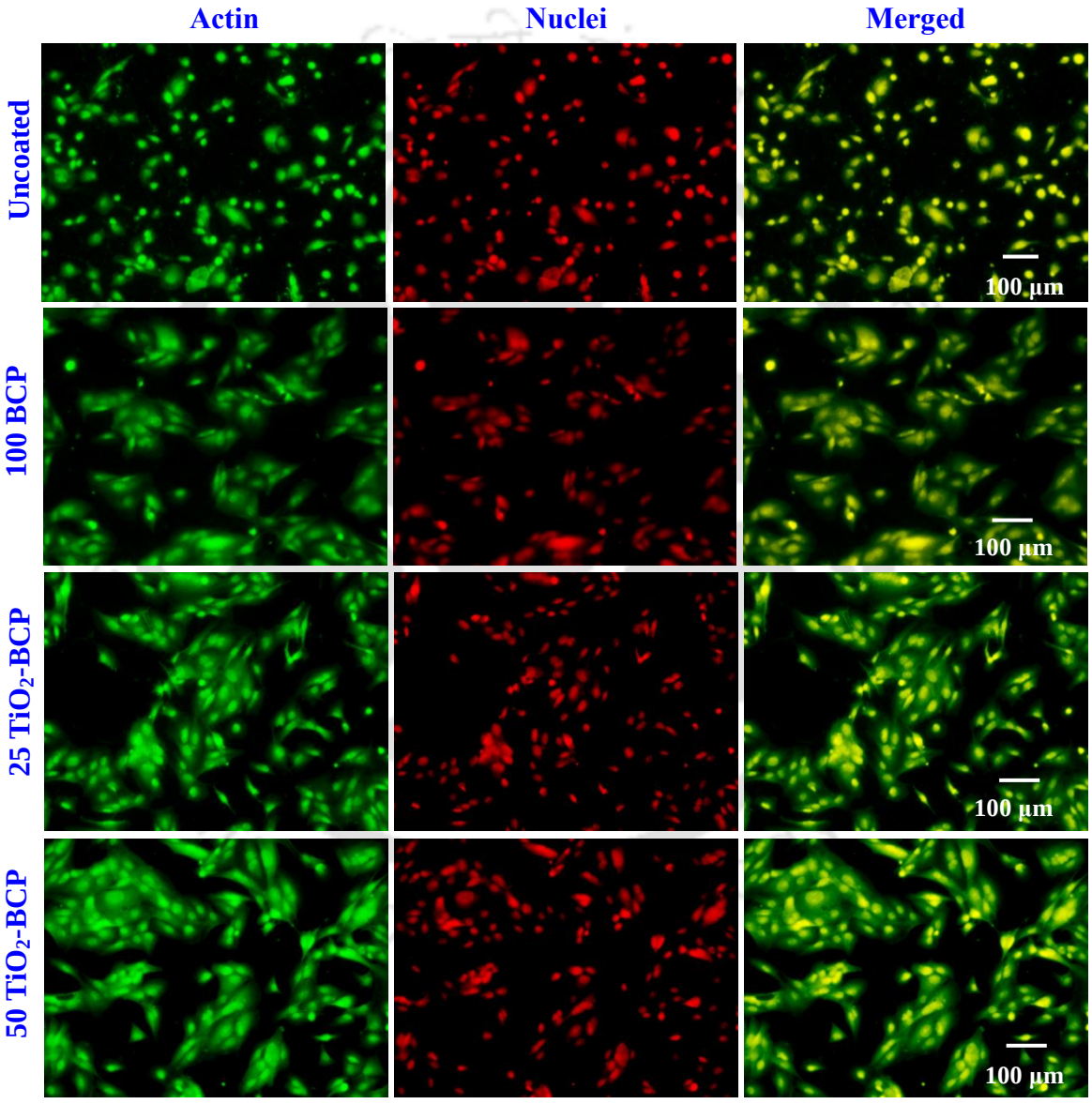

Figure 4.10: *Fluorescent images for MG63 cells adhered after 12 h of proliferation on 100 BCP, 25 TiO_2-BCP and 50 TiO_2-BCP films (before annealing), showing actin filaments (green, stained by FITC-Phalloidin), and the nucleus (red, stained by PI dye).*

Furthermore, the ECM is formed due to filopodia formation and extension on the vicinity, and interaction of the cells in the surrounding to facilitate cell-to-cell interactions (Pandey et al., 2018). Thus, the presence of larger filopodia extensions, cell-to-cell connectivity, ECM formation with higher cell density indicates that the 100 BCP, 25 TiO_2-BCP and 50 TiO_2-BCP films without annealing are superior bio-compatible. On the other hand, lesser cell density with shorter filopodial extension reveals that these surfaces after annealing have not so much strong adherence of cells with slower cell growth and hence, lesser biocompatibility in nature.

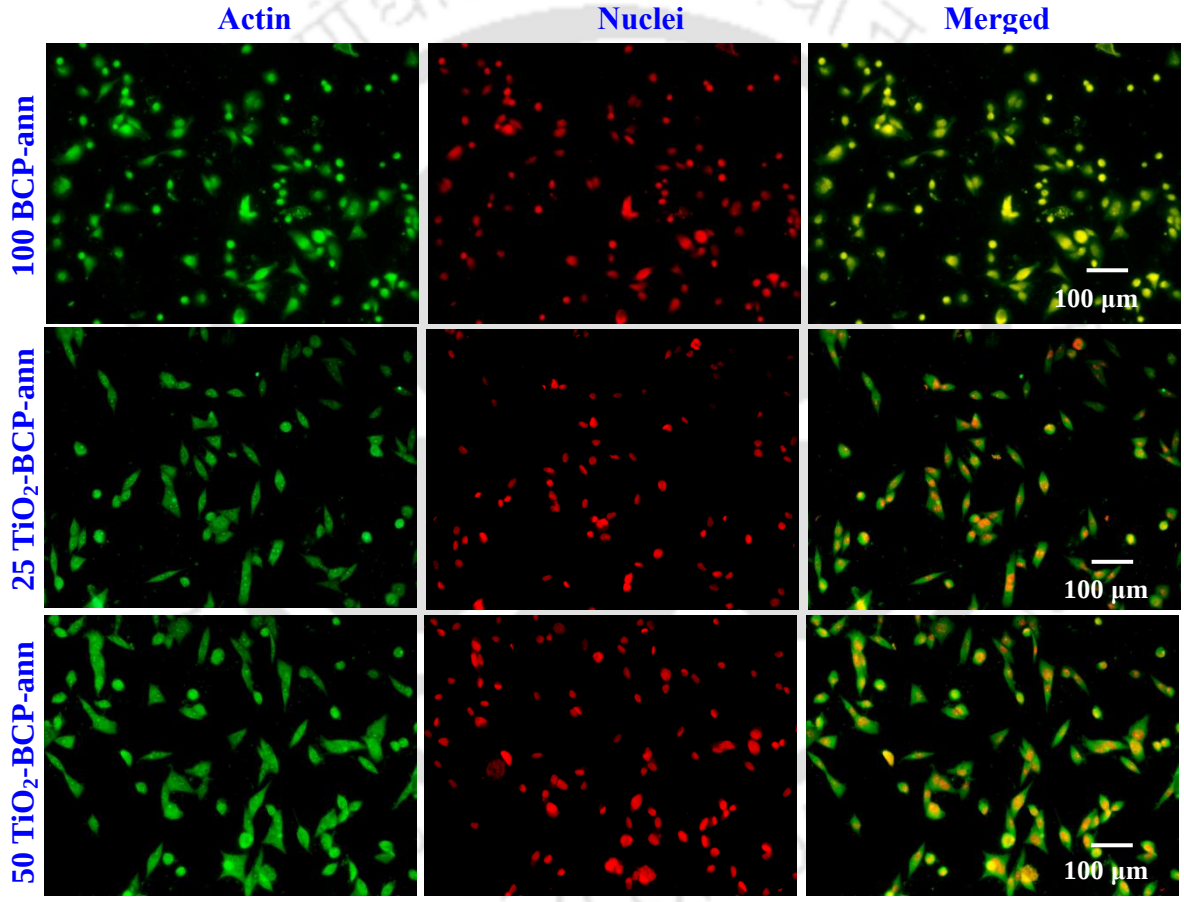

Figure 4.11: *Fluorescent images for MG63 cells adhered after 12 h of proliferation on 100 BCP, 25 TiO_2-BCP and 50 TiO_2-BCP films (after annealing), showing actin filaments (green, stained by FITC-Phalloidin), and the nucleus (red, stained by red, PI dye).*

The difference between 100 BCP, 25 TiO_2-BCP and 50 TiO_2-BCP films regarding biocompatibility cannot be analyzed from these figures, as all these have well-flattened cells spread entirely on the surfaces (Figure 4.14 (a, b, c)). Hence, quantitative analysis was

conducted by fluorescence microscopy to find out the effect of TiO_2 addition with the BCP film on cell adhesion, which is discussed in the following section.

Figure 4.16 and 4.17 display the fluorescent imaging of MG63 osteoblast cells cultured for 12 h on different sputtered surfaces before and after annealing, respectively. The green parts represent the actin filament, whereas the red ones show the nuclei, and the merged images show the combined actin filaments and nuclei of osteoblast cells (Figure 4.16 and 4.17). Actin filaments form the cytoskeleton, which helps the cells to spread by connecting the focal adhesion at the cell-materials sites. The adherence of cells is influenced by surface functional groups, wettability, roughness, protein adsorption and types of protein etc. (Hasan et al., 2018a; Hasan et al., 2018b).

The influence of surface modification on cell adhesion and spreading is illustrated in this study. The cell adherence and spreading on various modified surfaces are evaluated in terms of percentage of cell adherence, average cell area, nuclei area and circularity as already described in section 2.3.7. These cell features were determined from fluorescence microscopy images using image processing (ImageJ) software (Figure 4.18 and 4.19). As compared to uncoated Ti-6Al-4V, which shows spherical non-spread cells, RF sputtered samples showed higher % cells adhered as well as better spreading (Figure 4.16). 50 TiO_2-BCP (79±10%) exhibited a maximum % of cell adherence followed by 25 TiO_2-BCP (72±7%) and 100 BCP (66±6%). The minimum number of cells were seen on uncoated Ti-6Al-4V (54±4%), as presented in Figure 4.18 (a). In addition, the maximum cell spreading area was found on 50 TiO_2-BCP (2012±437 μm^2) followed by 25 TiO_2-BCP (1809±352 μm^2) and 100 BCP (1663±252 μm^2). The minimum cell spreading area was observed on uncoated Ti-6Al-4V (1365±230 μm^2) indicating poor focal adhesions as compared to sputtered samples (Figure 4.18 (a)). This clearly depicts that all the sputtered samples had an excellent affinity towards MG-63 cell adhesion than uncoated substrate. This is directly attributed to the presence of biocompatible functional groups such as HA, β-TCP and TiO_2 (rutile) on the substrate, resulting in the higher mass of proteins adsorbed on the sputtered surfaces (4.42 ± 0.12 to 7.23 ± 0.14 $\mu g/cm^2$) compared to uncoated Ti-6Al-4V (1.21 ± 0.05 $\mu g/cm^2$).

This higher adsorbed protein concentration is responsible for better adhesion and spreading of cells as proteins act as a cushion for upcoming and adhering cells. Therefore,

higher osteoblast cells adhere and spread on the sputtered substrates as compared to uncoated Ti-6Al-4V.

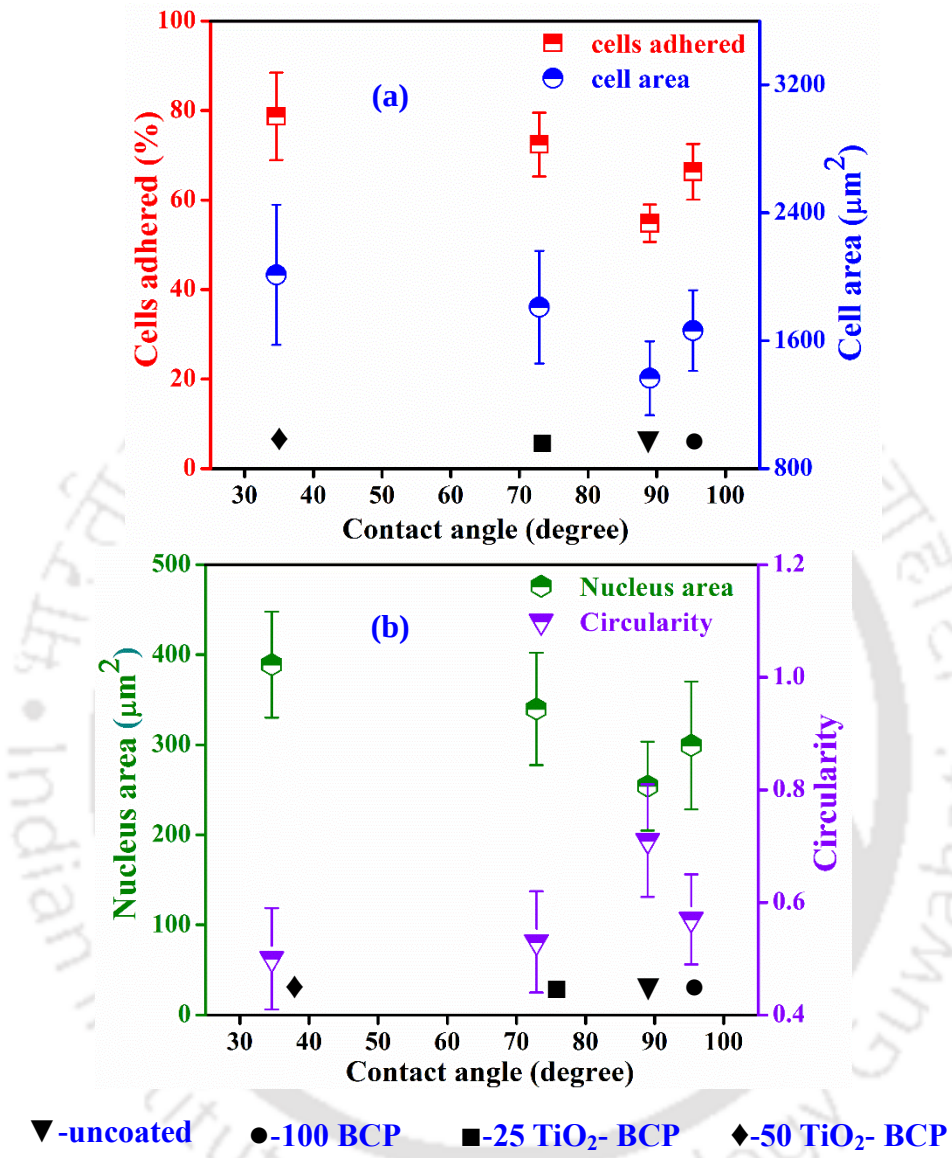

Figure 4.12: *Effect of different coated surfaces (before annealing) on (a) % cells adhered and average cell area, (b) average nuclei area and circularity of adhered cells.*

In addition, with the increase in the TiO_2 concentration in the BCP film, the wettability improved as the contact angle decreased from 95.3° to 34.6º. Due to the increase in wettability, the surface energy increases lead to higher interaction between the cells and surface. Furthermore, the surface roughness increased with increase in TiO_2 concentration in the BCP film, resulting in higher cell spreading area due to an increase in the surface area (Arima and Iwata, 2007; Surmenev et al., 2014). Hence, much more spreading of cells

occurred in super-hydrophilic 50 TiO_2-BCP film. It can be concluded that the wettability and surface roughness play a vital role on the adhesion and spreading of osteoblast cells.

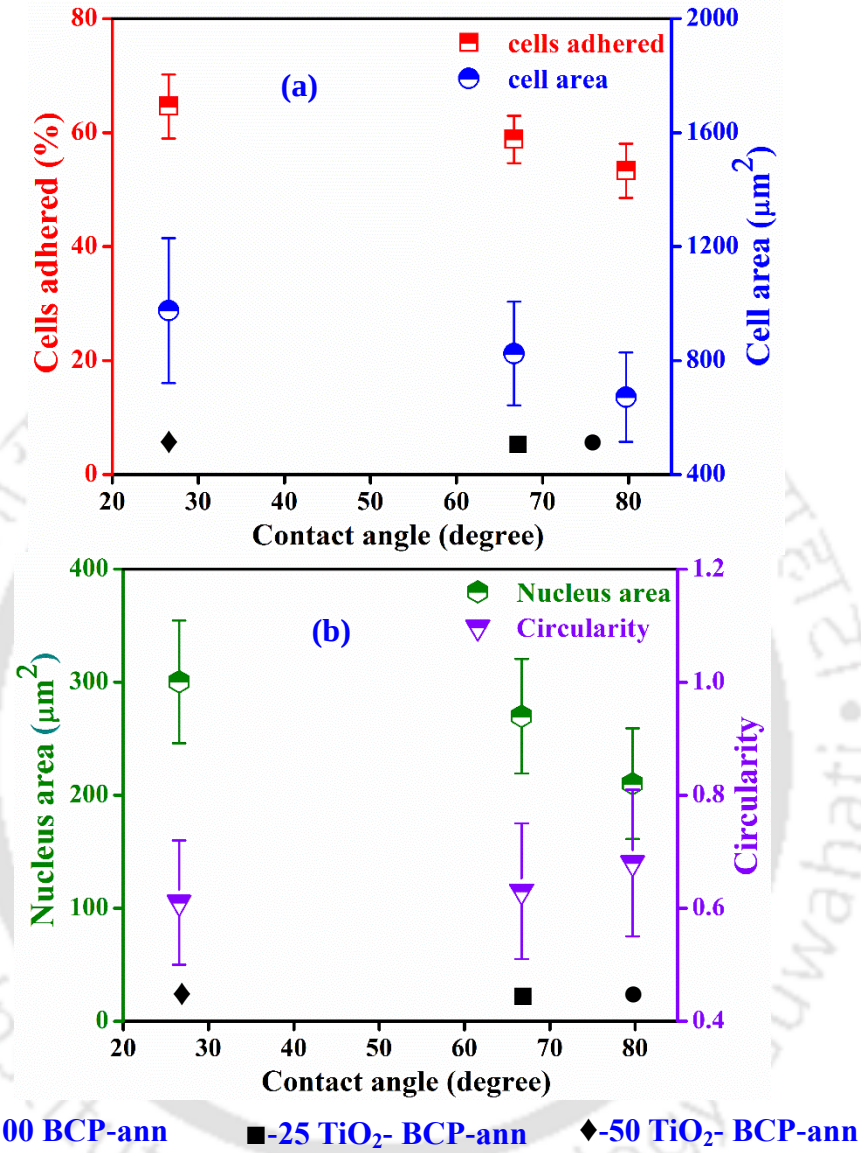

Figure 4.13: *Effect of different coated surfaces (after annealing) on (a) % cells adhered and average cell area, (b) average nuclei area and circularity of adhered cells.*

Similar trend as that of average cell area was also followed for average nuclei area of the adhered cells: 50 TiO_2-BCP > 25 TiO_2-BCP > 100 BCP > un-coated Ti-6Al-4V (Figure 4.16 and 4.18 (b)). Nuclei size plays a significant role during cell differentiation and proliferation, as larger nucleus size leads to higher division rate, indicating higher cyto-compatibility rate (Tutak et al., 2017). Circularity of the cells is defined in the scale range of 0 to 1. Generally better spreading of the cells is observed when the circularity value is less

and has been reported previously by Hasan et al. (2018b). The cell circularity value on 50 TiO_2-BCP (0.50±0.08), 25 TiO_2-BCP (0.53±0.09) and 100 BCP (0.57±0.09), showed smaller values indicating better spreading of the osteoblasts as compared to the uncoated substrate (0.72±0.12), as shown in Figure 4.18 (b).

Similar trends of % of cell adherence, average cell area, nuclei area as well as circularity were also seen for the 100 BCP, 25 TiO_2-BCP and 50 TiO_2-BCP films after annealing as found in those before annealing (Figure 4.19). However, the values for these cell features are less in case of the films after annealing as compared to those before annealing. i.e. the cell adherence and spreading are less in case of the annealed films, as confirmed by the fluorescence images (Figure 4.16 and 4.17). Furthermore, some spherical non-spread cells can be seen in annealed films (Figure 4.17). Though the annealed surfaces had higher wettability, larger surface roughness and higher protein adsorption compared to corresponding non-annealed films, still these annealed surfaces exhibited lesser cell adhesion and spreading. It has been previously reported by dos Santos et al. (2012) that higher dissolution of HA film takes place prior to annealing, which enriches the culture medium with the Ca^{2+} ions. This generates the mature actin filaments with larger cell spreading compared to annealed surfaces. However, in the present study, very less spreading of cells observed compared to as-deposited film. This may be due to the subsequent annealing of 700 °C after deposition of the film at 400 °C substrate temperature. This may enhance the crystallinity with very less dissolution of the film in the cell media. Hence, better cell behavior was observed on the composite surfaces before annealing as compared to the surface after annealing.

It can be concluded that the cellular adhesion of Ti-6Al-4V is enhanced by BCP as well as BCP-TiO_2 composite deposition on it. Higher cell spreading and adhesion was observed on 50 TiO_2-BCP film. However, the annealing of all these films deteriorates the cell adhesion and spreading.

4.3.4.3 Cell proliferation

In order to perform the cell proliferation on different modified surfaces with respect to uncoated Ti-6Al-4V, MTT assay was performed for 2, 4, and 6 days, as shown in Figure 4.20. The proliferation rate of different surfaces before and after annealing is displayed in

Figure 4.20 (a) and (b), respectively. It is clearly depicted that, for all the modified and uncoated surfaces also, the proliferation rate increased with an increase in the incubation period. This shows the cyto-compatibility of all the tested samples. Compared to bare Ti-6Al-4V, all modified surfaces exhibited higher cyto-compatibility rate for all the incubation time durations. At day 6, the proliferation rate of 50 TiO_2-BCP film (210.1±6.5%) was significantly higher than 25 TiO_2-BCP (196.8±5.8%) and 100 BCP (169.3±2.8%). On the other hand, the proliferation rate for annealed samples was substantially lower than that of films without annealing for all the incubation periods. For day 6, the proliferation rate of 100 BCP-ann, 25 TiO_2-BCP-ann and 50 TiO_2-BCP-ann films were 108.5±4.7%, 125.1±8.5% and 139.2±8.1%, respectively.

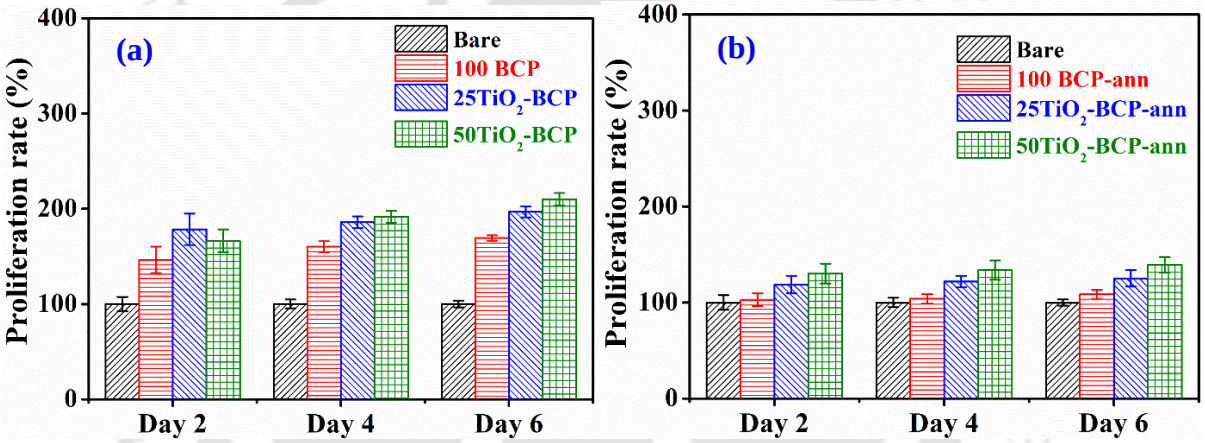

Figure 4.20: *Proliferation rate of MG63 cells after 2, 4 and 6 days on bare Ti-6Al-4V, 100 BCP, 25 TiO_2-BCP and 50 TiO_2-BCP films: (a) before annealing and (b) after annealing*

The enhancement of cyto-compatibility rate in all the modified surfaces can be attributed to the presence of biocompatible phases (HA, β-TCP and TiO_2 (rutile)) and higher protein adsorption, higher wettability as well as higher surface roughness as compared to uncoated Ti-6Al-4V. Furthermore, due to the increase in wettability and the surface roughness with the increase in TiO_2 concentration, the surface free energy and the surface area enhanced. This results in higher adhesion and spreading of osteoblast cells, which finally exhibiting larger % of adhered cells. In addition, because of larger nuclei area, a higher number of cells divided, resulting in higher cyto-compatibility in 50 TiO_2-BCP as compared to 25 TiO_2-BCP and 100 BCP film. Similarly, Kuwabara et al. (2012) found higher number of cell attachment and larger diameter of cell nucleus on the HA-TiO_2 hybrid coating

fabricated by dual sputtering technique and reported that the charge intensity of 0.5 to 1.0 nC for the optimum conditions of cell attachment. In this study, the higher surface roughness and higher wettability leads to higher cell proliferation. On the other hand, due to the less dissolution of the film, the culture medium could not be enriched with Ca^{2+} ions; hence, less cell adhesion and proliferation resulted. Similar behavior i.e. less adhesion and proliferation of cells was reported by dos Santos et al. (2012) in crystalline CaP coating compared to amorphous CaP film. On contradiction, Hu et al. (2007) found higher cell adhesion and proliferation of bone marrow mesenchymal stem cells on crystalized HA film as compared to amorphous CaP film of same crystal size and reported that size effect of nano-crystal plays an important role on cell adhesion and proliferation. In this study, the crystal size of the film before annealing is less compared to that after annealing. This could be a reason for the higher cell adhesion and proliferation in the film before annealing compared to the film after annealing.

4.3.4.4 In vitro bioactivity

Bioactivity is achieved by immersion of modified surfaces in SBF solution for certain days that results in bone-like apatite globules or layer formation on the modified surfaces. Moreover, the rapid generation of apatite layer is correlated to superior bioactivity (Sun et al., 2013). As the sputtered films before annealing were found to have better biocompatibility; hence, in the current study, the apatite formation was evaluated only on 100 BCP, 25 TiO_2-BCP and 50 TiO_2-BCP films without annealing. Figure 4.21 represents the XRD patterns of 100 BCP, 25 TiO_2-BCP and 50 TiO_2-BCP films (without annealing) after 7 days of SBF immersion. It can be seen that all the modified surfaces exhibited significantly improved apatite peaks with reduction of β-TCP peaks as compared to that in the surfaces before SBF immersion (Figure 4.2).

However, the intensity of the apatite peaks significantly enhanced with the increase in TiO_2% in the BCP film. The formation of apatite layer on BCP film is attributed to the formation of nucleation sites due to bioactive HA and *β*-TCP phases. When these phases came into contact with SBF, the hydroxyl (OH^-) and phosphate (PO_4^{3-}) units make the surface potential highly negative (Kim et al., 2004; Paital and Dahotre, 2009). The formation of negatively charged OH^- ions on the surface attracts Ca^{2+} ions from the SBF, followed by

PO_4^{3-} ions and reaction occur, and apatite nuclei are formed on the surface (Bakhsheshi-Rad et al., 2016a). Because of solubility of β-TCP, SBF gets supersaturated with Ca^{2+} and PO_4^{3-}; thus, more apatite can be precipitated by BCP film than pure HA deposited substrate. The apatite formation was observed on BCP deposited Ti-6Al-4V having different film thicknesses when soaked in SBF for 14 days, as already described in section 3.3.8, chapter 3.

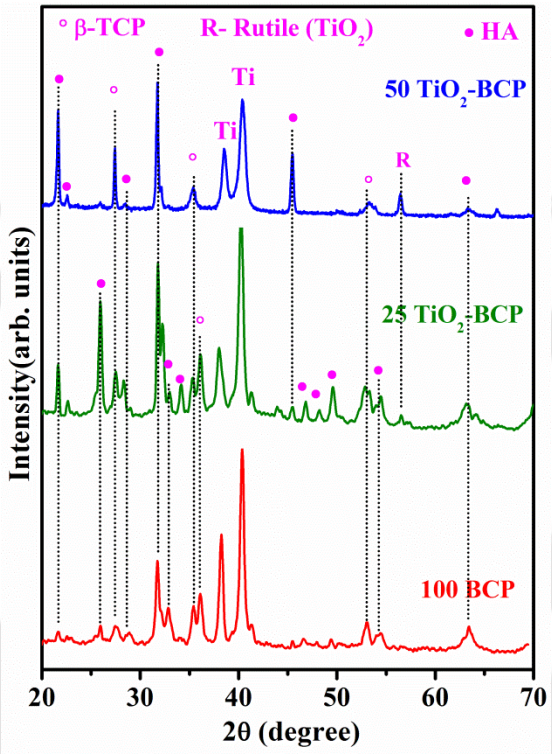

Figure 4.21: *Phases found in 100 BCP, 25 TiO_2-BCP and 50 TiO_2-BCP films after 7 days immersion in SBF.*

On the other hand, the high amount of precipitate deposited on 50 TiO_2-BCP films was due to the formation of OH^- group from both BCP as well as TiO_2, when they came to contact with SBF. Hence, more OH^- group attracted Ca^{2+} ions from the SBF, followed by PO_4^{3-} ions, resulting apatite layer on the surface of the film. In addition, due to the higher wettability of 50 TiO_2-BCP films more probability of reaction exists between surface and SBF ions. Therefore, more nucleation sites formed for the ions of SBF solution to come to the substrate and settle down on the surface. Again, due to the high surface roughness of 50 TiO_2-BCP film, surface area increased causing more amount of Ca^{2+} and PO_4^{3-} penetration from SBF (Arce et al., 2016). Hence, it can be concluded that, with the addition of TiO_2 in

BCP film, the bioactivity of the film is improved significantly with the enhancement of wettability.

The surface morphologies of different modified surfaces after 7 days of SBF immersion is demonstrated in Figure 4.22. After 7 days of SBF soaking, apatite layer in the form of globules was nucleated and grew on the surface of all BCP films (lower magnification, Figure 4.22 (a–c)). The higher magnification FESEM images clearly show the globular apatite on the films (Figure 4.22 (d, e)). Plate-like crystals were observed in the globules at higher magnification (Figure 4.22 (f)). The appearance of globular morphologies and plate-like crystals are the characteristics of bone-like apatite formation, which is favorable for osteoconductivity, as reported by Li et al. (2015c) and Surmeneva et al. (2013).

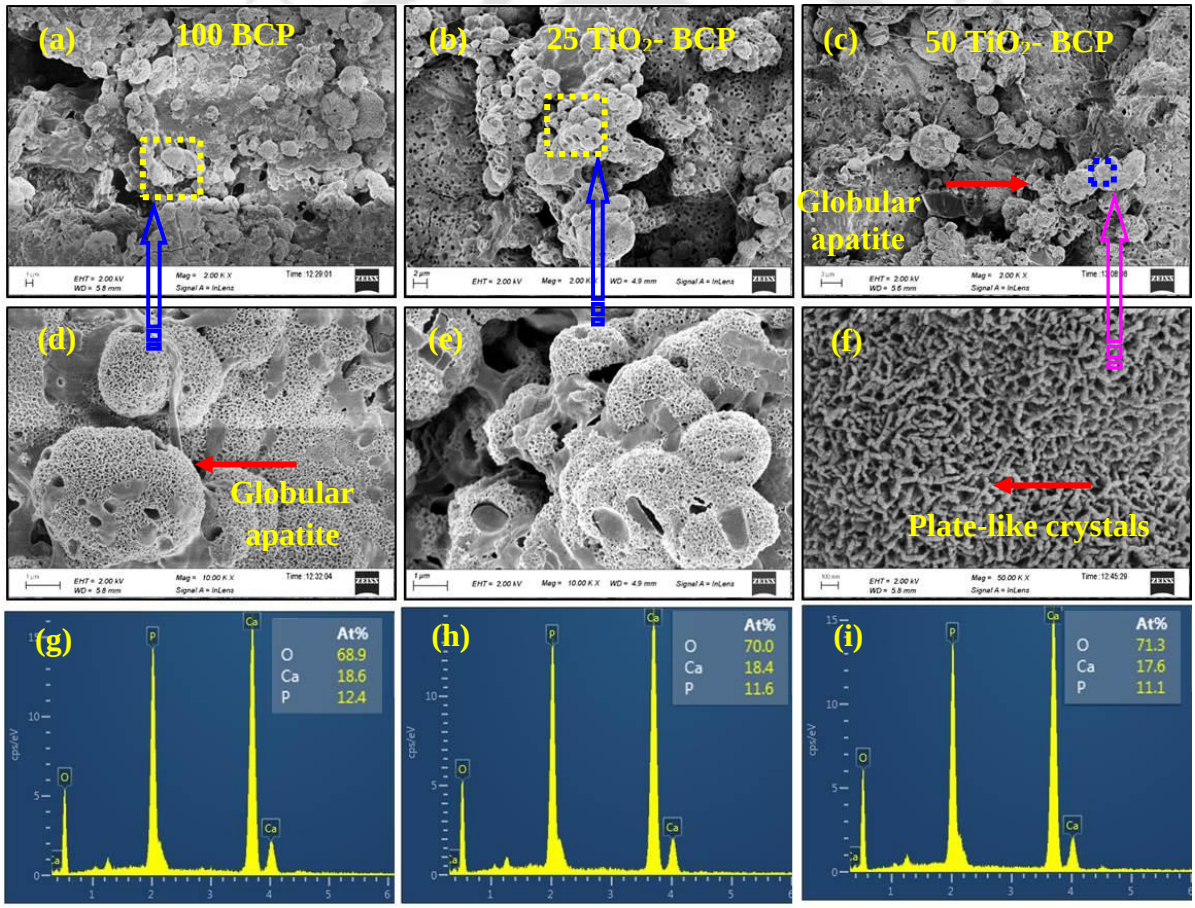

Figure 4.22: *Surface morphologies of (a) 100 BCP, (b) 25 TiO_2-BCP, (c) 50 TiO_2-BCP after 7 days immersion in SBF: (d, e) corresponding magnified views, (f) higher magnified view and (g, h, i) corresponding EDS spectra taken full area of (a, b, c).*

The EDS analysis of the globular particles precipitated on all the films showed a higher percentage of Ca, P and O with Ca/P atomic ratio of 1.5 -1.58 (nearly equal to 1.67).

This confirmed that the apatite grown on the substrate surfaces were calcium deficient apatite similar to that found in bones. The similar type of results was also reported by Mello et al. (2007) during HA deposition on Ti-6Al-4V using RF sputtering. From XRD, FESEM and EDS results, it was clearly confirmed that the apatite precipitated effectively from the SBF solution on the sputtered surface. The addition of TiO_2 with BCP deposition can enhance the wettability and apatite layer formation which stimulates osteointegration (Hasan et al., 2018b; Surmenev et al., 2014).

4.4 Findings from the research work

In the present study, 100 BCP, 25 TiO_2-BCP and 50 TiO_2-BCP composite films were successfully deposited on Ti-6Al-4V by RF magnetron sputtering. Annealing was performed on sputtered specimens at 700 ºC for 2 h to investigate the effect of thermal energy on different physical, adhesion and biological properties of the coated surface. The main findings reveal that R_a of film increased with the increase in wt.% of TiO_2 and was found to be maximum (7.2±1.6 nm) for 50 TiO_2-BCP film. The contact angle was found 95º(±3º) for 100 BCP film, 73º(±2º) for 25 TiO_2-BCP and 35º(±1º) for 50 TiO_2-BCP film, indicating improvement in wettability with increase of wt.% of TiO_2. The R_a value for all the films increased after annealing due to abnormal grain growth, resulting in a decrease of contact angle. The adhesion bonding between BCP film to Ti-6Al-4V substrate enhanced due to the addition of TiO_2 as well as annealing of the sputtered specimens. The value of L_{c1} and L_{c2} was found to be maximum for 50 TiO_2-BCP film (5.3 N and more than 19 N, respectively). The FBS adsorption increased from 4.42±0.17 to 7.11±0.25 µg/cm^2 with increase in contact angle. After annealing, the protein adsorption decreased for corresponding films. All films before annealing exhibited significantly higher cell adhesion and proliferation compared to bare Ti-6Al-4V. With the addition of TiO_2 with the BCP film, the cell adhesion and proliferation improved, indicating better cytocompatibility. However, the cell adhesion and proliferation reduced for the coated samples after annealing. Presence of filopodial extension, cell-to-cell connectivity and ECM indicated the good cytocompatibility of all the films before annealing. After 7 days of SBF immersion, globular bone-like apatite formed on all modified surfaces, making the surfaces more suitable to osteo-integration. Furthermore, the addition of TiO_2 in the BCP film improved the bioactivity.

The present study concludes that the TiO_2 addition in BCP film is beneficial for improving wettability, adhesion strength, bioactivity and cytocompatibility of the implants. Thermal annealing enhances the bonding strength of the films with the substrate; however, it deteriorates the biological properties. Hence, TiO_2 addition with the BCP film (without annealing) can be beneficial for the long duration use of implants for artificial tooth and bone applications.

Chapter 5

Deposition of Biphasic Calcium Phosphate Film on Laser Surface Textured Ti-6Al-4V and its Effect on Different Biological Properties

5.1 Theme of work

In chapter 3, good bioactivity as well as well adherence was found for all the BCP film having surface roughness varying from 112 – 153 nm. Enhancement in the functionality of the implant is always recommendable for the researchers. From the literature review, it was found that cell and tissue responses not only affect by surface chemistry, but also by surface topography as well as roughness of the implant surface. Many researches have been carried out to improve the biological performances of the implant either modifying the surface chemistry or varying the surface topography. However, very less research is available on simultaneous application of surface chemistry and surface topography for the improvement of implant functionality. Thereby, it is essential to develop an implant having different surface chemistry as well as surface topography to investigate the simultaneous effect of both on the bio-functionality of the implant.

This chapter illustrates the fabrication and characterization of BCP film deposited on different micro-dimpled textured Ti-6Al-4V along with the analysis of protein adsorption, cellular behavior and *in vitro* bioactivity. Initially, the surface micro-topography on Ti-6Al-4V metallic implants was obtained by laser surface texturing with various pulse overlapping factors such as 0%, 25% and 50%. Post texturing, BCP film was deposited on all the textured Ti-6Al-4V which can the nano-topography to the surface of implant. Hence, the surface with micro-/nano-hierarchical structure was developed. The deposition was carried out using RF magnetron sputtering with the same parameters as described in chapter 4. Subsequently, physicochemical, mechanical and biological properties of these films were investigated using various characterization techniques. Surface morphology, elemental analysis and phase composition of different films were studied using FESEM, EDS and XRD, respectively. The surface roughness as well as wettability of different films were investigated using 3-D

surface profilometer and goniometer, respectively. Furthermore, different biological performancec like protein adsorption, cell adhesion and proliferation, *in vitro* bioactivity of different films were investigated. The primary objective of this chapter is to investigate the effect of micro/nano-topography with the BCP film on cellular behavior of the Ti-6Al-4V implant and compared with those on BCP deposited bare Ti-6Al-4V.

5.2 Materials and methods

5.2.1 Materials

BCP target used for RF magnetron sputtering in chapter 3 and 4 was also utilized for this study. Ti-6Al-4V specimens with the same dimension were polished and cleaned with the same procedure as described in section 3.2.2, chapter 3.

5.2.2 Surface modifications

The polished Ti-6Al-4V substrates were first subjected to laser surface texturing followed by RF magnetron sputtering.

5.2.2.1 Laser surface texturing of Ti-6Al-4V

The polished Ti-6Al-4V samples were subjected to pulsed millisecond Nd-YAG laser (M/s Suresh Indu, Accucut-500) having wavelength of 1064 nm and 200 µm focused spot diameter (*D*) in order to fabricate micro-textures on the surface. The laser surface texturing (LST) system used in the study is shown in Figure 5.1. The laser beam with Gaussian intensity distribution was perpendicularly focused on the substrate by using a convex lens of 100 mm focal length. Argon (Ar) gas having pressure of 0.2 MPa was used as assist gas to discard the molten layer from the surface of the specimens. Initially, the influence of main laser parameter such as laser irradiance on the micro-machined geometry was investigated by varying input current (*I*) from 60–80 A and pulse duration (*PD*) from 1.2-1.5 ms. Pulse repetition frequency (*f*) was fixed at 30 Hz and the laser irradiance was determined according to Eq 5.1, (Behera et al., 2017; Behera et al., 2018b).

$$Laser\ irradiance(W/mm^2) = \frac{P_{avg}(W)}{(\pi/4) \times D^2(mm^2)} \qquad (5.1)$$

$$P_{avg} = P_{peak} \times PD \times f \quad (5.2)$$

$$P_{peak} = \eta \times V \times I \quad (5.3)$$

Where, P_{avg} is the average power determined by Eq. 5.2. P_{peak} is the peak power evaluated by Eq. 5.3, where V is the applied voltage of 600 V and η is the efficiency of laser (4%). These experiments were carried out at higher scanning speed (SS = 22 mm/s), so that there was no overlapping between two consecutive laser pulses in a single track. The diameter and depth of the micro-machined hole was measured with non-contact 3D surface profilometer (M/s Taylor Hobson, Talysurf Cclite-6000). In the second stage, LST was carried out with selected laser parameters varying the scanning speed and overlapping distance between two consecutive laser tracks. Scanning speed and overlapping distance were chosen in such a way that the OF such as 0%, 25% and 50% were obtained between two consecutive laser spots as well as lines. The required scanning speed for different overlapping factor was evaluated according to Eq. 5.4 (Sahoo and Masanta, 2015). All these parameters were selected to obtain surface roughness of textured Ti-6Al-4V in between 1-2 µm and to study the effect of surface roughness and topography on protein adsorption as well as cell adhesion. Different parameters used for LST are shown in Table 5.1.

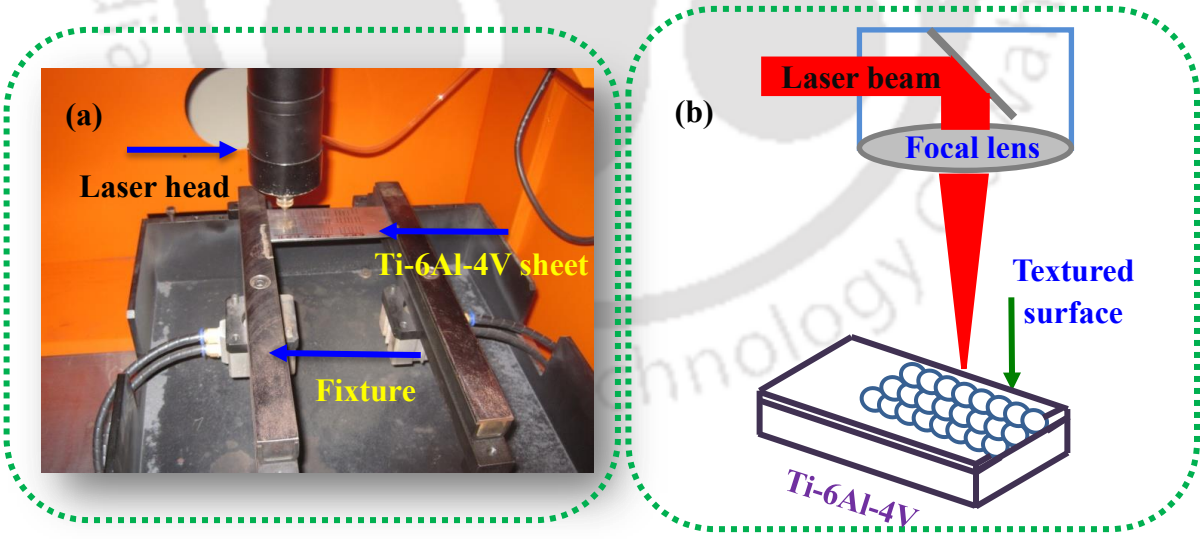

Figure 5.1: *(a) Experimental set up and (b) schematic diagram for laser surface texturing process.*

$$SS\ (mm/s) = f(1/s) \times d(mm) \times (1 - OF/100) \quad (5.4)$$

Where, d is the diameter of selected micro-hole and OF is the overlapping factor. After fabrication of micro-textures having different overlapping factor, all the textured specimens were ultrasonically rinsed with acetone, ethanol and DI water in order to remove the dust particles. The cleaned substrates were used for the further experiments and characterizations.

Table 5. 1: Input process parameters used for laser surface texturing

Input current (*I*), A	60
Pulse duration (*PD*), ms	1.5
Pulse repetition frequency (*f*), Hz	30
Ar gas pressure, MPa	0.2
Stand-off distance, mm	2
Focused spot diameter (D), µm	200
Diameter of selected micro-hole (*Dia*), µm	400
Overlapping factor (*OF*), %	0, 25, 50

5.2.2.2 RF magnetron sputtering of BCP film

The deposition of BCP film on polished as well as micro-textured Ti-6Al-4V was accomplished by RF magnetron sputtering with the same procedure as described in chapter 4. Same parameters used for sputtering in chapter 4 were also used for this study, and these are shown in Table 5.2. The BCP film deposited on bare and different textured Ti-6Al-4V (0% OF, 25% OF and 50% OF) substrates were renamed as BCP-bare Ti-6Al-4V, BCP-(0% OF)Ti-6Al-4V, BCP-(25% OF)Ti-6Al-4V and BCP-(50% OF)Ti-6Al-4V films, respectively throughout the study. Further, some sputtered samples were annealed at 700 °C for 2 h under atmospheric conditions in order to enhance the crystallinity (Prosolov et al., 2017) as well as to study the effect of annealing on different properties. Then the substrates were used for further characterization.

Table 5. 2: Deposition conditions used in present RF magnetron sputtering process

RF sputtering component	**Present study**
Substrate	Bare Ti-6Al-4V (0% OF)Ti-6Al-4V (25% OF)Ti-6Al-4V (50% OF)Ti-6Al-4V
Target	BCP
Base pressure	$3x10^{-6}$ mbar
Working pressure	$3x10^{-2}$ mbar
Sputtering gas	Ar (30 sccm)
Target to substrate distance	50 mm
RF power	30 W
Deposition time	7 h
Substrate temperature	400 °C

5.2.3 Characterization of modified surfaces

5.2.3.1 Measurement of surface topography

Different surface features (surface roughness, cross-sectional profile and 3-D topography) of polished as well as textured Ti-6Al-4V were analyzed using non-contact 3-D surface profilometer. The instrument was equipped with a 20X lens having 4.7 mm focal length. 850 × 850 μm^2 area was initially scanned and then a particular line was drawn in a direction along the laser scanned line to estimate the roughness (R_a) of the surface. The geometrical parameters such as pitch (P), depth (h) and diameter (d) were measured from the surface profile of the micro-dimpled texture. The average of three different values was considered as final output in the study. These parameters were further used for determining the aspect ratio (λ) and roughness factor (R_f), which are related to wettability of the surface. Aspect ratio (λ) is defined to be the ratio of micro-texture depth to diameter of micro-texture; whereas, roughness factor (R_f) is the ratio of actual surface area and projected area of micro-dimpled texture. λ and R_f are calculated using Eq. 5.5 and 5.6, respectively (Pratap and Patra, 2018b;

Wang and Bai, 2015). Since the laser beam had distributed with Gaussian intensity; hence, conical shaped micro-structure produced which can be seen in Figure 5.3.

$$\lambda = \frac{h}{d} \tag{5.5}$$

$$R_f = \frac{P^2 - \pi r^2 + \pi r\sqrt{r^2 + h^2}}{P^2} \tag{5.6}$$

Where, r is the radius of micro-dimpled texture.

5.2.3.2 Phase, elemental analysis and surface morphology

The phase compositions present on the surface of the samples were investigated by XRD analysis. The results were interpreted with the database of crystallographic structures (HA - JCPDS 09-0432, β-TCP - JCPDS 09-0169), TiO_2 (rutile) - JCPDS 211276 and Ti - JCPDS 441294). The surface morphology of BCP film deposited on polished and textured Ti-6Al-4V was distinguished by FESEM instrument with the magnification of 5-50 kX. EDS was used to analyze the elements present in the BCP film deposited on the polished and textured Ti-6Al-4V. The roughness and wettability of BCP film deposited on polished as well as textured surfaces were evaluated using non-contact 3-D surface profilometer and goniometer as reported previously in section 3.2.5.2, chapter 3.

5.2.4 Biological studies

Protein adsorption, cell adhesion, cell proliferation and *in vitro* bioactivity of BCP deposited bare and textured Ti-6Al-4V were performed by same protocol illustrated in section 4.2.6.1 - 4.2.6.4, chapter 4.

Statistical analysis

The experiments were conducted in triplicate and the results have been reported as the mean ± standard deviation for n = 3 at least. To determine the statistically significant differences ($p < 0.05$ (#) and $p < 0.005$ (##)) SigmaPlot version 14.0 was used with one-way analysis of variance (ANOVA).

5.3 Results and discussion

5.3.1 Surface modification of Ti-6Al-4V

5.3.1.1 Surface topography of micro-dimpled textures

The 3-D topography and 2-D cross-sectional view of non-textured and micro-dimpled textures are represented in Figure 5.2. The different geometrical features of the micro-dimpled texture such as pitch (*P*, horizontal distance between the centers of two consecutive micro-dimples), diameter (*d*, maximum horizontal distance at the top of micro-dimple) and depth (*h*, vertical distance between the bottom and top of the micro-dimple) are measured from the cross-sectional images, shown in the Figure 5.2. The average value of all the dimensions is reported in Table 5.3. The aspect ratio (λ) and roughness factor (R_f) are calculated using Eq. 5.5 and 5.6, respectively (Table 5.3). It was clearly observed from Figure 5.2 and Table 5.3 that with the increase in percentage overlapping, the *P*, *h* and *d* decreased. It is obvious that with increase in overlapping of micro-dimple, the center of micro-dimples come closer to each other, decreasing the *P* and *d*. Again, the overlapping portions of the adjacent micro-dimples got remelted, resulting decrease in the height of the micro-dimple. The λ increased with the increase in overlapping percentage of the micro-dimpled texture due to significant decrease of the diameter of the micro-dimple compared to decrease of depth with the overlapping.

It was also seen from Table 5.3 that the R_f is higher for micro-dimpled texture having 50% OF compared to others textured surfaces. Pratap and Patra (2018a) also found increase in R_f with increasing overlapping percentages in parallel micro-textured surfaces fabricated by ball end micro-milling process due to decrease in *P* as well as with increase in *h*, individually. Though *h* decreased in the present study with increase in OF%; however, R_f increased due to increase in *P*, indicating dominancy effect of pitch compared to the depth on the R_f of the micro-dimpled texture surface. The surface roughness (R_a) of the bare and laser textured specimens are represented in Figure 5.2 and Table 5.3. Though the average surface roughness of bare Ti-6Al-4V was in nanometer range, i.e. 94 nm, the textured substrate had R_a in micrometer range, and this R_a was increased from 0.98 µm to 1.84 µm with an increase in OF from 0% to 50%. Due to an increase of OF, the frequency of laser interaction increases, this generates waves and pits on the surface of molten Ti-6Al-4V after

solidification. This caused attachment as well as the incursion of other molecules to the surface of metal easily. Hence, the R_a increased, which may enhance the grip to retain the BCP particles deposited on the textured surface.

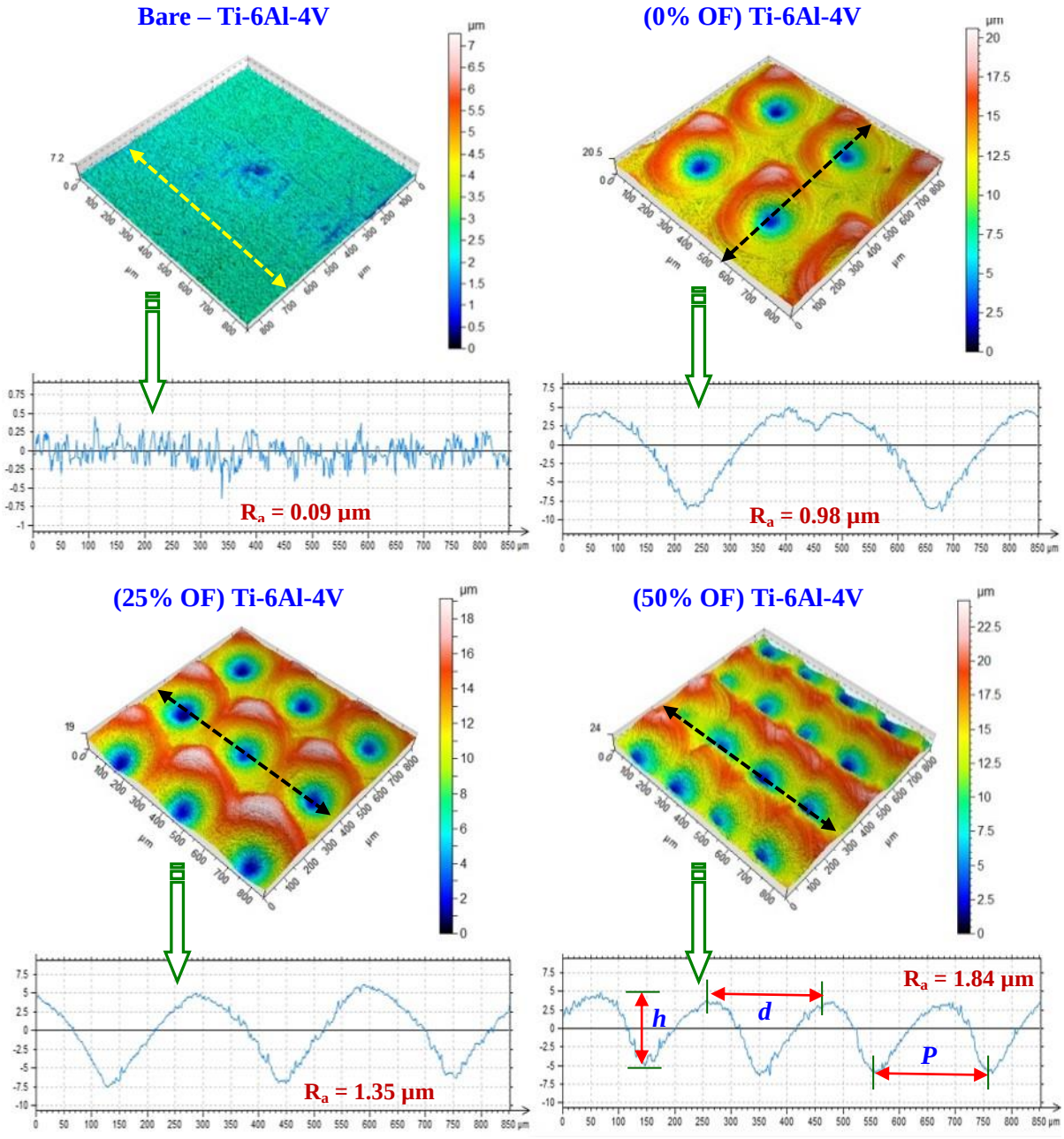

Figure 5.2. *3-D topography and corresponding 2-D surface profiles of bare and LST specimens with different overlapping factors 0%, 25% and 50%.*

Higher R_a value for the textured surface with higher overlapping factor was also found by Stango et al. (2018) during texturing of metal specimens. It was also observed that

the R_f also follows similar trend with R_a due to decrease in pitch values. Similar observations of increasing surface roughness with decreasing in pitch was also found by Pratap and Patra (2018a) for staggered and parallel textured surfaces fabricated using ball end micro-milling process. In addition, the micro-dimple density (number of micro-dimples per unit area) is increased with increasing the overlapping factor.

Table 5. 3: Geometry of the micro-dimple textured surfaces

Surface condition of Ti-6Al-4V	**Micro-dimple textured surface geometrical parameters**					
	P **(µm)**	***h*** **(µm)**	***d*** **(µm)**	**$\lambda = h/d$**	**R_f**	**R_a** **(µm)**
Bare	-	-	-	-	-	0.09±0.02
0% OF	360.78±8.49	12.77±0.39	338.89±11.15	0.037	1.001965	0.98±0.09
25% OF	288.64±4.31	10.89±0.31	272.17±5.40	0.040	1.002232	1.35±0.13
50% OF	204.13±2.76	9.36±0.44	203.41±4.01	0.046	1.003295	1.84±0.17

5.3.1.2 Phase and elemental composition of micro-dimpled texture surfaces after BCP sputtering

The thickness of the BCP film was found to be 540 ± 19 nm on the bare Ti-6Al-4V, as measured using a stylus profilometer (M/s Vecco Dektak 150). The compositional phases of RF sputtered film on laser textured Ti-6Al-4V at different OF (0%, 25% and 50%) are demonstrated in Figure 5.3 (a). The XRD spectra of sputtered film on different textured Ti-6Al-4V find peaks of β-TCP, HA and TiO_2 (rutile). The presence of HA and β-TCP peaks in all the textured substrates confirms the deposition of BCP films on the textured substrates. This is attributed to the sputtering technique that usually deposits a film of the same stoichiometry as the target (Das et al., 2018). However, TiO_2 (rutile) phase formed in all the textured substrates due to entrapping of oxygen into molten Ti-6Al-4V during LST. TiO_2 (rutile) phase is generated instead of TiO_2 (anatase) due to the high-temperature laser beam. Moreover, the TiO_2 (rutile) phase improved with an increase in OF. Increased interaction of

laser beam occurred at a higher OF, which resulted more melting and entrapped larger oxygen content into the molten Ti-6Al-4V and in-turn more TiO_2 formation. The apparent crystallite sizes of the BCP films deposited on textured Ti-6Al-4V having 0%, 25% and 50% OF were determined using Scherrer equation in XRD spectrum and are found to be 24.96 ±1 nm, 27.21 ±1 nm and 26.76 ±1 nm, respectively. It indicates that surface texturing has no significant effect on the crystallite size.

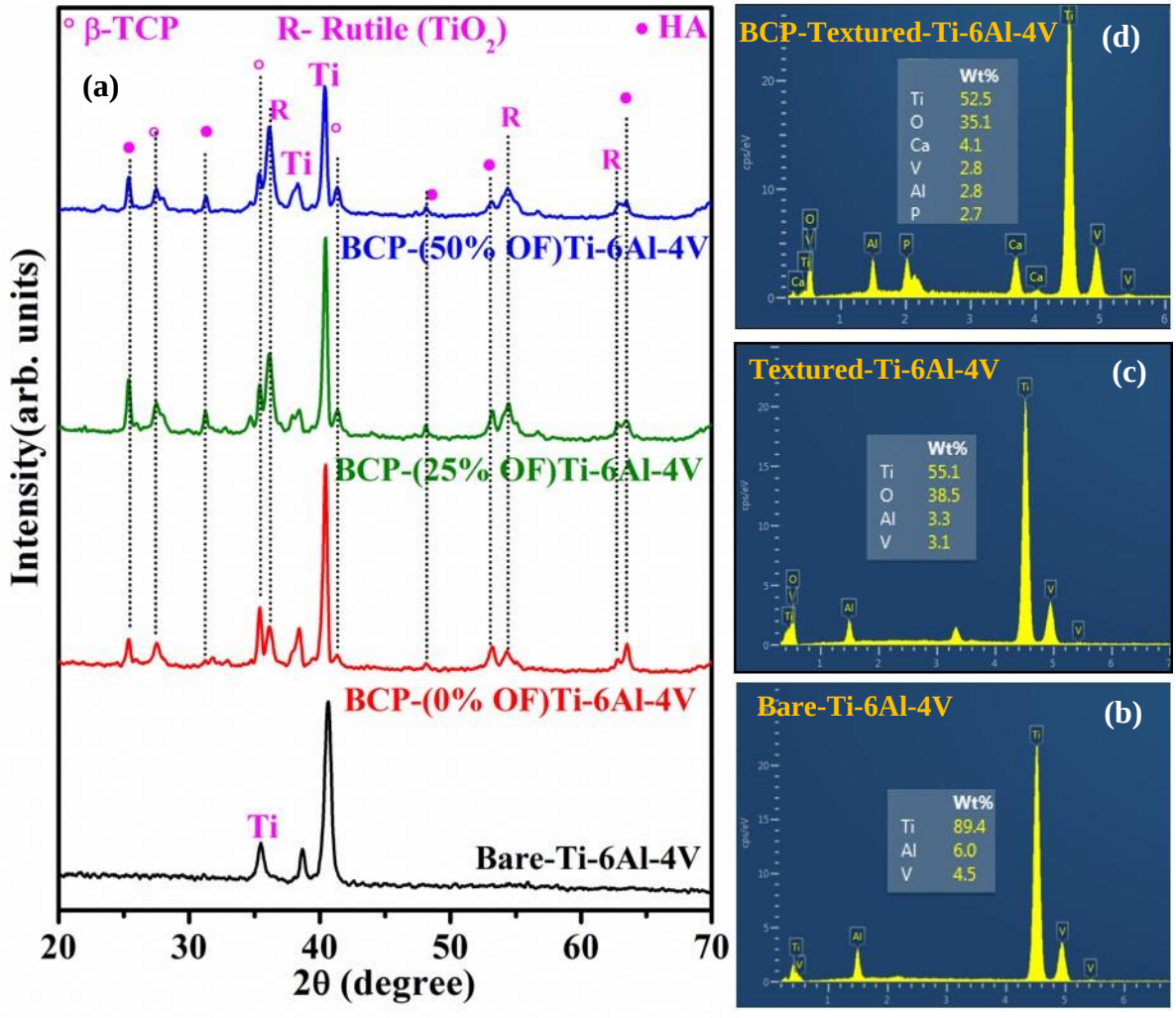

Figure 5.3. *Phases found in (a) BCP films deposited on laser textured Ti-6Al-4V specimens at different overlapping factors; elemental analysis of (b) bare Ti-6Al-4V, (c) textured Ti-6Al-4V and (d) BCP-coated-textured Ti-6Al-4V.*

The EDS analyses of bare, textured and BCP-coated-textured Ti-6Al-4V specimens are shown in Figure 5.3 (b), (c) and (d), respectively. There was no oxygen present in the bare specimen (Figure 5.3 (b)); however, a significant amount of oxygen content was

observed in all laser textured Ti-6Al-4V (Figure 5.3 (c)). The oxygen content was 32.6% in the laser textured sample with 0% OF, and it further enhanced to 35.7% and 38.5% for textured samples with 25% and 50% OF, respectively (Figure 5.4). This complemented the above discussed XRD data. A similar observation was also seen in laser peened stainless steel and Ti alloy (Stango et al., 2018). The presence of Ca, O and P with the Ti, Al and V confirms deposition of calcium phosphate film on the textured Ti-6Al-4V (Figure 5.3 (d)). However, there was no effect of different OF on different elements can be seen, as the same BCP deposited on all the textured specimens.

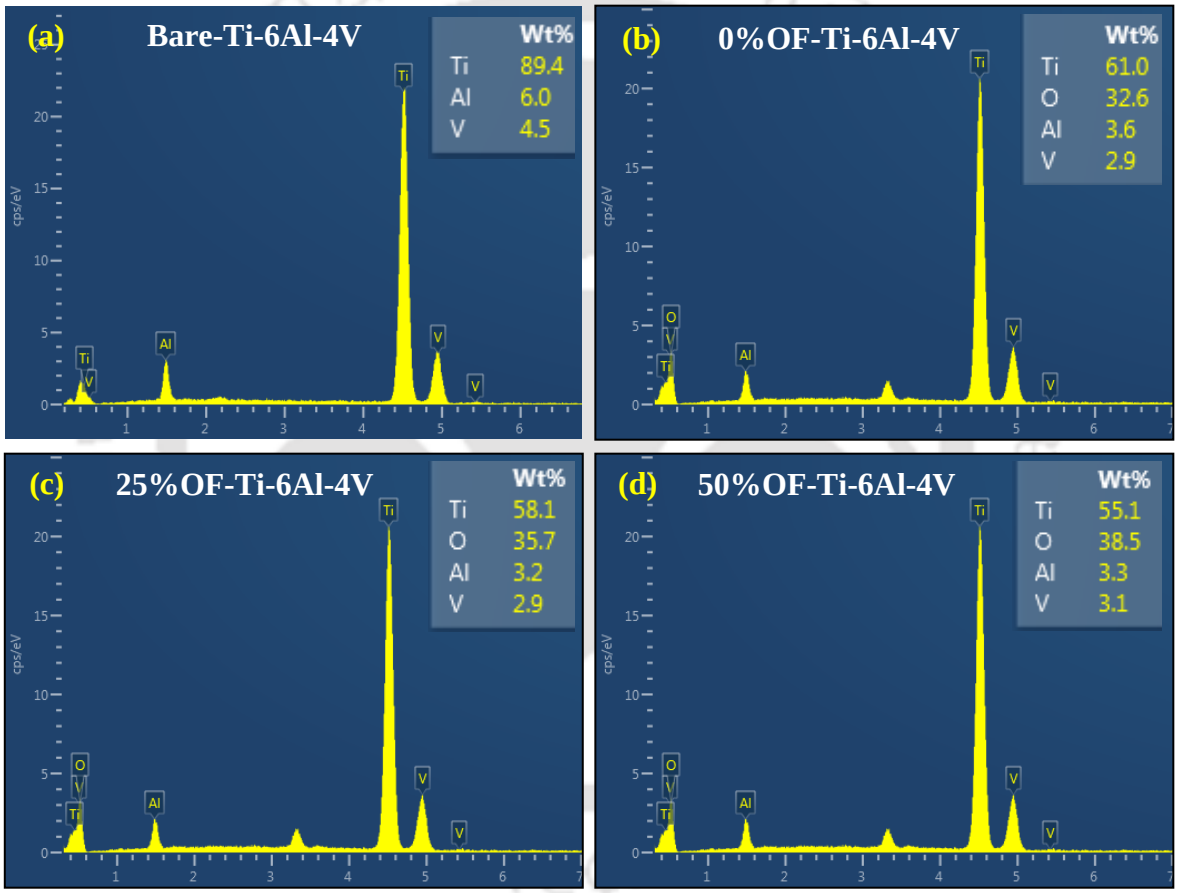

Figure 5.4. *Elemental analysis of (a) bare Ti-6Al-4V and laser textured specimens at different overlapping factor (b) 0%, (c) 25% and (d) 50%.*

5.3.1.3 Surface morphology of micro-dimpled texture surfaces after BCP sputtering

The surface morphology of BCP sputtered textured and non-textured Ti-6Al-4V specimens are shown in Figure 5.5. Clear patterns of mico-dimpled textures with 0%, 25% and 50% spot overlapping are seen in Figure 5.5 (b), (c) and (d), respectively. It was observed that at a

lower magnification (macro level) that, the patterns of micro-dimple textures were not changed after sputtering (120X zoom images of Figure 5.5). The micro-dimple dimensions were in hundreds of microns and the coating thickness was in nanometers range. Hence, the pattern dimensions remained almost same after BCP film deposition. Furthermore, it was seen at a higher magnification (micro level) that the BCP film on the bare Ti-6Al-4V had smooth and uniform surface; however, rough and non-uniform surface was observed in the BCP-coated-textured Ti-6Al-4V (5 kX zoom images of Figure 5.5).

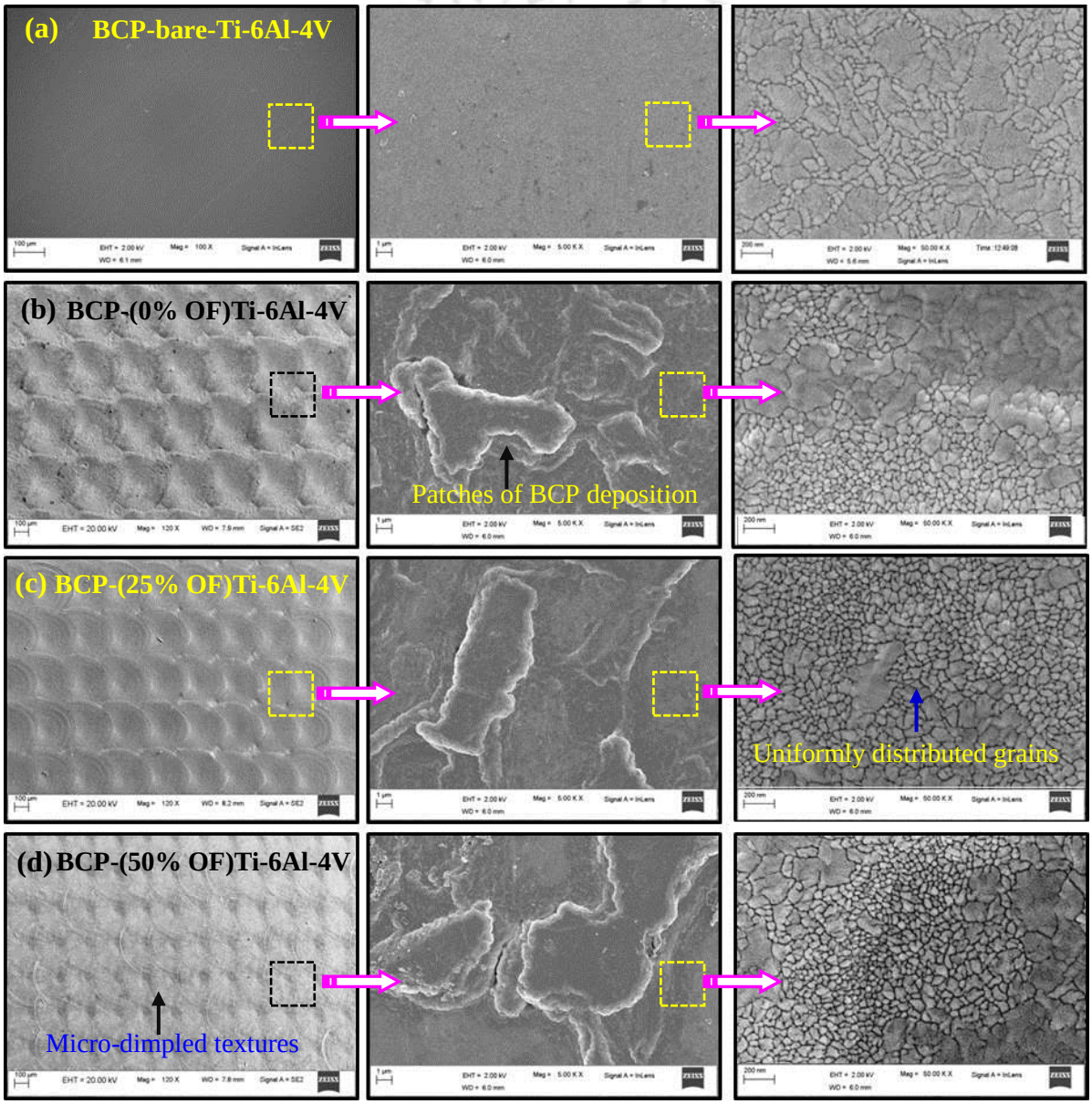

Figure 5.5. *Surface morphology of BCP film sputtered on (a) bare Ti-6Al-4V, (b) 0% OF-Ti-6Al-4V, (c) 25% OF-Ti-6Al-4V and (d) 50% OF-Ti-6Al-4V specimens.*

BCP films were deposited in small patches throughout the surface of textured Ti-6Al-4V. This can be attributed to the textured surface, which causes the distance between the substrate and target to be non-uniform, and hence, particles from the target could not be deposited uniformly on the substrate surface during sputtering. Again, at the higher magnification (nano level), bigger as well as smaller nano-particles were seen, which were uniformly distributed over the surface of BCP deposited textured as well as non-textured Ti-6Al-4V (50 kX zoom images of Figure 5.5). Similar types of surface morphology (uniformly distributed grains) was also observed by Surmenev et al. (2011) and Behera et al. (2018a). After BCP sputtering, the R_a of the bare-Ti-6Al-4V, 0%OF-Ti-6Al-4V, 25%OF-Ti-6Al-4V and 50%OF-Ti-6Al-4V was found to be 0.14±0.03 µm, 1.12±0.08 µm, 1.61±0.20 µm and 2.07±0.22 µm, respectively. It can be observed that the roughness increases after deposition BCP film on the textured surfaces. This is attributed to presence of non-uniformly distributed BCP patches on the textured surfaces (5 kX zoom images of Figure 5.5).

5.3.1.4 Wettability of the micro-dimpled texture surfaces

The wettability of bio-implant surface exhibits a vital role in protein adsorption, bioactivity, cell adhesion and proliferation (Sun and Huang, 2018; Xia et al., 2018). Further, the wettability of the surface mainly depends upon chemistry and topography of that surface (San Thian et al., 2011; Sun and Huang, 2018). The wettability at different surface conditions of Ti-6Al-4V is manifested in Figure 5.6. The SBF contact angle on bare Ti-6Al-4V was observed to be 89º(±1º); however, for textured substrates it decreased to 77°(±2º), 74°(±1º) and 71°(±2º) for 0%, 25% and 50% OF, respectively indicating enhancement of hydrophilicity with micro-dimpled surface texturing. This is attributed to the surface texturing, which formed micro-dimples on Ti-6Al-4V surface. So, the overall R_f increases compared to non-textured Ti-6Al-4V causing improvement in hydrophilicity. In addition, it was found that the contact angle further reduces with an increase in OF from 0% to 50%. As the R_f is determined by the different geometry of the micro-texture; hence, these dimensions play a crucial role on the wettability. The reduction of pitch and depth of micro-dimpled textures with the increase in OF decreased the contact angle. Pratap and Patra (2018a) also found decrease of contact angle with the reduction of pitch and increase of the depth of the micro-dimpled texture. Instead of lower depth of 50% OF textured substrate, the wettability

was better among all the different configurations of textured Ti-6Al-4V, as shown in Figure 5.6. This is attributed to higher R_f, which allows the SBF droplet to interact more with the textured substrates and hence decreases the contact angle by increasing the drop width and reducing the drop height. As per Wenzel's equation is concerned, the increase in roughness factor results in reduction of contact angle and improves the hydrophilicity of surfaces (Quéré, 2008).

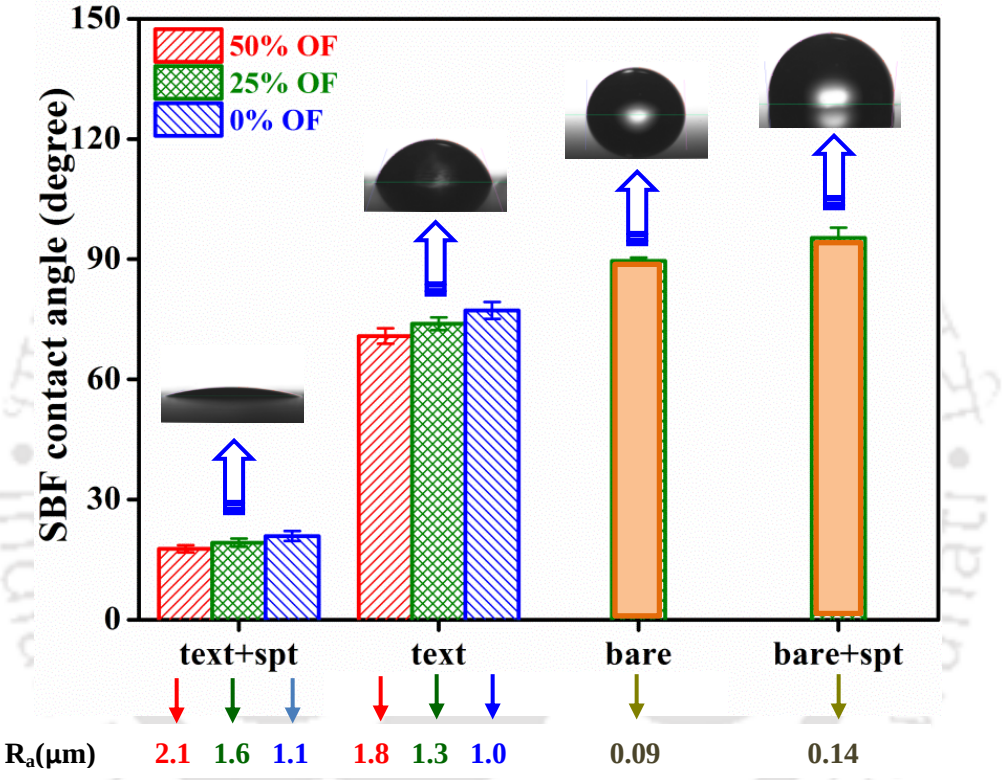

Figure 5.6. *SBF contact angles on different surface conditions of Ti-6Al-4V.*

Furthermore, it was also found that the wettability improves with the increase in the R_a. This is believed that the higher R_a value provides extra contacting area to interact with the droplet to spread more (Hosseinabadi et al., 2018; Majeed et al., 2015; Pratap and Patra, 2018a). Hence, wettability improves with the enhancement in surface roughness, which increases with the OF of micro-dimpled texture. Moreover, the formation of surface oxide (TiO_2) during laser texturing process, and the increment of oxide with the OF (Figure 5.4) improve the wettability of the surface. The improvement of wettability with the TiO_2-containing layer fabricated by laser process was reported by Sadeghi et al. (2019). In

addition, with the BCP film deposition, the textured Ti-6Al-4V behaved as super hydrophilic surface as the range of contact angle of surfaces decreased from 70-77º to 17-21º, indicating a significant improvement of hydrophilicity, after BCP film deposition.

This can be due to the presence of phosphate (PO_4^{3-}) and hydroxyl (OH^-) negative ions in BCP, which significantly attract the electro-positively-charged (H^+) ions from the SBF solution (Thian et al., 2005). Hence, BCP film deposited on textured surface exhibited super-hydrophilicity due to simultaneous involvement of surface chemistry and surface topography on Ti-6Al-4V. On the other hand, instead of hydrophilic BCP deposition on non-textured Ti-6Al-4V, the surface showed hydrophobicity with contact angle of 95°(±3º). This is attributed to deposition of nano-sized grains with nano-roughness of the film (R_a = 142 nm) and positive skewness (0.292) (Figure 4.5 (a), 4.6 (a), chapter 4), which prevent the SBF droplet to spread (Surmeneva et al., 2016). All the results indicate that the wettability of the surface is directly influenced by chemical composition, surface roughness and topography, as reported in previous studies (Mirhosseini et al., 2007; Sadeghi et al., 2019).

5.3.3 Biological studies

5.3.3.1 Protein adsorption

In the present study, BCP film on bare and textured Ti-6Al-4V was explored to understand the role of wettability and surface topography on FBS protein adsorption. Figure 5.7 represents the adsorbed mass of protein on different surface conditions, determined by BCA assay. Higher mass of adsorbed protein (5.32 ± 0.14 - 7.11 ± 0.30 µg/cm^2) was obtained for all the modified surfaces compared to bare Ti-6Al-4V (2.83 ± 0.15 µg/cm^2), which is because of the protein binding groups such as Ca^{2+}, PO_4^{3-} and OH^- in BCP film. PO_4^{3-}/OH^- bind positive amino groups, whereas Ca^{2+} binds with negative carboxylates groups of protein (Wang et al., 2012). Thus, hydrogen bonding as well as electrostatic interaction occurs between protein and surface, resulting in higher adsorbed mass on BCP-bare Ti-6Al-4V. It was further noticed from Figure 5.7 that the adsorbed protein mass directly varies with surface hydrophobicity. Hasan et al. (2018a) also reported the increase of FBS adsorbed amount with increase in hydrophobicity. As albumin is the major constituent of FBS, it exhibits albumin-like adsorption behavior with respect to hydrophobicity (Hasan et al., 2018a; Pandey and Pattanayek, 2013a; Pandey et al., 2013). It is a well-known fact that

proteins have a very high tendency to adsorb on hydrophobic surfaces due to the availability of hydrophobic patches in its structure. Therefore, due to hydrophobic interaction protein unfolds and spreads its hydrophobic cores over the surface causes higher protein adsorption (Wang et al., 2012). Hence, the FBS adsorption was found to be higher for BCP-bare-Ti-6Al-4V due to the hydrophobicity (CA=95°). In addition, FBS is a mixture of serum proteins having the size in nanometer domain; hence the nano-roughness of the BCP-bare-Ti-6Al-4V (R_a = 142 nm) provides a significant spatial effect to the protein adsorption, which results in a higher mass of FBS protein.

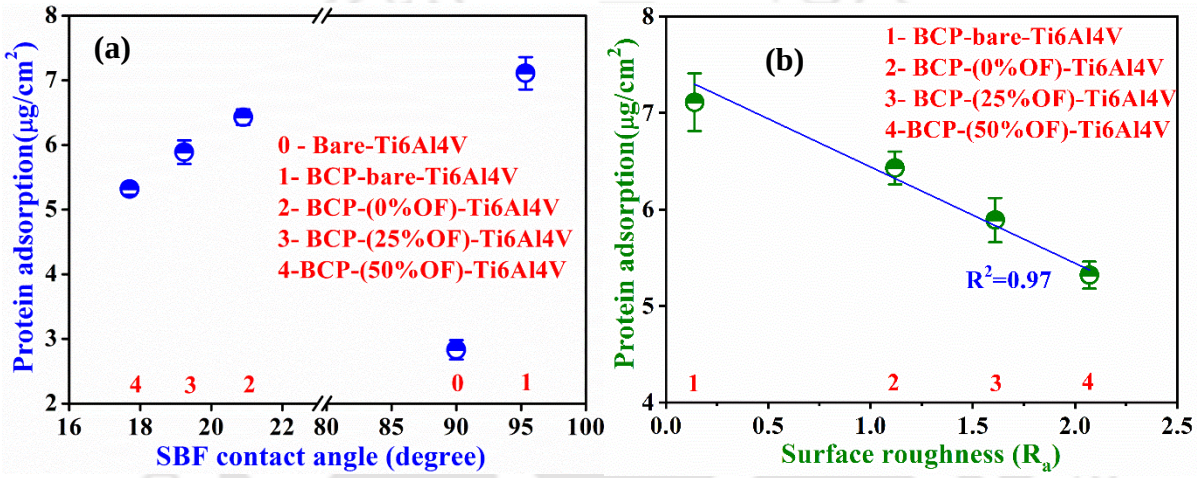

Figure 5.7. *Adsorbed protein mass as a function of (a) contact angle and (b) surface roughness.*

On the other hand, the adsorbed protein mass on the surface of BCP-textured-Ti-6Al-4V was found lesser as compared to BCP-bare-Ti-6Al-4V. Due to hydrophilic behavior of BCP-textured-Ti-6Al-4V (CA = 17°-21°), these surfaces showed lesser FBS adsorption. In addition, the micro-roughness of BCP-textured-Ti-6Al-4V (R_a = 1.12 - 2.07 µm) exhibited the smooth topography to the nano-sized protein, thus comparatively less effect on protein adsorption (Wang et al., 2012). With the increase in OF of micro-dimpled textures, the protein adsorption decreases in spite of increasing surface roughness. This may be due to an increase in micro-surface roughness with OF; the surface became more smooth for the proteins to adsorb.

Table 5.4 represents the SBF contact angles on BCP sputtered bare as well as textured Ti-6Al-4V surfaces prior to and after FBS protein adsorption. Post FBS adsorption, the hydrophobic BCP-bare-Ti-6Al-4V became super-hydrophilic (CA ≈ 29°); whereas, the

contact angle of BCP-textured-Ti-6Al-4V surfaces increased to moderately hydrophobic (CA ≈ 50-80º), indicating the formation of protein layer (Sharma and Pattanayek, 2017). Protein adsorption occurs due to electrostatic as well as the hydrophobic interaction between surfaces and proteins. The macroscopic properties (surface energy) and microscopic topographies vary after protein adsorption, due to the different chemico-physical properties of various modified surfaces, which regulate the protein packing and their behavior (Sharma and Pattanayek, 2017). Therefore, different surfaces showed the different SBF contact angle after protein adsorption.

Table 5. 4: SBF contact angles on the surface of BCP films sputtered on non-textured and textured Ti-6Al-4V without and with FBS protein adsorption.

	Contact angle, CA (º)	
Surface condition	**Without FBS**	**With FBS**
BCP – bare Ti-6Al-4V	95 ± 3	29 ± 1
BCP-(0% OF)Ti-6Al-4V	21 ± 1	55 ± 2
BCP-(25% OF)Ti-6Al-4V	19 ± 1	53 ± 1
BCP-(50% OF)Ti-6Al-4V	17 ± 1	59 ± 2

5.3.3.2 Cell adhesion and proliferation

Osteoblast-like cells (MG63) were used to analyze cellular responses of different modified surface for bone tissue regeneration. FESEM images were acquired after 24 h of incubation to study the morphology, and adhesion behavior of attached MG63 cells on BCP film sputtered on bare as well as textured Ti-6Al-4V. The cell morphology and cell density are shown by the lower magnification images (Figure 5.8 (a-c)), whereas the adhesion behavior of cells is displayed in the higher magnification images (Figure 5.8 (d-f)) on different modified surfaces. It was observed that bare Ti-6Al-4V exhibits with very less number of round shaped cells, indicating less spreading on the surface (Figure 5.8 (a)). Polygonal-shaped cells with high numbers are observed on the surface of BCP-bare Ti-6Al-4V, indicating well spreading of the cells (Figure 5.8 (b)). Furthermore, well-flattened cells with high cell density are prominently distributed throughout the surface of BCP-textured Ti-6Al-4V (Figure 5.8 (c)). This indicates strong adherence of cells with BCP film deposited on bare

as well as textured Ti-6Al-4V compared to non-textured non-coated Ti-6Al-4V. The cell adhesion behavior of MG63 cells on bare Ti-6Al-4V as well as different modified surfaces was studied by analyzing the higher magnification FESEM images (Figure 5.8 (d-f)).

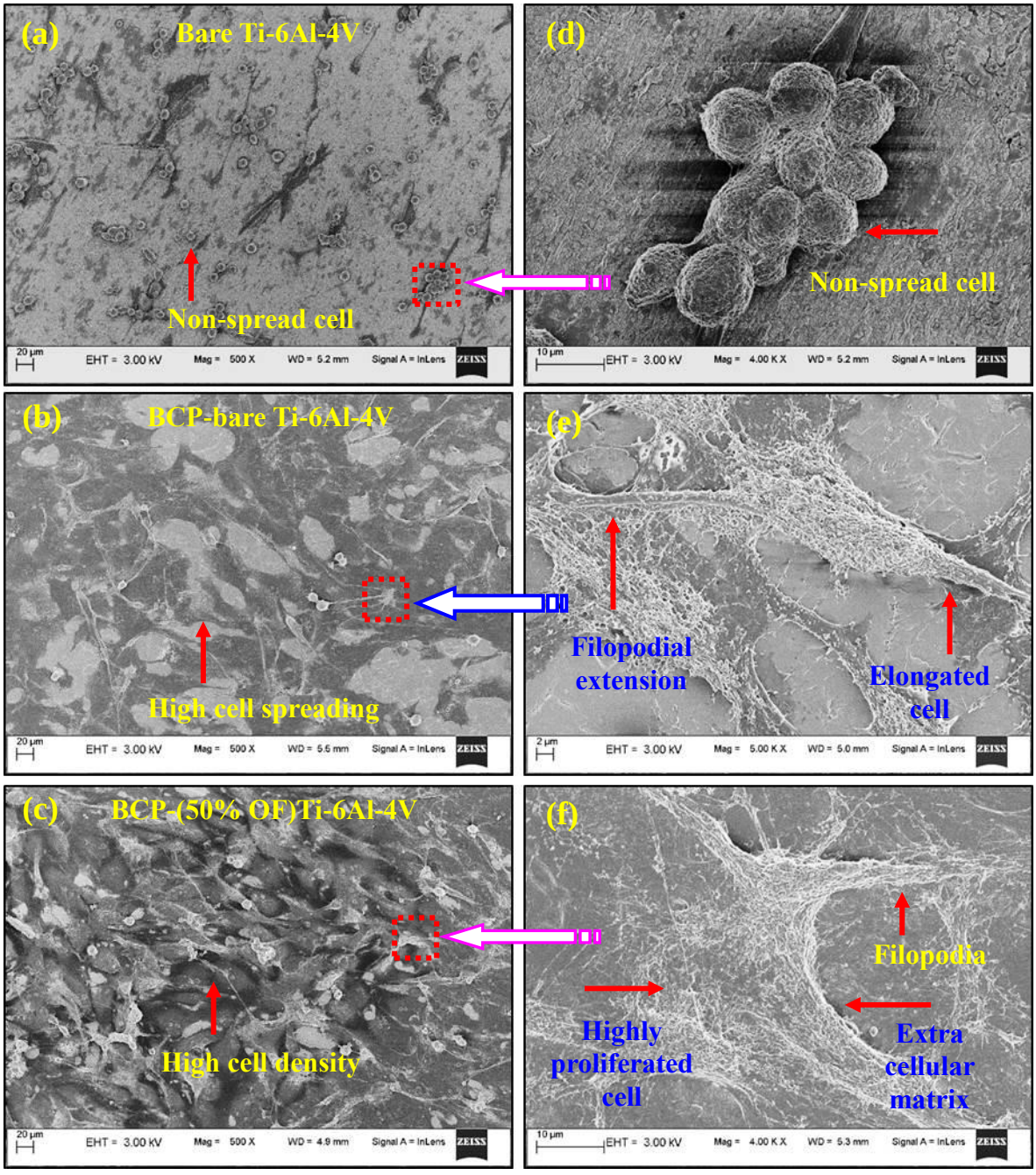

Figure 5.8. *Morphology of MG63 cells after 24 h of proliferation on bare Ti-6Al-4V, BCP - bare Ti-6Al-4V and BCP-(50% OF)Ti-6Al-4V surfaces: (a, b, c) lower magnification and (d, e, f).higher magnification.*

The groups of round cells on bare Ti-6Al-4V indicate less spreading and adhesion (Figure 5.8 (d)). As shown in Figure 5.8 (e), elongated cell with longer filopodial extensions is observed on BCP sputtered bare Ti-6Al-4V, indicating spreading and intimacy of the osteoblast to the surface (Li et al., 2012). Highly proliferated cells with extracellular matrix (ECM) is manifested on BCP-(50% OF)Ti-6Al-4V (Figure 5.8 (f)), revealing the synergy of reinforcements with the surface (Pandey et al., 2018). Due to the formation of filopodial extension and interaction with the cells in the surrounding ECM formation occurs (Pandey et al., 2018). All these features such as filopodial extensions, cell-to-cell connectivity and ECM formation indicate the superior cyto-compatibility of the modified surfaces.

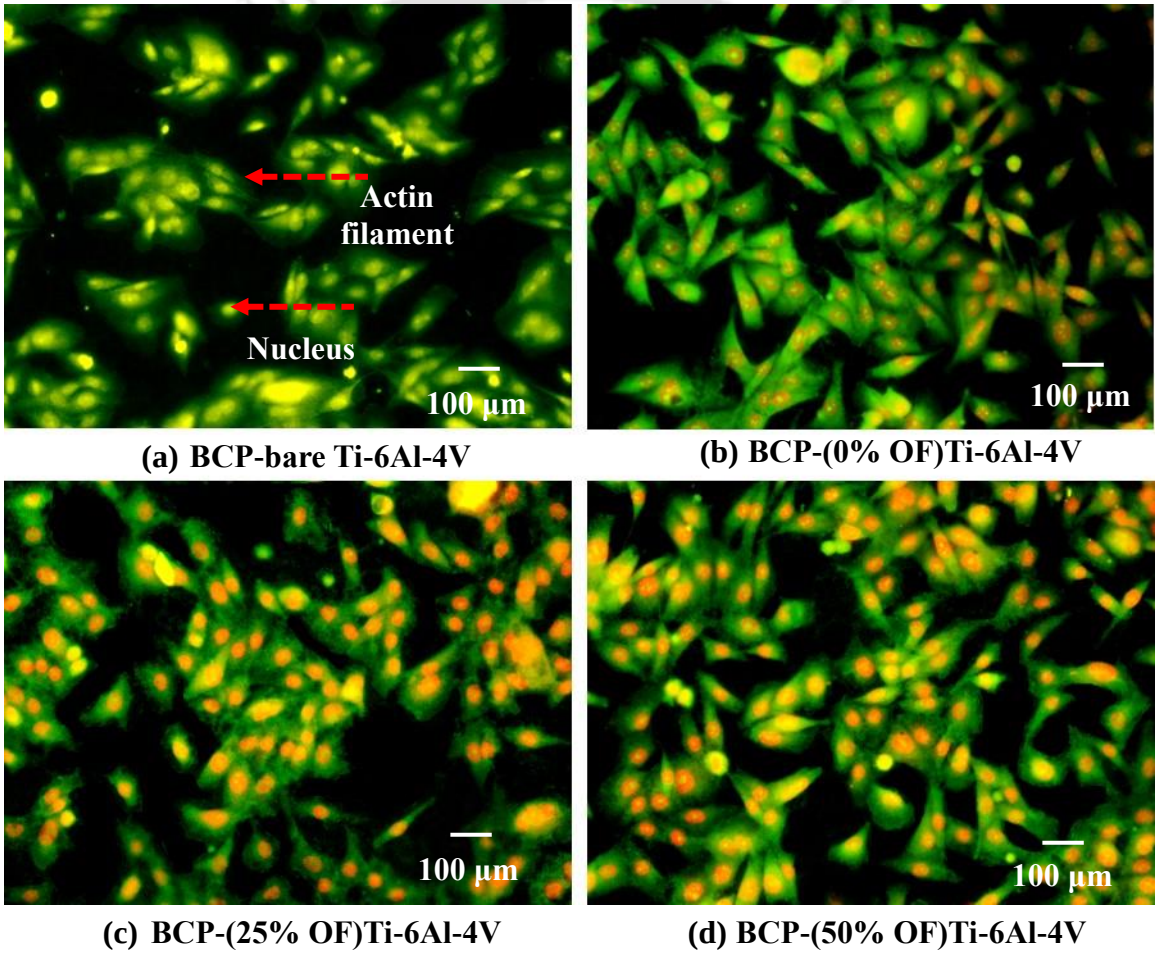

Figure 5.9: *Fluorescent images of MG63 cells adhered on the surface of (a) BCP-bare Ti-6Al-4V, (b) BCP-(0% OF)Ti-6Al-4V, (c) BCP-(25% OF)Ti-6Al-4V and (d) BCP-(50% OF)Ti-6Al-4V after 12 h, showing the nucleus (red) and actin filaments (green).*

The above findings were also confirmed by fluorescence microscopy study and quantitative analysis of different cell features such as percentage of cell adhered, nuclei area,

average cell spreading area and circularity. The fluorescent imaging of MG63 osteoblast cells after culturing for 12 h on different sputtered surfaces are presented in Figure 5.9. Actin filaments (green color) and nuclei (red color) are used for analyzing the adhesion behavior of the osteoblast cells on the modified surfaces, as previously reported by our group (Behera et al., 2018b; Hasan et al., 2018b). The effect of surface texturing with BCP film on regulation of cell adhesion and spreading for better osteointegration is illustrated in this study.

Lesser number of spherical cells with less spreading was seen on the surface of bare Ti-6Al-4V (Figure 4.16, chapter 4). However, well spread-flattened cells are seen on the surface of BCP-bare-Ti-6Al-4V (Figure 5.9 (a)) as well as BCP-textured-Ti-6Al-4V (Figure 5.9 (b-d)). These observations complemented FESEM data (Figure 5.8). This phenomenon is due to the presence of biocompatible phases like HA and β-TCP on Ti alloy surface, enhances the protein adsorption on the modified surfaces (5.32 ± 0.14 - 7.11 ± 0.30 μg/cm^2) in comparison to the bare Ti-6Al-4V surface (2.83 ± 0.15 μg/cm^2). These protein acts as a cushion for the cells to be adhered, resulting in more spreading and adherence of osteoblasts (Hasan et al., 2018a). Furthermore, it is noticed that all the BCP-textured-Ti-6Al-4V surfaces exhibited with larger actin filaments (Figure 5.9 (b-d)) than that of BCP-bare-Ti-6Al-4V (Figure 5.9 (a)), indicating higher cell adhesion and growth capability.

The super-hydrophilic (17-20º), as well as the highly roughened (1.12 - 2.07 μm) surfaces of the BCP deposited textured film provide a more compatible structure to the osteoblasts to spread and adhere (Ahn et al., 2012). An improvement in adhesion and proliferation of fibroblast with the enhancement of surface wettability was also observed by Altankov et al. (1996) and Sadeghi et al. (2019). The increase in surface energy and surface roughness also enhanced the cell attachment and proliferation, as reported by Mirhosseini et al. (2007). Moreover, the size of MG63 cells varied in the range of 50-200 μm which was less than the size of the micro-dimples in the micro-textured surface (Figure 5.8). Thus, the number of cells adhered to the substrate increased. Again, these micro-dimples provided higher surface area to avail more serum proteins and medium for the cell spreading and growth compared to nano-rough hydrophobic BCP-bare-Ti-6Al-4V film (Li et al., 2012). Hence, higher cells spreading and growth occurred in BCP-textured-Ti-6Al-4V than BCP-bare-Ti-6Al-4V. Furthermore, it can be noticed that, among the BCP-textured-Ti-6Al-4V specimens, BCP-(50% OF)-Ti-6Al-4V had higher number of cell with larger cell spreading.

This increased with increase in the OF. Because of increase in R_a and R_f with the rise in OF, more interaction occurs between the cells and surface because of enhanced surface area. Hence, better cell behavior was observed on the BCP-(50% OF)-Ti-6Al-4V in comparison to the other textured surfaces.

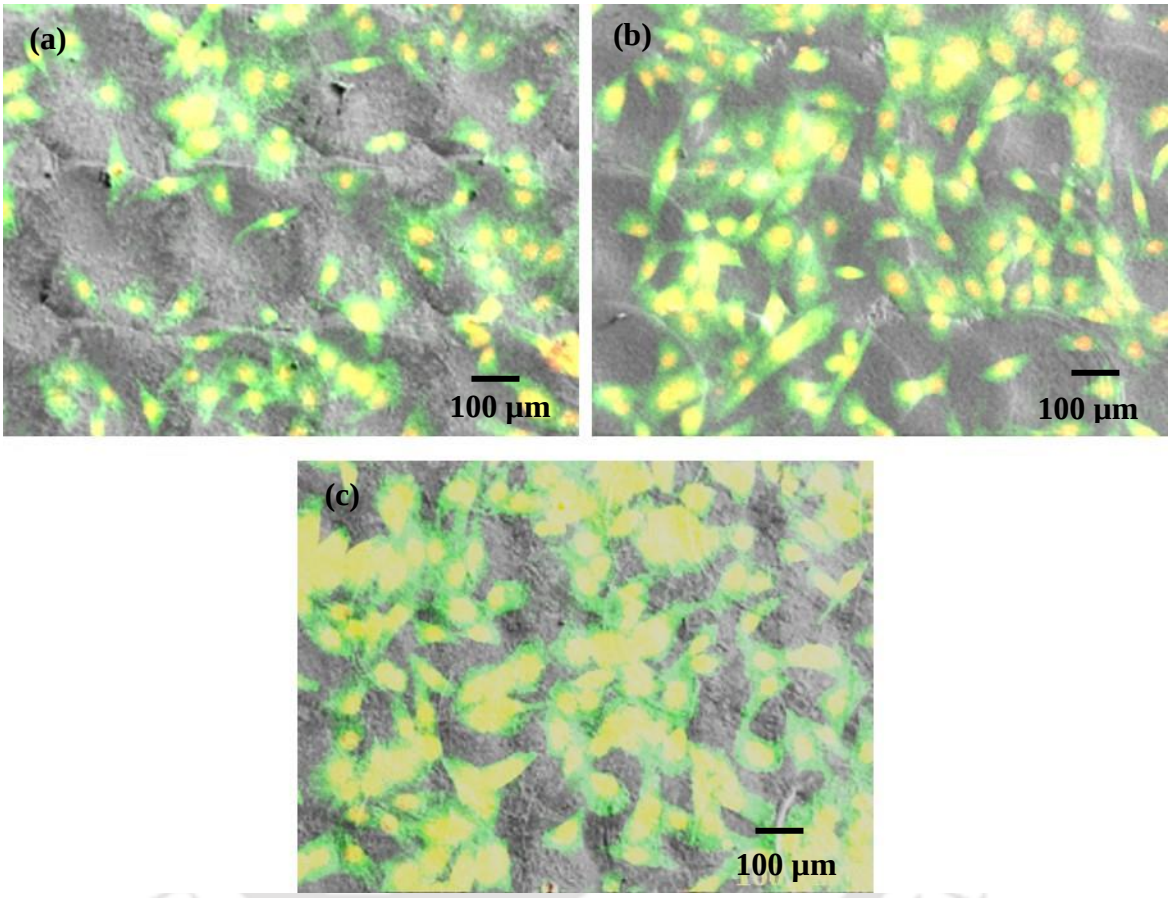

Figure 5.10: *Distribution of MG63 cells on the BCP sputtered micro-dimpled texture surfaces: (a) BCP-(0% OF)Ti-6Al-4V, (b) BCP-(25% OF)Ti-6Al-4V and (c) BCP-(50% OF)Ti-6Al-4V after 12 h of cell culture.*

Figure 5.10 shows the distribution of MG63 cells on the BCP deposited micro-dimpled texture Ti-6Al-4V having different OFs. It could be clearly seen that the cell adhered percentages increased with the enhancement in OF of the micro-dimpled texture surfaces. Higher count of cells were observed on the BCP-(50% OF)Ti-6Al-4V due to higher roughness R_a and R_f values with higher hydrophilicity. In addition, the cells were distributed on both the central part as well as the periphery of the micro-dimples. However, higher numbers of cells were aligned on the central portion of the micro-dimples in all three textured surfaces. This may be due to the micro-dimple which acts as the micro-reservoir to

supply extra amount of medium and proteins to cells for growth. Similarly, Hu et al. (2014) found most of the cells at the throughs of the micro-wavy patterned surfaces. Ishizaki et al. (2010) also observed higher amount of cell adhesion and proliferation on the hydrophilic grooves; whereas, lesser amount of cells were found on the adjacent hydrophobic ridges of micro-patterned surfaces. In addition, when the OF increased, the micro-dimple density (number of micro-dimples per unit area) increased. This provided more number of micro-reservoirs for availability of mediums and proteins to cells attachment and spreading. Hence, BCP-(50% OF)Ti-6Al-4V exhibited the highest number of cells with well spreading compared to BCP-(25% OF)Ti-6Al-4V and BCP-(0% OF)Ti-6Al-4V.

In addition, to determine the cell adhesion behavior quantitatively, image processing (ImageJ) software was used to evaluate different cell features from the fluorescence microscopy images, as reported previously by our group (Behera et al., 2018b; Hasan et al., 2018b). The different cell features such as percentage of cell adherence, nuclei area, average cell area and circularity were analyzed (Figure 5.11). It was clearly observed that BCP-(50% OF)Ti-6Al-4V exhibited the maximum cell adherence of 84.8±5.1% followed by BCP-(25% OF)Ti-6Al-4V (74.1±1.8%), and BCP-(0% OF)Ti-6Al-4V (69.1±5.6%). The hydrophobic BCP-bare Ti-6Al-4V film showed 61.4±4.5% adhered cells, while the least number of cells (52.0±4.8%) was observed on bare Ti-6Al-4V (Figure 5.11 (a)). Furthermore, it was noticed that the average cell area is maximum for BCP-(50% OF)Ti-6Al-4V film (2864±484 μm^2) (Figure 5.11 (a)). The higher cell area indicates excellent focal adhesion of cells with the BCP-(50% OF)Ti-6Al-4V surface; whereas, the lower value confirms the poor focal adhesion of osteoblast with the bare Ti-6Al-4V surface.

Furthermore, Figure 5.11 (b) shows the circularity and the average nuclei area of the adhered cells on various modified surfaces. Nuclei size plays a significant role during cell differentiation and proliferation; whereas, circularity defines the degree of polarization in a scale range of 0 to 1. Larger nucleus size leads to higher division rate, while the lesser value of circularity results in better spreading of cells, indicating higher cyto-compatibility rate (Tutak et al., 2017). The trend obtained for the average nuclei area was found similar to the trend of average cell area of the adhered cells: BCP-(50% OF)Ti-6Al-4V > BCP-(25% OF)Ti-6Al-4V > BCP-(0% OF)Ti-6Al-4V > BCP-bare Ti-6Al-4V > bare Ti-6Al-4V. On the

other hand, the opposite trend was obtained for the circularity of adhered cells (Figure 5.11 (b)).

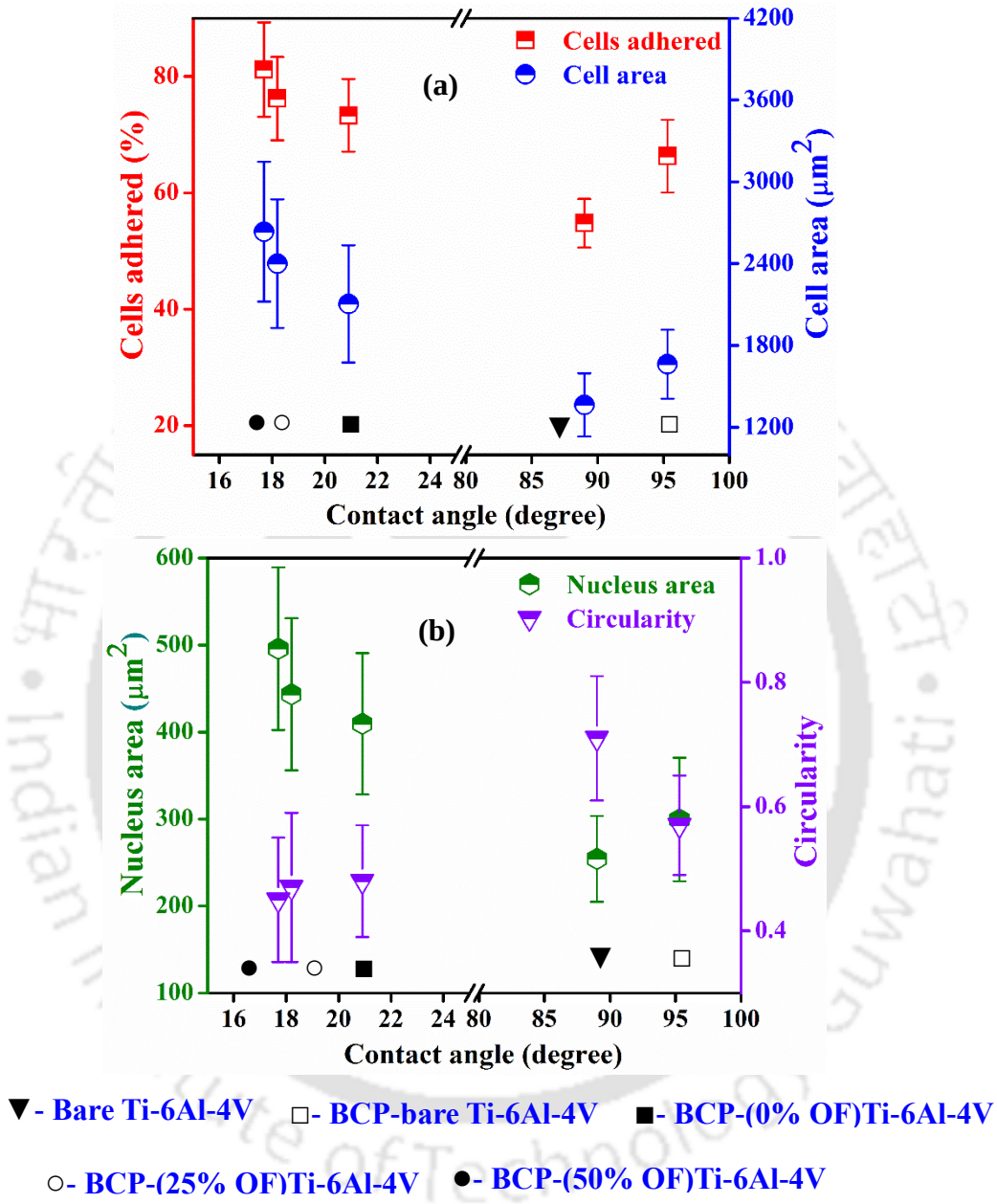

Figure 5.11: *Influence of various modified surfaces on (a) average cell area and % cells adhered, (b) circularity and average nuclei area of adhered cells.*

This clearly depicts that compared to BCP-bare Ti-6Al-4V and bare Ti-6Al-4V, MG-63 cells exhibited good affinity towards BCP sputtered micro-textured surface. Furthermore, among the textured substrates, the cell adhesion improved with the increase in overlapping rate. This is attributed to increase in surface roughness from 1.12-2.07 μm, which provides

greater surface area to avail more serum proteins and medium for cell growth, making the implant with improved osteointegration (Li et al., 2012).

Figure 5.12 shows the co-relation between % cells adhered and average cell area with the R_a. Both the cell adhered % and average cell area were found to be linearly increase with R_a, having R^2 = 0.91 and R^2 = 0.93, respectively. This confirmed that for the same surface chemistry, increase in surface area (roughness) improves cellular behavior, which can be explored to design a biocompatible surface. In addition, it is clear that with the wettability, the surface roughness and protein adsorption also cooperatively regulate the cell spreading and adhesion.

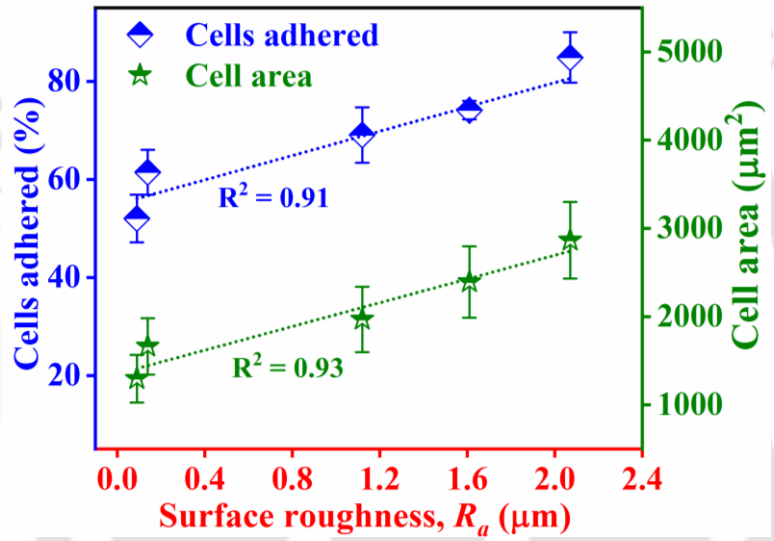

Figure 5.12. *Relationship between cells adhered % and average cell area with the surface roughness (R_a)*

The proliferation rate of MG63 cells grown on different modified surfaces as a function of incubation time (days) is demonstrated in Figure 5.13. Compared to bare Ti-6Al-4V surfaces, all other modified surfaces exhibited higher proliferation rate for all the incubation periods, suggesting better cyto-compatibility for bone tissue regeneration applications. This is attributed to the availability of biocompatible phases (β-TCP and HA), higher protein adsorption, higher wettability as well as higher surface roughness as compared to bare Ti-6Al-4V. At day 6, the proliferation rate of BCP-(50% OF)Ti-6Al-4V surface (298.4±12.5%) was significantly higher than BCP-bare Ti-6Al-4V (169.5±6.5%) and other textured surfaces, BCP-(25% OF)Ti-6Al-4V (271.7±10.3%), and BCP-(0% OF)Ti-6Al-4V (234.7±8.1%). Due to the higher surface roughness of 50% Ti-6Al-4V, the average cell area

and cell adherence percentage were higher (Figure 5.12). Furthermore, due to larger nuclei area (Figure 5.11 (b)), higher number of cells divided, resulting in a better proliferation in case of BCP-(50% OF)Ti-6Al-4V film in comparison to other modified surfaces. Costa et al. (2013) found greater osteoblast attachment and proliferation on more complex, micro-rough HA surfaces (Ra ~2 μm) than on smoother topographies (Ra ~1 μm). The microtopography creates an environment, i.e. the so-called niches, which are favourable for cells and cell–ECM interactions and increases the production of growth factors. In addition, nanotopography also improves the HOS cell attachment and adhesion in CaP coating surface, as reported by (Lee et al., 2009). In this study, a hierarchical structure of micro/nano topography surface provides more surface area for protein and cell medium as well as adsorbed mass of protein to adhere and proliferate higher number of cells as compared to nanotopogarphy BCP film surface. Hence, BCP-textured surfaces exhibited higher cell proliferation compared to BCP-bare Ti-6Al-4V.

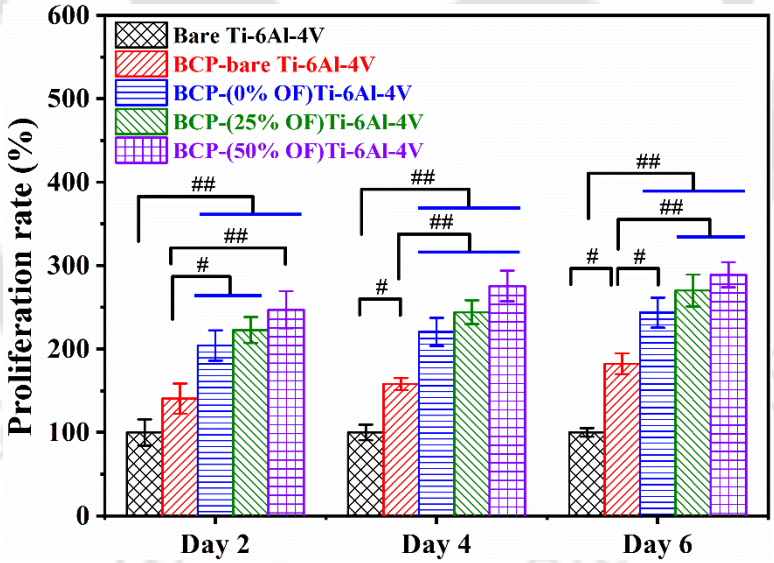

Figure 5.13. *MG63 cells proliferation on bare Ti-6Al-4V, BCP-bare Ti-6Al-4V, BCP-(0% OF)Ti-6Al-4V, BCP(25% OF)Ti-6Al-4V and BCP-(50% OF)Ti-6Al-4V films after 2, 4 and 6 days of incubation. Values represent the mean ± SD. # denotes $p < 0.05$ and ## denotes $p < 0.005$.*

5.3.3.3 In vitro bioactivity

In section 3.3.7, chapter 3, the apatite formation was observed on BCP deposited Ti-6Al-4V having different film thicknesses when soaked in SBF for 14 days. In the current study, the

apatite formation was evaluated on BCP films deposited on different textured Ti-6Al-4V. Different modified surfaces were soaked in SBF for 7 days followed by XRD, FESEM and EDS analyses. Figure 5.14 represents the XRD patterns of BCP films on bare and textured Ti-6Al-4V, after 7 days of SBF immersion. All the modified surfaces had significantly improved HA peaks with a decrease of β-TCP peaks compared to that in the surfaces before SBF immersion (Figure 5.3). Owing to the presence of bioactive HA and β-TCP phases, nucleation sites generate when these phases immerse in the SBF, resulting in the apatite layer formation on BCP film (Paital et al., 2010). When BCP is exposed to SBF, the hydroxyl (OH^-) and phosphate (PO_4^{3-}) units make the surface potential highly negative (Kim et al., 2004; Paital and Dahotre, 2009). The formation of OH^- ions on the surface attracts positively charged Ca^{2+} ions from the SBF, followed by PO_4^{3-} ions and reaction occur, leads to formation of apatite nuclei on the surface (Bakhsheshi-Rad et al., 2016a). Because of the higher solubility rate of β-TCP (Ogose et al., 2005), SBF gets supersaturated with Ca^{2+} and PO_4^{3-}; thus, more apatite can be precipitated by BCP film than pure HA deposited substrate.

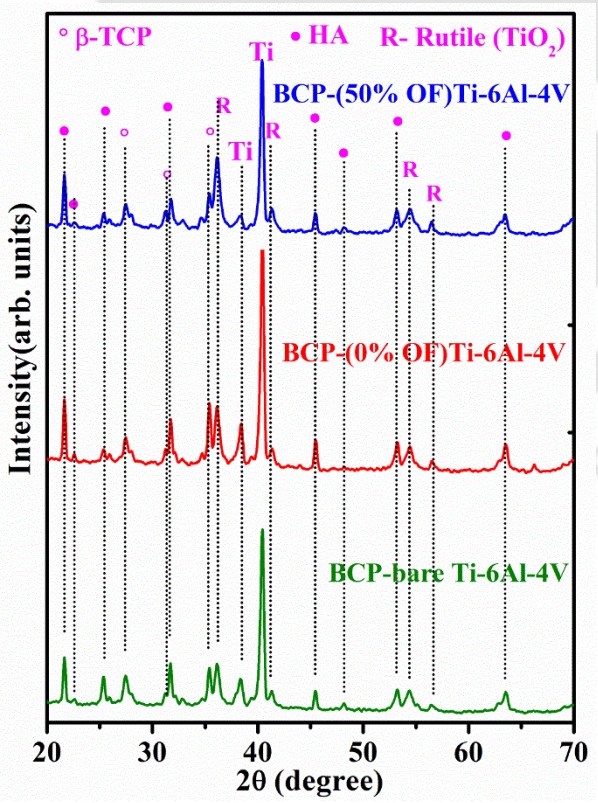

Figure 5.14. *Phases found in BCP film deposited on laser textured Ti-6Al-4V specimens at different overlapping factors after 7 days immersion in SBF.*

Furthermore, compared to BCP film sputtered on bare Ti-6Al-4V, BCP-textured Ti-6Al-4V exhibited more intense HA peaks. It indicates that the films deposited on the textured surface provide more nucleation sites for the ions present in SBF solution to come to the substrate and settle down on the surface. As the surface area and roughness enhanced with micro-texturing, the number of cavities increased, causing more amount of Ca^{2+} and PO_4^{3-} deposition from SBF (Arce et al., 2016). Moreover, the super-hydrophilicity causes more reaction between the coating surface ions and SBF ions. Thereby, higher apatite precipitated on the surface of BCP film deposited textured Ti-6Al-4V than that on bare Ti-6Al-4V. The presence of Ti in the XRD spectrum is attributed to the base material, whereas, TiO_2 (rutile) formation was due to laser surface texturing. In addition, it was noticed that, the apatite peaks are more intense for BCP-(50%OF)-Ti-6Al-4V compared to BCP-(0%OF)-Ti-6Al-4V. This is due to higher overall R_f and wettability of BCP-(50%OF)-Ti-6Al-4V, more interactions of SBF with the surface, and more apatite generation.

Figure 5.15 shows the surface morphologies of different modified surfaces after incubating the samples in SBF for 7 days. Globular structures can be found on the surface of all BCP films (lower magnification, Figure 5.15 (a–c)). Bridges were formed to connect the globular apatite (Figure 5.15 (d)). Plate-like crystals were observed in the globules at higher magnification (Figure 5.15 (e)). The appearance of globular morphologies and plate-like crystals is the characteristic of apatite formation, which is favorable for osteoconductivity, as reported by Li et al. (2015c) and Surmeneva et al. (2013). However, a higher amount of globules was seen in the BCP-textured Ti-6Al-4V (Figure 5.15 (b, c)) compared to BCP-bare Ti-6Al-4V (Figure 5.15 (a)), due to higher nucleation sites available for the textured substrate.

The elemental analysis of the globular particles exhibited a higher percentage of Ca, O and P with Ca/P atomic ratio of 1.58 (close to 1.67) (Figure 5.15 (f)). This confirmed that those crystals were corresponding to calcium deficient carbonated apatite similar to that found in bones. Mello et al. (2007) observed similar behavior on Ti surface during sputtering of HA coating on Ti-6Al-4V. The ability of surface micro-texturing with BCP deposition to enhance the wettability and to generate apatite layer can improve cell adhesion, proliferation and differentiation which stimulate osteointegration (Hasan et al., 2018b; Surmenev et al., 2014).

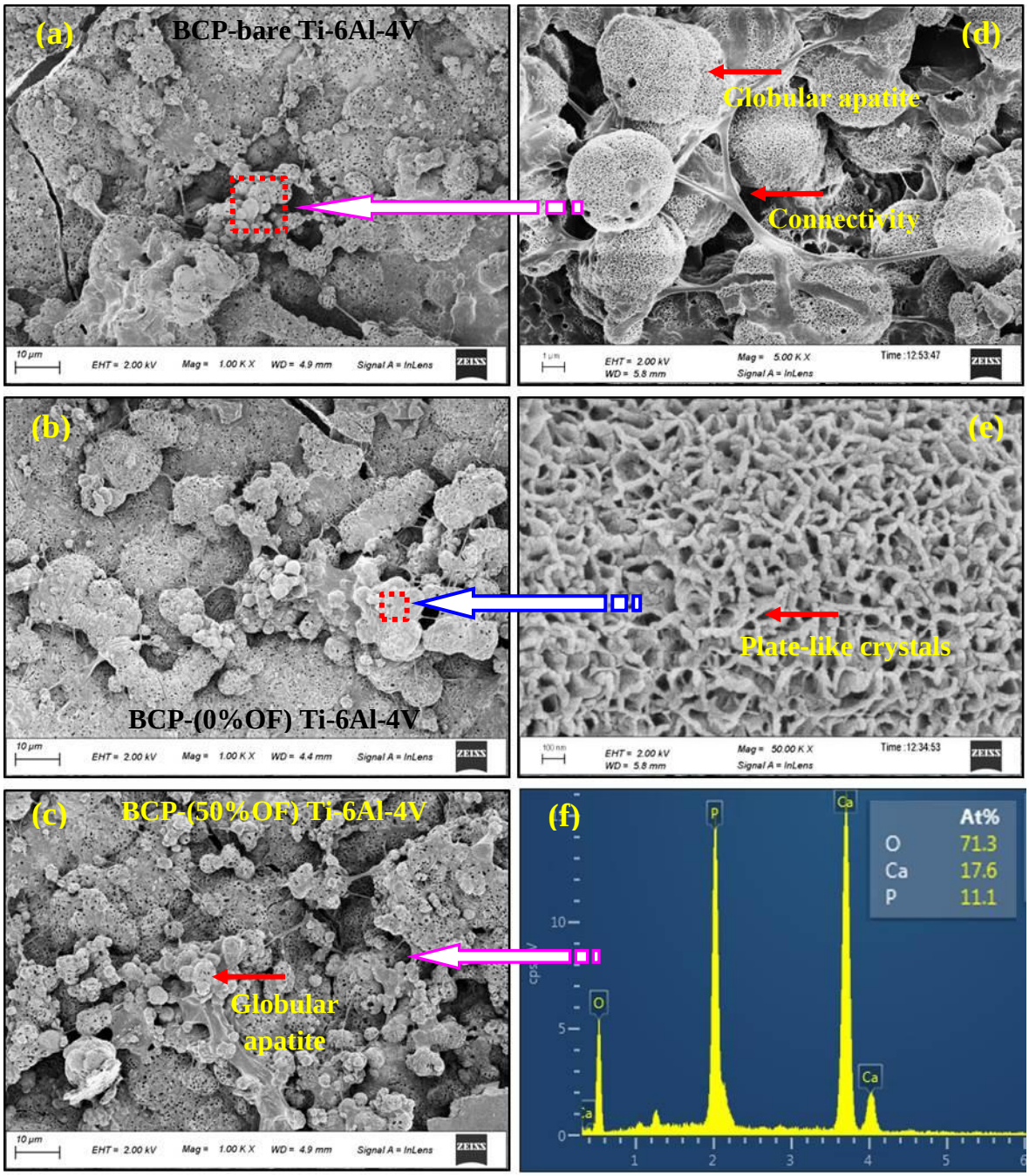

Figure 5.15. *Surface morphologies of (a) BCP – bare Ti-6Al-4V, (b) BCP-(0% OF)Ti-6Al-4V, (c) BCP-(50% OF)Ti-6Al-4V after 7 days immersion in SBF: (d) magnified view, (e) higher magnified view and (f) EDS spectra taken full area of (c).*

5.4 Findings from the research work

The present study deals with the surface modification of Ti-6Al-4V carried out by both laser surface micro-texturing followed by RF sputtering. Micro-dimpled texturing was fabricated

using Nd:YAG laser with three different OF such as 0%, 25% and 50% between two consecutive dimples to obtain three different micro-rough surfaces. Later, BCP film was sputtered on the different micro-dimpled textured surface for 7 h in order to modify its surface chemistry. The effect of surface texturing with the BCP film deposition on physical and biological properties were explored and compared with the bare Ti-6Al-4V as well as BCP deposited bare Ti-6Al-4V. The main findings show that the surface of nano-rough, bare Ti-6Al-4V ($R_a \approx 94$ nm) becomes micro-rough ($R_a \approx 0.98$-1.84 µm) after laser surface micro-texturing. In addition, the R_f improves with the OF due to variation of different geometrical features such as pitch, diameter and depth of the textured surface. The wettability of bare Ti-6Al-4V (89º) enhances after micro-dimpled texturing as contact angle decreased to 71º-77º for different overlapping factor. Post depositions of BCP film, the textured surfaces behave as super-hydrophilic as the contact angle further reduced to 17º-21º. The dimensions of micro-dimpled textured are not changed after BCP deposition; however, a non-uniform film is deposited with increase in surface roughness. The FBS adsorption increased from 5.3 to 7.11 µg/cm^2 with a rise in hydrophobicity of the surface; hence, it was higher for BCP deposited bare Ti-6Al-4V than that deposited on the textured specimen. As compared to bare Ti-6Al-4V as well as BCP-bare-Ti-6Al-4V surfaces, the BCP deposited textured surfaces exhibit higher number of well spread MG63 osteoblast cells. In addition, % cell adhered and the average cell area increased with increasing the OF, and BCP-(50% OF)-Ti-6Al-4V is found to have the maximum cell adhesion and proliferation. After 7 days of SBF immersion, carbonated apatite layer formed on all modified surfaces, making the surfaces more suitable to osteointegration.

The current study reveals that the texturing of Ti-6Al-4V with BCP film deposition on it, which is beneficial for improving surface roughness, wettability, cell adhesion and proliferation of the implants. Hence, this strategy can be advantageous for the implants being used for bone and dental applications.

Chapter 6

Conclusion and Future Scope

6.1 Conclusion

From the findings of the different works done in the present study, the following conclusion is withdrawn. In chapter 3, RF magnetron sputtering was used to deposit BCP (HA+βTCP) with three different film thicknesses on Ti-6Al-4V. Uniform films with no crack and thermal decomposition were obtained. Scratch test revealed that all the BCP films were well bonded with the Ti-6Al-4V substrate. Moreover, all the BCP films exhibited high-intensity apatite peaks after immersion in 14 days in SBF immersion, indicating better bioactivity. Among these, 1000 nm film thickness exhibited maximum wettability and bioactivity. Increase in BCP film thickness enhances the hydrophilicity of the film, which ultimately improves the bioactivity of the film.

In chapter 4, BCP-TiO_2 composite coatings with two different compositions were deposited on Ti-6Al-4V by RF sputtering. In addition, post annealing was carried out in order to investigate the effect of heat treatment on adhesion and biological behavior of the modified surface. It was found that TiO_2 addition with BCP film significantly enhances the adhesion between the coating and substrate due to physical and chemical stability of TiO_2 with Ti-6Al-4V substrate. Furthermore, the biological performance also improved with addition of TiO_2 concentration in the BCP film. Among these, 50 TiO_2-BCP film exhibits highest cyto-compatibility as well as maximum adhesion strength compared to 50 TiO_2-BCP and 100 BCP films. On the other hand, annealing improves the adhesion strength; however, it significantly degrades the biological performances.

Afterwards, in chapter 5, surface texturing (0%, 25%, 50% overlapping factor) on Ti-6Al-4V was performed by Nd:YAG laser followed by BCP film deposition using RF magnetron sputtering. A micro/nano hierarchical structure was generated using the combination of laser surface texturing followed by BCP film deposition. It was observed that all the textured substrates exhibited higher wettability than bare Ti-6Al-4V, and the hydrophilicity significantly improved after BCP film deposition for all the textured Ti-6Al-4. The BCP deposited textured substrates exhibited higher bioactivity, cell adhesion and

proliferation compared to BCP deposited bare Ti-6Al-4V. Among these, BCP deposited on 50% overlapping factor Ti-6Al-4V (BCP-50% Ti-6Al-4V) exhibited maximum cell adhesion and proliferation due to higher roughness factor and wettability.

Finally, it can be summarized that RF magnetron sputtering is a better technique for deposition of BCP bio-ceramic on Ti-6Al-4V implant. TiO_2 addition with BCP film enhances the biological performance of implant compared to BCP film. Furthermore, due to increase in bonding strength due to addition of TiO_2 in BCP film, TiO_2-BCP composite can be a good choice for the long-term application of orthopedic and dental implants. In addition, surface texturing on Ti-6Al-4V with 1-2 μm roughness followed by BCP film deposition, which forms micro/nano hierarchical structure is a better option for the orthopedic as well as dental applications due to higher cell adhesion and proliferation. Again, with the surface chemistry, surface roughness and wettability plays an important role, as with the increase in surface roughness and wettability, cell adhesion and proliferation improves.

6.2 Future scope

There is a lot of scope for further bio-ceramic coating research work as briefly stated in the following section.

6.2.1 RF magnetron sputtering for bio-ceramic coating

- Effect of BCP film with different ratios of HA and β-TCP can be investigated for different structural, mechanical and biological properties.
- Influence of different annealing temperatures can be explored on adhesion behavior as well as biological properties of BCP film.
- Simultaneous effect of micro and nano-texturing as well as TiO_2 addition can be studied on the adhesion as well as biological properties.
- In order to enhance the biological properties, hydrothermal treatment of the sputtering film can be carried out.
- Osteointegration of BCP sputtering film can be investigated by considering different cell lines.

6.3 Publications

6.3.1 List of publications from thesis work

6.3.1.1 International Journals published

1. **Rasmi Ranjan Behera**, Abshar Hasan, Mamilla Ravi Sankar, Lalit Mohan Pandey, **"Laser Cladding with HA and Functionally Graded TiO_2-HA Precursors on Ti–6Al–4V Alloy for Enhancing Bioactivity and Cyto-compatibility",** Surface & Coatings Technology. 2018, Volume 352, Pages 420-436 **(DOI:** 10.1016/j.surfcoat.2018.08.044).
2. **R. R. Behera,** A. Das, D. Pamu, L. M. Pandey, M. R. Sankar, "**Mechano-Tribological Properties and *In Vitro* Bioactivity of Biphasic Calcium Phosphate Coating on Ti-6Al-4V",** Journal of Mechanical Behavior of Biomedical Materials. 2018**,** Volume 86, Pages 143-157 **(DOI:** 10.1016/j.jmbbm.2018.06.020).
3. Apurba Das, Anil Kumar Chikkala, Gyan Prakash Bharti, **Rasmi Ranjan Behera,** Ravi Sankar Mamilla, Alika Khare, Pamu Dobbidi, **"Effect of thickness on optical and microwave dielectric properties of Hydroxyapatite films deposited by RF magnetron sputtering",** Journal of Alloys and Compounds. 2018, Volume 739, Pages 729-736. (**DOI:** 10.1016/j.jallcom.2017.12.293)

6.3.1.2 International Journals under review

4. **R. R. Behera,** A. Hasan, A. Das, D. Pamu, L. M. Pandey, M. R. Sankar, **"Adhesion behavior and Biocompatibility properties of Biphasic Calcium Phosphate (BCP) and BCP-TiO_2 Coating fabricated by RF magnetron sputtering",** Materials science and Engineering: C **(Under Review)**.
5. **R. R. Behera,** A. Das, V. Saxena, D. Pamu, L. M. Pandey, M. R. Sankar, **"Effect of Laser Surface Texturing on Biological Properties of Biphasic Calcium Phosphate Coating made by RF magnetron sputtering",** ACS Applied Materials and Interface **(Under Review)**.

6.3.1.3 Conferences/symposia

1. **R. R. Behera**, A. Das, D. Pamu, L. M. Pandey, M. R. Sankar, **"Calcium phosphate coating on Ti-6Al-4V alloy using RF magnetron sputtering process"**, Research

Conclave, 8-10 March, 2018, IIT Guwahati, Assam, India **(2nd Prize in Poster Presentation).**

2. **Rasmi Ranjan Behera**, Abshar Hasan, Mamilla Ravi Sankar, Lalit Mohan Pandey, **Bioactivity and Biocompatibility of Laser Deposited CaP-TiO_2 Functionally Graded Biocoating on Ti–6Al–4V Alloy for Orthopedic Applications",** Asian Biomaterials Congress (ABMC6), 25-27 October, 2017, Thiruvananthapuram, India
3. **Rasmi Ranjan Behera**, Mamilla Ravi Sankar, **"Laser Surface Cladding of Titania-Hydroxyapatite Functionally Graded Bio-coatings on Ti-6Al-4V Alloy",** 6th International and 27th All India Manufacturing Technology, Design and Research (AIMTDR), 16-18 December, 2016, COE Pune, India.
4. **Rasmi Ranjan Behera**, Abshar Hasan, Sandeep Bhoi, Mamilla Ravi Sankar, Lalit Mohan Pandey, "**Osteoblast Interaction with Laser Coated HA and TiO_2-HA Coatings on Ti–6Al–4V Alloy**", National Conference on Emerging Biomaterials (NCEB), 19-21 October, 2016, Bharathiar university, Coimbatore, India.

6.3.2 List of publications from miscellaneous works

6.3.2.1 International Journals published

1. **Rasmi Ranjan Behera**, Mamilla Ravi Sankar, Prahlad Kumar Baruah, Ashwini Kumar Sharma, Alika Khare, **Experimental investigations of nanosecond-pulsed Nd:YAG laser beam micromachining on 304 stainless steel**, Journal of Micromanufacturing, 2018, Volume 1 (1), Pages 1–14. (**DOI:** 10.1177/2516598418766937)
2. **Rasmi Ranjan Behera**, Palaganti Madhu Babu, Kishor Kumar Gajrani, Mamilla Ravi Sankar, **"Fabrication of micro-channels on 304 stainless steel (SS-304) using Nd:YAG laser beam micro-machining",** International Journal of Additive and Subtractive Materials Manufacturing, 2017, Volume 1 (3/4), Pages 338−359. **(DOI:** 10.1504/IJASMM.2017.10010934).
3. **Rasmi Ranjan Behera**, Mamilla Ravi Sankar, J. Swaminathan, Indrajeet Kumar, Ashwini Kumar Sharma, Alika Khare, **"Experimental investigation of underwater laser beam micromachining (UW-LBμM) on 304 stainless steel",** International

Journal of Advanced Manufacturing Technology, 2016, Volume 85, Pages 1969–1982. (**DOI:** 10.1007/s00170-016-8635-z)

4. **Rasmi Ranjan Behera**, M. Ravi Sankar, **"State of the art on Under Liquid Laser Beam Machining", Materials Today: Proceedings,** 2015, Volume 2, Pages 1731 – 1740. (**DOI:** 10.1016/j.matpr.2015.07.007)
5. **R. R. Behera**, E. Anisha, M. Ravi Sankar, U. S. Dixit, **"Experimental Investigations of CO_2 Laser Micro Channel Engraving on Hardened AISI 1040 Alloy Steel",** Journal of Manufacturing Technology Research, 2014, Volume 5 (3/4), Pages 179-194. (ISSN: 1943-8095)

6.3.2.2 Conferences/symposia

1. **R. R. Behera**, P. M. Babu, M. Yogi, K. K. Gajrani, M. R.Sankar, "**Fabrication of Micro-Channels on 304 Stainless Steel (SS-304) Using Nd:YAG Laser Beam Micro-Machining**", 4th International Conference on Production and Industrial Engineering (CPIE-2016), NIT Jalandhar, India.
2. **Rasmi Ranjan Behera**, M. Ravi Sankar, **"Laser Beam Thick Film Coating of Silicon Carbide on Stainless Steel"**, Research Conclave (2016), IIT Guwahati, Assam, India.
3. **Rasmi Ranjan Behera**, M. Ravi Sankar, **"Effect of surface texturing on microstructure and property of 304 stainless steel laser surface alloyed with SiC-Co"**, 27th MRSI North East Symposium on Advanced Materials for Sustainable Applications (MRSI-2016), NEIST Jorhat, India **(Best Poster Presentation).**
4. **Rasmi Ranjan Behera**, M. Ravi Sankar**, "State of the art on Under Liquid Laser Beam Machining",** International Conference on Materials Processing and Characterization, ICMPC-2015, GRIET-Hyderabad, India
5. **Rasmi Ranjan Behera**, Mamilla Ravi Sankar, Indrajeet Kumar, Ashwini Kumar Sharma, Alika Khare, J. Swaminathan, **"Experimental Study on Micromachining of 304 Stainless Steel Under Water Using Pulsed Nd:YAG Laser Beam",** 5th International and 26th All India Manufacturing Technology, Design and Research (AIMTDR-2014), IIT Guwahati, India.
6. M. Ravi Sankar**,** Tarun K.S., **R. R. Behera**, **"Experimental Study on CO_2 Laser Beam Micromachining of Silicon Carbide (SiC) Cylindrical Tube",** International

Conference on Precision, Meso, Micro and Nano Engineering (COPEN-8: 2013), NIT Calicut, India.

References

- Advincula, M.C., Rahemtulla, F.G., Advincula, R.C., Ada, E.T., Lemons, J.E., Bellis, S.L., 2006. Osteoblast adhesion and matrix mineralization on sol–gel-derived titanium oxide. Biomaterials 27, 2201-2212.
- Ahn, S., Kim, Y., Lee, H., Kim, G., 2012. A new hybrid scaffold constructed of solid freeform-fabricated PCL struts and collagen struts for bone tissue regeneration: fabrication, mechanical properties, and cellular activity. Journal of Materials Chemistry 22, 15901-15909.
- Albayrak, O., Altintas, S., 2010. Production of "Tricalcium Phosphate/Titanium Dioxide" Coating Surface on Titanium Substrates. Journal of materials science & technology 26, 1006.
- Altankov, G., Grinnell, F., Groth, T., 1996. Studies on the biocompatibility of materials: Fibroblast reorganization of substratum-bound fibronectin on surfaces varying in wettability. Journal of Biomedical Materials Research: An Official Journal of The Society for Biomaterials and The Japanese Society for Biomaterials 30, 385-391.
- Amaravathy, P., Sathyanarayanan, S., Sowndarya, S., Rajendran, N., 2014. Bioactive HA/TiO2 coating on magnesium alloy for biomedical applications. Ceramics international 40, 6617-6630.
- Anil, S., Anand, P., Alghamdi, H., Jansen, J., 2011. Dental implant surface enhancement and osseointegration, Implant dentistry-A rapidly evolving practice. IntechOpen.
- Araghi, A., Hadianfard, M., 2015a. Fabrication and characterization of functionally graded hydroxyapatite/TiO 2 multilayer coating on Ti–6Al–4V titanium alloy for biomedical applications. Ceramics International 41, 12668-12679.
- Araghi, A., Hadianfard, M.J., 2015b. Fabrication and characterization of functionally graded hydroxyapatite/TiO2 multilayer coating on Ti–6Al–4V titanium alloy for biomedical applications. Ceramics International 41, 12668-12679.
- Arce, J.E., Arce, A.E., Aguilar, Y., Yate, L., Moya, S., Rincón, C., Gutiérrez, O., 2016. Calcium phosphate–calcium titanate composite coatings for orthopedic applications. Ceramics International 42, 10322-10331.
- Arima, Y., Iwata, H., 2007. Effect of wettability and surface functional groups on protein adsorption and cell adhesion using well-defined mixed self-assembled monolayers. Biomaterials 28, 3074-3082.
- Aufderheide, B.E., 2006. Sputtered thin film coatings. Coatings technology handbook, 1-10.

- Bächle, M., Kohal, R.J., 2004. A systematic review of the influence of different titanium surfaces on proliferation, differentiation and protein synthesis of osteoblast-like MG63 cells. Clinical Oral Implants Research 15, 683-692.
- Badea, M., Braic, M., Kiss, A., Moga, M., Pozna, E., Pana, I., Vladescu, A., 2016. Influence of Ag content on the antibacterial properties of SiC doped hydroxyapatite coatings. Ceramics International 42, 1801-1811.
- Bailey, M., Coe, S., Grant, D., Grime, G., Jeynes, C., 2009. Accurate determination of the Ca: P ratio in rough hydroxyapatite samples by SEM-EDS, PIXE and RBS—a comparative study. X-Ray Spectrometry: An International Journal 38, 343-347.
- Bajpai, S., Chand, N., Ahuja, S., 2015. Investigation of curcumin release from chitosan/cellulose micro crystals (CMC) antimicrobial films. International journal of biological macromolecules 79, 440-448.
- Bakhsheshi-Rad, H., Hamzah, E., Ismail, A., Kasiri-Asgarani, M., Daroonparvar, M., Parham, S., Iqbal, N., Medraj, M., 2016a. Novel bi-layered nanostructured SiO2/Ag-FHAp coating on biodegradable magnesium alloy for biomedical applications. Ceramics International 42, 11941-11950.
- Bakhsheshi-Rad, H., Hamzah, E., Ismail, A., Kasiri-Asgarani, M., Daroonparvar, M., Parham, S., Iqbal, N., Medraj, M., 2016b. Novel bi-layered nanostructured SiO 2/Ag-FHAp coating on biodegradable magnesium alloy for biomedical applications. Ceramics International.
- Balla, V.K., DeVasConCellos, P.D., Xue, W., Bose, S., Bandyopadhyay, A., 2009. Fabrication of compositionally and structurally graded Ti–TiO 2 structures using laser engineered net shaping (LENS). Acta biomaterialia 5, 1831-1837.
- Bauer, T.W., Muschler, G.F., 2000. Bone graft materials: an overview of the basic science. Clinical Orthopaedics and Related Research® 371, 10-27.
- Behera, R.R., Babu, P., Gajrani, K.K., Sankar, M.R., 2017. Fabrication of micro-features on 304 stainless steel (SS-304) using Nd: YAG laser beam micro-machining. International Journal of Additive and Subtractive Materials Manufacturing 1, 338-359.
- Behera, R.R., Das, A., Pamu, D., Pandey, L.M., Sankar, M.R., 2018a. Mechano-tribological properties and in vitro bioactivity of biphasic calcium phosphate coating on Ti-6Al-4V. Journal of the Mechanical Behavior of Biomedical Materials 86, 143-157.
- Behera, R.R., Hasan, A., Sankar, M.R., Pandey, L.M., 2018b. Laser cladding with HA and functionally graded TiO2-HA precursors on Ti–6Al–4V alloy for enhancing bioactivity and cyto-compatibility. Surface and Coatings Technology 352, 420-436.
- Berezhnaya, A.Y., Mittova, V., Kukueva, E., Mittova, I.Y., 2010. Effect of high-temperature annealing on solid-state reactions in hydroxyapatite/TiO 2 films on titanium substrates. Inorganic Materials 46, 971-977.

- Berube, P., Yang, Y., Carnes, D.L., Stover, R.E., Boland, E.J., Ong, J.L., 2005. The effect of sputtered calcium phosphate coatings of different crystallinity on osteoblast differentiation. Journal of periodontology 76, 1697-1709.
- Bhatia, D., Bejarano, T., Novo, M., 2013. Current interventions in the management of knee osteoarthritis. Journal of pharmacy & bioallied sciences 5, 30.
- Bigi, A., Boanini, E., Capuccini, C., Fini, M., Mihailescu, I.N., Ristoscu, C., Sima, F., Torricelli, P., 2009. Biofunctional alendronate–hydroxyapatite thin films deposited by matrix assisted pulsed laser evaporation. Biomaterials 30, 6168-6177.
- Boccaccini, A., Keim, S., Ma, R., Li, Y., Zhitomirsky, I., 2010. Electrophoretic deposition of biomaterials. Journal of the Royal Society Interface 7, S581-S613.
- Bohner, M., 2000. Calcium orthophosphates in medicine: from ceramics to calcium phosphate cements. Injury 31, D37-D47.
- Bosco, R., Van Den Beucken, J., Leeuwenburgh, S., Jansen, J., 2012. Surface engineering for bone implants: a trend from passive to active surfaces. Coatings 2, 95-119.
- Boyd, A., Akay, M., Meenan, B., 2003. Influence of target surface degradation on the properties of rf magnetron-sputtered calcium phosphate coatings. Surface and Interface Analysis: An International Journal devoted to the development and application of techniques for the analysis of surfaces, interfaces and thin films 35, 188-198.
- Boyd, A., Burke, G., Duffy, H., Holmberg, M., O'Kane, C., Meenan, B., Kingshott, P., 2011. Sputter deposited bioceramic coatings: surface characterisation and initial protein adsorption studies using surface-MALDI-MS. Journal of Materials Science: Materials in Medicine 22, 71-84.
- Boyd, A., Duffy, H., McCann, R., Meenan, B., 2008. Sputter deposition of calcium phosphate/titanium dioxide hybrid thin films. Materials Science and Engineering: C 28, 228-236.
- Boyd, A., Meenan, B., Leyland, N., 2006. Surface characterisation of the evolving nature of radio frequency (RF) magnetron sputter deposited calcium phosphate thin films after exposure to physiological solution. Surface and Coatings Technology 200, 6002-6013.
- Boyd, A.R., Rutledge, L., Randolph, L.D., Meenan, B.J., 2015. Strontium-substituted hydroxyapatite coatings deposited via a co-deposition sputter technique. Materials Science and Engineering: C 46, 290-300.
- Bramowicz, M., Braic, L., Azem, F.A., Kulesza, S., Birlik, I., Vladescu, A., 2016. Mechanical properties and fractal analysis of the surface texture of sputtered hydroxyapatite coatings. Applied Surface Science 379, 338-346.
- Branemark, R., Branemark, P., Rydevik, B., Myers, R.R., 2001. Osseointegration in skeletal reconstruction and rehabilitation: a review. Journal of rehabilitation research and development 38, 175-182.

- Brohede, U., Zhao, S., Lindberg, F., Mihranyan, A., Forsgren, J., Strømme, M., Engqvist, H., 2009. A novel graded bioactive high adhesion implant coating. Applied Surface Science 255, 7723-7728.
- Brown, P.D., Edwards, H., Fay, M.W., 2010. Microscopy at the life sciences/physical sciences interface, Journal of Physics: Conference Series. IOP Publishing, p. 012019.
- Cairns, M., Meenan, B., Burke, G., Boyd, A., 2010. Influence of surface topography on osteoblast response to fibronectin coated calcium phosphate thin films. Colloids and Surfaces B: Biointerfaces 78, 283-290.
- Chakraborty, R., Bepari, S., Banerjee, A., 2011. Application of calcined waste fish (Labeo rohita) scale as low-cost heterogeneous catalyst for biodiesel synthesis. Bioresource technology 102, 3610-3618.
- Chen, Q., Mohn, D., Stark, W.J., 2011. Optimization of Bioglass® scaffold fabrication process. Journal of the American Ceramic Society 94, 4184-4190.
- Chen, X., Nouri, A., Li, Y., Lin, J., Hodgson, P.D., Wen, C.e., 2008. Effect of surface roughness of Ti, Zr, and TiZr on apatite precipitation from simulated body fluid. Biotechnology and bioengineering 101, 378-387.
- Cheng, G.J., Pirzada, D., Cai, M., Mohanty, P., Bandyopadhyay, A., 2005. Bioceramic coating of hydroxyapatite on titanium substrate with Nd-YAG laser. Materials Science and Engineering: C 25, 541-547.
- Chien, C., Hong, T., Han, T., Kuo, T., Liao, T., 2011a. Effects of different binders on microstructure and phase composition of hydroxyapatite Nd–YAG laser clad coatings. Applied Surface Science 257, 2387-2393.
- Chien, C., Liao, T., Hong, T., Kuo, T., Wu, J., Lee, T., 2011b. Investigation into microstructural properties of fluorapatite Nd-YAG laser clad coatings with PVA and WG binders. Surface and Coatings Technology 205, 3141-3146.
- Choi, J., Bogdanski, D., Köller, M., Esenwein, S.A., Müller, D., Muhr, G., Epple, M., 2003. Calcium phosphate coating of nickel–titanium shape-memory alloys. Coating procedure and adherence of leukocytes and platelets. Biomaterials 24, 3689-3696.
- Choong, P.F., 2009. The challenges of joint replacement surgery in the 21st century. ANZ journal of surgery 79, 669-671.
- Chu, S.-F., Huang, M.-T., Ou, K.-L., Sugiatno, E., Cheng, H.-Y., Huang, Y.-H., Chiu, W.-T., Liou, T.-H., 2016. Enhanced biocompatible and hemocompatible nano/micro porous surface as a biological scaffold for functionalizational and biointegrated implants. Journal of Alloys and Compounds 684, 726-732.
- Ciobanu, G., Carja, G., Ciobanu, O., Sandu, I., Sandu, A., 2009. SEM and EDX studies of bioactive hydroxyapatite coatings on titanium implants. Micron 40, 143-146.
- Combes, C., Rey, C., 2010. Amorphous calcium phosphates: synthesis, properties and uses in biomaterials. Acta biomaterialia 6, 3362-3378.

- Costa, D.O., Prowse, P.D.H., Chrones, T., Sims, S.M., Hamilton, D.W., Rizkalla, A.S., Dixon, S.J., 2013. The differential regulation of osteoblast and osteoclast activity by surface topography of hydroxyapatite coatings. Biomaterials 34, 7215-7226.
- Cui, W., Qin, G., Duan, J., Wang, H., 2017. A graded nano-TiN coating on biomedical Ti alloy: Low friction coefficient, good bonding and biocompatibility. Materials Science and Engineering: C 71, 520-528.
- Cunningham, B.W., Hu, N., Zorn, C.M., McAfee, P.C., 2009. Bioactive titanium calcium phosphate coating for disc arthroplasty: analysis of 58 vertebral end plates after 6-to 12-month implantation. The Spine Journal 9, 836-845.
- d'Haese, R., Pawlowski, L., Bigan, M., Jaworski, R., Martel, M., 2010. Phase evolution of hydroxapatite coatings suspension plasma sprayed using variable parameters in simulated body fluid. Surface and Coatings Technology 204, 1236-1246.
- Daculsi, G., LeGeros, R.Z., Heughebaert, M., Barbieux, I., 1990. Formation of carbonate-apatite crystals after implantation of calcium phosphate ceramics. Calcified Tissue International 46, 20-27.
- Das, A., Chikkala, A.K., Bharti, G.P., Behera, R.R., Mamilla, R.S., Khare, A., Dobbidi, P., 2018. Effect of thickness on optical and microwave dielectric properties of Hydroxyapatite films deposited by RF magnetron sputtering. Journal of Alloys and Compounds 739, 729-736.
- Dimitrievska, S., Bureau, M.N., Antoniou, J., Mwale, F., Petit, A., Lima, R.S., Marple, B.R., 2011. Titania–hydroxyapatite nanocomposite coatings support human mesenchymal stem cells osteogenic differentiation. Journal of Biomedical Materials Research Part A 98, 576-588.
- Dinda, G., Shin, J., Mazumder, J., 2009. Pulsed laser deposition of hydroxyapatite thin films on Ti–6Al–4V: effect of heat treatment on structure and properties. Acta biomaterialia 5, 1821-1830.
- Ding, S.J., Ju, C.P., Lin, J.H.C., 1999. Characterization of hydroxyapatite and titanium coatings sputtered on Ti-6Al-4V substrate. Journal of Biomedical Materials Research: An Official Journal of The Society for Biomaterials, The Japanese Society for Biomaterials, and The Australian Society for Biomaterials 44, 266-279.
- Dinu, M., Kiss, A.E., Parau, A.C., Braic, V., Vitelaru, C., Braic, M., Pana, I., Balaceanu, M., Vladescu, A., 2014. Influence of thermal treatment on the roughness, corrosion resistance and wettability of hydroxyapatite films deposited by RF magnetron sputtering, Key Engineering Materials. Trans Tech Publ, pp. 297-302.
- Dobzyniak, M., Fehring, T.K., Odum, S., 2006. Early failure in total hip arthroplasty. Clinical Orthopaedics and Related Research® 447, 76-78.
- Dong, S., Zeng, J., Li, L., Sun, J., Yang, X., Liao, H., 2017. Significance of in-situ dry-ice blasting on the microstructure, crystallinity and bonding strength of plasma-

sprayed hydroxyapatite coatings. Journal of the mechanical behavior of biomedical materials 71, 136-147.

- Dos Santos, E., Farina, M., Soares, G., Anselme, K., 2009. Chemical and topographical influence of hydroxyapatite and β-tricalcium phosphate surfaces on human osteoblastic cell behavior. Journal of Biomedical Materials Research Part A: An Official Journal of The Society for Biomaterials, The Japanese Society for Biomaterials, and The Australian Society for Biomaterials and the Korean Society for Biomaterials 89, 510-520.
- dos Santos, E.A., Moldovan, S., Mateescu, M., Faerber, J., Acosta, M., Pelletier, H., Anselme, K., Werckmann, J., 2012. Physical–chemical and biological behavior of an amorphous calcium phosphate thin film produced by RF-magnetron sputtering. Materials Science and Engineering: C 32, 2086-2095.
- Du, S., Li, Y., 2015. Effect of annealing on microstructure and mechanical properties of magnetron sputtered Cu thin films. Advances in Materials Science and Engineering 2015.
- Dulski, M., Dudek, K., Grelowski, M., Kubacki, J., Hertlein, J., Wojtyniak, M., Goryczka, T., 2018. Impact of annealing on features of BCP coating on NiTi shape memory alloy: Preparation and physicochemical characterization. Applied Surface Science 437, 28-40.
- Dumbleton, J., Manley, M.T., 2004. Hydroxyapatite-coated prostheses in total hip and knee arthroplasty. JBJS 86, 2526-2540.
- Duta, L., Mihailescu, N., Popescu, A.C., Luculescu, C.R., Mihailescu, I.N., Çetin, G., Gunduz, O., Oktar, F.N., Popa, A.C., Kuncser, A., Besleaga, C., Stan, G.E., 2017. Comparative physical, chemical and biological assessment of simple and titanium-doped ovine dentine-derived hydroxyapatite coatings fabricated by pulsed laser deposition. Applied Surface Science 413, 129-139.
- Ebrahimi, M., Botelho, M.G., Dorozhkin, S.V., 2017. Biphasic calcium phosphates bioceramics (HA/TCP): concept, physicochemical properties and the impact of standardization of study protocols in biomaterials research. Materials Science and Engineering: C 71, 1293-1312.
- Ergun, C., Liu, H., Halloran, J.W., Webster, T.J., 2007. Increased osteoblast adhesion on nanograined hydroxyapatite and tricalcium phosphate containing calcium titanate. Journal of Biomedical Materials Research Part A 80, 990-997.
- Evis, Z., Webster, T., 2011. Nanosize hydroxyapatite: doping with various ions. Advances in Applied Ceramics 110, 311-321.
- Farnoush, H., Mohandesi, J.A., Çimenoğlu, H., 2015. Micro-scratch and corrosion behavior of functionally graded HA-TiO2 nanostructured composite coatings fabricated by electrophoretic deposition. Journal of the mechanical behavior of biomedical materials 46, 31-40.

- Fehring, T.K., Odum, S., Griffin, W.L., Mason, J.B., Nadaud, M., 2001. Early failures in total knee arthroplasty. Clinical orthopaedics and related research 392, 315-318.
- Fernández-Pradas, J., Garcıa-Cuenca, M., Cleries, L., Sardin, G., Morenza, J., 2002. Influence of the interface layer on the adhesion of pulsed laser deposited hydroxyapatite coatings on titanium alloy. Applied Surface Science 195, 31-37.
- Gaasbeek, R.D., Toonen, H.G., van Heerwaarden, R.J., Buma, P., 2005. Mechanism of bone incorporation of β-TCP bone substitute in open wedge tibial osteotomy in patients. Biomaterials 26, 6713-6719.
- Gadow, R., Killinger, A., Stiegler, N., 2010. Hydroxyapatite coatings for biomedical applications deposited by different thermal spray techniques. Surface and Coatings Technology 205, 1157-1164.
- Gao, Y., Hu, J., Guan, T., Wu, J., Zhang, C., Gao, B., 2014. Physical properties and cellular responses to calcium phosphate coating produced by laser rapid forming on titanium. Lasers in medical science 29, 9-17.
- García-Gareta, E., Hua, J., Knowles, J.C., Blunn, G.W., 2013. Comparison of mesenchymal stem cell proliferation and differentiation between biomimetic and electrochemical coatings on different topographic surfaces. Journal of Materials Science: Materials in Medicine 24, 199-210.
- Ge, X., Leng, Y., Ren, F., Lu, X., 2011. Integrity and zeta potential of fluoridated hydroxyapatite nanothick coatings for biomedical applications. Journal of the mechanical behavior of biomedical materials 4, 1046-1056.
- Geetha, M., Singh, A.K., Asokamani, R., Gogia, A.K., 2009. Ti based biomaterials, the ultimate choice for orthopaedic implants–a review. Progress in materials science 54, 397-425.
- Gentleman, M.M., Gentleman, E., 2014. The role of surface free energy in osteoblast–biomaterial interactions. International Materials Reviews 59, 417-429.
- Gittens, R.A., McLachlan, T., Olivares-Navarrete, R., Cai, Y., Berner, S., Tannenbaum, R., Schwartz, Z., Sandhage, K.H., Boyan, B.D., 2011. The effects of combined micron-/submicron-scale surface roughness and nanoscale features on cell proliferation and differentiation. Biomaterials 32, 3395-3403.
- Gomes, P.S., Botelho, C., Lopes, M.A., Santos, J.D., Fernandes, M.H., 2010. Evaluation of human osteoblastic cell response to plasma-sprayed silicon-substituted hydroxyapatite coatings over titanium substrates. Journal of Biomedical Materials Research Part B: Applied Biomaterials 94, 337-346.
- Groth, T., Altankov, G., 1996. Studies on cell-biomaterial interaction: role of tyrosine phosphorylation during fibroblast spreading on surfaces varying in wettability. Biomaterials 17, 1227-1234.
- Hahn, B.-D., Lee, J.-M., Park, D.-S., Choi, J.-J., Ryu, J., Yoon, W.-H., Choi, J.-H., Lee, B.-K., Kim, J.-W., Kim, H.-E., 2011. Enhanced bioactivity and biocompatibility

of nanostructured hydroxyapatite coating by hydrothermal annealing. Thin Solid Films 519, 8085-8090.

- Hamrit, S., Djessas, K., Brihi, N., Viallet, B., Medjnoun, K., Grillo, S.E., 2016. The effect of thickness on the physico-chemical properties of nanostructured ZnO:Al TCO thin films deposited on flexible PEN substrates by RF-magnetron sputtering from a nanopowder target. Ceramics International 42, 16212-16219.
- Han, I., Lee, I., Song, J., Lee, M., Park, J., Lee, G., Sun, X., Chung, S., 2007. Characterization of a silver-incorporated calcium phosphate film by RBS and its antimicrobial effects. Biomedical Materials 2, S91.
- Han, M., Sethuraman, A., Kane, R.S., Belfort, G., 2003. Nanometer-scale roughness having little effect on the amount or structure of adsorbed protein. Langmuir 19, 9868-9872.
- Hao, J., Li, Y., Wang, X., Zhang, X., Li, B., Li, H., Zhou, L., Yin, F., Liang, C., Wang, H., 2017. Corrosion resistance and biological properties of a micro–nano structured Ti surface consisting of TiO 2 and hydroxyapatite. RSC Advances 7, 33285-33292.
- Harsha, K.S., 2005. Principles of vapor deposition of thin films. Elsevier.
- Hasan, A., Pandey, L.M., 2015. Review: polymers, surface-modified polymers, and self assembled monolayers as surface-modifying agents for biomaterials. Polymer-Plastics Technology and Engineering 54, 1358-1378.
- Hasan, A., Pandey, L.M., 2016. Kinetic studies of attachment and re-orientation of octyltriethoxysilane for formation of self-assembled monolayer on a silica substrate. Materials Science and Engineering: C 68, 423-429.
- Hasan, A., Pattanayek, S.K., Pandey, L.M., 2018a. Effect of Functional Groups of Self-Assembled Monolayers on Protein Adsorption and Initial Cell Adhesion. ACS Biomaterials Science & Engineering 4, 3224-3233.
- Hasan, A., Saxena, V., Pandey, L.M., 2018b. Surface Functionalization of Ti6Al4V via Self-assembled Monolayers for Improved Protein Adsorption and Fibroblast Adhesion. Langmuir 34, 3494-3506.
- Hasan, A., Waibhaw, G., Saxena, V., Pandey, L.M., 2018c. Nano-biocomposite scaffolds of chitosan, carboxymethyl cellulose and silver nanoparticle modified cellulose nanowhiskers for bone tissue engineering applications. International Journal of Biological Macromolecules 111, 923-934.
- Hasan, A., Waibhaw, G., Tiwari, S., Dharmalingam, K., Shukla, I., Pandey, L.M., 2017. Fabrication and characterization of chitosan, polyvinylpyrrolidone, and cellulose nanowhiskers nanocomposite films for wound healing drug delivery application. Journal of Biomedical Materials Research Part A 105, 2391-2404.
- He, G., Hu, J., Wei, S., Li, J., Liang, X., Luo, E., 2008. Surface modification of titanium by nano-TiO 2/HA bioceramic coating. Applied Surface Science 255, 442-445.

- Heimann, R.B., 2013. Structure, properties, and biomedical performance of osteoconductive bioceramic coatings. Surface and Coatings Technology 233, 27-38.
- Hench, L.L., Polak, J.M., 2002. Third-generation biomedical materials. Science 295, 1014-1017.
- Holzapfel, B.M., Reichert, J.C., Schantz, J.-T., Gbureck, U., Rackwitz, L., Nöth, U., Jakob, F., Rudert, M., Groll, J., Hutmacher, D.W., 2013. How smart do biomaterials need to be? A translational science and clinical point of view. Advanced drug delivery reviews 65, 581-603.
- Hong, J.-Y., Kim, Y.J., Lee, H.-W., Lee, W.-K., Ko, J.S., Kim, H.-M., 2003. Osteoblastic cell response to thin film of poorly crystalline calcium phosphate apatite formed at low temperatures. Biomaterials 24, 2977-2984.
- Hong, Z., Mello, A., Yoshida, T., Luan, L., Stern, P.H., Rossi, A., Ellis, D.E., Ketterson, J.B., 2010. Osteoblast proliferation on hydroxyapatite coated substrates prepared by right angle magnetron sputtering. Journal of Biomedical Materials Research Part A 93, 878-885.
- Hoppe, A., Güldal, N.S., Boccaccini, A.R., 2011. A review of the biological response to ionic dissolution products from bioactive glasses and glass-ceramics. Biomaterials 32, 2757-2774.
- Hosseinabadi, H.N., Sajjady, S.A., Amini, S., 2018. Creating micro textured surfaces for the improvement of surface wettability through ultrasonic vibration assisted turning. The International Journal of Advanced Manufacturing Technology 96, 2825-2839.
- Hotchkiss, K.M., Reddy, G.B., Hyzy, S.L., Schwartz, Z., Boyan, B.D., Olivares-Navarrete, R., 2016. Titanium surface characteristics, including topography and wettability, alter macrophage activation. Acta biomaterialia 31, 425-434.
- Hovgaard, M.B., Rechendorff, K., Chevallier, J., Foss, M., Besenbacher, F., 2008. Fibronectin adsorption on tantalum: the influence of nanoroughness. The Journal of Physical Chemistry B 112, 8241-8249.
- Howlett, C.R., Evans, M.D., Walsh, W.R., Johnson, G., Steele, J.G., 1994. Mechanism of initial attachment of cells derived from human bone to commonly used prosthetic materials during cell culture. Biomaterials 15, 213-222.
- Hu, J., Hardy, C., Chen, C.-M., Yang, S., Voloshin, A.S., Liu, Y., 2014. Enhanced cell adhesion and alignment on micro-wavy patterned surfaces. PLoS One 9, e104502.
- Hu, Q., Tan, Z., Liu, Y., Tao, J., Cai, Y., Zhang, M., Pan, H., Xu, X., Tang, R., 2007. Effect of crystallinity of calcium phosphate nanoparticles on adhesion, proliferation, and differentiation of bone marrow mesenchymal stem cells. Journal of Materials Chemistry 17, 4690-4698.
- Huang, Q., Elkhooly, T.A., Liu, X., Zhang, R., Yang, X., Shen, Z., Feng, Q., 2016. Effects of hierarchical micro/nano-topographies on the morphology, proliferation and

differentiation of osteoblast-like cells. Colloids and Surfaces B: Biointerfaces 145, 37-45.

- Huang, Y., Song, G., Chang, X., Wang, Z., Zhang, X., Han, S., Su, Z., Yang, H., Yang, D., Zhang, X., 2018. Nanostructured Ag+-substituted fluorhydroxyapatite-TiO2 coatings for enhanced bactericidal effects and osteoinductivity of Ti for biomedical applications. International journal of nanomedicine 13, 2665.
- Huang, Y., Song, L., Liu, X., Xiao, Y., Wu, Y., Chen, J., Wu, F., Gu, Z., 2010. Hydroxyapatite coatings deposited by liquid precursor plasma spraying: controlled dense and porous microstructures and osteoblastic cell responses. Biofabrication 2, 045003.
- Ishizaki, T., Saito, N., Takai, O., 2010. Correlation of cell adhesive behaviors on superhydrophobic, superhydrophilic, and micropatterned superhydrophobic/superhydrophilic surfaces to their surface chemistry. Langmuir 26, 8147-8154.
- ISO, I., 2008. 13779-2. Implants for surgery—Hydroxyapatite. Switzerland.
- Jafari, A., Ghoranneviss, Z., Elahi, A.S., Ghoranneviss, M., Yazdi, N.F., Rezaei, A., 2014. Effects of annealing on TiN thin film growth by DC magnetron sputtering. Advances in Mechanical Engineering 6, 373847.
- Jansen, J., Wolke, J., Swann, S., Van Der Waerden, J., De Groof, K., 1993. Application of magnetron sputtering for producing ceramic coatings on implant materials. Clinical oral implants research 4, 28-34.
- Jansen, J.A., Leon, B., 2009. Thin calcium phosphate coatings for medical implants. Springer.
- Jeevitha, D., Amarnath, K., 2013. Chitosan/PLA nanoparticles as a novel carrier for the delivery of anthraquinone: Synthesis, characterization and in vitro cytotoxicity evaluation. Colloids and Surfaces B: Biointerfaces 101, 126-134.
- Jin, H.-B., Guo, C.-B., Mao, K.-Y., Dorozhkin, S., Agathopoulos, S., 2010. Preparation of porous biphasic β-TCP/HA bioceramics with a natural trabecular structure from calcined cancellous bovine bone. Journal of the Ceramic Society of Japan 118, 52-56.
- Johnson, S., Haluska, M., Narayan, R.J., Snyder, R.L., 2006. In situ annealing of hydroxyapatite thin films. Materials Science and Engineering: C 26, 1312-1316.
- Kagawa, A., Ohta, Y., Nakayama, K., 2002. Mechanism of crack generation in carbide surface layer of laser-clad iron alloys. Materials Transactions 43, 1261-1265.
- Karimi, E., Khalil-Allafi, J., Khalili, V., 2016. Electrophoretic deposition of double-layer HA/Al composite coating on NiTi. Materials Science and Engineering: C 58, 882-890.
- Khalili, V., KHALIL, A.J., MALEKI, G.H., 2013. Titanium oxide (TiO2) coatings on NiTi shape memory substrate using electrophoretic deposition process.

- Kim, H.-M., Himeno, T., Kawashita, M., Kokubo, T., Nakamura, T., 2004. The mechanism of biomineralization of bone-like apatite on synthetic hydroxyapatite: an in vitro assessment. Journal of the Royal Society Interface 1, 17-22.
- Klein, C., Wolke, J., de Blieck-Hogervorst, J., De Groot, K., 1994. Calcium phosphate plasma-sprayed coatings and their stability: An in vivo study. Journal of biomedical materials research 28, 909-917.
- Koch, C., Johnson, S., Kumar, D., Jelinek, M., Chrisey, D., Doraiswamy, A., Jin, C., Narayan, R., Mihailescu, I., 2007. Pulsed laser deposition of hydroxyapatite thin films. Materials Science and Engineering: C 27, 484-494.
- Kokubo, T., 1991. Bioactive glass ceramics: properties and applications. Biomaterials 12, 155-163.
- Kongsri, S., Janpradit, K., Buapa, K., Techawongstien, S., Chanthai, S., 2013. Nanocrystalline hydroxyapatite from fish scale waste: Preparation, characterization and application for selenium adsorption in aqueous solution. Chemical engineering journal 215, 522-532.
- Kourkoumelis, N., Balatsoukas, I., Tzaphlidou, M., 2012. Ca/P concentration ratio at different sites of normal and osteoporotic rabbit bones evaluated by Auger and energy dispersive X-ray spectroscopy. Journal of biological physics 38, 279-291.
- Koutsopoulos, S., 2002. Synthesis and characterization of hydroxyapatite crystals: a review study on the analytical methods. Journal of Biomedical Materials Research Part A 62, 600-612.
- Kremers, H.M., Larson, D.R., Crowson, C.S., Kremers, W.K., Washington, R.E., Steiner, C.A., Jiranek, W.A., Berry, D.J., 2015. Prevalence of total hip and knee replacement in the United States. The Journal of bone and joint surgery. American volume 97, 1386.
- Krishna, D.S.R., Sun, Y., Chen, Z., 2011. Magnetron sputtered TiO2 films on a stainless steel substrate: Selective rutile phase formation and its tribological and anti-corrosion performance. Thin Solid Films 519, 4860-4864.
- Kujala, S., Ryhänen, J., Danilov, A., Tuukkanen, J., 2003. Effect of porosity on the osteointegration and bone ingrowth of a weight-bearing nickel–titanium bone graft substitute. Biomaterials 24, 4691-4697.
- Kumari, R., Majumdar, J.D., 2017. Studies on corrosion resistance and bio-activity of plasma spray deposited hydroxylapatite (HA) based TiO2 and ZrO2 dispersed composite coatings on titanium alloy (Ti-6Al-4V) and the same after post spray heat treatment. Applied Surface Science 420, 935-943.
- Kushiro, K., Lee, C.-H., Takai, M., 2016. Simultaneous characterization of protein–material and cell–protein interactions using dynamic QCM-D analysis on SAM surfaces. Biomaterials science 4, 989-997.
- Kuwabara, A., Hori, N., Sawada, T., Hoshi, N., Watazu, A., Kimoto, K., 2012. Enhanced biological responses of a hydroxyapatite/TiO2 hybrid structure when

surface electric charge is controlled using radiofrequency sputtering. Dental materials journal, 2011-2220.

- Kweh, S., Khor, K., Cheang, P., 2002. An in vitro investigation of plasma sprayed hydroxyapatite (HA) coatings produced with flame-spheroidized feedstock. Biomaterials 23, 775-785.
- Le Guehennec, L., Lopez-Heredia, M.-A., Enkel, B., Weiss, P., Amouriq, Y., Layrolle, P., 2008. Osteoblastic cell behaviour on different titanium implant surfaces. Acta Biomaterialia 4, 535-543.
- Lee, C., Park, H., Yoo, J., Lee, C., Woo, W., Park, S., 2015. Residual stress and crack initiation in laser clad composite layer with Co-based alloy and WC+NiCr. Applied Surface Science 345, 286-294.
- Lee, J.W., 2014. Characterisation of hydroxyapatite-coated titanium for biomedical applications. University of Nottingham.
- Lee, K., Park, M., Kim, H., Lim, Y., Chun, H.J., Kim, H., Moon, S., 2006a. Ceramic bioactivity: progresses, challenges and perspectives. Biomedical materials 1, R31.
- Lee, W.-K., Lee, S.-M., Kim, H.-M., 2009. Effect of surface morphology of calcium phosphate on osteoblast-like HOS cell responses. Journal of Industrial and Engineering Chemistry 15, 677-682.
- Lee, Y.-J., Ko, J.S., Kim, H.-M., 2006b. The role of cell signaling defects on the proliferation of osteoblasts on the calcium phosphate apatite thin film. Biomaterials 27, 3738-3744.
- LeGeros, R.Z., 1993. Biodegradation and bioresorption of calcium phosphate ceramics. Clinical Materials 14, 65-88.
- Legeros, R.Z., Craig, R.G., 1993. Strategies to affect bone remodeling: osteointegration. Journal of Bone and Mineral Research 8, S583-S596.
- Legostaeva, E., Kulyashova, K., Komarova, E., Epple, M., Sharkeev, Y.P., Khlusov, I.A., 2013. Physical, chemical and biological properties of micro-arc deposited calcium phosphate coatings on titanium and zirconium-niobium alloy. Materialwissenschaft und Werkstofftechnik 44, 188-197.
- Li, H., Wang, D., Chen, C., Weng, F., 2015a. Effect of CeO2 and Y2O3 on microstructure, bioactivity and degradability of laser cladding CaO–SiO2 coating on titanium alloy. Colloids and Surfaces B: Biointerfaces 127, 15-21.
- Li, H., Wang, D., Chen, C., Weng, F., 2015b. Effect of CeO 2 and Y 2 O 3 on microstructure, bioactivity and degradability of laser cladding CaO–SiO 2 coating on titanium alloy. Colloids and Surfaces B: Biointerfaces 127, 15-21.
- Li, H., Wang, D., Chen, C., Weng, F., Shi, H., 2015c. Phase composition, microstructure and in vitro bioactivity of laser cladding CaO–ZrO2–SiO2 system coatings on titanium alloy. Materials Letters 157, 139-142.

- Li, H., Wang, D., Chen, C., Weng, F., Shi, H., 2015d. Phase composition, microstructure and in vitro bioactivity of laser cladding CaO–ZrO 2–SiO 2 system coatings on titanium alloy. Materials Letters 157, 139-142.
- Li, J., Habibovic, P., Yuan, H., van den Doel, M., Wilson, C.E., de Wijn, J.R., van Blitterswijk, C.A., de Groot, K., 2007. Biological performance in goats of a porous titanium alloy–biphasic calcium phosphate composite. Biomaterials 28, 4209-4218.
- Li, L., Crosby, K., Sawicki, M., Shaw, L.L., Wang, Y., 2012. Effects of surface roughness of hydroxyapatite on cell attachment and proliferation. J. Biotechnol. Biomater 2, 1-5.
- Li, T., Lee, J., Kobayashi, T., Aoki, H., 1996. Hydroxyapatite coating by dipping method, and bone bonding strength. Journal of Materials Science: Materials in Medicine 7, 355-357.
- Liang, H., Shi, B., Fairchild, A., Cale, T., 2004. Applications of plasma coatings in artificial joints: an overview. Vacuum 73, 317-326.
- Lin, J.C., Liu, M., Ju, C., 1994. Structure and properties of hydroxyapatite-bioactive glass composites plasma sprayed on Ti6Al4V. Journal of Materials Science: Materials in Medicine 5, 279-283.
- Liu, S., Li, B., Liang, C., Wang, H., Qiao, Z., 2016. Formation mechanism and adhesive strength of a hydroxyapatite/TiO2 composite coating on a titanium surface prepared by micro-arc oxidation. Applied Surface Science 362, 109-114.
- Liu, X., Chu, P.K., Ding, C., 2004. Surface modification of titanium, titanium alloys, and related materials for biomedical applications. Materials Science and Engineering: R: Reports 47, 49-121.
- Liu, X., Man, H., 2017. Laser fabrication of Ag-HA nanocomposites on Ti6Al4V implant for enhancing bioactivity and antibacterial capability. Materials Science and Engineering: C 70, 1-8.
- Lopez-Heredia, M.A., Sohier, J., Gaillard, C., Quillard, S., Dorget, M., Layrolle, P., 2008. Rapid prototyped porous titanium coated with calcium phosphate as a scaffold for bone tissue engineering. Biomaterials 29, 2608-2615.
- Losina, E., Barrett, J., Mahomed, N.N., Baron, J.A., Katz, J.N., 2004. Early failures of total hip replacement: effect of surgeon volume. Arthritis & Rheumatism: Official Journal of the American College of Rheumatology 50, 1338-1343.
- Lu, X., Leng, Y., 2009. Comparison of the osteoblast and myoblast behavior on hydroxyapatite microgrooves. Journal of Biomedical Materials Research Part B: Applied Biomaterials 90, 438-445.
- Lukić, M., Stojanović, Z., Škapin, S.D., Maček-Kržmanc, M., Mitrić, M., Marković, S., Uskoković, D., 2011. Dense fine-grained biphasic calcium phosphate (BCP) bioceramics designed by two-step sintering. Journal of the European Ceramic Society 31, 19-27.

- Lusquiños, F., Pou, J., Arias, J., Boutinguiza, M., León, B., Pérez-Amor, M., Driessens, F., Merry, J., Gibson, I., Best, S., 2001. Production of calcium phosphate coatings on Ti6Al4V obtained by Nd: yttrium–aluminum–garnet laser cladding. Journal of Applied Physics 90, 4231-4236.
- Majeed, A., He, J., Jiao, L., Zhong, X., Sheng, Z., 2015. Surface properties and biocompatibility of nanostructured TiO 2 film deposited by RF magnetron sputtering. Nanoscale research letters 10, 56.
- Mansur, M.R., Wang, J., Berndt, C.C., 2013. Microstructure, composition and hardness of laser-assisted hydroxyapatite and Ti-6Al-4V composite coatings. Surface and Coatings Technology 232, 482-488.
- Mantripragada, V.P., Lecka-Czernik, B., Ebraheim, N.A., Jayasuriya, A.C., 2013. An overview of recent advances in designing orthopedic and craniofacial implants. Journal of biomedical materials research Part A 101, 3349-3364.
- Matsuzaka, K., Walboomers, X.F., Yoshinari, M., Inoue, T., Jansen, J.A., 2003. The attachment and growth behavior of osteoblast-like cells on microtextured surfaces. Biomaterials 24, 2711-2719.
- Mattox, D.M., 2010. Handbook of physical vapor deposition (PVD) processing. William Andrew.
- Maya, A.A., Grana, D., Hazarabedian, A., Kokubu, G., Luppo, M., Vigna, G., 2012. Zr–Ti–Nb porous alloys for biomedical application. Materials Science and Engineering: C 32, 321-329.
- Mayrhofer, P., Kunc, F., Musil, J., Mitterer, C., 2002. A comparative study on reactive and non-reactive unbalanced magnetron sputter deposition of TiN coatings. Thin Solid Films 415, 151-159.
- Mccafferty, M.H., Lepow, M., Saba, T.M., Cho, E., Meuwissen, H., White, J., Zuckerbrod, S.F., 1983. Normal fibronectin levels as a function of age in the pediatric population. Pediatric research 17, 482-485.
- McPherson, R., Gane, N., Bastow, T., 1995. Structural characterization of plasma-sprayed hydroxylapatite coatings. Journal of Materials Science: Materials in Medicine 6, 327-334.
- Mello, A., Hong, Z., Rossi, A., Luan, L., Farina, M., Querido, W., Eon, J., Terra, J., Balasundaram, G., Webster, T., 2007. Osteoblast proliferation on hydroxyapatite thin coatings produced by right angle magnetron sputtering. Biomedical Materials 2, 67.
- Mirhosseini, N., Crouse, P., Schmidth, M., Li, L., Garrod, D., 2007. Laser surface micro-texturing of Ti–6Al–4V substrates for improved cell integration. Applied Surface Science 253, 7738-7743.
- Mohseni, E., Zalnezhad, E., Bushroa, A.R., 2014. Comparative investigation on the adhesion of hydroxyapatite coating on Ti–6Al–4V implant: A review paper. International Journal of Adhesion and Adhesives 48, 238-257.

- Mohseni, E., Zalnezhad, E., Bushroa, A.R., Abdel Magid, H., Goh, B.T., Yoon, G.H., 2015. Ti/TiN/HA coating on Ti–6Al–4V for biomedical applications. Ceramics International 41, 14447-14457.
- Moon, B.-S., Kim, S., Kim, H.-E., Jang, T.-S., 2017. Hierarchical micro-nano structured Ti6Al4V surface topography via two-step etching process for enhanced hydrophilicity and osteoblastic responses. Materials Science and Engineering: C 73, 90-98.
- Morks, M., 2008. Fabrication and characterization of plasma-sprayed HA/SiO2 coatings for biomedical application. Journal of the mechanical behavior of biomedical materials 1, 105-111.
- Moura, C.C., Souza, M.A., Dechichi, P., Zanetta-Barbosa, D., Teixeira, C.C., Coelho, P.G., 2010. The effect of a nanothickness coating on rough titanium substrate in the osteogenic properties of human bone cells. Journal of Biomedical Materials Research Part A: An Official Journal of The Society for Biomaterials, The Japanese Society for Biomaterials, and The Australian Society for Biomaterials and the Korean Society for Biomaterials 94, 103-111.
- Mukhametkaliyev, T.M., Surmeneva, M.A., Vladescu, A., Cotrut, C.M., Braic, M., Dinu, M., Vranceanu, M.D., Pana, I., Mueller, M., Surmenev, R.A., 2017. A biodegradable AZ91 magnesium alloy coated with a thin nanostructured hydroxyapatite for improving the corrosion resistance. Materials Science and Engineering: C 75, 95-103.
- Nag, S., Banerjee, R., 2012. Fundamentals of medical implant materials. ASM handbook 23, 6-17.
- Nag, S., Paital, S.R., Nandawana, P., Mahdak, K., Ho, Y.H., Vora, H.D., Banerjee, R., Dahotre, N.B., 2013. Laser deposited biocompatible Ca–P coatings on Ti–6Al–4V: Microstructural evolution and thermal modeling. Materials Science and Engineering: C 33, 165-173.
- Narushima, T., Ueda, K., Goto, T., Masumoto, H., Katsube, T., Kawamura, H., Ouchi, C., Iguchi, Y., 2005. Preparation of calcium phosphate films by radiofrequency magnetron sputtering. Materials transactions 46, 2246-2252.
- Nelea, V., Morosanu, C., Bercu, M., Mihailescu, I.N., 2007. Interfacial titanium oxide between hydroxyapatite and TiAlFe substrate. Journal of Materials Science: Materials in Medicine 18, 2347-2354.
- Nelea, V., Morosanu, C., Iliescu, M., Mihailescu, I., 2004. Hydroxyapatite thin films grown by pulsed laser deposition and radio-frequency magnetron sputtering: comparative study. Applied Surface Science 228, 346-356.
- Nelea, V., Ristoscu, C., Chiritescu, C., Ghica, C., Mihailescu, I., Pelletier, H., Mille, P., Cornet, A., 2000. Pulsed laser deposition of hydroxyapatite thin films on Ti-5Al-2.5 Fe substrates with and without buffer layers. Applied Surface Science 168, 127-131.

- Nguyen, H., Deporter, D., Pilliar, R., Valiquette, N., Yakubovich, R., 2004. The effect of sol–gel-formed calcium phosphate coatings on bone ingrowth and osteoconductivity of porous-surfaced Ti alloy implants. Biomaterials 25, 865-876.
- Nimkerdphol, A.R., Otsuka, Y., Mutoh, Y., 2014. Effect of dissolution/precipitation on the residual stress redistribution of plasma-sprayed hydroxyapatite coating on titanium substrate in simulated body fluid (SBF). Journal of the mechanical behavior of biomedical materials 36, 98-108.
- Novaes Jr, A.B., Souza, S.L.S.d., Barros, R.R.M.d., Pereira, K.K.Y., Iezzi, G., Piattelli, A., 2010. Influence of implant surfaces on osseointegration. Brazilian dental journal 21, 471-481.
- Nuss, K.M., von Rechenberg, B., 2008. Biocompatibility issues with modern implants in bone-a review for clinical orthopedics. The open orthopaedics journal 2, 66.
- Ogose, A., Hotta, T., Kawashima, H., Kondo, N., Gu, W., Kamura, T., Endo, N., 2005. Comparison of hydroxyapatite and beta tricalcium phosphate as bone substitutes after excision of bone tumors. Journal of Biomedical Materials Research Part B: Applied Biomaterials: An Official Journal of The Society for Biomaterials, The Japanese Society for Biomaterials, and The Australian Society for Biomaterials and the Korean Society for Biomaterials 72, 94-101.
- Okauchi-Yabuuchi, M., Tamamura, R., Nagaoka, N., Takagi, S., Kishimoto, E., Takagi, T., Rodriguez, A., Inoue, M., Nagatsuka, H., Akao, M., 2008. Chemical analysis of a novel coating material, CaTiO3-ac. Journal of hard tissue biology 17, 115-120.
- Okazaki, Y., Rao, S., Asao, S., Tateishi, T., Katsuda, S.-i., Furuki, Y., 1998. Effects of Ti, Al and V concentrations on cell viability. Materials Transactions, JIM 39, 1053-1062.
- Ong, J., Lucas, L., Lacefield, W., Rigney, E., 1992. Structure, solubility and bond strength of thin calcium phosphate coatings produced by ion beam sputter deposition. Biomaterials 13, 249-254.
- Oshida, Y., 2010. Bioscience and bioengineering of titanium materials. Elsevier.
- Oyane, A., Kim, H.M., Furuya, T., Kokubo, T., Miyazaki, T., Nakamura, T., 2003. Preparation and assessment of revised simulated body fluids. Journal of Biomedical Materials Research Part A 65, 188-195.
- Ozeki, K., Yuhta, T., Aoki, H., Nishimura, I., Fukui, Y., 2001. Push-out strength of hydroxyapatite coated by sputtering technique in bone. Bio-medical materials and engineering 11, 63-68.
- Paital, S.R., Balani, K., Agarwal, A., Dahotre, N.B., 2008. Fabrication and evaluation of a pulse laser-induced Ca–P coating on a Ti alloy for bioapplication. Biomedical Materials 4, 015009.

- Paital, S.R., Dahotre, N.B., 2009. Wettability and kinetics of hydroxyapatite precipitation on a laser-textured Ca–P bioceramic coating. Acta biomaterialia 5, 2763-2772.
- Paital, S.R., He, W., Dahotre, N.B., 2010. Laser pulse dependent micro textured calcium phosphate coatings for improved wettability and cell compatibility. Journal of Materials Science: Materials in Medicine 21, 2187-2200.
- Pamu, D., Sudheendran, K., Ghanashyam Krishna, M., James Raju, K., 2008. Crystallographic texture, morphology, optical, and microwave dielectric properties of dc magnetron sputtered nanostructured zirconia thin films. Journal of Vacuum Science & Technology A: Vacuum, Surfaces, and Films 26, 185-192.
- Pandey, A., Midha, S., Sharma, R.K., Maurya, R., Nigam, V.K., Ghosh, S., Balani, K., 2018. Antioxidant and antibacterial hydroxyapatite-based biocomposite for orthopedic applications. Materials Science and Engineering: C 88, 13-24.
- Pandey, L.M., Le Denmat, S., Delabouglise, D., Bruckert, F., Pattanayek, S.K., Weidenhaupt, M., 2012. Surface chemistry at the nanometer scale influences insulin aggregation. Colloids and Surfaces B: Biointerfaces 100, 69-76.
- Pandey, L.M., Pattanayek, S.K., 2011. Hybrid surface from self-assembled layer and its effect on protein adsorption. Applied Surface Science 257, 4731-4737.
- Pandey, L.M., Pattanayek, S.K., 2013a. Properties of competitively adsorbed BSA and fibrinogen from their mixture on mixed and hybrid surfaces. Applied Surface Science 264, 832-837.
- Pandey, L.M., Pattanayek, S.K., 2013b. Relation between the wetting effect and the adsorbed amount of water-soluble polymers or proteins at various interfaces. Journal of Chemical & Engineering Data 58, 3440-3446.
- Pandey, L.M., Pattanayek, S.K., Delabouglise, D., 2013. Properties of adsorbed bovine serum albumin and fibrinogen on self-assembled monolayers. The Journal of Physical Chemistry C 117, 6151-6160.
- Pantojas, V.M., Velez, E., Hernandez, D., Otano, W., 2009. Initial study on fibers and coatings for the fabrication of bioscaffolds. Puerto Rico health sciences journal 28.
- Pichugin, V.F., Surmenev, R.A., Shesterikov, E.V., Ryabtseva, M.A., Eshenko, E.V., Tverdokhlebov, S.I., Prymak, O., Epple, M., 2008. The preparation of calcium phosphate coatings on titanium and nickel–titanium by rf-magnetron-sputtered deposition: Composition, structure and micromechanical properties. Surface and Coatings Technology 202, 3913-3920.
- Pisarek, M., Roguska, A., Andrzejczuk, M., Marcon, L., Szunerits, S., Lewandowska, M., Janik-Czachor, M., 2011. Effect of two-step functionalization of Ti by chemical processes on protein adsorption. Applied Surface Science 257, 8196-8204.
- Porter, A., Rea, S., Galtrey, M., Best, S., Barber, Z., 2004. Production of thin film silicon-doped hydroxyapatite via sputter deposition. Journal of materials science 39, 1895-1898.

- Pradhan, S.S., Sahoo, S., Pradhan, S., 2010. Influence of annealing temperature on the structural, mechanical and wetting property of TiO2 films deposited by RF magnetron sputtering. Thin Solid Films 518, 6904-6908.
- Pratap, T., Patra, K., 2018a. Fabrication of micro-textured surfaces using ball-end micromilling for wettability enhancement of Ti-6Al-4V. Journal of Materials Processing Technology 262, 168-181.
- Pratap, T., Patra, K., 2018b. Mechanical micro-texturing of Ti-6Al-4V surfaces for improved wettability and bio-tribological performances. Surface and Coatings Technology 349, 71-81.
- Prosolov, K., Popova, K., Belyavskaya, O., Rau, J., Gross, K., Ubelis, A., Sharkeev, Y.P., 2017. RF magnetron-sputtered coatings deposited from biphasic calcium phosphate targets for biomedical implant applications. Bioactive Materials 2, 170-176.
- Putkonen, M., Sajavaara, T., Rahkila, P., Xu, L., Cheng, S., Niinistö, L., Whitlow, H.J., 2009. Atomic layer deposition and characterization of biocompatible hydroxyapatite thin films. Thin Solid Films 517, 5819-5824.
- Qi, J., Chen, Z., Han, W., He, D., Yang, Y., Wang, Q., 2017. Effect of deposition parameters and heat-treatment on the microstructure, mechanical and electrochemical properties of hydroxyapatite/titanium coating deposited on Ti6Al4V by RF-magnetron sputtering. Materials Research Express 4, 096409.
- Qiu, D., Yang, L., Yin, Y., Wang, A., 2011. Preparation and characterization of hydroxyapatite/titania composite coating on NiTi alloy by electrochemical deposition. Surface and Coatings Technology 205, 3280-3284.
- Quéré, D., 2008. Wetting and roughness. Annu. Rev. Mater. Res. 38, 71-99.
- Quirama, A., Echavarría, A.M., Meza, J., Osorio, J., Bejarano, G., 2017. Improvement of the mechanical behavior of the calcium phosphate coatings deposited onto Ti6Al4V alloy using an intermediate TiN/TiO2 bilayer. Vacuum 146, 22-30.
- Rabiei, A., Thomas, B., Jin, C., Narayan, R., Cuomo, J., Yang, Y., Ong, J., 2006. A study on functionally graded HA coatings processed using ion beam assisted deposition with in situ heat treatment. Surface and Coatings Technology 200, 6111-6116.
- Rakngarm, A., Mutoh, Y., 2009. Characterization and fatigue damage of plasma sprayed HAp top coat with Ti and HAp/Ti bond coat layers on commercially pure titanium substrate. Journal of the mechanical behavior of biomedical materials 2, 444-453.
- Ramesh, S., Aw, K.L., Tolouei, R., Amiriyan, M., Tan, C.Y., Hamdi, M., Purbolaksono, J., Hassan, M.A., Teng, W.D., 2013. Sintering properties of hydroxyapatite powders prepared using different methods. Ceramics International 39, 111-119.

- Ratner, B.D., Hoffman, A.S., 2013. Chapter I.2.12 - Physicochemical Surface Modification of Materials Used in Medicine, In: Ratner, B.D., Hoffman, A.S., Schoen, F.J., Lemons, J.E. (Eds.), Biomaterials Science (Third Edition). Academic Press, pp. 259-276.
- Ratner, B.D., Hoffman, A.S., Schoen, F.J., Lemons, J.E., 2004. Biomaterials science: an introduction to materials in medicine. Elsevier.
- Ratner, B.D., Hoffman, A.S., Schoen, F.J., Lemons, J.E., 2006. Biomaterials science: an introduction to materials in medicine. MRS Bull 31, 59.
- Rechendorff, K., Hovgaard, M.B., Foss, M., Zhdanov, V., Besenbacher, F., 2006. Enhancement of protein adsorption induced by surface roughness. Langmuir 22, 10885-10888.
- Rho, J.-Y., Kuhn-Spearing, L., Zioupos, P., 1998. Mechanical properties and the hierarchical structure of bone. Medical engineering & physics 20, 92-102.
- Richard, D., Dumelié, N., Benhayoune, H., Bouthors, S., Guillaume, C., Lalun, N., Balossier, G., Laurent-Maquin, D., 2006. Behavior of human osteoblast-like cells in contact with electrodeposited calcium phosphate coatings. Journal of Biomedical Materials Research Part B: Applied Biomaterials: An Official Journal of The Society for Biomaterials, The Japanese Society for Biomaterials, and The Australian Society for Biomaterials and the Korean Society for Biomaterials 79, 108-115.
- Rocha, R.C., Galdino, A.G.d.S., Silva, S.N.d., Machado, M.L.P., 2018. Surface, microstructural, and adhesion strength investigations of a bioactive hydroxyapatite-titanium oxide ceramic coating applied to Ti-6Al-4V alloys by plasma thermal spraying. Materials Research 21.
- Rodriguez, O., Matinmanesh, A., Phull, S., Schemitsch, E.H., Zalzal, P., Clarkin, O.M., Papini, M., Towler, M.R., 2016. Silica-based and borate-based, titania-containing bioactive coatings characterization: critical strain energy release rate, residual stresses, hardness, and thermal expansion. Journal of functional biomaterials 7, 32.
- Roguska, A., Hiromoto, S., Yamamoto, A., Woźniak, M.J., Pisarek, M., Lewandowska, M., 2011. Collagen immobilization on 316L stainless steel surface with cathodic deposition of calcium phosphate. Applied Surface Science 257, 5037-5045.
- Roşu, R.A., Şerban, V.-A., Bucur, A.I., Dragoş, U., 2012. Deposition of titanium nitride and hydroxyapatite-based biocompatible composite by reactive plasma spraying. Applied Surface Science 258, 3871-3876.
- Roy, M., Balla, V.K., Bandyopadhyay, A., Bose, S., 2011a. Compositionally graded hydroxyapatite/tricalcium phosphate coating on Ti by laser and induction plasma. Acta biomaterialia 7, 866-873.

- Roy, M., Bandyopadhyay, A., Bose, S., 2011b. Induction plasma sprayed nano hydroxyapatite coatings on titanium for orthopaedic and dental implants. Surface and Coatings Technology 205, 2785-2792.
- Sadeghi, M., Kharaziha, M., Salimijazi, H., Tabesh, E., 2019. Role of micro-dimple array geometry on the biological and tribological performance of Ti6Al4V for biomedical applications. Surface and Coatings Technology 362, 282-292.
- Sahoo, C.K., Masanta, M., 2015. Effect of pulse laser parameters on TiC reinforced AISI 304 stainless steel composite coating by laser surface engineering process. Optics and Lasers in Engineering 67, 36-48.
- Sahoo, S., Goel, M., Gandhi, P., Saxena, S., 2013. Biological aspects of dental implant; Current knowledge and perspectives in oral implantology. Dental Hypotheses 4, 87.
- Saju, K., Reshmi, R., Jayadas, N., James, J., Jayaraj, M., 2009. Polycrystalline coating of hydroxyapatite on TiAl6V4 implant material grown at lower substrate temperatures by hydrothermal annealing after pulsed laser deposition. Proceedings of the Institution of Mechanical Engineers, Part H: Journal of Engineering in Medicine 223, 1049-1057.
- Samanta, A., Bhattacharya, M., Ratha, I., Chakraborty, H., Datta, S., Ghosh, J., Bysakh, S., Sreemany, M., Rane, R., Joseph, A., Mukherjee, S., Kundu, B., Das, M., Mukhopadhyay, A.K., 2018. Nano- and micro-tribological behaviours of plasma nitrided Ti6Al4V alloys. Journal of the Mechanical Behavior of Biomedical Materials 77, 267-294.
- San Thian, E., Huang, J., Barber, Z.H., Best, S.M., Bonfield, W., 2011. Surface modification of magnetron-sputtered hydroxyapatite thin films via silicon substitution for orthopaedic and dental applications. Surface and Coatings Technology 205, 3472-3477.
- Sarma, B.K., Das, A., Barman, P., Pal, A.R., 2016. Biomimetic growth and substrate dependent mechanical properties of bone like apatite nucleated on Ti and magnetron sputtered TiO2 nanostructure. Journal of Physics D: Applied Physics 49, 145304.
- Schmidt, C., Kaspar, D., Sarkar, M.R., Claes, L.E., Ignatius, A.A., 2002. A scanning electron microscopy study of human osteoblast morphology on five orthopedic metals. Journal of biomedical materials research 63, 252-261.
- Schutz, R.W., 1987. Corrosion of titanium and titanium alloys;(ASMI Handbook Committee. Metals Handbook, Corrosion 13, 669-706.
- Schwartz, Z., Lohmann, C., Vocke, A., Sylvia, V., Cochran, D., Dean, D., Boyan, B., 2001. Osteoblast response to titanium surface roughness and 1α, 25-(OH) 2D3 is mediated through the mitogen-activated protein kinase (MAPK) pathway. Journal of Biomedical Materials Research: An Official Journal of The Society for Biomaterials, The Japanese Society for Biomaterials, and The Australian Society for Biomaterials and the Korean Society for Biomaterials 56, 417-426.

- Schwartz, Z., Olivares-Navarrete, R., Wieland, M., Cochran, D.L., Boyan, B.D., 2009. Mechanisms regulating increased production of osteoprotegerin by osteoblasts cultured on microstructured titanium surfaces. Biomaterials 30, 3390-3396.
- Sharma, I., Pattanayek, S.K., 2017. Effect of surface energy of solid surfaces on the micro- and macroscopic properties of adsorbed BSA and lysozyme. Biophysical Chemistry 226, 14-22.
- Sima, L.E., Stan, G.E., Morosanu, C.O., Melinescu, A., Ianculescu, A., Melinte, R., Neamtu, J., Petrescu, S.M., 2010. Differentiation of mesenchymal stem cells onto highly adherent radio frequency-sputtered carbonated hydroxylapatite thin films. Journal of Biomedical Materials Research Part A 95, 1203-1214.
- Singh, G., Singh, S., Prakash, S., 2011. Surface characterization of plasma sprayed pure and reinforced hydroxyapatite coating on Ti6Al4V alloy. Surface and Coatings Technology 205, 4814-4820.
- Snyders, R., Bousser, E., Music, D., Jensen, J., Hocquet, S., Schneider, J.M., 2008. Influence of the Chemical Composition on the Phase Constitution and the Elastic Properties of RF-Sputtered Hydroxyapatite Coatings. Plasma Processes and Polymers 5, 168-174.
- Socol, G., Macovei, A., Miroiu, F., Stefan, N., Duta, L., Dorcioman, G., Mihailescu, I., Petrescu, S., Stan, G., Marcov, D., 2010. Hydroxyapatite thin films synthesized by pulsed laser deposition and magnetron sputtering on PMMA substrates for medical applications. Materials Science and Engineering: B 169, 159-168.
- Stango, S.A.X., Karthick, D., Swaroop, S., Mudali, U.K., Vijayalakshmi, U., 2018. Development of hydroxyapatite coatings on laser textured 316 LSS and Ti-6Al-4V and its electrochemical behavior in SBF solution for orthopedic applications. Ceramics International 44, 3149-3160.
- Sun, L., Berndt, C.C., Gross, K.A., Kucuk, A., 2001. Material fundamentals and clinical performance of plasma-sprayed hydroxyapatite coatings: A review. Journal of Biomedical Materials Research: An Official Journal of The Society for Biomaterials, The Japanese Society for Biomaterials, and The Australian Society for Biomaterials and the Korean Society for Biomaterials 58, 570-592.
- Sun, Y.-S., Chang, J.-H., Huang, H.-H., 2013. Corrosion resistance and biocompatibility of titanium surface coated with amorphous tantalum pentoxide. Thin Solid Films 528, 130-135.
- Sun, Y.-S., Huang, H.-H., 2018. Biphasic calcium phosphates/tantalum pentoxide hybrid layer and its effects on corrosion resistance and biocompatibility of titanium surface for orthopedic implant applications. Journal of Alloys and Compounds 743, 99-107.
- Surmenev, R.A., 2012. A review of plasma-assisted methods for calcium phosphate-based coatings fabrication. Surface and Coatings Technology 206, 2035-2056.

- Surmenev, R.A., Ryabtseva, M., Shesterikov, E.V., Pichugin, V.F., Peitsch, T., Epple, M., 2010. The release of nickel from nickel–titanium (NiTi) is strongly reduced by a sub-micrometer thin layer of calcium phosphate deposited by rf-magnetron sputtering. Journal of Materials Science: Materials in Medicine 21, 1233-1239.
- Surmenev, R.A., Surmeneva, M.A., Evdokimov, K.E., Pichugin, V.F., Peitsch, T., Epple, M., 2011. The influence of the deposition parameters on the properties of an rf-magnetron-deposited nanostructured calcium phosphate coating and a possible growth mechanism. Surface and coatings technology 205, 3600-3606.
- Surmenev, R.A., Surmeneva, M.A., Grubova, I.Y., Chernozem, R.V., Krause, B., Baumbach, T., Loza, K., Epple, M., 2017. RF magnetron sputtering of a hydroxyapatite target: A comparison study on polytetrafluorethylene and titanium substrates. Applied Surface Science 414, 335-344.
- Surmenev, R.A., Surmeneva, M.A., Ivanova, A.A., 2014. Significance of calcium phosphate coatings for the enhancement of new bone osteogenesis–A review. Acta biomaterialia 10, 557-579.
- Surmeneva, M., Vladescu, A., Surmenev, R., Pantilimon, C., Braic, M., Cotrut, C., 2016. Study on a hydrophobic Ti-doped hydroxyapatite coating for corrosion protection of a titanium based alloy. RSC Advances 6, 87665-87674.
- Surmeneva, M.A., Chaikina, M.V., Zaikovskiy, V.I., Pichugin, V.F., Buck, V., Prymak, O., Epple, M., Surmenev, R.A., 2013. The structure of an RF-magnetron sputter-deposited silicate-containing hydroxyapatite-based coating investigated by high-resolution techniques. Surface and Coatings Technology 218, 39-46.
- Surmeneva, M.A., Mukhametkaliyev, T.M., Tyurin, A., Teresov, A., Koval, N.N., Pirozhkova, T., Shuvarin, I., Shuklinov, A., Zhigachev, A., Oehr, C., 2015. Effect of silicate doping on the structure and mechanical properties of thin nanostructured RF magnetron sputter-deposited hydroxyapatite films. Surface and Coatings Technology 275, 176-184.
- Surmeneva, M.A., Sharonova, A.A., Chernousova, S., Prymak, O., Loza, K., Tkachev, M.S., Shulepov, I.A., Epple, M., Surmenev, R.A., 2017. Incorporation of silver nanoparticles into magnetron-sputtered calcium phosphate layers on titanium as an antibacterial coating. Colloids and Surfaces B: Biointerfaces 156, 104-113.
- Surmeneva, M.A., Surmenev, R.A., 2015a. Microstructure characterization and corrosion behaviour of a nano-hydroxyapatite coating deposited on AZ31 magnesium alloy using radio frequency magnetron sputtering. Vacuum 117, 60-62.
- Surmeneva, M.A., Surmenev, R.A., 2015b. Microstructure characterization and corrosion behaviour of a nano-hydroxyapatite coating deposited on AZ31 magnesium alloy using radio frequency magnetron sputtering. Vacuum 117, 60-62.
- Surmeneva, M.A., Surmenev, R.A., Pichugin, V.F., Chernousova, S., Epple, M., 2011. In-vitro investigation of magnetron-sputtered coatings based on silicon-

substituted hydroxyapatite. Journal of Surface Investigation. X-ray, Synchrotron and Neutron Techniques 5, 1202-1207.

- Suzuki, Y., Nomura, N., Hanada, S., Kamakura, S., Anada, T., Fuji, T., Honda, Y., Masuda, T., Sasaki, K., Kokubun, S., 2007. Osteoconductivity of porous titanium having young's modulus similar to bone and surface modification by OCP, Key Engineering Materials. Trans Tech Publ, pp. 951-954.
- Tampieri, A., Celotti, G., Sprio, S., Mingazzini, C., 2000. Characteristics of synthetic hydroxyapatites and attempts to improve their thermal stability. Materials Chemistry and Physics 64, 54-61.
- Terleeva, O., Sharkeev, Y.P., Slonova, A.e.a., Mironov, I., Legostaeva, E., Khlusov, I.A., Matykina, E., Skeldon, P., Thompson, G., 2010. Effect of microplasma modes and electrolyte composition on micro-arc oxidation coatings on titanium for medical applications. Surface and Coatings Technology 205, 1723-1729.
- Thian, E., Huang, J., Best, S., Barber, Z., Bonfield, W., 2005. Magnetron co-sputtered silicon-containing hydroxyapatite thin films—an in vitro study. Biomaterials 26, 2947-2956.
- Thian, E., Huang, J., Best, S., Barber, Z., Bonfield, W., 2006a. Novel silicon-doped hydroxyapatite (Si-HA) for biomedical coatings: An in vitro study using acellular simulated body fluid. Journal of Biomedical Materials Research Part B: Applied Biomaterials: An Official Journal of The Society for Biomaterials, The Japanese Society for Biomaterials, and The Australian Society for Biomaterials and the Korean Society for Biomaterials 76, 326-333.
- Thian, E., Huang, J., Best, S., Barber, Z., Bonfield, W., 2006b. Silicon-substituted hydroxyapatite thin films: Effect of annealing temperature on coating stability and bioactivity. Journal of Biomedical Materials Research Part A: An Official Journal of The Society for Biomaterials, The Japanese Society for Biomaterials, and The Australian Society for Biomaterials and the Korean Society for Biomaterials 78, 121-128.
- Thian, E., Huang, J., Best, S., Barber, Z., Bonfield, W., 2007. Silicon-substituted hydroxyapatite: The next generation of bioactive coatings. Materials Science and Engineering: C 27, 251-256.
- Tlotleng, M., Akinlabi, E., Shukla, M., Pityana, S., 2014. Microstructures, hardness and bioactivity of hydroxyapatite coatings deposited by direct laser melting process. Materials Science and Engineering: C 43, 189-198.
- Toque, J., Herliansyah, M., Hamdi, M., Ide-Ektessabi, A., Sopyan, I., 2010. Adhesion failure behavior of sputtered calcium phosphate thin film coatings evaluated using microscratch testing. Journal of the mechanical behavior of biomedical materials 3, 324-330.

- Toque, J.A., Hamdi, M., Ide-Ektessabi, A., Sopyan, I., 2009. Effect of the processing parameters on the integrity of calcium phosphate coatings produced by RF-magnetron sputtering. International Journal of Modern Physics B 23, 5811-5818.
- Türk, S., Altınsoy, I., Efe, G.Ç., Ipek, M., Özacar, M., Bindal, C., 2019. Biomimetic synthesis of Ag, Zn or Co doped HA and coating of Ag, Zn or Co doped HA/fMWCNT composite on functionalized Ti. Materials Science and Engineering: C 99, 986-998.
- Tutak, W., Jyotsnendu, G., Bajcsy, P., Simon, C.G., 2017. Nanofiber scaffolds influence organelle structure and function in bone marrow stromal cells. Journal of Biomedical Materials Research Part B: Applied Biomaterials 105, 989-1001.
- UEDA, K., KAWASAKI, Y., NARUSHIMA, T., GOTO, T., KURIHARA, J., NAKAGAWA, H., KAWAMURA, H., TAIRA, M., 2009. Calcium phosphate films with/without heat treatments fabricated using RF magnetron sputtering. Journal of Biomechanical Science and Engineering 4, 392-403.
- Ueda, K., Narushima, T., Goto, T., Taira, M., Katsube, T., 2007. Fabrication of calcium phosphate films for coating on titanium substrates heated up to 773 K by RF magnetron sputtering and their evaluations. Biomedical Materials 2, S160.
- Ungula, J., Dejene, B.F., Swart, H.C., 2017. Effect of annealing on the structural, morphological and optical properties of Ga-doped ZnO nanoparticles by reflux precipitation method. Results in Physics 7, 2022-2027.
- van der Wal, E., Oldenburg, S.J., Heij, T., Denier van der Gon, A.W., Brongersma, H.H., Wolke, J.G.C., Jansen, J.A., Vredenberg, A.M., 2006. Adsorption and desorption of Ca and PO4 species from SBFs on RF-sputtered calcium phosphate thin films. Applied Surface Science 252, 3843-3854.
- Van Dijk, K., Schaeken, H., Wolke, J., Jansen, J., 1996. Influence of annealing temperature on RF magnetron sputtered calcium phosphate coatings. Biomaterials 17, 405-410.
- Vandrovcova, M., Hanus, J., Drabik, M., Kylian, O., Biederman, H., Lisa, V., Bacakova, L., 2012. Effect of different surface nanoroughness of titanium dioxide films on the growth of human osteoblast-like MG63 cells. Journal of biomedical materials research Part A 100, 1016-1032.
- Variola, F., Brunski, J.B., Orsini, G., de Oliveira, P.T., Wazen, R., Nanci, A., 2011. Nanoscale surface modifications of medically relevant metals: state-of-the art and perspectives. Nanoscale 3, 335-353.
- Verket, A., Tiainen, H., Haugen, H.J., Lyngstadaas, S.P., Nilsen, O., Reseland, J.E., 2012. Enhanced osteoblast differentiation on scaffolds coated with TiO 2 compared to SiO 2 and CaP coatings. Biointerphases 7, 36.
- Vilotijević, M., Marković, P., Zec, S., Marinković, S., Jokanović, V., 2011. Hydroxyapatite coatings prepared by a high power laminar plasma jet. Journal of Materials Processing Technology 211, 996-1004.

- Viswanath, B., Raghavan, R., Gurao, N.P., Ramamurty, U., Ravishankar, N., 2008. Mechanical properties of tricalcium phosphate single crystals grown by molten salt synthesis. Acta Biomaterialia 4, 1448-1454.
- Wan, T., Aoki, H., Hikawa, J., Lee, J.H., 2007. RF-magnetron sputtering technique for producing hydroxyapatite coating film on various substrates. Bio-medical materials and engineering 17, 291-297.
- Wang, C., Ma, J., Cheng, W., Zhang, R., 2002. Thick hydroxyapatite coatings by electrophoretic deposition. Materials Letters 57, 99-105.
- Wang, D., Chen, C., Ma, J., Lei, T., 2007. Microstructure of yttric calcium phosphate bioceramic coatings synthesized by laser cladding. Applied surface science 253, 4016-4020.
- Wang, D., Chen, C., Ma, J., Zhang, G., 2008. In situ synthesis of hydroxyapatite coating by laser cladding. Colloids and Surfaces B: biointerfaces 66, 155-162.
- Wang, G., Zreiqat, H., 2010. Functional coatings or films for hard-tissue applications. Materials 3, 3994-4050.
- Wang, K., Zhou, C., Hong, Y., Zhang, X., 2012. A review of protein adsorption on bioceramics. Interface focus, rsfs20120012.
- Wang, M.L., Sharkey, P.F., Tuan, R.S., 2004. Particle bioreactivity and wear-mediated osteolysis. The Journal of arthroplasty 19, 1028-1038.
- Wang, R., Bai, S., 2015. Wettability of laser micro-circle-dimpled SiC surfaces. Applied Surface Science 346, 107-110.
- Wang, Y., Li, Y., Yu, H., Ding, J., Tang, X., Li, J., Zhou, Y., 2005. In situ fabrication of bioceramic composite coatings by laser cladding. Surface and Coatings Technology 200, 2080-2084.
- Wang, Y., Wang, L., Zheng, H., Du, C., Shi, Z., Xu, C., 2010. Effect of frequency on the structure and cell response of Ca-and P-containing MAO films. Applied Surface Science 256, 2018-2024.
- Weidong, Z., Qibin, L., Min, Z., Xudong, W., 2008. Biocompatibility of a functionally graded bioceramic coating made by wide-band laser cladding. Journal of Biomedical Materials Research Part A 87, 429-433.
- Weng, F., Chen, C., Yu, H., 2014. Research status of laser cladding on titanium and its alloys: A review. Materials & Design 58, 412-425.
- Wolke, J., Van Dijk, K., Schaeken, H., De Groot, K., Jansen, J., 1994. Study of the surface characteristics of magnetron-sputter calcium phosphate coatings. Journal of biomedical materials research 28, 1477-1484.
- Wolke, J.G.C., van der Waerden, J.P.C.M., Schaeken, H.G., Jansen, J.A., 2003. In vivo dissolution behavior of various RF magnetron-sputtered Ca-P coatings on roughened titanium implants. Biomaterials 24, 2623-2629.

- Xia, L., Xie, Y., Fang, B., Wang, X., Lin, K., 2018. In situ modulation of crystallinity and nano-structures to enhance the stability and osseointegration of hydroxyapatite coatings on Ti-6Al-4V implants. Chemical Engineering Journal 347, 711-720.
- Xu, J., Khor, K.A., 2007. Chemical analysis of silica doped hydroxyapatite biomaterials consolidated by a spark plasma sintering method. Journal of Inorganic Biochemistry 101, 187-195.
- Xue, W., Hosick, H.L., Bandyopadhyay, A., Bose, S., Ding, C., Luk, K., Cheung, K., Lu, W., 2007. Preparation and cell–materials interactions of plasma sprayed strontium-containing hydroxyapatite coating. Surface and Coatings technology 201, 4685-4693.
- Yamashita, K., Arashi, T., Kitagaki, K., Yamada, S., Umegaki, T., Ogawa, K., 1994. Preparation of apatite thin films through rf-sputtering from calcium phosphate glasses. Journal of the American Ceramic Society 77, 2401-2407.
- Yang, S., Man, H.C., Xing, W., Zheng, X., 2009. Adhesion strength of plasma-sprayed hydroxyapatite coatings on laser gas-nitrided pure titanium. Surface and Coatings Technology 203, 3116-3122.
- Yang, Y., Kim, K.-H., Ong, J.L., 2005. A review on calcium phosphate coatings produced using a sputtering process—an alternative to plasma spraying. Biomaterials 26, 327-337.
- Yang, Y., Paital, S.R., Dahotre, N.B., 2010. Effects of SiO2 substitution on wettability of laser deposited Ca-P biocoating on Ti-6Al-4V. Journal of Materials Science: Materials in Medicine 21, 2511-2521.
- Yang, Y., Serpersu, K., He, W., Paital, S.R., Dahotre, N.B., 2011. Osteoblast interaction with laser cladded HA and SiO 2-HA coatings on Ti–6Al–4V. Materials Science and Engineering: C 31, 1643-1652.
- Yap, F., Zhang, Y., 2007. Protein and cell micropatterning and its integration with micro/nanoparticles assembly. Biosensors and Bioelectronics 22, 775-788.
- Yılmaz, E., Çakıroğlu, B., Gökçe, A., Findik, F., Gulsoy, H.O., Gulsoy, N., Mutlu, Ö., Özacar, M., 2019. Novel hydroxyapatite/graphene oxide/collagen bioactive composite coating on Ti16Nb alloys by electrodeposition. Materials Science and Engineering: C 101, 292-305.
- Yonggang, Y., Wolke, J., Yubao, L., Jansen, J., 2007. The influence of discharge power and heat treatment on calcium phosphate coatings prepared by RF magnetron sputtering deposition. Journal of Materials Science: Materials in Medicine 18, 1061-1069.
- Yongli, C., Xiufang, Z., Yandao, G., Nanming, Z., Tingying, Z., Xinqi, S., 1999. Conformational changes of fibrinogen adsorption onto hydroxyapatite and titanium oxide nanoparticles. Journal of colloid and interface science 214, 38-45.
- Yoon, H.-J., Song, J.-E., Um, Y.-J., Chae, G.J., Chung, S.-M., Lee, I.-S., Jung, U.-W., Kim, C.-S., Choi, S.-H., 2009. Effects of calcium phosphate coating to SLA surface

implants by the ion-beam-assisted deposition method on self-contained coronal defect healing in dogs. Biomedical Materials 4, 044107.

- Yoshinari, M., Hayakawa, T., Wolke, J., Nemoto, K., Jansen, J., 1997. Influence of rapid heating with infrared radiation on RF magnetron-sputtered calcium phosphate coatings. Journal of Biomedical Materials Research: An Official Journal of The Society for Biomaterials and The Japanese Society for Biomaterials 37, 60-67.
- Zelzer, M., Albutt, D., Alexander, M.R., Russell, N.A., 2012. The role of albumin and fibronectin in the adhesion of fibroblasts to plasma polymer surfaces. Plasma Processes and Polymers 9, 149-156.
- Zhang, J., Guan, R., Zhang, X., 2011a. Synthesis and characterization of sol–gel hydroxyapatite coatings deposited on porous NiTi alloys. Journal of Alloys and Compounds 509, 4643-4648.
- Zhang, M.Y., Ye, C., Erasquin, U.J., Huynh, T., Cai, C., Cheng, G.J., 2011b. Laser engineered multilayer coating of biphasic calcium phosphate/titanium nanocomposite on metal substrates. ACS applied materials & interfaces 3, 339-350.
- Zhao, G., Raines, A., Wieland, M., Schwartz, Z., Boyan, B., 2007. Requirement for both micron-and submicron scale structure for synergistic responses of osteoblasts to substrate surface energy and topography. Biomaterials 28, 2821-2829.
- Zhao, L., Mei, S., Chu, P.K., Zhang, Y., Wu, Z., 2010. The influence of hierarchical hybrid micro/nano-textured titanium surface with titania nanotubes on osteoblast functions. Biomaterials 31, 5072-5082.
- Zhao, X., Liu, X., Ding, C., Chu, P.K., 2006a. In vitro bioactivity of plasma-sprayed TiO2 coating after sodium hydroxide treatment. Surface and Coatings Technology 200, 5487-5492.
- Zhao, Y., Zhang, Z., Dai, Q., Lin, D., Li, S., 2006b. Microstructure and bond strength of HA (+ ZrO2+ Y2O3)/Ti6Al4V composite coatings fabricated by RF magnetron sputtering. Surface and Coatings Technology 200, 5354-5363.
- Zheng, M., Fan, D., Li, X.-K., Li, W.-F., Liu, Q.-B., Zhang, J.-B., 2008. Microstructure and osteoblast response of gradient bioceramic coating on titanium alloy fabricated by laser cladding. Applied Surface Science 255, 426-428.
- Zhu, Z., Yu, H., Zeng, Q., He, H., 2008. Characterization and biocompatibility of fluoridated biphasic calcium phosphate ceramics. Applied Surface Science 255, 552-554.

APPENDIX-A

Specification of field emission scanning electron microscope (FESEM)

Make	Zeiss
Model	Sigma
Chamber	330 mm inner diameter, 270 mm height
Specimen weight	up to 200 g
Movement	X = 125 mm, Y = 125 mm, Z = 50 mm
Stage	5-axis Motorized Cartesian
Detector	In lens, SE-2, BSD
Magnification range	100 X to 2000 kX

Specification of optical microscope

Make	Carl Zeiss
Model	Axiotech-100 HD, 3D
Chamber	330 mm inner diameter, 270 mm height
Specimen weight	up to 200g
Stage movement	3 axis measuring system, reflect light measuring
	X = 75 mm, Y = 50 mm, Z = 50 mm
Lens	Binocular photo tube
Magnification range	5 X to 200 X
Software	Axio-Cam and Axiovision 4.8.2 (in built)

Specification of Raman spectrometer

Make	Horiba Jobin Vyon
Model	LabRAM HR
Wavelength	632.8 nm
Laser power	13.5 mW

Specification of non-contact 3-D profilometer

Make	Taylor Hobson
Model	CCI-Lite
Magnification range	20 X
Precision	1 megapixel
Power supply	220 V
Focal distance	4.7 mm
Field of view	0.825 mm × 0.825 mm

Specification of X-ray Diffractometer (XRD)

Make	Rigaku
Model	TTRAX 3
Radiation	Cu-Kα
Wavelength	1.54059 A^{o}
Voltage	50 kV
Current	160 mA
speed	3^{o}/min

Specification of Fourier-transform infrared spectroscopy (FTIR)

Make	Perkin Elmer
Model	Spectrum BXII
Mode	Reflectance
Scanning rate	12 scan/sec
Resolution	4 cm^{-1}
Wavenumber	400 to 4000 cm^{-1}

APPENDIX-B

Laser Cladding with HA and Functionally Graded TiO_2-HA Precursors on Ti–6Al–4V for Enhancing Bioactivity as well as Cyto-compatibility

A.1 Theme of work

Laser cladding (LC) process was developed to fabricate Ca-P coatings due to its ability to form a strong metallurgical bonding between the coated material and Ti-6Al-4V substrate. Also, LC has the potential to obtain suitable surface chemistry and surface textures to enhance the biocompatibility as well as bioactivity of metallic surfaces at tissue–implant interface (Paital et al., 2010). Though LC is superior to other surface modification treatment, there indeed are some defects, such as cracks and pores in the laser cladded layer. Due to a significant mismatch in elastic moduli, thermal coefficient of expansion and hardness between CaP based bioceramic and Ti alloy, a sharp interface is generated between coating and base material. i.e. no gradual change in microstructure between coating and substrate. This leads to a reduction of bond strength and crack formation (Weng et al., 2014). To control the cracks and improve the bonding strength, many researchers mixed a certain percentage of pure Ti powders with CaP based bioceramic due to similar thermal expansion coefficient of Ti with that of the substrate (Mansur et al., 2013). Furthermore, to enhance metallurgical bonding at the interface and bioactivity on the surface of coating, a functionally graded coating (consisting CaP and Ti) was designed and fabricated with laser cladding (Weidong et al., 2008; Zhang et al., 2011b; Zheng et al., 2008).

Instead of pure Ti powder, Titania (TiO_2) powder was mixed with CaP-based bioceramic to enhance the adhesion between bioceramic and Ti substrate as its coefficient of thermal expansion is nearly equal to Ti substrate (Araghi and Hadianfard, 2015a). Also, TiO_2 promotes calcium and phosphate precipitation and has the chemical affinity for both Ti substrates as well as CaP based bioceramic (Balla et al., 2009; He et al., 2008).

Even though CaP-TiO_2 coatings have been carried out successfully on Ti alloy by various processes, however, there is limited reported literature regarding LC of CaP-TiO_2 on Ti alloy. Besides, less attention has been paid for observing different biological responses during LC of CaP-TiO_2 on Ti alloy. Hence, in the present study, a pulsed Nd:YAG laser was used during LC of CaP based bio-ceramic coating on Ti-6Al-4V with different precursors:

100 wt.% HA and functionally graded HA-TiO_2 material (FGM) in order to obtain multiphase, micro-textured coating with better metallurgical bonding at the interface. The coating characterisation such as surface morphology, elemental composition, phases and wettability of produced coatings were studied in this study. *In vitro* bioactivity, protein adsorption as well as *in vitro* biocompatibility consisting cell adhesion and cyto-compatibility were also investigated and compared with that in bare Ti-6Al-4V.

A.2.Materials and methods

A.2.1 Substrate preparation and preplacing of coating

Ti-6Al-4V plates with 40×30×3 mm^3 dimension were cut by wire-electro discharge machining process and used as the substrate. In order to remove the oxide layer from the surface, the cut substrates were polished with 80 µm grit silicon carbide emery papers and then rinsed with acetone. The substrate surface was immediately preplaced by the mixture of precursor and PVA in order to prevent oxidation after sandpaper grinding. HA and TiO2 was used as the cladding material. Two different compositions of preplaced powders were used for LC: (1) 100% HA and (2) functionally graded TiO_2-HA material (FGM). The composition design for preplacing of 100% HA and FGM consisting of five layers are shown in Figure A.1. PVA, a water-based organic solvent was used as the binder material in the current investigation. PVA binder was prepared in the laboratory according to the procedure described previously (Tlotleng et al., 2014).

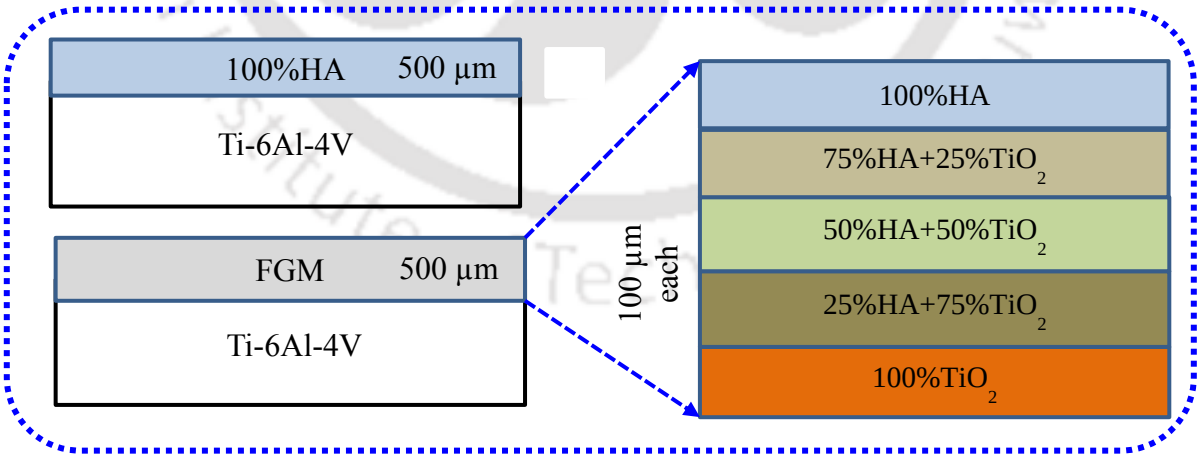

Figure A.1: *Composition design for preplacing of 100% HA and FGM precursor on Ti-6Al-4V.*

The precursor powders were mixed with PVA binder with a ratio of 50:50 in wt.% and then well blended for 20 min to obtain a viscous slurry which was painted with a brush onto the preheated (50 ºC) Ti–6Al–4V substrate. The preplaced powder beds were dried in a

fume cupboard for 6 h to remove moisture. The thickness of each preplaced layer was controlled to 100 µm, as measured using a digital micrometre. The same procedure was repeated for each layer of preplacing to make the pre-coating sample as the functionally graded composite of 500 µm thickness.

A.2.2 Experimental set-up and procedure

LC was carried out by scanning the already prepared pre-placed powder beds using pulsed Nd:YAG laser (Model: Accucut-500, Suresh Indu Pvt. Ltd., India) with 500 W maximum power and wavelength of 1.064 µm to obtain a textured surface with metallurgical bonding between the Ti-6Al-4V and coating material. Figure A.2 represents the LC system consisting of central laser source unit, gas supply and cooling unit was used in the present investigation.

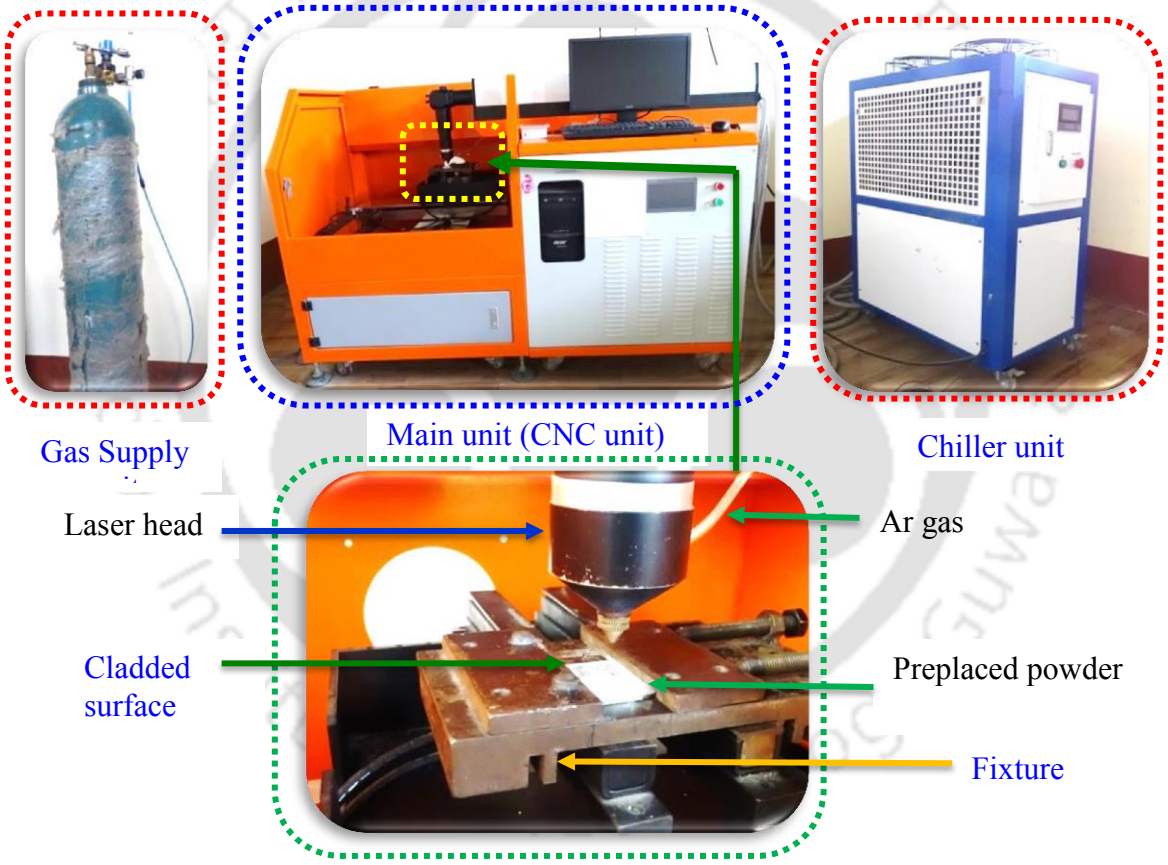

Figure A.2: *Experimental set up for laser cladding process.*

The laser beam had a Gaussian intensity distribution. Using a 100 mm focal length convex lens, the laser beam was focused on the preplaced substrate surface, giving a spot diameter of approximately 200 µm. The spot size was maintained at 1 mm approximately on the substrate surface by keeping the defocused laser beam 10 mm above the workpiece surface. Different parameters of laser beam such as current (which determines average power), pulse width and pulse repetition rate were regulated by the control panel of laser

system. In order to protect the surface from oxidization, experiments were carried out in an argon (Ar) gas shielded atmosphere with a minimum flow rate of 10 lit/min. This Ar gas was fed at 0.2 MPa pressure through a nozzle which is coaxial with the laser beam.

The quality of the cladded layer generated in LC process relies on the choice of laser processing parameters, such as average power (P_{avg}), scanning speed (*SS*) and laser beam size (*D*). The P_{avg} depends upon peak power (P_{peak}), laser pulse duration (*PD*) and laser pulse repetition rate (*f*) during processing with the pulsed laser, as shown in Eq. (A.1). Furthermore, P_{peak} depends upon input current (*I*), applied voltage (*V*) and efficiency of the laser (η = 4%), as shown in Eq. (A.2). All these input parameters finally determine the laser energy density (LED), which is nothing but the incident of laser energy per unit area of the sample. This LED is also termed as laser fluence (F) which can be calculated according to Eq. (A.3) (Liu and Man, 2017). Laser irradiance is another essential factor determined by laser power per unit area (Eq. (A.4)).

$$P_{avg} = P_{peak} \times PD \times f \tag{A.1}$$

$$P_{peak} = \eta \times V \times I \tag{A.2}$$

$$LED(J/mm^2) = \frac{P_{avg}(J/s)}{SS(mm/s) \times D(mm)} \tag{A.3}$$

$$Laser\ irradiance(W/mm^2) = \frac{P_{avg}(W)}{(\pi/4) \times D^2(mm^2)} \tag{A.4}$$

In order to obtain the desired cladding, a particular value of LED is required. Thus, preliminary experimental trials were done using different values of LED by changing the values of *I* and keeping other parameters like *SS*, *PD* and *f* constant. Table A.1 presents the processing parameters used in the present investigation. When LED of 18 J /mm^2 was applied to Ti-6Al-4V with 100% HA preplaced layer, a complete layer of coating was not formed on the substrate due to insufficient energy to melt and bond the preplaced layer with the substrate (Figure A.3 (a)). Furthermore, when very high LED (25.2 J/mm^2) was applied, much more cracks were observed on the surface of the clad layer due to the generation of high thermal stress between preplaced layer and substrate at high LED, as seen in Figure A.3 (c). So, a middle value of LED (21.6 J/mm^2) was applied to obtain a complete clad layer without any crack, as shown in Figure A.3 (b). Thus the required LED to obtain desired coating was 21.6 J/mm^2 with corresponding input parameter set: *I* = 60 A, *SS* = 4 mm/s, *PD* = 3 ms and *f* = 20 Hz. The same LED was also applied to Ti-6Al-4V containing FGM

preplaced layer, and the results are shown in Figure A.3 (d, e, f). In order to achieve continuous coating of the whole sample surface, same LED (21.6 J/mm^2) was applied multi times with track spacing of 0.8 mm (gap between centers of two adjacent tracks), since the laser beam diameter at the substrate surface was retained at 1 mm. After LC, the substrates were ultrasonically cleaned with deionized water and then prepared for characterization.

Table A. 1: Input parameters used in the present work

Laser fluence or LED, J/mm^2	18, 21.6, 25.2
Laser irradiance, W/mm^2	91.7, 110, 128.3
Input current (*I*), A	50, 60, 70
Scanning speed (*SS*), mm/s	4
Pulse duration (*PD*), ms	3
Pulse repetition frequency (*f*), Hz	20
Defocus distance, mm	10
Spot diameter on the surface, mm	1
Ar gas flow rate, l/min	10
Line spacing, mm	0.8

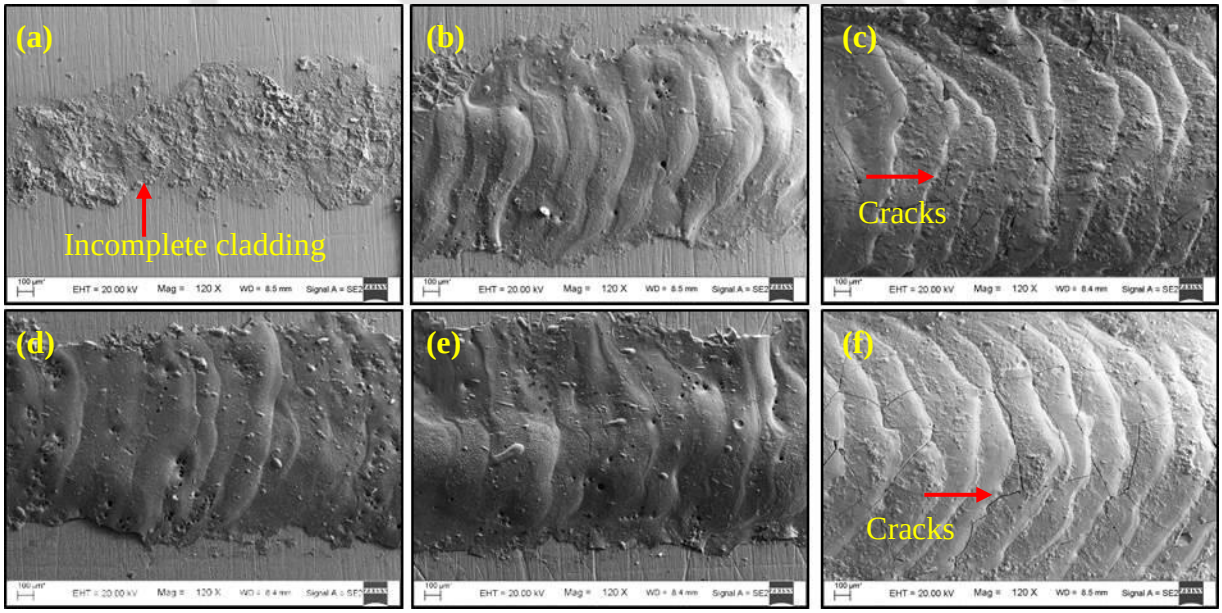

Figure A.3: *Top surfaces of single line 100% HA and FGM cladding at different LED: (a, d) 18.0 J/mm^2, (b, e) 21.6 J/mm^2 and (c, f) 25.2 J/mm^2.*

A.2.3 Characterization

A.2.3.1 Clad dimension, microstructure and elemental analysis

The clad dimension including clad width and thickness was measured by FESEM. The microstructure and morphological studies of LC at the surface as well as cross-section were

investigated by FESEM and attached EDS to determine the elemental contents of the cladding samples. Before EDS analysis on the cladding sample, calibration was conducted on cobalt (Co) which was used as a standard. Different areas were scanned on the cladding samples, and the corresponding atomic percentages of elements were noted down. The average values of all the corresponding elements were taken as the final output. For cross-section morphology observation, the produced claddings were cut, mounted and grounded for microstructural observation. The polished samples were etched with a solution of HF, HNO_3 and distilled H_2O at a ratio of 1:2:25 by volume to predict the microstructure as well as growth morphologies of different compounds in LC.

A.2.3.2 Characterization and wettability

The phase, surface morphology and elemental analyses of cladded surfaces were investigated by XRD, FESEM and EDS, respectively. The wettability of surfaces of bare Ti-6Al-4V, 100% HA and FGM cladding were evaluated by the procedure as described in chapter 2. The average value of five contact angles taken at various positions was considered as the mean contact angle for each LC. The surface roughness of cladded samples was measured by using a contact type 2-D surface profilometer (Taylor Hobson, UK). Roughness parameter like center line average height (R_a) was recorded. As the surface roughness of the cladded samples was more, hence, the sampling length of 12 mm was taken into consideration with a cut-off length of 2.4 mm. A total of five random readings parallel to the laser track were taken for each sample, and the average one was considered as output response.

A.2.3.3 Biological performances

Protein adsorption, cell adhesion and proliferation, in vitro bioactivity of different clad surfaces were investigated by the procedure described in chapter 4.

A.3 Results and discussion

A.3.1 Clad dimensions

The top surface of single line laser cladding with 100% HA and FGM precursor at different LEDs: 18.0 J/mm^2, 21.6J/mm^2 and 25.2 J/mm^2 are shown in Figure A.3. It can be seen that the clad width for 100% HA cladding is gradually increasing from 0.75 mm to 1.33 mm with the increase in LED from 18 J/mm^2 to 25.2 J/mm^2 (Figure A.3 (a-c)). Also, it is higher in case of FGM cladding as compared to 100% HA cladding for all the LEDs (Figure A.3 (d-f)).

Figure A.4 represents the low magnification cross-sectional images of 100% HA and FGM laser cladded sample at two different LED 21.6 J/mm^2 and 25.2 J/mm^2. It can be visible that, the cladding profiles of both 100% HA, as well as FGM, consists of two distinct layers at lower as well as higher LED. The top layer of cladding is identified as the crust layer (CL). Beneath the CL, transition layer (TL) is present where the transition of elements between cladding and substrate occurs. Table A.2 shows the variation of clad width and thickness (including CL and TL thickness) concerning LED for both 100% HA and FGM cladding.

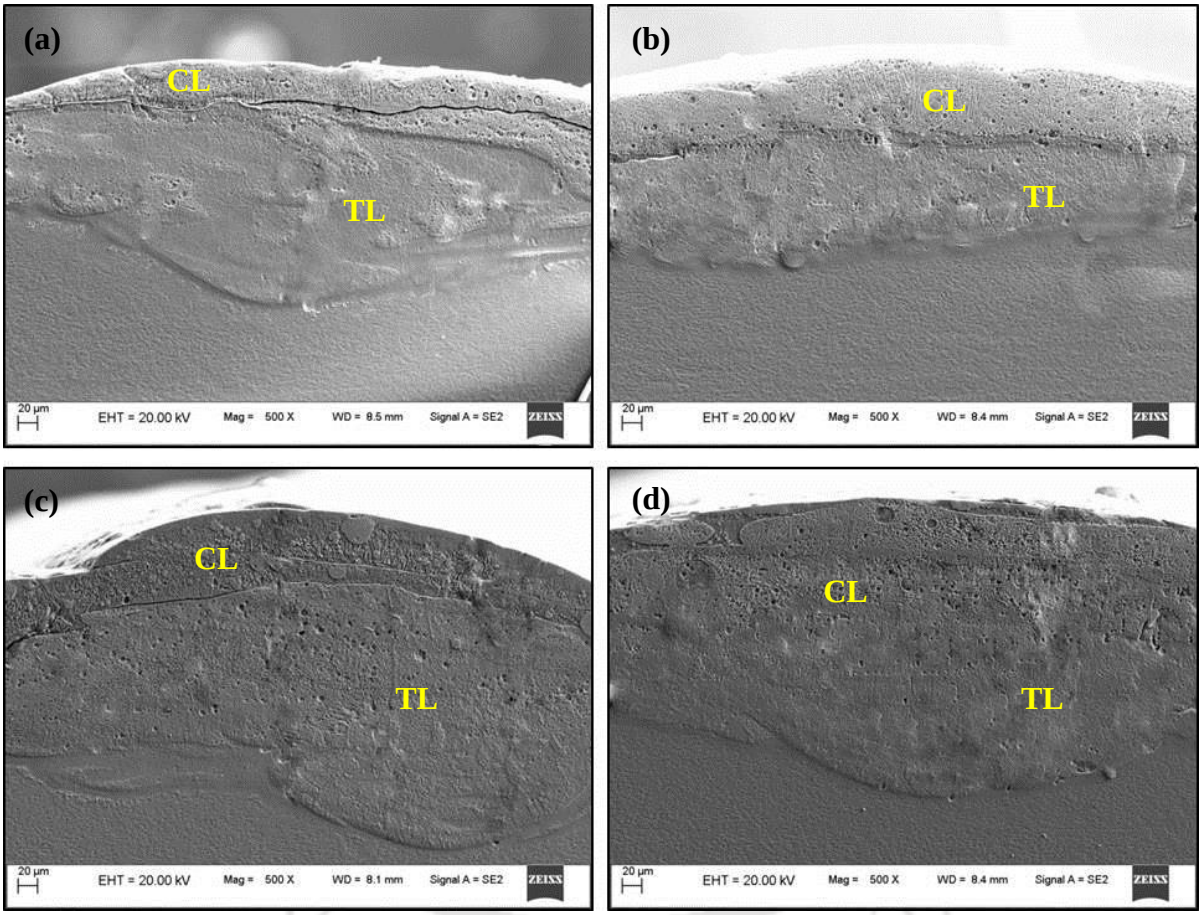

Figure A.4: *Cross-section of clad profiles of 100% HA and FGM cladding samples at LED of (a, b) 21.6 J/mm^2 and (c, d) 25.2 J/mm^2.*

Though the preplaced layer thickness for both the specimens before cladding was maintained to 500 µm, however, the CL thickness was found in between 40-120 µm depending upon the composition of the precursor as well as LED. The PVA binder was vaporized from the precursor (PVA: powder = 50:50) during laser cladding due to its vaporization temperature is 240 ºC, as reported by Chien et al. (2011a). Hence, the thickness was reduced. Additional reduction of the thickness of CL was due to melting and dilution of precursor during laser cladding process. Furthermore, the total thickness of clad with CL and

TL thickness was more at higher LED (25.2 J/mm^2). As laser cladding is a thermal process, where laser beam melts the precursor and little portion of the substrate, hence, with the increase in LED, both the precursor as well as the substrate material were melted more. So, larger clad width and thickness (including CL as well as TL thickness) was found with a higher value of LED. Therefore, with no cracks in the clad surface and less dilution (i.e. lower TL thickness) at 21.6 J/mm^2 LED, this was chosen for other characterization.

Table A. 2: Variation of clad dimensions with respect to LED

Cladding	LED (J/mm^2)	Clad width (mm)	Clad thickness (µm)	CL thickness (µm)	TL thickness (µm)
100% HA	21.6	1.12±0.15	227±19	40±5	189±17
	25.2	1.33±0.24	306±24	75±6	229±26
FGM	21.6	1.28±0.26	175±16	74±10	103±17
	25.2	1.56±0.38	254±39	115±17	141±28

In addition, it was observed that the total thickness of clad was higher in case of 100% HA cladding as compared to FGM cladding. However, the CL thickness was less in case of 100% HA cladding than FGM cladding. i.e. TL thickness was bigger in 100% HA cladding than FGM cladding (Figure A.4). Also, the width of the clad was bigger in FGM cladding compared to 100% HA cladding (Figure A.3).

It is a well-known fact that laser cladding is a heat treatment process where metallurgical bonding takes place between cladding material and substrate. The metallurgical bonding is generally enhanced if the cladding material or one of the constituents of the same is matched with the substrate material (Zheng et al., 2008). Due to the presence of TiO_2 in FGM cladding, the chemical affinity between cladding and substrate was more compared to HA cladding. Hence, higher CL width and thickness were found in FGM cladding. With the same applied LED, the fraction of energy required for melting the precursor is higher in case of FGM cladding compared to HA cladding. This is due to the higher melting point of TiO_2 (~1800 ºC) compared to HA (~1670 ºC) and Ti (~1668 ºC) (Balla et al., 2009; Cheng et al., 2005). Hence, less energy is transferred to substrate material indicating lower TL thickness in case of FGM cladding. In other words, it can be concluded that LED required to obtain the

same dimension of the clad layer is less in case of FGM cladding compared to 100% HA cladding. From the observations as mentioned above in FGM cladding, it was revealed that all the different precursor layers are converted into two layers, such as CL and TL after laser cladding indicating proper mixing and melting of precursor layers with the dilution of the substrate layer.

A.3.2 Microstructural and elemental analysis

Figure A.5 shows the cross-sectional images of 100% HA and FGM sample after laser cladding at 21.6 J/mm^2. In 100% HA cladding, cellular microstructure was observed in bottom part of CL just above the TL (Figure A.5 (a)), whereas dendritic structure existed in the upper part of CL (Figure A.5 (b)). However, in FGM cladding, the dendritic structure was present at the bottom part of CL (Figure A.5 (c)) and the cellular structure was observed in upper part of CL (Figure A.5 (d)). A sound interface with higher thickness was existed in FGM cladding indicating better metallurgical bonding between CL and TL as compared to 100% HA cladding (Figure A.5 (a, c)).

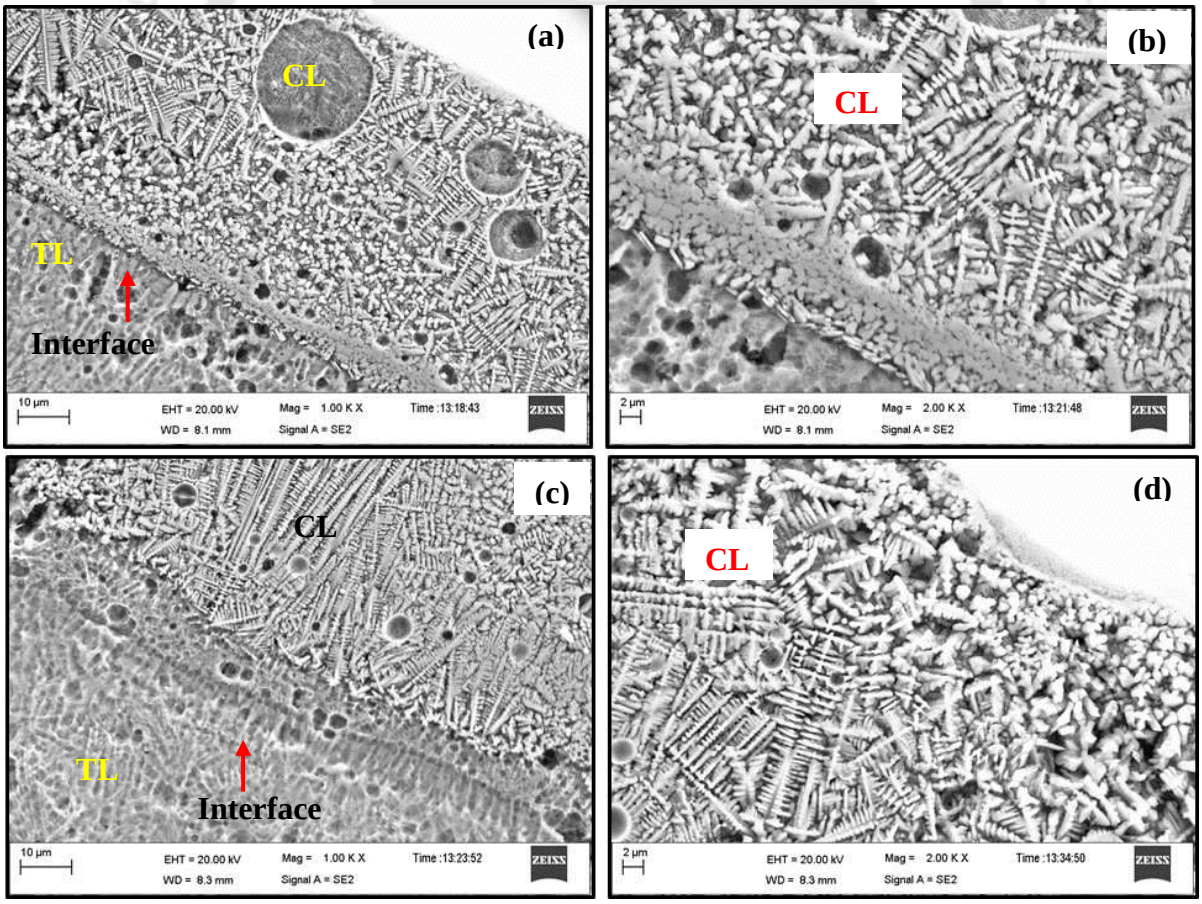

Figure A.5: *Cross-sectional morphology of 100% HA and FGM laser cladding at LED 21.6 J/mm^2 (a, c) interface between CL and TL (low magnification) and (b, d) CL (high magnification).*

As LC is a rapid heating and solidification process, the ratio of the temperature gradient (G) to solidification rate (R) plays a vital role on microstructure evolution of each region during LC (Li et al., 2015a).

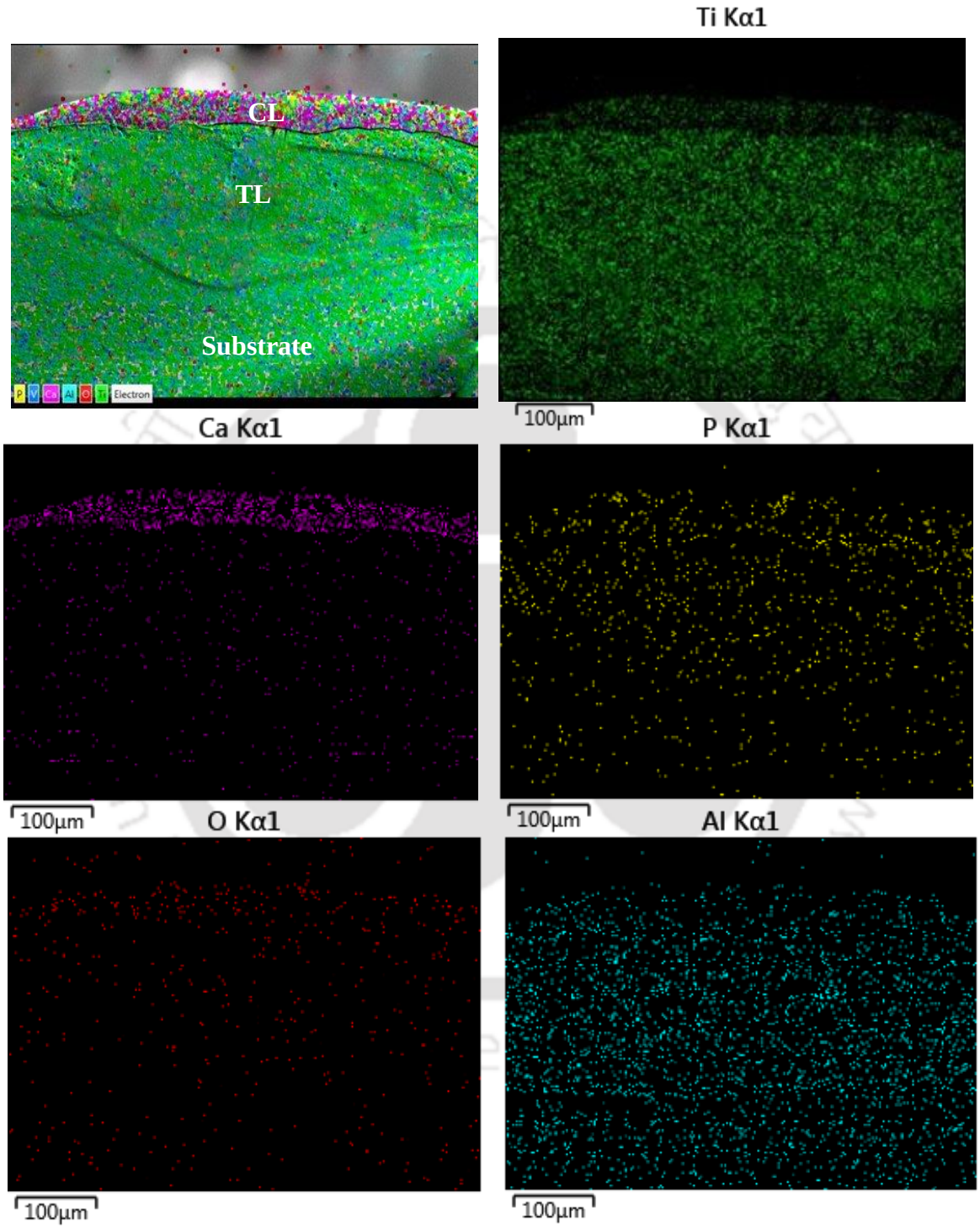

Figure A.6: *Elemental mapping comparison of Ca, P, Ti, O, Al contents in CL and TL in 100% HA laser cladding.*

With the constant process parameter, R gradually increases from the bottom of the molten pool to top, while G is decreased. This causes a decrease of G/R ratio from bottom to

top of the CL (Wang et al., 2005). With the higher value of G/R ratio at the bottom of CL, the cellular structure was formed.

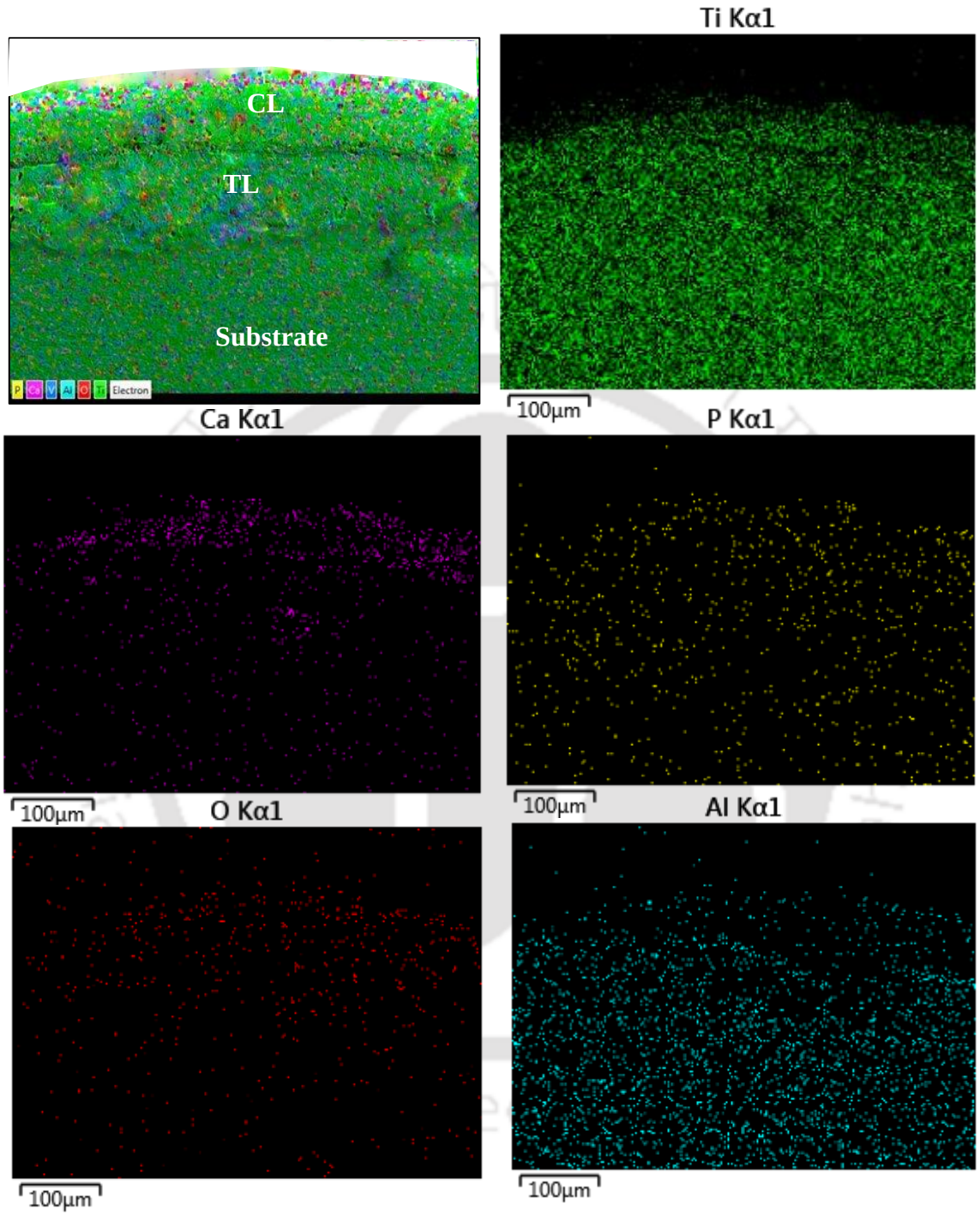

Figure A.7: *Elemental mapping comparison of Ca, P, Ti, O, Al contents in CL and TL in FGM laser cladding.*

This cellular structure was gradually converted to dendritic structure with gradually decreasing G/R ratio from bottom to top of the molten pool. The complete dendritic structure was found at the top part of CL of 100% HA cladding due to the lower value of G/R ratio (Li et al., 2015a). Similarly, the dendritic structure was observed in the CL of FGM cladding;

however, the cellular structure was found at the uppermost part of CL. This may be due to constitutional supercooling in FGM cladding which induces necking of dendritic crystal. Because of high-speed convection in the molten pool, the necking part is ruptured and generates cellular structure (Wang et al., 2007). Hence, the cellular crystal was formed in the top part of the CL layer in FGM cladding.

The elemental mapping of CL and TL of 100% HA and FGM cladding are illustrated in Figure A.6 and Figure A.7, respectively. It can be seen that the five different preplaced layers were converted into one single composite layer after LC (Figure A.7). Due to the melting of precursor and a little portion of the substrate, mixing occurred between these two, which resulted in one single composite layer after solidification. In 100% HA cladding sample, CL was mainly consisted of Ca as well as O (Figure A.6). In TL, the amount of P was higher than that in CL. Similarly, Ca and O were mainly present in CL in FGM cladding; however, P was almost distributed equally in both CL and TL. Hence, it was concluded that more amount of P was diffused into TL in 100% HA cladding than FGM cladding.

Due to high temperature in laser cladding, HA was decomposed to $Ca_3(PO_4)_2$, $Ca_2P_2O_7$ and then CaO. Thus significant evaporation of P from CL and diffusion of P into TL occurred (Chien et al., 2011a; Chien et al., 2011b). Higher Ti was distributed in TL in 100% HA cladding, whereas CL consisted lower amount of Ti. However, higher Ti was seen in CL in FGM than 100% HA cladding because of the presence of TiO_2 in the FGM preplaced layer. In both the cladding, Al was distributed in the coating as well as in substrate; however, higher Al was observed in CL of 100% HA than FGM cladding indicating lower dilution of the substrate in FGM cladding.

From these results, it can be concluded that inter-diffusion of elements occurred between coating and substrate during both LC. However, less dilution of substrate occurred in FGM than 100% HA cladding. Due to diffusion of elements from coating to substrate and vice-versa concludes that, strong metallurgical bonding occurred between coating and substrate for both claddings. In addition, the total percentage of calcium phosphate HA was almost half in 500 μm thick FGM preplaced layer compared to 500 μm thick 100% HA layer before the cladding process. This was due to the presence of an equal mass of TiO_2 and HA in five layers FGM precursor. Hence, a larger composition gradient was observed in 100% HA cladding than FGM cladding after melting and subsequent solidification.

In order to clad a particular area multiline laser cladding was done with 21.6 J/mm^2 LED and 0.8 mm line gap. The surface morphologies of (a) 100% HA and (b) FGM multiline

laser cladding are shown in Figure A.8. The textured surface can be observed in 100% HA cladding sample (low magnification, Figure A.8 (a)), whereas plane surface can be seen in case of FGM cladding sample (low magnification, Figure A.8 (b)). As shown in Figure A.3 and A.4, lower clad width and CL height were observed during single line 100% HA cladding than FGM cladding. Further, with same line gap (0.8 mm) between laser tracks, less overlapping was occurred between cladded lines in 100% HA cladding as compared to FGM cladding. In addition, with a pulsed laser, overlapping between laser pulses occurred, however, due to less melting, overlapping between cladded spots was reduced in 100% HA cladding; hence, textured surface was obtained. Because of more overlapping between cladded spots as well as lines, plane or smooth coated surface was found in FGM cladding sample.

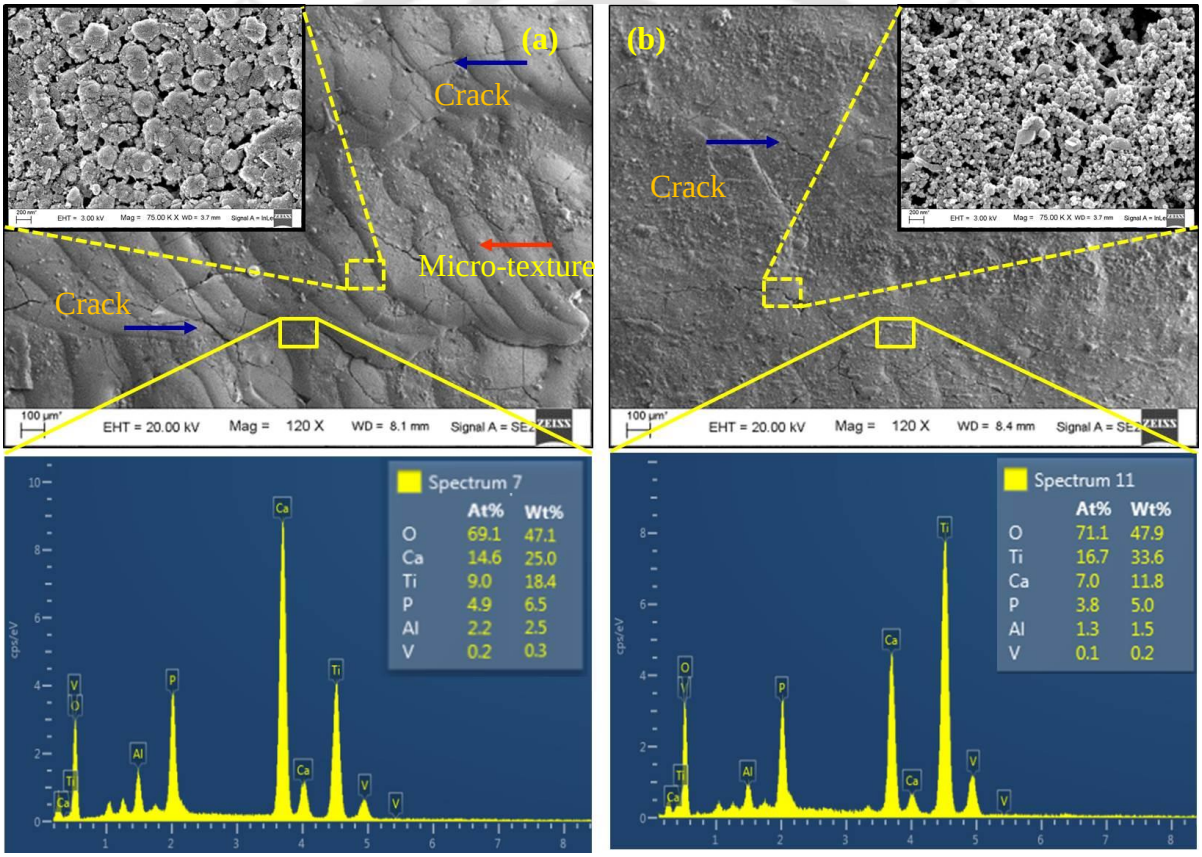

Figure A.8: *Surface morphologies and corresponding EDS analysis of (a) 100% HA and (b) FGM laser cladding. The inset figures (scale bar: 200 nm) indicate the magnified view of selected region.*

Furthermore, more number of cracks can be noticed on the surface of 100% HA cladding (Figure A.8 (a)). However, FGM cladding comprised of less number of cracks on the surface (Figure A.8 (b)). It is a well known fact that laser cladding is a thermal process where coating as well as a little portion of substrate material melted and solidified at a very

high cooling rate. Generally, cracks are generated during solidification due to the stress developed from the steep temperature gradient, solidification shrinkage and difference in the coefficient of thermal expansion (CTE) between coating and substrate (Kagawa et al., 2002). CTEs of HA, TiO_2 and Ti-6Al-4V are 13.3×10^{-6}/K, 9.4×10^{-6}/K and 8.6×10^{-6}/K, respectively (Chien et al., 2011a). The percentage difference of CTE between coating and substrate is calculated concerning the substrate, as reported by Rodriguez et al. (2016). Hence, in 100% HA cladding, the percentage difference of CTE between coating (HA) and substrate (Ti-6Al-4V) is 54.6%. Due to this considerable percentage difference, compressive stress was generated in the rapidly solidified surface, i.e. in the coating material (Lee et al., 2015). This induced the tensile stress in Ti-6Al-4V which is mainly responsible for crack generation and propagation.

In FGM cladding, almost equal percentage of HA and TiO_2 were preplaced in five layers. Thus, the percentage difference of CTE between coating (average of HA-TiO_2) and the substrate is almost 31.9%. Due to this decrease of the percentage difference in TCE between coating and substrate, tensile stress induced in the substrate was reduced. Hence less crack was generated in FGM cladding. In addition, the overlapping area between two consecutive clads during multiline laser cladding was larger due to higher CL thickness and width in FGM cladding compared to 100% HA cladding (Figure A.3 and A.4). Thus, the preheated area in FGM cladding was larger after first laser scanning. Hence, the preheating effect was more in FGM cladding, resulted in the lesser temperature gradient. So, reduction of cracks was found in FGM cladding compared to 100% HA cladding. Hence, due to the simultaneous effect of the higher overlapping area as well as a lesser difference in CTE between coating and substrate, lesser cracks were resulted in FGM cladding compared to 100% HA cladding.

The magnified view of the selected region of claddings (100% HA and FGM) presented as inset clearly indicates the morphology of the corresponding surfaces. Both the cladded surfaces consisted of fine nano-metric spherical particles as well as rough surface morphology. As compared to 100% HA cladding, FGM cladding had smaller nano-sized spherical particles, as shown in the inset, Figure A.8 (a and b). Because of smaller nano-sized particles as well as rough surface, the surface area was increased more in FGM cladding compared to 100% HA cladding which can attract more number of osteoblasts and enhance the cell adhesion with the implants (Wang et al., 2007; Zhang et al., 2011b).

The EDS spectra from a selected area revealed the presence of different elements like Ca, P, Ti, O, Al and V in the cladded layer (Figure A.8). The atomic percentage (at%), as well as weight percentage (wt%) of each and individual elements, are also provided with the corresponding figures. It was found that 100% HA cladding sample contains 14.6 % Ca and 4.9% P, however, FGM cladding sample consists of 7.0% Ca and 3.8% P. The individual atomic % of Ca and P was more in case of coating with 100% HA cladding than that of FGM cladding. Though the presence of Ti in FGM cladding surface indicates the presence of TiO_2, however, in 100% HA cladding it reveals the indication of dilution. Again, the presence of Al and V in both the cladding surfaces indicating dilution, however, more amounts of Al and V with the presence of Ti confirms much more dilution in 100% HA cladding as compared to FGM cladding. From the above findings, it is concluded that dilution of the substrate occurs due to the melting of the precursor as well as the substrate. In addition, comparatively less dilution occurs in FGM cladding as compared to 100% HA cladding.

A.3.3 Phase analysis

The XRD spectrum of the 100% HA and FGM cladding at LED of 21.6 J/mm^2 is shown in Figure A.9. For 100% HA cladding, the cladded surface was composed of calcium titanate ($CaTiO_3$), β-dicalcium pyrophosphate (β-$Ca_2P_2O_7$), calcium oxide (CaO), Ti and TiO_2 (rutile). For FGM cladding, the surface was composed of $CaTiO_3$, tricalcium phosphate (α-$Ca_3(PO_4)_2$, β-$Ca_2P_2O_7$ and TiO_2 (both anatase and rutile).

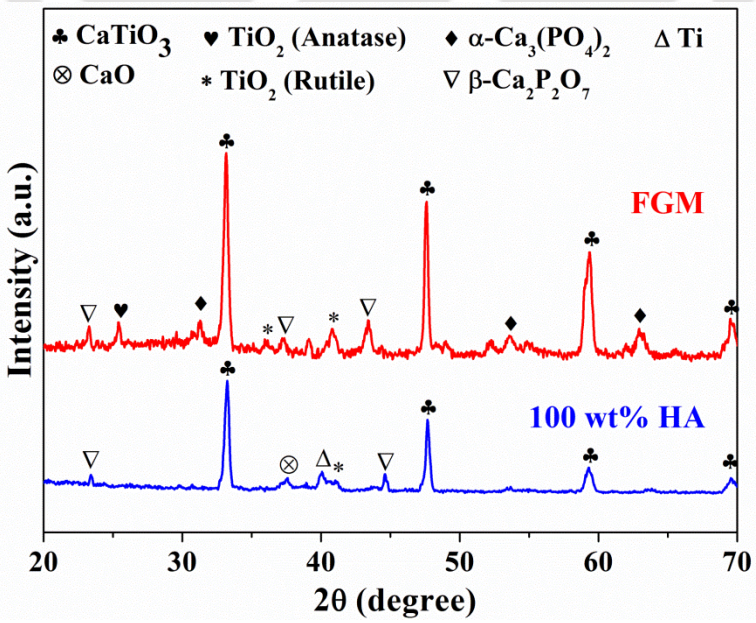

Figure A.9: *Phase analysis of 100% HA and FGM laser cladding by XRD diagram.*

It was found that the main characteristic peaks corresponded to $CaTiO_3$ phases for both the claddings. However, no HA compound was found in any of the cladded surfaces. The presence of low-intensity peaks such as α-$Ca_3(PO_4)_2$ and β-$Ca_2P_2O_7$ in the coated layer can enhance the apatite formation (bioactivity) at the interface between the implant and host tissue (Paital et al., 2010; Yang et al., 2010). As compared to 100% HA cladding, more and intense bioactive peaks were present in FGM cladding. Additionally, some peaks of TiO_2 (both anatase and rutile) were also observed in FGM cladding. TiO_2 enhances apatite formation and cell-material interaction as reported by Balla et al. (2009) during structurally graded Ti-TiO_2 coating on Pure Ti. During immersion in SBF solution, TiO_2 generates Ti-OH groups which act as preferential nucleation sites for apatite deposition (Balla et al., 2009; Paital and Dahotre, 2009). The obtained XRD peaks were compared to XRD patterns of HA (JCPDS no. 09-0432), $CaTiO_3$ (JCPDS no. 750437), α-$Ca_3(PO_4)_2$ (JCPDS no. 090169), β-$Ca_2P_2O_7$ (JCPDS no. 730440), CaO (JCPDS no. 772010), Ti (JCPDS no. 441294), TiO_2 (anatase, JCPDS no. 841286) and TiO_2 (rutile, JCPDS no. 211276).

The phase compositions found in the surfaces of both cladded layers were highly complex. This indicated that the precursor powders were completely melted and formed bioactive phases during the LC process. The process included occurrence of (1) thermal decomposition of HA at high temperature, (2) reaction of HA and its decomposition phases with TiO_2 as well as Ti-6Al-4V alloy and (3) non-equilibrium effect of rapid remelting and solidification during LC process. The high-temperature laser beam induces a chemical interaction between Ti alloy and 100% HA or FGM precursor. The possible reactions between HA or HA-TiO_2 and substrate can be represented in Eq. A.5 - Eq. A.8 (Lusquiños et al., 2001; Roy et al., 2011a; Yang et al., 2011):

$$HA + TiO_2 \rightarrow CaTiO_3 + Ca_3(PO_4)_2 + H_2O \quad \text{(A.5)}$$

$$Ca_3(PO_4)_2 + TiO_2 \rightarrow CaTiO_3 + Ca_2P_2O_7 \quad \text{(A.6)}$$

$$Ca_2P_2O_7 + Ti \rightarrow CaTiO_3 + CaO + P_2O_3 \uparrow \quad \text{(A.7)}$$

$$2P_2O_3 + 3Ti \rightarrow 3TiO_2 + 4P \quad \text{(A.8)}$$

Pure HA phase was not obtained in any of the laser cladding samples, indicating complete decomposition of HA in both the laser cladding. When HA is preplaced and subjected to a high-temperature laser beam, it decomposes to $Ca_3(PO_4)_2$, further increase in temperature evolves $Ca_2P_2O_7$ and finally, CaO is formed due to subsequent thermal

decomposition. From XRD analysis, it can be seen that 100% HA cladding comprised of CaO and less number of β-$Ca_2P_2O_7$ peaks, while FGM cladding consisted more number of α-$Ca_3(PO_4)_2$ and β-$Ca_2P_2O_7$ peaks. It indicates that less heat was absorbed by HA present in FGM cladding as compared to HA present in 100% HA cladding. Hence, it can be concluded that less decomposition of precursor occurs in FGM cladding than that in 100% HA cladding due to the presence of TiO_2. Besides, the presence of more and biocompatible peaks (α-$Ca_3(PO_4)_2$ and β-$Ca_2P_2O_7$) in FGM cladding may induce good bioactivity behavior than that of 100% HA cladding.

TiO_2 (anatase) was observed in FGM cladding but not in 100% HA cladding; however, due to the high-temperature laser beam, the substrate was oxidized, and TiO_2 (rutile) was generated. More and higher intensity peaks belonged to $CaTiO_3$ in both the cladding, which forms due to the interaction between HA and its decompositions with TiO_2 and Ti-6Al-4V substrate. Hence, it can be concluded that more dilution of the substrate occurs during LC, which was in good agreement with EDS analysis (Figure A.8).

In 100% HA sample, a small CaO phase appeared, however, it was utterly absent in FGM samples. CaO is toxic and irritates when comes in direct contact with skin or eye, but the formation of CaO from HA post laser treatment may not be hazardous as it is present in the blended form. Moreover, upon exposure to SBF, 100% HA cladded samples exhibited no CaO compound and showed better bioactivity and cell adhesion as compared to non-cladded Ti-6Al-4V (as discussed later in section A.3.6-A.3.8). FGM cladding shows better cell adhesion and cyto-compatibility as compared to 100% HA cladding and non-cladded Ti-6Al-4V. CaO converts to $Ca(OH)_2$ as it is soluble in water present in SBF (Paital et al., 2008). Zheng et al. (2008) and Yang et al. (2011) also obtained bioactivity and osteoblast response on the surface of laser cladded bioceramic coating despite the presence of CaO phase in the surface of coating. Li et al. (2015a) found apatite layer precipitation after soaking the laser cladded CaO-SiO_2 coating in SBF.

The appearance of Ti can be attributed to the high penetration depth of X-ray because of significant loss of HA during laser melting. This loss is due to vaporization as well as dilution of precursor with Ti-6Al-4V through intermixing of elements. Again, the penetration depth of X-rays is generally in the order of few hundred microns, as discussed by Nag et al. (2013). As the CL thickness was varied in between 50-100 µm, thus, Ti was observed with other phases in the XRD graph. Similar findings were reported by Nag et al. (2013) during laser melting of Ca-P bioceramic on Ti-6Al-4V. According to section A.3.1, more CL and less TL thickness are observed in FGM cladding. This indicated less dilution of Ti-6Al-4V in

FGM cladding; hence, Ti peak did not appeared in FGM cladding. Due to more dilution of Ti-6Al-4V substrate, Ti peak appeared in 100% HA cladding; however, the intensity of Ti peak was very less.

In between two different precursors, one consisted only HA, and the other contained HA and TiO_2 with graded structure. All the layers in FGM precursor were converted to one layer due to melting, and Ti-6Al-4V substrate was oxidized at high-temperature to form TiO_2. Hence, the chemical reaction took place between HA and TiO_2, resulted in $CaTiO_3$. Also, $Ca_3(PO_4)_2$ was obtained due to decomposition of HA when the high-temperature laser beam was irradiated on it. Again the reaction took place between $Ca_3(PO_4)_2$ and TiO_2 to generate $CaTiO_3$. Now, $Ca_3(PO_4)_2$ was decomposed to form $Ca_2P_2O_7$. Finally, $Ca_2P_2O_7$ reacted with TiO_2 from which all the P evaporated, and CaO evolved, and $CaTiO_3$ formed. Since CaO was only seen in 100% HA cladding and all other compositions were observed in both the cladding, it can be concluded that the first three chemical reactions occurred during 100% HA cladding (Eq. A.5 – Eq. A.7)., whereas first two reactions exhibited during FGM cladding (Eq. A.6 and Eq. A.8).

A.3.4 Wettability and surface roughness

The wettability of surface has a significant influence on bioactivity, protein adsorption as well as cell adhesion, which generally depends upon the chemical phases and roughness of surface (Bakhsheshi-Rad et al., 2016b; Paital and Dahotre, 2009). The optical images of SBF liquid droplet shadow on non-cladded Ti-6Al-4V, 100% HA and FGM cladding surfaces are demonstrated in Figure A.10 (a, b, c), respectively. Figure A.10 (d, e, f) shows the wettability of different surfaces after protein adsorption, as discussed later in section A.3.5. SBF contact angle on non-cladded Ti–6Al–4V, 100% HA and FGM cladding surfaces are 91.9° (±1º), 71.3° (±2º), and 60.6° (±2º), respectively. This indicates that hydrophilicity of non-cladded Ti-6Al-4V increases upon 100% HA and FGM laser cladding. Although, there was no formation of hydrophilic HA phase in the cladded surface, the reduced contact angle was attributed to the effect of surface texture and other biocompatible phases (α-$Ca_3(PO_4)_2$, β-$Ca_2P_2O_7$ and TiO_2 (rutile and anatase)) evolved during LC (Bakhsheshi-Rad et al., 2016b; Paital et al., 2010). The FGM cladded surface showed better-improved wettability as compared to 100% HA cladded surface. This may be attributed to the formation of smaller nano-metric particles on the FGM cladded surface (Figure A.8 (b)), which provides a higher surface area to spread the SBF drop more. So, wettability was improved as compared to 100% HA cladded surface. In addition, because of formation of more bioactive phases (α-

$Ca_3(PO_4)_2$ and TiO_2 (anatase)) with the phases (β-$Ca_2P_2O_7$ and TiO_2 (rutile)) in the FGM cladding as these phases provide a synergistic effect to make the surface more hydrophilic.

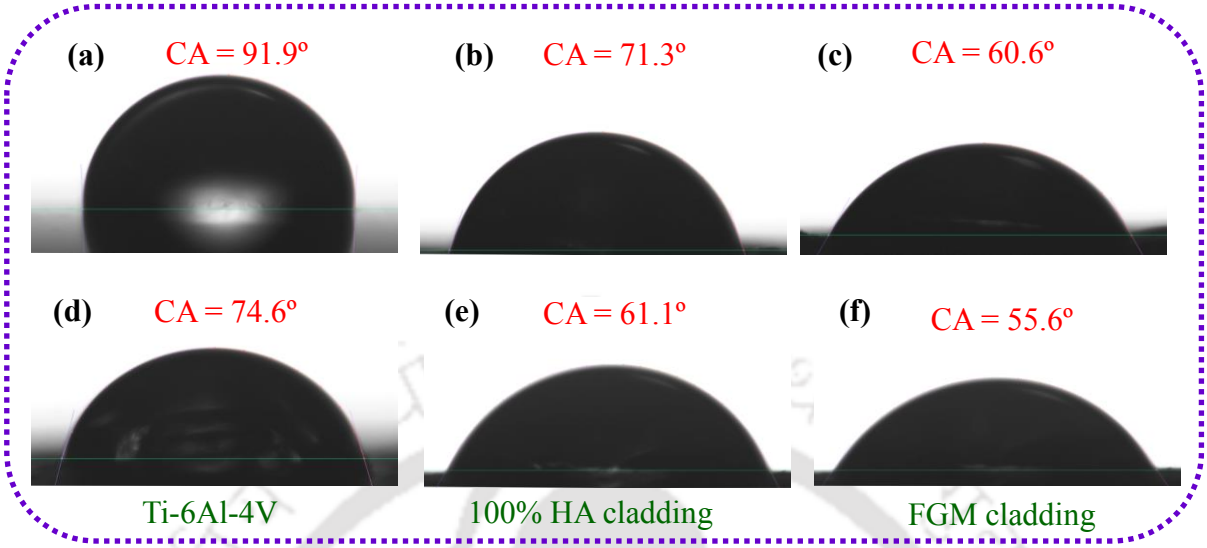

Figure A.10: *Optical images of SBF contact angle of non-cladded Ti-6Al-4V, 100% HA and FGM cladding (a, b, c) before and (d, e, f) after protein adsorption.*

The roughness (R_a) of non-cladded Ti-6Al-4V was 0.99±0.1 µm. The FGM cladding had a plane surface with less roughness (R_a = 3.57±0.4 µm) whereas 100% HA cladding had textured surface with higher roughness (R_a = 5.16±0.5 µm). Thus, the intrinsic energy related with SBF liquid drop was overcome the energy barrier associated with the FGM cladded surface more compared to that with 100% HA cladded surface. So, the liquid droplet spread more and wettability was higher in FGM cladded surface. A similar trend of varying wettability with surface roughness was reported by Paital and Dahotre (2009).

A.3.5 Protein adsorption

Protein adsorption is an important and initial most process that takes place on implant surface when it comes in contact with blood. Protein adsorption regulates the fate of implant as these proteins act as cushions for cell adhesion and moreover help them in spreading and in extracellular matrix (ECM) formation (Hasan and Pandey, 2015). Various surface physicochemical properties such as surface chemistry and wettability play a major role in regulating protein adsorption (Pandey and Pattanayek, 2011, 2013b). Hence, the effect of surface-modified titanium alloy in comparison to non-cladded Ti-6Al-4V alloy on protein adsorption was studied (Figure A.11). 100%HA (2.94 µg/cm^2) and FGM (4.14 µg/cm^2) claddings showed a significantly higher amount of adsorbed mass of protein than non-cladded Ti alloy (1.31 µg/cm^2). Comparatively higher amount of adsorbed protein mass on

FGM may be attributed to the surface's composition and wettability of FGM cladding (θ=60.6°) as compared to 100% HA (θ=71.3°) cladding.

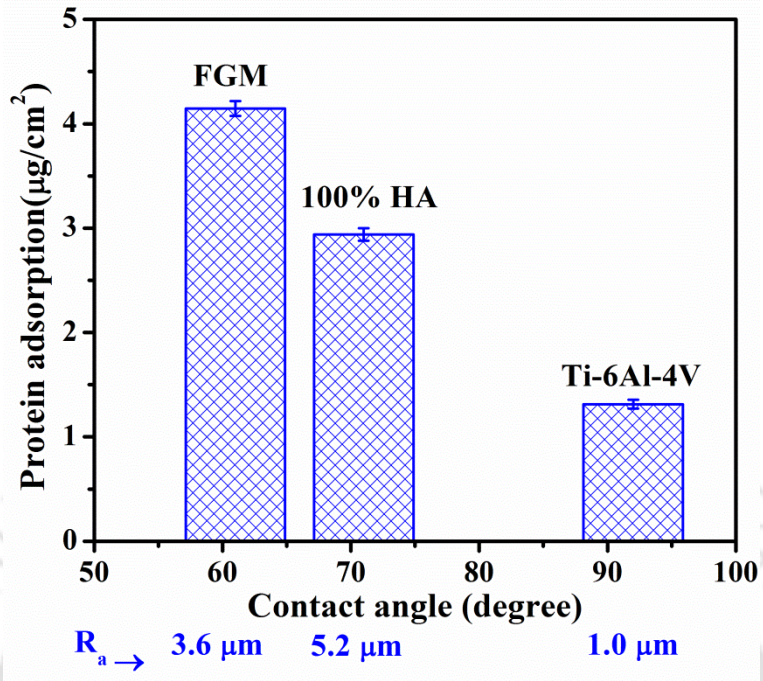

Figure A.11: *Adsorbed protein mass on non-cladded Ti-6Al-4V, 100% HA and FGM cladding.*

The inorganic phases of decomposed HA in ionic form carry and impart the negative charge to the surfaces. FGM cladded surface carried more negative charge density due to more number of multivalent anions as compared to 100%HA claddings. Hence, it was assumed that due to more negative charge density on FGM cladding, more hydrogen bonding interactions took place between positively charged amino acid residues of protein and surface as compared to 100% HA cladded surface. Due to such enhanced interactions, more protein adsorption took place at FGM relatively to 100%HA cladding.

There was no relationship found between surface roughness and adsorbed protein mass, as protein adsorption was maximum for FGM cladding (R_a=3.6 μm) and decreased for 100%HA cladding with higher surface roughness (R_a=5.2 μm), and again it was found reducing when roughness reduced to 1 μm in non-cladded Ti-6Al-4V (Figure A.11). Surface roughness although increases surface area available for protein adsorption (Rechendorff et al., 2006) but may not always be universally true for all the surfaces. For instance, upon increasing the surface roughness from nano to micrometers, surface topology appears smoother to protein adsorption, having very little influence on adsorption process (Han et al., 2003; Yap and Zhang, 2007). Hence, it was concluded that surface roughness of present

cladded surfaces at micrometers scale plays no significant role in serum protein adsorption; however, it is mainly influenced by surface chemistry and wettability.

Figure A.10 (d, e, f) shows the contact angles on non-cladded Ti-6Al-4V, 100% HA and FGM cladding surfaces after protein adsorption. Post protein adsorption, the wettability increased on all the surfaces indicating the formation of the protein layer (Sharma and Pattanayek, 2017). Electrostatic and hydrophobic interactions between proteins and surfaces lead to protein adsorption. Different physicochemical properties of surfaces regulate protein behavior and their packing which further results in varying microscopic topographies and macroscopic properties (surface energy) (Sharma and Pattanayek, 2017), hence different contact angle on different surfaces post adsorption was observed.

A.3.6 Cell adhesion study

The FESEM images of cell morphology after 24 h of proliferation on Ti-6Al-4V, and 100% HA and FGM cladding are shown in Figure A.12. It was observed that both cladded substrates had more number of cells (Figure A.12 (b, c)) on the surfaces as compared to non-cladded Ti alloy (Figure A.12 (a)). However, FGM cladding showed more cells spreading and cell-cell interaction compared to that 100% HA cladding. Non-cladded Ti alloy mostly had osteoblast cells with polygonal shape (inset, Figure A.12 (a)). 100% HA cladding (inset, Figure A.12 (b)) showed a mixed morphologies of cells having leaf and triangular shaped osteoblast cells; however, FGM cladding (Figure A.12 (d)) revealed triangular shape osteoblast distributed throughout its surface, indicating better adhesion and spreading. Magnified image of cell spreading on FGM cladding (Figure A.12 (d)) reveals the presence of lamellipodia (inset, Figure A.12 (d)) which indicates strong adherence of cells at cladding surface (Yang et al., 2011).

However, cell cultured on non-cladded Ti alloy showed irregular cell morphology with less spreading area indicating poor adherence of cells on non-cladded Ti surface. The increase in the number of osteoblast cells and their strong adherence to the cladding can be attributed to the formation of biocompatible phases (α-$Ca_3(PO_4)_2$, β-$Ca_2P_2O_7$ and TiO_2 (anatase and rutile)) as well as nano-sized particles on the cladded surface (Figure A.8) which in turn improve the wettability of the surface. The surface with higher wettability shows higher surface free energy, and thus FGM cladded surface exhibited more adhesion toward bone cells and cell binding proteins than lower wettability 100% HA cladded surface.

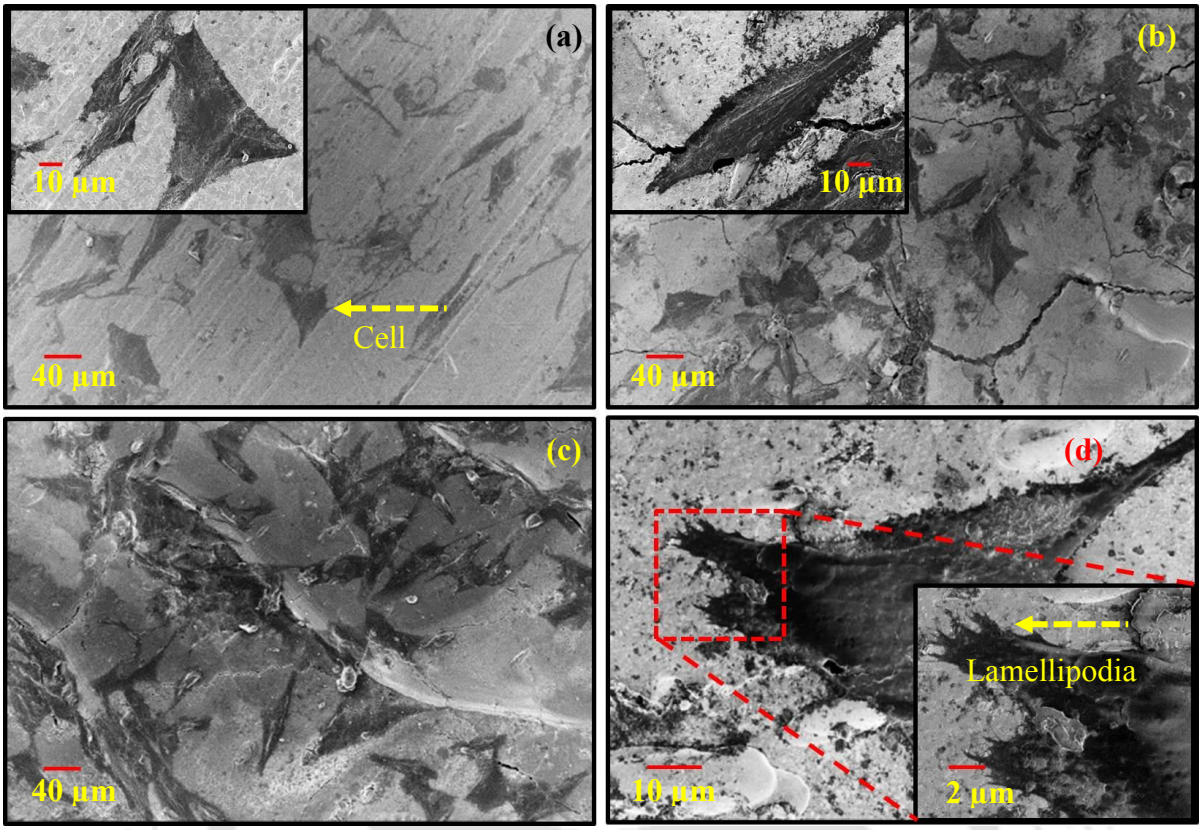

Figure A.12: *FESEM images for cell morphology after 24 h of proliferation on (a) non-cladded Ti-6Al-4V, inset shows magnified image (b) 100% HA cladding, inset shows magnified image, (c) FGM cladding and (d) Magnified image of FGM sample having inset that shows lamellipodia indicating strong cellular adhesion.*

Figure A.13-A.14 shows the adhesion of osteoblast cells cultured on different surfaces for 12 h. The morphology of the adhered cells varies with properties like surface wettability, roughness and cell type. The effect of surface treatment in regulating cell adhesion and spreading process for better osteointegration was reported in this work. Cells adhered to non-cladded and LC samples showed a substantial difference regarding of % cells adhered and spreading, as shown in Figure A.13. The maximum cell density was observed on FGM cladding (85±8%) followed by 100% HA (71±11%) while the least number of cells were observed at non-cladded Ti-6Al-4V (60±2%), as shown in Figure A.14 (a). This clearly indicates that both cladded samples exhibited good affinity towards MG-63 cells as compared to the non-cladded substrate. This can be directly attributed to the amount of adsorbed proteins which serve as the cushion for upcoming and adhering cells. Apart from BSA which constitutes 50-60% (35-50 mg/mL) of the serum proteins, fibronectin (FN) concentration (220 µg/mL) (Mccafferty et al., 1983) too is sufficient enough for promoting cell adhesion and spreading (Zelzer et al., 2012). Increase in adsorbed protein concentration at FGM cladding as compared to 100%HA and non-cladded Ti-6Al-4V may be held responsible for

better adhesion of cells at FGM cladding as compared to both non-cladded Ti-6Al-4V and 100%HA cladding.

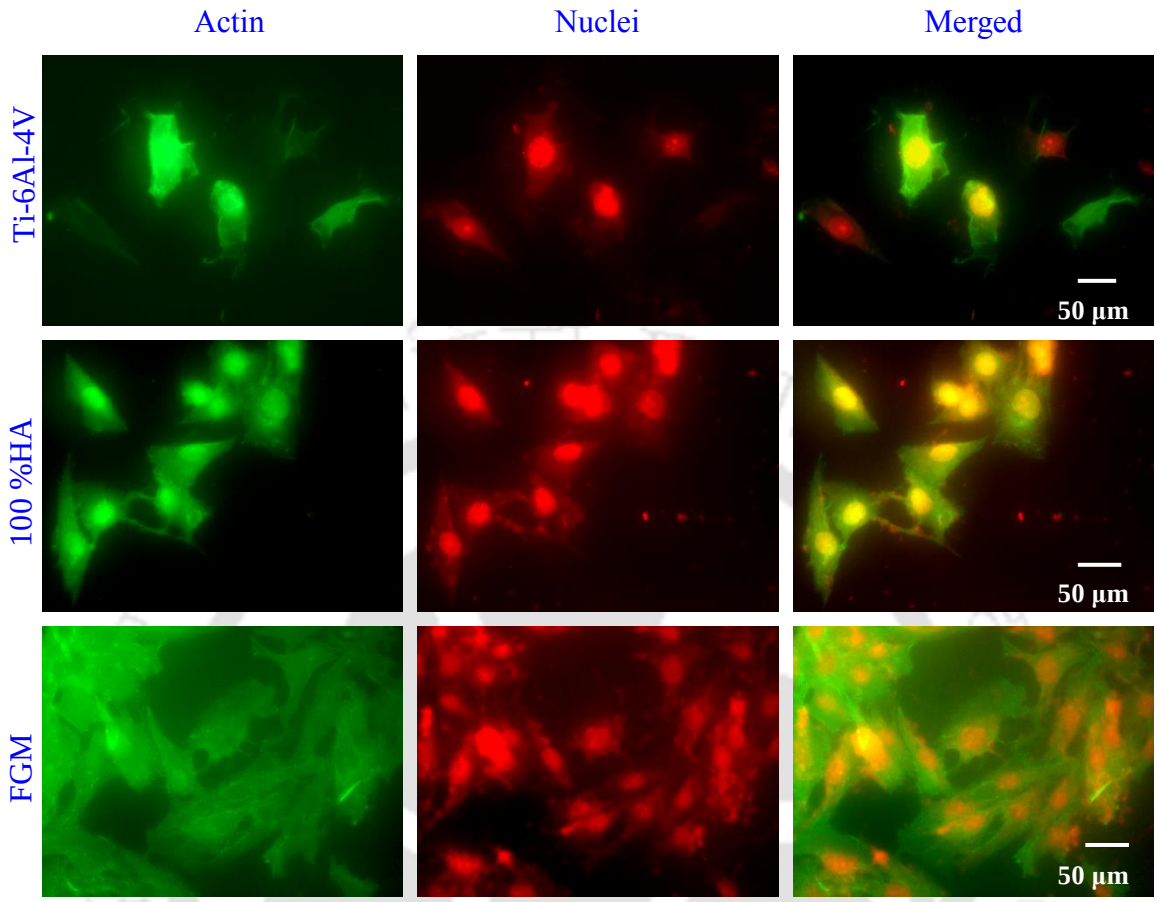

Figure A.13: *Fluorescent images for MG63 cells adhered on the surface of non-cladded Ti–6Al–4V, 100% HA cladding, FGM cladding after 12 h, showing actin filaments (green, stained by FITC-Phalloidin), and the nucleus (red, stained by PI dye).*

In addition, the various cell features such as average cell area, nuclei area and circularity on different samples were investigated, using image processing (ImageJ) software. As shown in Figure A.14 (a), FGM cladding exhibited maximum cell spreading area (2135±437 µm^2) followed by 100% HA (1772±253 µm^2) and non-cladded Ti-6Al-4V (1525±231 µm^2) substrates. Less spreading on non-cladded Ti-6Al-4V indicates poor focal adhesions as compared to cladded samples. Moreover, the numbers of filopodia and cytoplasmic extensions were also less on cells grown on non-cladded Ti-6Al-4V. The nuclei area of the adhered cells also followed the similar trend, FGM cladding > 100% HA cladding > non-cladded Ti-6Al-4V as that of the cell area. Nuclei size of the adhered cells signifies the nuclear functional activity occurring during cell differentiation and cyto-compatibility (Tutak et al., 2017). More the nucleus area higher will be the division rate which leads to higher cyto-compatibility rate.

Cells circularity is described on the scale range of 0 to 1 and defines the degree of polarization and is used to describe the shapes of the cell which can exist in circular (circularity=1), square (circularity=0.79), or in various rectangular (circularity=0.7, 0.5 or 0.26) forms (Kushiro et al., 2016). The lesser the circularity value, the better is cell spreading having more focal points due to which cell shape changes. Cell circularity on FGM (0.60±0.11) and 100% HA cladding (0.70±0.1) showed least values indicating better adhesion and spreading in comparison to non-cladded Ti-6Al-4V (0.73±0.1), as presented in Figure A.14 (b).

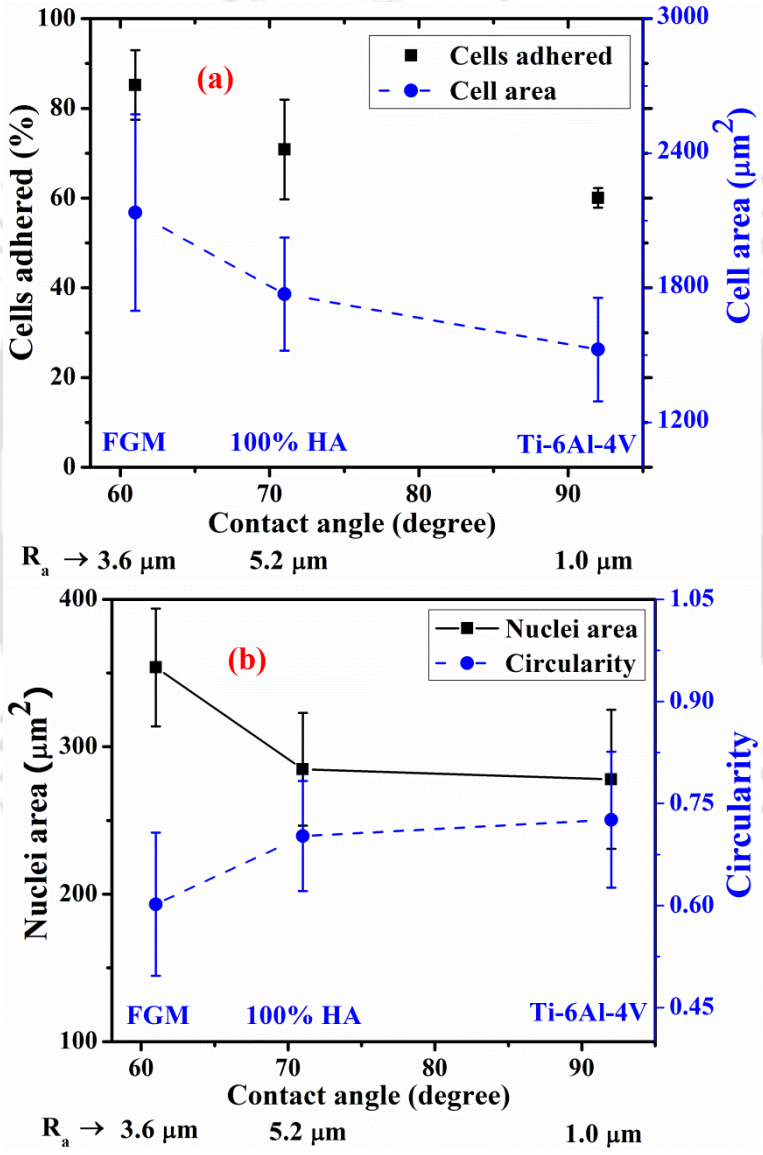

Figure A.14: *Effect of different surfaces on (a) % cells adhered, average cell area and (a) average nuclei area and circularity of adhered cells.*

Surface properties like wettability, topologies, surface charge, and roughness play an essential role in regulating protein adsorption which in turns regulates cell adhesion and spreading (Chu et al., 2016; Huang et al., 2016; Moon et al., 2017). Figure A.15 illustrates the

schematic diagram of the mechanism of protein adsorption, cell adhesion and spreading on non-cladded as well as LC samples. Generally, surfaces with a moderate hydrophobicity, i.e. water contact angle (θ) in the range 40-70º, exhibit better protein adsorption and hence supports cell adhesion. However, there exist huge discrepancies among the scientific community about the exact role of surface wettability in regulating biocompatibility.

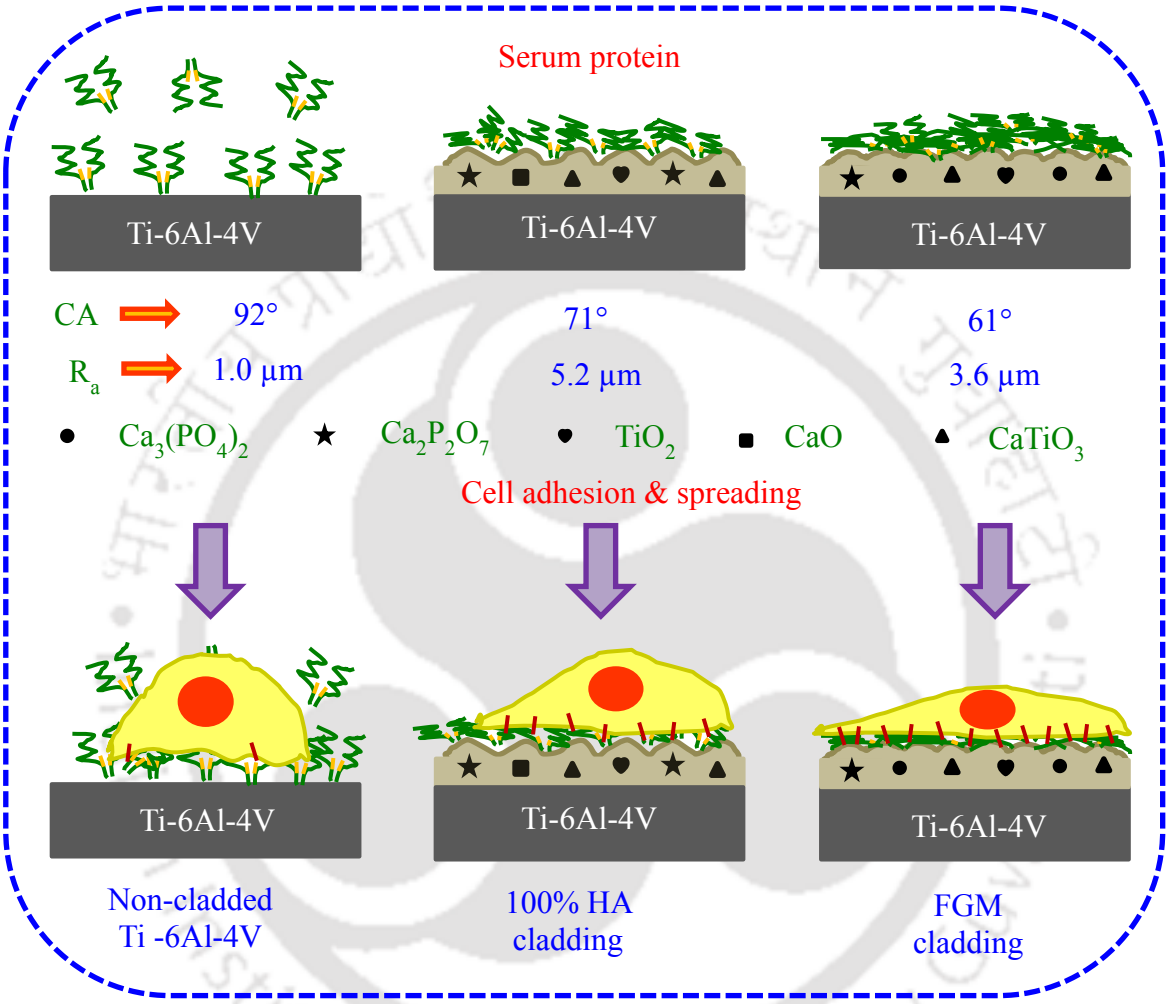

Figure A.15: *Schematic diagram of mechanism of protein adsorption, cell adhesion and spreading on non-cladded as well as LC surfaces.*

Many reports suggest that high wettability and surface energy promote cell adhesion and spreading while few argued that hydrophobic surfaces enhance protein adsorption and cell behavior (Gentleman and Gentleman, 2014; Groth and Altankov, 1996; Howlett et al., 1994). In the present study, the adsorbed mass of serum proteins increased with the increase in the wettability of the surfaces, as shown in Figure A.11 with the FGM (4.14 µg/cm^2 at θ=60.6º) exhibiting maximum adsorbed mass. Better protein adsorption promotes cell adhesion as they serve as a soft layer which helps them to adhere to the surface. It was observed that maximum cell adhesion and spreading on hydrophilic FGM cladding (θ=60.6º)

followed by 100% HA cladding (θ=71.3º) and hydrophobic non-cladded Ti-6Al-4V (θ=91.9º) substrates. Similar cell behavior has been previously reported by various research groups (Hotchkiss et al., 2016; Le Guehennec et al., 2008; Zhao et al., 2007).

A.3.7 *In vitro* bioactivity

In vitro bioactivity of an artificial material can be estimated by checking the formation of apatite layer after soaking in SBF (Paital et al., 2008). This apatite layer provides the required surface chemistry for cell attachment and cyto-compatibility (Paital et al., 2010). The phase compositions of both LC samples after 14 days immersion in SBF are displayed in Figure A.16. The HA apatite peaks observed in XRD pattern correspond to characteristics HA peaks at 2θ ≈ 25.9°, 31.7°, 32.3°, 35.6°, 53.2° and 63.9° (representing the planes (002), (211), (112), (301), (004) and (304), respectively) from the JCPDS 09-0432. Compared to XRD pattern before SBF immersion (Figure A.9), it is seen that HA was precipitated on both LC surfaces after SBF immersion. However, more intense HA peaks appeared in FGM cladding than 100% HA cladding indicating more apatite precipitation for FGM cladding. This may be attributed to more wettability and biocompatible phases of FGM cladding so that more nucleation and formation of apatite occurred as compared to 100% HA cladding.

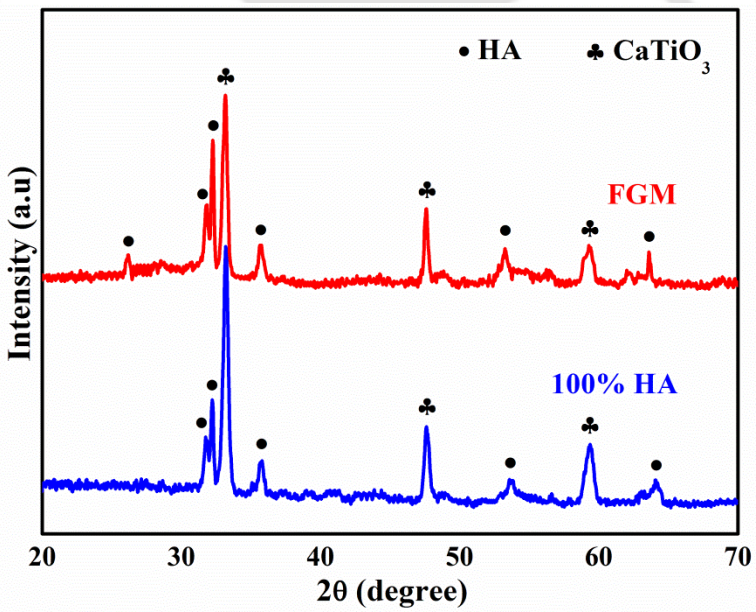

Figure A.16: *Phase analysis of 100% HA and FGM cladding surfaces after 14 days immersion in SBF.*

Figure A.17 represents the surface morphologies as well as elemental analysis of both LC substrates after immersion in SBF for 14 days. Since there was no significant amount of apatite layer on non-cladded Ti-6Al-4V even after immersing in SBF for 14 days; hence, the

related surface morphology and elemental analysis related to it are not provided herein. After 14 days of soaking, small globular or spherical-like precipitate layer nucleated and grew on the surface of both 100% HA and FGM samples (Figure A.17 (a, b)).

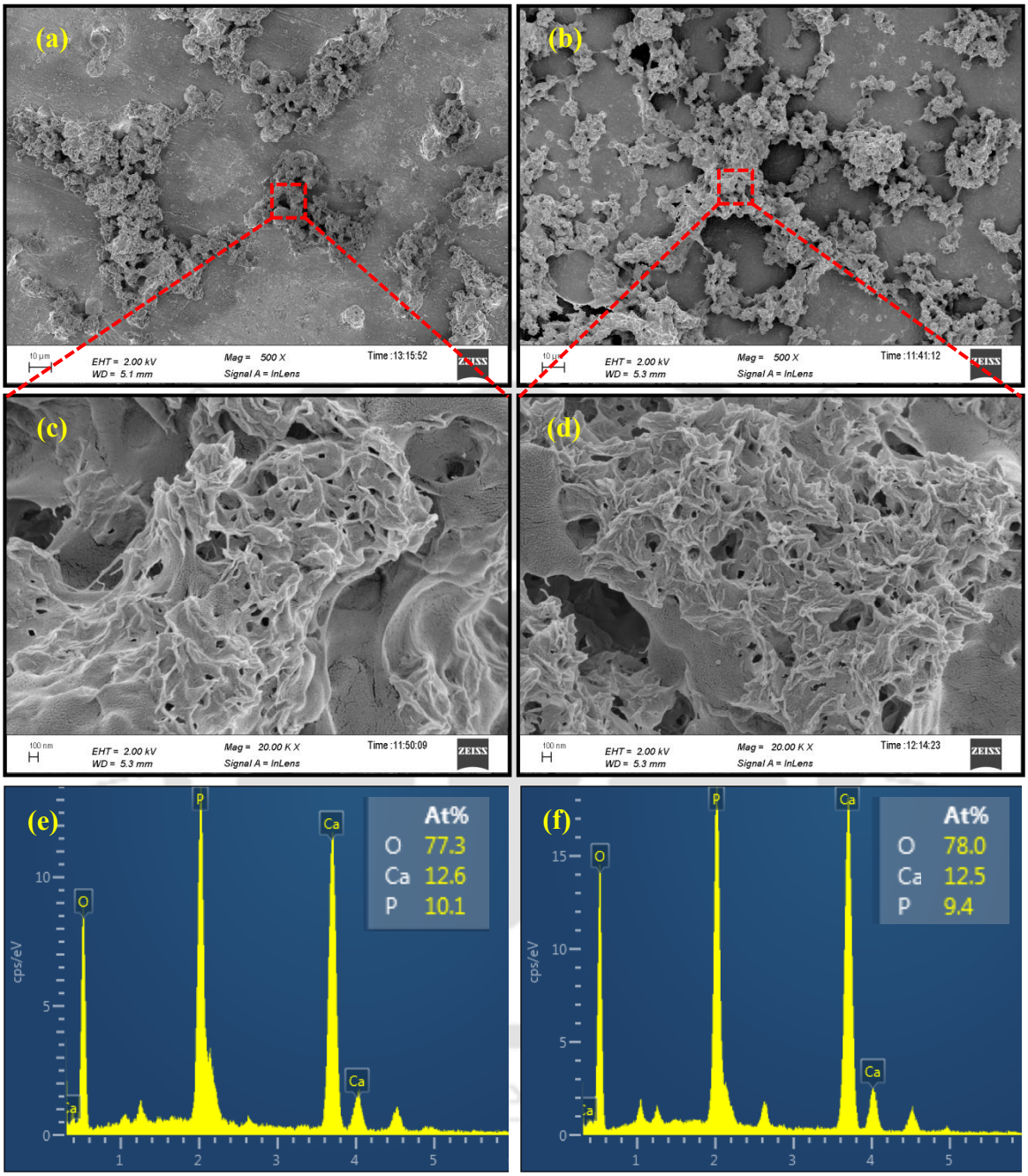

Figure A.17: *Surface morphologies and EDS analysis of 100% HA and FGM cladding after soaking in SBF for 14 days: (a, b) lower magnification, (c, d) higher magnification and (e, f) EDS spectra taken at small area shown in (a, b).*

The presence of globular-like morphologies is the characteristics of apatite formation, which is beneficial for osseous connection (Li et al., 2015d; Paital and Dahotre, 2009). However, the amount and size of globular-like precipitate layer were more prominent on the FGM sample as compared to 100% HA sample as shown in Figure A.17 (a, b). These

findings are matched with XRD results (Figure A.16). From higher magnification images, it was clearly visible that, the precipitate layer contained nano-sized crystals (Figure A.17 (c, d)). It can be observed from EDS spectra that both claddings contained major peaks of Ca, P and O only, confirming the presence of apatite layer on cladding samples after immersion in SBF (Figure A.17 (e, f)). Since the EDS spectrum was taken at a small area on the apatite formed on the cladding samples, no element from cladded material was detected. So, from all these XRD, FESEM and EDS results, it can be concluded that both LC samples immersed in SBF have the potential to produce apatite layer more effectively as compared to non-cladded Ti alloy. The production of globular particles as well as the presence of major peaks of Ca, P and O on the cladding samples after soaking in SBF was also reported previously (Paital and Dahotre, 2009; Yang et al., 2011).

The formation of calcium phosphate apatite layer on the surface of LC after immersion in SBF solution is a process of heterogeneous nucleation and growth. There were many phases evolved in the LC surface, such as $CaTiO_3$, β-$Ca_2P_2O_7$, α-$Ca_3(PO_4)_2$, β-$Ca_3(PO_4)_2$, Ti, CaO and TiO_2 (anatase and rutile). Different phases like $Ca_3(PO_4)_2$, $Ca_2P_2O_7$, CaO and TiO_2 are the crucial biomaterial components which cause bone bonding with the bone tissue (Balla et al., 2009; Paital et al., 2010). Because of the presence of $Ca_3(PO_4)_2$, $Ca_2P_2O_7$, CaO and TiO_2 in the cladded surface, the cladding immersed in SBF solution has the potential to form apatite.

When LC samples were immersed in SBF, O-H bond was easily formed by $Ca_3(PO_4)_2$, CaO, TiO_2 under wetting conditions (Li et al., 2015b; Paital et al., 2008; Paital and Dahotre, 2009).

$$3Ca_3(PO_4)_2 + H_2O \rightarrow Ca_9HPO_4(PO_4)_5OH \quad \text{(A.9)}$$

$$CaO + H_2O \rightarrow Ca(OH)_2 \quad \text{(A.10)}$$

$$TiO_2 + 2H_2O \rightarrow (TiOH)_4 \quad \text{(A.11)}$$

With these negatively charged OH^- ions present on the surface, Ca^{2+} ions from the SBF were attracted towards the negatively charged (OH^-) surface and got accumulated there. Then negatively charged phosphate ions (PO_4^{3-}) present in the SBF were attracted towards the surface and reacted, which leads to form apatite nuclei on the surface as per the following equation (Bakhsheshi-Rad et al., 2016b; Daculsi et al., 1990; LeGeros, 1993):

$$2OH^- + 10Ca^{2+} + 6PO_4{}^{3-} \rightarrow Ca_{10}(PO_4)_6(OH)_2 \quad \text{(A.12)}$$

With the increase of soaking time, massive amount Ca^{2+} and $PO_4{}^{3-}$ ions were precipitated on the negatively charged OH^- surface and finally a thick layer of apatite was generated on the cladded surface. As compared to 100% HA, FGM cladding showed improved bioactivity or apatite formation. This improvement in bioactivity was attributed to higher wettability with SBF and presence of more biocompatible phases (α-$Ca_3(PO_4)_2$, β-$Ca_3(PO_4)_2$ and TiO_2 (anatase)). This improved wettability enhanced the reaction between $Ca_3(PO_4)_2$ and TiO_2 with the water molecules present in SBF solution. More biocompatible phases as well as the substantial time of reaction with SBF led to evolving of more OH- ions and attracted higher Ca^{2+} and $(PO_4)^{3-}$ ions on the FGM cladded surface. So, more apatite layer was deposited as compared to 100% HA cladded surface.

A.3.8 Cyto-compatibility assay

MTT assay was performed to study cyto-compatibility on non-cladded Ti-6Al-4V, 100%HA and FGM claddings for 2, 4, and 6 days as shown in Figure A.18. It is clearly revealed that the absorbance for all the samples increased with increase in incubation time, indicating cyto-compatibility on all the tested samples. For all the incubation time periods, the cyto-compatibility rate of both LC samples was comparable and higher than the non-cladded Ti alloy control. At day 6, both cladded samples induced a significant increase in cyto-compatibility than non-cladded Ti alloy while the cyto-compatibility rate of FGM cladding (215.6±17.2%) was significantly higher than 100%HA cladding (134.6±9.5%).

The improvement of the cyto-compatibility rate in FGM cladding can be attributed to the formation of more biocompatible phases (α-$Ca_3(PO_4)_2$, β-$Ca_2P_2O_7$ and TiO_2 (anatase and rutile)), as well as smaller nano size surface particles which in turn improve the wettability of the surface. Moreover, the higher concentration of adsorbed protein molecules at interface promote cell adhesion and spreading as evident by FGM cladding exhibiting more % of adhered cells due to higher protein adsorbed mass. Also due to larger nucleus area, the division rate of cells was higher which led to higher cyto-compatibility in FGM than 100% HA cladding and non-cladded Ti alloy. The surface with higher wettability shows higher surface free energy and has more adhesion toward bone cells and cell binding proteins than those with lower wettability (Paital et al., 2010; Yang et al., 2011).

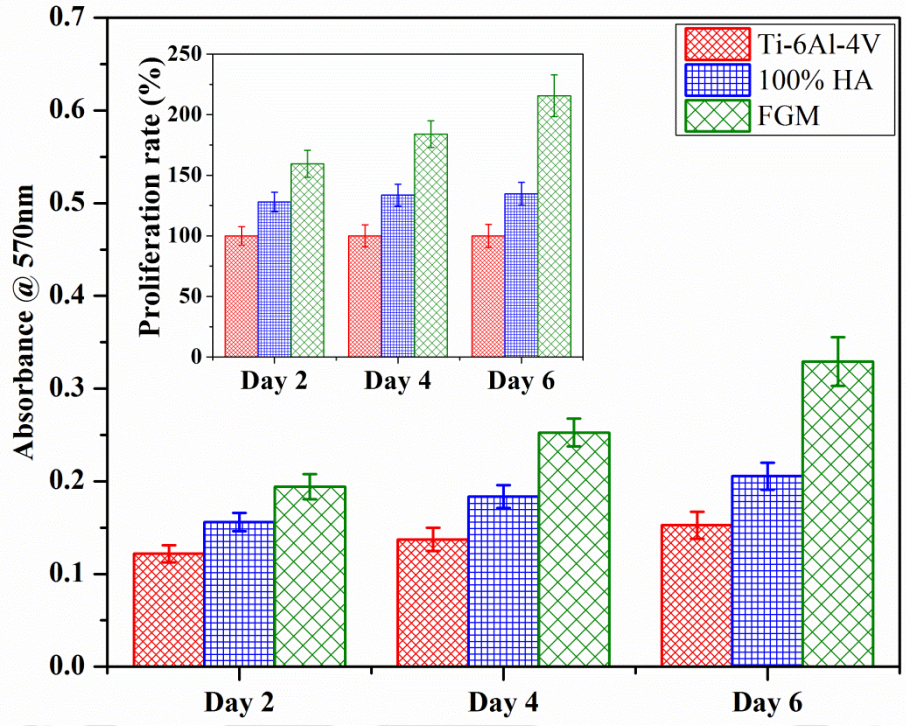

Figure A.18: *Histograms of MTT assay representing cyto-compatibility activities of MG63 cells after 2, 4 and 6 days of growth; inset results are expressed as percentage cyto-compatibility rate on non-cladded Ti-6Al-4V, 100% HA and FGM cladding.*

A.4 Findings from the research work

CaP-TiO_2 bio-ceramic coating was successfully carried out on Ti-6Al-4V substrate by LC process with 100% HA and FGM precursors in order to compare cell interaction with the substrate. For 100% HA cladding, different phases like $CaTiO_3$, CaO, β-$Ca_2P_2O_7$ and TiO_2 (rutile) were formed; however, with FGM cladding, also with new phases like α-$Ca_3(PO_4)_2$, and TiO_2 (anatase) were generated. Due to the addition of TiO_2 in the precursor, the decomposition of HA, cracks and surface particles were reduced during LC. The wettability was improved for both LC samples as compared to non-cladded Ti-6Al-4V; however, FGM cladding shows better-improved wettability as compared to 100% HA cladding.

The FGM cladding showed a significantly higher HA precipitation than 100% HA cladding after immersing in SBF. Both cladded samples had a significantly higher amount of adsorbed mass of protein compared to non-cladded Ti-6Al-4V alloy; however, FGM cladding had more protein adsorption than 100% HA cladding. Compared to 100% HA cladding, there was significantly higher cellular interaction in FGM cladding. Better cell adhesion and spreading of cells were observed for FGM and 100% HA cladding than non-cladded Ti–6Al–4V. A significantly higher cyto-compatibility rate was observed for both 100% HA and FGM claddings. All the outcomes reveal that the LC process improves the biocompatibility and

bioactivity of Ti–6Al–4V. In addition, FGM cladding enhances the biocompatibility as well as bioactivity more as compared to 100% HA cladding.

In this study, better and improved results are found in FGM cladding. However, laser cladding used to obtain the coatings is very complex which comprises of five different preplaced layers. It is complicated to apply five different preplaced layers to real implants having a complex non-flat surface subjected to coating. Up to now, the pre-placed powder laser cladding method has been only used at lab scale on flat surfaces, which are not found on real implants.